Multiple Turbine Wakes

Machefaux, Ewan

Publication date:
2015

Document Version
Publisher's PDF, also known as Version of record

Multiple turbine wakes.

Ewan Machefaux

DTU Risø Campus 2015
Department of Wind Energy-PhD-2015-0043 (EN)

Author Ewan Machefaux
Title: Multiple Turbine Wakes
Institute: DTU Wind Energy

DTU Wind Energy PhD-0043 (EN)
January 2015

ISBN: 978-87-93278-21-9

Summary (max. 2000 char.):

The central goal of the present research was to study single and multiple interacting wind turbine wakes using both full-scale lidar experiments and high fidelity CFD numerical approach, highly relevant for accurate predictions of load and power production of turbines located in wind farm environments. The full-scale wake measurements were obtained using cutting-edge technologies in wind energy remote sensing such as LiDAR (i.e. WindScanner developed at DTU Wind Energy, WindCube and ZephiR). The goal of the experimental analysis was to characterize the organized flow structures as well as the wake generated turbulence resulting from a single wake or the interaction of two wakes as function of downstream distance from the wake generating rotors. The characterization of the organized part of the flow field encompassed a generic analysis of the interaction of the flow structures as well as their downstream attenuation, expansion and transportation. The numerical study was conducted using the in house EllipSys3D flow solver, and covered a large range of generic wind turbine operation. Non-stationary flow conditions were accounted for using the LES (Large Eddy Simulation) approach, and non neutral atmospheric flow were simulated using a newly developed extension of the EllipSys3D flow solver which includes buoyancy effects. The results from experiments and numerical studies are then condensed into several engineering models capturing the essential physics though still sufficiently computational efficient to be of practical relevance. These models are consistent with the existing model entitled the Dynamic Wake Meandering model, thus improving the model formulation for single wakes and extending its application from solitary turbines to wind farms.

Project period:
2011-01-11 to 2014-15-12

Education:
Ph.D.

Research field:
Wind Energy

Supervisor:
Gunner C. Larsen, Jakob Mann

Contract nr.:
DSF Flow Center, Danish Council for Strategic Research (2104-09-0026)

Sponsorship:
G.A Hagemanns Mindefond
Otto Mønsted fond

Pages: 204
Tables: 10
References: 163

Denmark Technical University
DTU Wind Energy
Frederiksborgvej 399
Building 118
DK-4000 Roskilde
+45 25 25 25 25
ewma@dtu.dk
www.vindenergi.dtu.dk

Summary (English)

The central goal of the present research was to study single and multiple interacting wind turbine wakes using both full-scale lidar experiments and high fidelity CFD numerical approaches.

Firstly, single wake dynamics have been studied experimentally using full-scale (nacelle based) pulsed lidar measurements conducted on a stall regulated 500 kW turbine at the DTU Wind Energy, Risø campus test site. As part of the experimental analysis, basic Dynamic Wake Meandering modeling assumptions were validated. A wake center tracking algorithm was used to estimate the measured wake advection velocity and to obtain an estimate of the wake expansion in a fixed frame of reference. A comparison of selected datasets from the campaign showed good far wake agreements of mean wake expansion with Actuator Line CFD computations and simpler engineering models. An empirical relationship, relating maximum wake induction and wake advection velocity, is derived and linked to the characteristics of a spherical vortex structure. Additionally, a new empirical model for single wake expansion is proposed based on an initial wake expansion in the pressure driven flow regime and a spatial gradient computed from the large scale lateral velocities, and thus inspired by the basic assumption behind the Dynamic Wake Meandering model.

Secondly, the impact of the atmospheric stability on wind turbine wake deficit is studied experimentally and numerically. The measurements collected from the previous pulsed lidar campaign was reused as part of the experimental analysis. An inflow wind sector of 30° is selected based on both a wind resource and a lidar data assessment. Wake measurements are averaged within a mean wind speed bin of 1 m/s and classified according to atmospheric stability using 3 different approaches: the Obukhov length, the Bulk-Richardson and the Froude number approach. Three test cases are subsequently defined covering various atmospheric conditions. Simulations based on the EllipSys3D ABL flow solver are carried out using Large Eddy Simulation and Actuator disc rotor modeling. The turbulence properties of the incoming wind are adapted to the thermal stratification using a newly developed spectral tensor, which includes buoyancy effects. Discrepancies are discussed as basis for future model development and improvement. Moreover, the impact of atmospheric stability and terrain on large/small scale wake flow characteristics

was investigated.

Later, wake interaction resulting from two stall regulated turbines aligned with the incoming wind were studied experimentally and numerically. The experimental work was based on a new dedicated full-scale measurement campaign involving 3 nacelle mounted Continuous Wave scanning lidars. A thorough analysis and interpretation of the measurements was performed to overcome either the lack or the poor calibration of relevant turbine operational sensors, as well as other uncertainties inherent to wake resolving from full-scale experiments. The numerical work was based on the in-house EllipSys3D CFD flow solver, using Large Eddy Simulation and fully turbulent inflow, where the rotors are modeled using the Actuator Disc technique. A mutual validation of the CFD model with the measurements is proposed for a selected dataset where wake interactions occur. An excellent agreement between measurement and simulation is seen in both the fixed and the meandering frame of reference. A benchmark of several wake accumulation models is performed as a basis for the subsequent development of an engineering model for wake interaction.

Finally, the validated numerical CFD model is used as part of a parametric study where wake interaction is studied in a generic way, under several turbine spacings, mean wind speeds and turbulence intensities and in the fixed and the moving frame of reference of the wake. The analysis revealed that the industry widely used quadratic summation of single wake deficits for modeling the resulting double wake deficit is only relevant at high turbine thrust coefficients. For high wind speed and low thrust coefficient, linear summation should be primarily used. The first iteration of a new engineering model capable of modeling the overlapped wake deficit is formulated and its performance is tested again double, triple and quadruple wake deficits. Good performance in the prediction of both the maximum merged wake deficit and wake width is observed.

Summary (Danish)

Formålet med nærvæ rende forskningsprojekt har dels været at studere wakes efter enkeltstående vindmøller, dels at studere flere interagerende wakes - baseret på så vel fuldskala LiDAR må linger som på detaljerede CFD simuleringer.

Indledningsvist er dynamikken af enkelt-wakes studeret gennem analyser af fuldskala (nacelle-baserede) pulsede LiDAR målinger udført på en 500kW vindmølle placeret på testområdet ved DTU's Risø campus. Som en del af den eksperimentelle analyse er der foretaget en validering af den basale antagelse bag Dynamic Wake Meandering (DWM) modellen. Baseret på en wake lokaliseringsalgoritme er waken's nedstrøms transporthastighed herudover fastlagt, og der er udviklet en empirisk relation som sammenknytter waken's nedstrøms transporthastighed med wake-deficittet's amplitude. Denne relation er afslutningsvist sammenkædet med karakteristika en sfærisk hvirvelstruktur. Endelig er målingerne anvendt til at kvantificere wake-ekspansion i et fast initial system, og analyser af udvalgte datasæt viser fin overensstemmelse med analoge numeriske resultater opnået fra Actuator Linje (AL) CDF simuleringer. For så vidt angår fjernfeltet er overensstemmelsen med eksisterende simple empiriske modeller også god, mens større afvigelser ses i nærfeltet. Som konsekvens heraf er der udviklet en ny empirisk model inspireret af de grundlæggende antagelser bag DWM modellen. Denne model er således baseret på en initial wake-ekspansion i det trykdominerede strømningsregime kombineret med en rumlig ekspansionsgradient defineret i termer af stor-skala laterale turbulenskarakteristika.

Dernæst er effekten af atmosfærisk stabilitet på wake-karakteristika studeret eksperimentelt og numerisk. Den eksperimentelle analyse bygger på de ovenfor beskrevne fuldskala data, hvor en indstrømningssektor på 30° er udvalgt baseret på analyser af såvel vindresurse- som LiDAR data. Derpå er wake-målingerne midlet indenfor individuelle 1m/s middelvindhastigheds bins og efterfølgende klassificeret i forhold til atmosfærisk stabilitet ved anvendelse af 3 forskellige klassifikationsparametre: 1) Monin-Obukhov længde; 2) Bulk Richardson tallet; og 3) Froude tallet. Tre testtilfælde, som repræsenterer forskellige atmosfæriske stabilitets tilstande, er derefter udvalgt for nærmere analyse og modellering ved anvendelse af EllipSys3D ABL CFD koden. Modelleringen er baseret på Large Eddy Simulering (LES) med rotoren modelleret som en Actuator Disc (AD), og turbulensegenskaberne af det indstrømmende vindfelt er tilpasset den aktuelle termiske stratifikation

ved hjælp af en nyligt udviklet spektraltensor som på konsistent vis inkluderer opdriftseffekter. Afvigelser mellem modelforudsigelser og målingerne er diskuteret med henblik på udvikling af fremtidige forbedringer. Endvidere er effekten fra atmosfærisk stabilitet samt terræn på så vel stor- som småskala wake strømningskarakteristika undersøgt.

Efter analyserne af wakes efter enkeltstående vindmøller rettes fokus mod vekselvirkning mellem flere wakes. Til dette formål er vekselvirkningen mellem wakes hidrørende fra to stall regulerede vindmøller analyseret, så vel eksperimentelt som numerisk, i tilfælde hvor den indkommende vindretning er rettet langs møllernes forbindelseslinje. Den eksperimentelle del er baseret på en ny dedikeret fuldskala målekampagne som involverer 3 synkroniserede nacelle-monterede Continuous Wave LiDAR's. Der er gennemført en meget detaljeret analyse og fortolkning af målingerne dels for at kompensere for mangel på - eller ringe kalibrering - af relevante mølledriftssensorer, dels for at håndtere andre udfordringer knyttet til at oplø se wake's baseret på fuldskalamå lingerne. Den numeriske del af analysen er baseret på DTU's EllipSys3D CFD løser under anvendelse af LES med fuldt turbulent indstrømning og med vindmøllerotorerne repræsenteret som AD's. En indbyrdes validering af CFD modellen og målingerne er udført for et udvalgt datasæt, hvor vekselvirkning mellem wakes optræder, og der er opnået en meget fin overensstemmelse mellem disse i så vel det meandrerende som i det faste koordinatsystem.

Afslutningsvist er den validerede CFD model anvendt til et parameterstudie, hvori vekselvirkning mellem wakes er studeret for forskellige afstande mellem de wake-genererende mø ller, for forskellige middelvindshastigheder, og for forskellige turbulensintensiteter. Analyserne er gennemført i både det faste og i det meandrerende koordinatsystem. Disse analyser viser at den udbredte "industristandard", hvor enkelt-wakes sammensættes til integrerede/akkumulerede wakes under anvendelse af kvadratisk addition, kun kan retfærdiggøres for store aksialtrykskoefficienter. For høje vindhastigheder, og dermed lave aksialtrykskoefficienter, bør en lineær akkumulering anvendes. Som konsekvens heraf er der formuleret en ny wake-akkumuleringsalgoritme, og dens performance er efterfølgende testet mod dobbelte, tredobbelte og firedobbelte wake deficits. Resultaterne af testen er tilfredsstillende både hvad angår bredden og amplituden af deficittet.

Preface

This thesis was prepared at the department of Wind Energy at the Technical University of Denmark (DTU), and partially at the National Renewable Energy Laboratory (NREL), Louisville Colorado, USA, in fulfillment of the requirements for acquiring a Ph.D. degree. The work as the whole is a collection of scientific publications published by the author Ewan Machefaux, under the supervision of Gunner C. Larsen and Jakob Mann during the 3 years Ph.D. study. Parts of the present thesis are yet unpublished work.

The central goal of the present research was to study single and multiple interacting wind turbine wakes using both full-scale lidar experiments and high fidelity CFD numerical approach, highly relevant for accurate predictions of load and power production of turbines located in wind farm environments. The full-scale wake measurements were obtained using cutting-edge technologies in wind energy remote sensing such as LiDAR (i.e. WindScanner developed at DTU Wind Energy, WindCube and ZephiR). The goal of the experimental analysis was to characterize the organized flow structures as well as the wake generated turbulence resulting from a single wake or the interaction of two wakes as function of downstream distance from the wake generating rotors. The characterization of the organized part of the flow field encompassed a generic analysis of the interaction of the flow structures as well as their downstream attenuation, expansion and transportation. The numerical study was conducted using the in house EllipSys3D flow solver, and covered a large range of generic wind turbine operation. Non-stationary flow conditions were accounted for using the LES (Large Eddy Simulation) approach, and non neutral atmospheric flow were simulated using a newly developed extension of the EllipSys3D flow solver which includes buoyancy effects. The results from experiments and numerical studies are then condensed into several engineering models capturing the essential physics though still sufficiently computational efficient to be of practical relevance. These model are consistent with the existing model entitled the Dynamic Wake Meandering model, thus improving the model formulation for single wakes and extending its application from solitary turbines to wind farms.

Roskilde, December 10th, 2014

Ewan Machefaux

Acknowledgements

I would like to thank my main supervisor Gunner C. Larsen, senior scientist and my co-supervisor Jakob Mann, Professor for their constant support and scientific advising throughout the course of my Ph.D. study. As special thank to Gunner C. Larsen for his great support and supervision, and for giving me the motivation and the freedom to carry out my Ph.D. work in the best possible conditions.

I would like to thank Emmanuel Branlard for sharing with me his great computing and scientific knowledge, and for taking the time to teach his computing techniques for Unix scripting, and tools development aiming at gaining substantial productivity on every day's work.

I would like to thank my colleagues Niels Troldborg, Niels Sørensen, Mac Gaunaa, Pierre-Elouan Réthoré, Frederik Zahle, Paul Van Der Laan, Tilman Koblitz and Andreas Bechmann from the Aeroelastic Design group (AED) for their collaboration on the numerical part of my research, and for their high expertize on Computational Fluid Dynamics. A special thank to Niels Troldborg for sharing his knowledge of the EllipSys3D solver and its various turbulence models, rotor modeling techniques and expertize on numerical wake simulations.

I would like to thank Kurt Hansen, Torben Mikkelsen, Nikolas Angelou, Rozenn Wagner, Mikael Sjöholm and Ameya Sathe for their great collaboration on the experimental part of the Ph.D. study, especially for their valuable expertize on lidar technologies and other remote sensing devices. I would like to acknowledge the work of Per Hansen, Karen Enevoldsen and Steen Sørensen in the technical installation and operation of the various full-scale experimental campaign conducted at the DTU Risø campus test site. I would aslo like to acknowledge John Medley, Michael Harris and Chris Slinger from ZephIR Lidar, UK, for their collaboration and technical expertize on the ZephIR lidar systems.

I would like to thank Patrick Moriarty and Matthew Churchfield from the National Renewable Energy Laboratory for being great hosts and for their good collaboration during my Ph.D. external stay.

I would also like to thank my friend Philipp Haselbach, Ph.D. student at DTU Wind Energy for the good time we had on our daily commuting from Copenhagen to DTU

Wind Energy Risø campus.

Last but not least, I would like to thank my wife Helle and my son Hugo for their love, patience and support.

The major part of this research has been funded and carried out within the DSF Flow-Center project under the Danish Council for Strategic Research contract 2104-09-0026. Part of this research has also been funded by the EUDP Grant 64010-0462 'Impact of atmospheric stability conditions on wind farm' and the EU-TOPFARM project (contract REN07 / FP6EN / 507.73680 / 038641). The Ph.D. external stay at the National Renewable Energy Laboratory, Golden, Colorado has been fully funded by the G.A. Hagemanns Mindefond and the Otto Mønsted fond.

Contents

Nomenclature

Lower case letters

a	Axial induction factor
a'	Tangential induction factor
a_B	Axial induction factor local to the blade
c	Chord
c_p	Specific heat capacity of air at a constant pressure
h	Height of terrain or obstacle
h_{yaw}	Wake center displacement by yawing
h_{tilt}	Wake center displacement by tilting
k_p	Gaussian process peak factor
n	Normal vector to rotor
n_{rot}	Rotational speed in revolutions per second: $\Omega/(2\pi)$
p	Static pressure
q	Heat flux
q	Specific humidity
r	Radial position along the blade
$\bar{r}$	Dimensionless radial position r/R
t	Time
t_{adv}	Wake advection time
u	Streamwise wind component
u_c	Large scale streamwise wind component
u_*	Friction velocity
v	Lateral wind component
v_c	Large scale lateral wind component
w	Vertical wind component
w_c	Large scale vertical wind component
w	Wake relative longitudinal velocity
x_i	Spatial Cartesian coordinates
z_0	Surface roughness length

Upper case letters

A	Area
B	Number of blades
C_d	Drag coefficients
C_l	Lift coefficients
C_n	Normal component of the aerodynamic coefficients
C_p	Power coefficient
C_T	Thrust coefficient
D, D_0	Rotor diameter
D_N	Nordtank turbine rotor diameter
D_T	Tellus turbine rotor diameter
D_w	Instantaneous wake deficit diameter
E	Wake expansion
E_F	Frandsen's modeled wake expansion
$\tilde{E}$	Wake expansion coefficient
f_c	Coriolis parameter
f_c	Cut-off frequency
Fr	Froude number
g_i	Graviational acceleration
H	Turbine hub height
I_u	Streamwise turbulence intensity
I_v	Lateral turbulence intensity
I_w	Vertical turbulence intensity
I_{ref}	Total turbulence intensity
L	Lift force
L	Obukhov length
L	Mann model turbulence length scale
L_i	Computational domain length, x-, y- and z-
N_{bv}	Brunt-Väisälä frequency
P	Power
P	Pressure
P_0	Atmospheric standard pressure
R	Rotor radius
Re	Reynolds Number
Ri	Richardson number
Ri_b	Bulk- Richardson number
Ri_g	Gradient-Richardson number
T	Thrust force
T	Temperature
U	Longitudinal velocity at the rotor in 1D
U_0	Longitudinal velocity far upstream
U_a , U_{adv}	Advection velocity
U_i	Induced velocity in 1D
U_{los}	Line-of-sight velocity
U_n	Velocity normal to the rotor
U_t	Velocity tangent to the rotor

U_T	Taylor advection velocity
U_w	Longitudinal velocity in the far wake in 1D
V	Velocity vector
V_n	Normal velocity in the far wake
V_{r}	Rotor velocity Ωr
V_{rel}	Relative velocity
V_t	Tangential velocity in the far wake
$\mathcal{V}$	Volume
W	Induced velocity at the rotor
W_T	Characteristic obstacle length

Lower case Greek letters

α	Angle of attack
$\alpha\epsilon^{2/3}$	Viscous dissipation of TKE
α	Wind shear exponent
β	Twist angle
κ	Von Karman constant
γ	Euler constant
γ	Eddy life time
ϵ	Dissipation
θ	Azimuthal coordinate in polar coordinates, same as ψ
λ	Tip speed ratio $= \Omega R/U_0$
λ_r	Local speed ratio $= \lambda r/R$
μ	Dynamic viscosity
μ_t	Turbulent eddy viscosity
ν	Kinematic viscosity $= \mu/\rho$
α	Wind shear exponent
ρ	Air density
σ	Standard deviation
τ	Shear stress, viscous stress tensor
ϕ	Flow angle
ϕ	Conical lidar phase angle
ψ	Azimuthal coordinate, positive with the rotor rotation, same as θ
ω	Rotational speed of the wake (momentum and vortex theory)
ω	Vorticity

Upper case Greek letters

Δ	Error or differential operator
Δ_i	Domain grid spacing, x-, y- and z-
Δ_u	Wake deficit
Θ	Potential temperature
Θ_c	Lidar opening angle
Θ_{tilt}	Tilt misalignment angle
Θ_{yaw}	Yaw misalignment angle
Θ_p	Lidar pan angle

Θ_t	Lidar tilt angle
Φ	Velocity Potential
Φ_m	Stability function MOST
χ_y	Lateral wake skew angle
χ_z	Vertical wake skew angle
Ψ	Stream function
Ψ_m	Stream function MOST
Ω	Rotational speed of the rotor

Abbreviations

1D	One dimension
2D	Two dimensions
3D	Three dimensions
ABL	Atmospheric Boundary Layer
AD	Actuator Disc
AL (ACL)	Actuator Line
AS	Actuator Shape
AEP	Annual Energy Production
A.G.L.	Above Ground Level
ARL	Averaging RSS & Linear
A.S.L.	Above Sea Level
BEM	Blade Element Momentum
CBL	Convective (unstable) boundary layer
CDS	Central Difference Scheme
CNR	Carrier to Noise Ratio
CFD	Computational Fluid Dynamics
CW	Continuous Wave
DM	Dual Mode
DTU	Denmark Technical University
DSF	Det Strategisk Forskningråd
DW	Double Wake
DWM	Dynamic Wake Meandering
FC	Lidar Focus Distance
FFOR	Fixed frame of reference
IBL	Internal Boundary Layer
IEC	International Electrotechnical Commission
LIDAR	Light Detection And Ranging
LES	Large Eddy Simulation
MFOR	Moving frame of reference
MM	Meteorological Mast
MO	Monin-Obukhov
MOST	Monin- Obukhov similarity theory
MT	Momentum Theory
MW	Merged Wake
NTK	Nordtank 500 kW wind turbine
NOJ	N.O Jensen Wake model

POD	Proper Orthogonal Decomposition
PC	Power Curve
QUICK	Quadratic Upwind Interpolation for Convective Kinematics
RANS	Reynolds-Averaged Navier-Stokes
RPM	Round Per Minute
RSS	Root Sum Square
RW	Reference Wake
SCADA	Supervisory Control and Data Acquisition
SGS	Sub-grid scale
STRM	Shuttle Radar Topography Mission
TEM	Test and Measurements
TI	Turbulence intensity
TKE	Turbulent Kinetic Energy
WALTZ	ZephIR LTD. post processing program
WS	Wind speed
WD	Wind direction
WT	Wind Turbine
LES	Large Eddy Simulation

List of publications

Author

Experimental and Numerical study of Wake to Wake Interaction in Wind Farms. Machefaux, Ewan; Troldborg, Niels; Larsen, Gunner Chr.; Mann, Jakob; Aagaard Madsen , Helge. Oral presentation and proceedings of EWEA 2012 - European Wind Energy Conference & Exhibition. European Wind Energy Association (EWEA), Copenhagen, 2012.

Single Wake Meandering, Advection and Expansion - An analysis using an adapted Pulsed Lidar and CFD LES-ACL simulations. Machefaux, Ewan ; Larsen, Gunner Chr.; Troldborg, Niels; Rettenmeier, Andreas. Oral presentation and proceedings of EWEA 2013 - European Wind Energy Conference & Exhibition. European Wind Energy Association (EWEA). Vienna, 2013.

Empirical modeling of single-wake advection and expansion using full-scale pulsed lidar-based measurements. Machefaux, Ewan; Larsen, Gunner Chr.; Troldborg, Niels; Gaunaa, Mac; Rettenmeier, Andreas. Wind Energy, 2014.

Investigation of Wake Interaction using Full-Scale Lidar Measurements and Large Eddy Simulation. Machefaux, Ewan; Larsen, Gunner Chr.; Troldborg, Niels; Hansen, Kurt S.; Angelou, Nikolas; Mikkelsen, Torben; Mann, Jakob. In review: Wind Energy, 2014.

Experimental and numerical study of the atmospheric stability impact on wind turbine wake. Machefaux, Ewan; Larsen, Gunner Chr.; Koblitz, T.; Troldborg, N., Kelly, M., Chougule, A., Hansen K.S. and Rodrigo J.S. In review: Wind Energy, 2014.

Co-author

Validation of vortex code viscous models using lidar wake measurements and CFD. Branlard, Emmanuel; Machefaux, Ewan; Gaunaa, Mac; Sørensen, Hans Henrik

Brandenborg; Troldborg, Niels. Proceedings of EWEA 2014. European Wind Energy Association (EWEA), 2014.

Investigation of a new model accounting for rotors of finite tip-speed ratio in yaw or tilt. Branlard, Emmanuel; Gaunaa, Mac; Machefaux, Ewan. In: Journal of Physics: Conference Series (Online), Vol. 524, No. 1, 012124, 2014.

IEA-Task 31 WAKEBENCH: Towards a protocol for wind farm flow model evaluation. Part 1: Flow-over-terrain models. Rodrigo, Javier Sanz; Gancarski, Pawel; Arroyo, Roberto Chavez; Moriarty, Patrick; Chuchfield, Matthew; Naughton, Jonathan W.; Hansen, Kurt Schaldemose; Machefaux, Ewan; Koblitz, Tilman; Maguire, Eoghan; Castellani, Francesco; Terzi, Ludovico; Breton, Simon-Philippe; Ueda, Yuko; Prospathopoulos, John; Oxley, Gregory S.; Peralta, Carlos; Zhang, Xiadong; Witha, Björn. In: Journal of Physics: Conference Series (Online), Vol. 524, No. 1, 012105, 2014.

IEA-Task 31 WAKEBENCH: Towards a protocol for wind farm flow model evaluation. Part 2: Wind farm wake models. Moriarty, Patrick; Rodrigo, Javier Sanz; Gancarski, Pawel; Chuchfield, Matthew; Naughton, Jonathan W.; Hansen, Kurt Schaldemose; Machefaux, Ewan; Maguire, Eoghan; Castellani, Francesco; Terzi, Ludovico; Breton, Simon-Philippe; Ueda, Yuko. In: Journal of Physics: Conference Series (Online), Vol. 524, No. 1, 012185, 2014.

An improved k-ϵ model applied to a wind turbine wake in atmospheric turbulence. Laan, van der, Paul Maarten; Sørensen, Niels N.; Réthoré, Pierre-Elouan; Mann, Jakob; Kelly, Mark C.; Troldborg, Niels; Schepers, J. Gerard; Machefaux, Ewan. In: Wind Energy, 2014.

Chapter 1

Introduction

1.1 Motivation

According to the latest half year 2014 report from the World Wind Energy association [1], the world wide wind energy market has reached an installed capacity over 336 Gigawatt, with an expected 360 Gigawatt by the end of the year 2014. For the first time, Asia has overtaken Europe as leading wind continent in installed capacity, where China represents more than 100 GW on its own. Newcomers are directly responsible for the sustained growth of wind power capacity: Brazil is now the third largest market for new wind turbines installation. Such momentum of growth can not only be attributed to the dynamic of emerging economies in China, Brazil and India. The increasing competitiveness of wind energy driven by technology development and fundamental research, and the pressing need for emission-free energy solutions due to an increased awareness of the human responsibilities in climate change, are direct contributor to the wind energy growth.

In order to fulfill the continuously increasing wind energy demand while ensuring practicability and economical viability, the majority of wind turbines are clustered in wind farms. Specifically, erecting wind turbine in wind farms reduces land ownership, facilitate maintenance operations and mitigate the electrical infrastructure costs. There is however a major drawback with wind turbine clustering known as wind farm wake losses. A wake is defined as the flow regime downstream of a wind turbine rotor, characterized by a reduced wind speed associated to an increased turbulence intensity. The lower wind speed behind an upstream turbine can severely affect the performance of the downwind turbines. Another major impact on turbine-to-turbine wake interaction is a substantial increase on fatigue loads for the downwind turbines. On a modern wind farm level, wake losses typically account for 10 to 20 % of annual energy production losses [15], whereas downwind turbines experience a flapwise loading which can increase up to 100% in the most severe cases [33].

This is why modeling the complex flow fields in a wind farm has become one of the most prioritized topics of wind energy research in the past decade. Despite the large breakthrough in wake modeling, facilitated by the ever increase in computational power, wind turbine wakes modeling and its integration in wind turbine and wind farm design remains challenging for the wind industry. The complexity of wind farm flow fields is not only due to the highly turbulent nature of the wake, but also influenced by its interaction with other wakes and the atmospheric boundary layer. The dynamic of the wake flow field thus covers a large range of turbulence length scales, which can only be predicted by computationally expensive models. In turns, the wind energy industry relies on lower order models capturing the essential physics of the wake while remaining of practical relevance for their integration in wind farm topology optimization tool.

The present PhD thesis aims at a more detailed characterization and modeling of wind farm flow fields, highly relevant for accurate predictions of loads and power production of turbines located in wind farms. The project in particular focus on the dynamic of a single wind turbine wake and its interaction with downwind rotors, resulting in multiple or 'merged' wakes. The scientific approach proposed in the present thesis is based on detailed Computational Fluid Dynamics studies combined with analysis of dedicated innovative full-scale recordings using cutting-edge remote sensing technologies such as lidars. The condensed results from experiments and numerical studies are utilized to, among others, validate an existing model entitled the Dynamic Wake Meandering model and make proposal to extend its application from solitary turbines to wind farms.

1.2 State-of-the-art of wind turbine wake research

The present section aims to give a condensed overview of the key aspects of the horizontal axis wind turbine wake dynamics, and how the improvements on wake modeling can contribute to lowering the cost of wind energy. Furthermore, a brief introduction of the wind turbine wake and wind farm flow models of relevance for the present PhD study is given, where the challenges associated to the extension from single wake to multiple wake dynamics is emphasized. This section is not meant to provide a complete state-of-art litterature survey of wind turbine wake but rather a list of key aspect and useful concepts used throughout the present research thesis.

1.2.1 Wake research and the Cost of Energy (CoE)

There are several key drivers for lowering the cost of wind energy. Over the last 20 years of research, most of the effort have been put in reducing costs at the wind turbine level. Specifically, improvements of the aerodynamic and structural design associated to the development of better turbine control strategy have improved drastically the overall efficiency of a wind turbine, i.e. its capacity to extract as much (available) energy as possible and to operate closer to the theoretical limit known as the the Lanchester-Betz limit. Material and components research breakthrough have also contributed to improve the operational availability of wind turbines. Modern wind farms have reduced their downtime for technical maintenance to less than 2% [76].

Moreover, increasing or 'upscaling' the turbine size contributes to lowering the Cost of Energy (CoE) as they produce more power with less infrastructure and maintenance costs, and benefits from higher and less turbulent wind resources due to the use of taller towers. However, upscaling introduces new design and manufacturing challenges and therefore requires substantial development of aero-elastic models and design tool as for the 10MW DTU reference turbine [13].

The last driver is based on the cost reduction at the wind farm level, highly relevant in the present PhD study. Wake effects are considered as a major source of uncertainties in the wind farm design process and were not accounted for in a sufficient manner in the early IEC standards according to Crespo et al. in [33]. This is mainly because the standard design process does not include any physical based model for the wind turbine wake that account for both individual turbine loads and overall wind farm power performance together. The EU-TOPFARM project ([64]) objective was therefore to develop a comprehensive wind farm design platform, where wakes are treated in a physical manner to model their unsteady effect on both the turbine loading and production.

The PhD study is primarily based on the core wake model of this optimization platform, the Dynamic Wake Meandering model [71] which is described subsequently. In this project, validations techniques and solutions for extending its application to improve the modeling of overlapping wakes are proposed. By developing more powerful wake superposition models, the uncertainty in power production of the overall wind farm can be reduced, thus participating in lowering the financial risks of a wind farm project and therefore the CoE.

1.2.2 Wind turbine wake dynamics

1.2.2.1 Wake development

In this section, a concise description of the dynamic behavior of a wind turbine wake is proposed. Very detailed literature survey of wind turbine wake can be found in the article by Crespo et al. in [33], the survey by Sanderse [123] and the literature text book by Burton et al [22]. The air flow accross a wind turbine rotor can be divided into 4 regions.

In the *induction zone*, defined as the area upstream and in the vicinity of the rotor, the approaching air experiences a gradual slow down in wind speed and an increase in pressure. As the air parcel crosses the rotor disk, a sudden drop of air pressure is observed to reach a level below the atmospheric pressure. At this stage, kinetic energy from the incoming wind is convert to mechanical energy on the rotor, and the air is slowed down.

In the *near wake region*, corresponding to the region immediately downstream of the rotor as depicted in Fig. 1.1, the flow is highly non-uniform and complex. Vortex structures are shed from the blades trailing edge and become to form a coherent vortex system consisting of helical tip vortices, interpreted as a cylindrical *shear layer* which separates the fast moving fluid of the ambient flow with the slow one in the wake. As the pressure gradually increases to reach the ambient pressure, the cylindrical *shear layer* expands and the wake centerline velocity drops until reaching its minimum between 1 and 2 diameters downstream. At this stage, the end of the *near wake region* is reached.

In the *intermediate wake region*, often referred to as the transition region to the *far wake* and typically extending from 2-3 to 5 rotor diameters downstream, the turbulent production in the shear layer, where the velocity gradients is the highest, is the dominant mechanism in the flow. This turbulent diffusion causes the shear layer thickness to increase until it reaches the wake centerline axis.

In the *far wake* region, the wake velocity and turbulence intensity profiles are assumed axisymmetric (or Gaussian) if the contribution of the atmospheric sheared flow is removed. Under this assumption, the wake has a self similar cross sectional distribution, and the only turbine properties influencing the characteristic of the wake profiles is the thrust on the turbine and the total kinetic energy produced by the rotor itself. The rate of recovery of the advected wake is influenced by both the turbulence generated in the wake shear layer and the level of ambient turbulence in the atmosphere. The latter, according to the description by Ainslie in [5], is primarily a function of the surface roughness, the turbine hub height and the atmospheric stability. The large scale turbulent structures in the atmosphere with eddy size large in comparison with the rotor size, are responsible for the *wake meandering*, referred to as the sideways motion of the wake deficit as it is transported downstream of the rotor. The combination of wake deficit evolution and wake meandering together describe the key aspect of the dynamic of a solitary wind turbine wake in the atmospheric boundary layer.

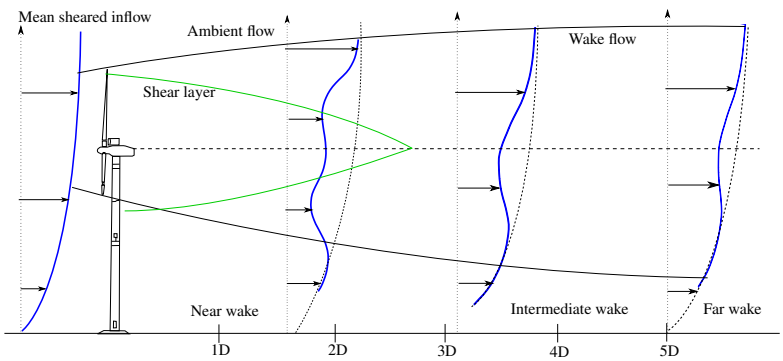

Figure 1.1: Sketch of the wake deficit profile associated to three flow regions: the near wake ($< 2D$), the intermediate wake (3 to $5D$) and the far wake ($5D$). The mean wind profile at different location in the flow is sketched in blue whereas the boundary of the shear layer is shown in green. The double bell shape of the near wake velocity profile reflects the distribution of the axial force (thrust) on the blades.

1.2.2.2 Wake meandering

Wake meandering is a key aspect in modeling the power production and wind turbine loading in the wind farm, as it describes the unsteady motion of the wake deficit as it as transported or 'advected' downstream. The effect of wake meandering is long known

empirically from comparison of wind tunnel wake measurements with available field data in the early 1980s, where the measured wake deficits in the field were systematically smaller than those from the wind tunnel. It was initially attributed that wind direction variability causes the wake to meander and thus the resulting average profile to display lower deficit, as first modeled by Ainslie [4].

However, Högström et al. [47] argued that Ainslie's approach is incorrect as the wind direction variability is caused by eddies of all sizes including those that are smaller than the wake diameter, and that a corresponding low pass filter must be applied to the wind direction fluctuation signal to accurately model wake meandering.

It is only recently with the work of Larsen et al. [71] that the single wake meandering was addressed in a consistent and physical way in the so-called Dynamic Wake Meandering model (DWM). In this approach, the wake is assumed to follow the large scale eddies in the atmosphere (with length scale larger than 2 rotor diameters), using a passive tracer analogy as depicted in Fig. 1.2. This conjecture was further validated by dedicated full-scale lidar based measurements in the work by Bingöl et al. [18] and Trujillo et al. [152]. Wind tunnel experiments conducted by España et al. in [36] also revealed that the wake meandering is governed by the incoming turbulence and specifically correlates with the large eddies.

In a situation where the mean wind direction is perfectly aligned with two rotors, the downstream one will experience situation of full and partial wakes due to the meandering of the upstream wake. By properly adressing wake meandering, better prediction of power production and turbine load are achieved.

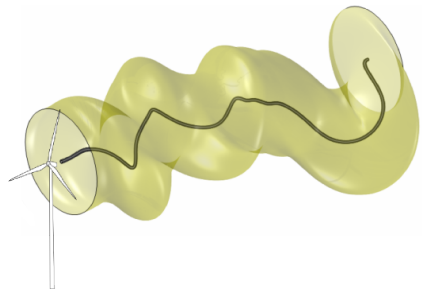

Figure 1.2: Sketch of the idealized wake meandering using the passive tracer analogy. Courtesy of G. Larsen, from [70].

1.2.2.3 Influencing parameters in wake dynamics

Wind turbine wakes in the atmospheric boundary layer are complex turbulent flow, and their accurate physical description cannot be reduced to a set of few parameters. Modeling wakes on the wind farm level combines environmental aspects such as terrain topography, site roughness, ambient turbulence and wind farms characteristics such as turbine spacing and wind farm control strategy. However, comprehensive wind tunnel, full-scale experi-

ment and detailed high fidelity CFD study allows to study the effect of key parameters influencing single wake characteristics, and thus facilitating the development of lower order engineering wind farm models. The following is not an exhaustive list but focus on the commonly used parameters in engineering models, as they are strongly correlated to other omitted flow and turbine properties.

The ambient turbulence intensity is a key parameter governing the wake downstream evolution. Several experimental and numerical studies by Larsen at al. [74], Schepers at al. [128], Barthelmie et al. [16], Hansen et al. [44], Toldborg et al. [144], and Keck [56] demonstrated that wake recovery occurs faster for increased ambient turbulent level. The magnitude of wake meandering is also increased with increased turbulence intensity as demonstrated by España [36] and Bingöl et al. [18].

In the present thesis, the impact of atmospheric stability on the wake characteristics is also studied experimentally and numerically. As observed by Larsen at al. [70], the change in length and velocity scale of the inflow turbulence due to varying atmospheric stability has a direct impact on the magnitude of meandering and recovery of the wake. Specifically, stable conditions are characterized by a decrease of energy content of the low frequency part of the turbulent spectrum and thus by an attenuation of the wake meandering. For a downstream turbine perfectly aligned with the 10 minutes mean wind direction of the wake generating turbine, this will lead to a more pronounced mean wake deficit and therefore to an increase in mean production loss. Contrary, unstable conditions are dealing with an increased in the energy content of the low frequency part of the turbulent spectrum leading to more intense wake meandering compared to the neutral situation. The downstream turbine experiences an attenuated mean wake and thus lower power deficit.

One of the key turbine-related parameter that governs the wake is the thrust. As extensively described in [113], the thrust is the axial force acting on the wind turbine rotor. It is often defined as the actual reaction force of the wind turbine on the wind, as the rotor acts as an obstacle to the flow. Thus, the wake of a highly loaded rotor has a deeper velocity deficit and larger wake expansion, as demonstrated experimentally and numerically [81]. According to 1-D momentum theory [46], the axial induction factor is related to the thrust, which is in turn used to determine the wake velocity deficit in the N.O. Jensen model [54] and the wake expansion in the semi-analytical wake model by Larsen [60].

When considering operational conditions of modern, variable speed, wind turbines, the tip-speed ratio affects the wake dynamics drastically as depicted in Fig. 1.3 from the study by Troldborg [144]. At high tip speed ratio, the vortex structures break down after a short downstream distance whereas they are preserved over the entire wake span for low tip speed ratio. This implies that the wake dynamics above rated power on variable speed turbine is affected as the tip speed ratio decreases.

1.2.3 Wind turbine wake modeling

Wake models have been intensively developed by the research community over the last 40 years. In fact, the diversity of available models is so large that confusion arises within wind farm developers on what specific assumptions, design envelop and calibration procedures

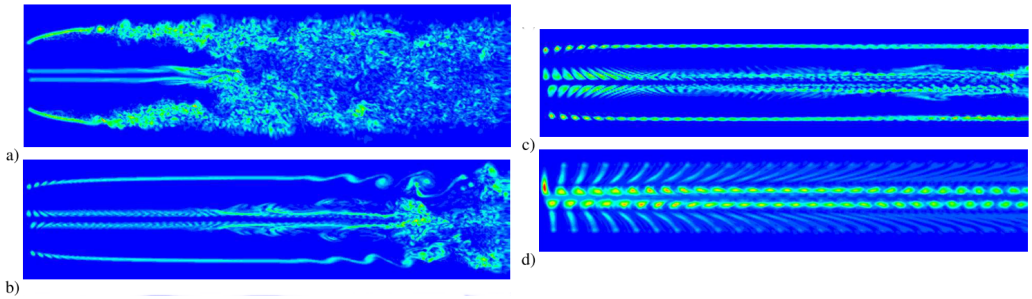

Figure 1.3: Downstream development of the wake visualized using vorticity contours. The rotor is located to the left; a) $\lambda = 11.78$ ($U_\infty = 6$ m/s); b) $\lambda = 7.07$ ($U_\infty = 10$ m/s); c) $\lambda = 5.05$ ($U_\infty = 14$ m/s); d) $\lambda = 3.21$ ($U_\infty = 22$ m/s). Courtesy of Troldborg [144].

are used for each of them. Lack of clear guidelines associated to the wake models have been exposed in the study in [107]. Wake models comes with a wide degree of complexity and practicability. They are commonly classified in three families: the *kinematic* 'explicit' models, the *roughness length* based models and the *field* 'implicit' models. A complete overview of the state-of-the-art in wake modeling of various complexities can be found in the literature survey by Crespo et al. [33], Vermeer et al. [153], Sanderse [123], [124] and Gaumond [40].

1.2.3.1 Kinematic models

Kinematic models are the simplest and fastest wake models as they rely on crude assumption of the wake flow: rotational symmetry and self-similarity of the velocity deficit. The velocity profile is often assumed of Gaussian type, and obtained from experimental and theoretical analysis on co-flowing jets as in [3]. The wake growth or 'expansion' rate is related to the ambient turbulence, the turbulence created by the shear in the wake (the so-called *added wake turbulence*) and the turbulence generated by the turbine itself. The magnitude of the downstream transported velocity deficit is then obtained from global momentum conservation, whereas ground effect is often treated as a reflexion (or symmetrical) surface for the velocity deficit. The advantage of kinematic models is the simplicity of their formulation and low computer power requirements, however their performance is only acceptable when empirical coefficients are properly adjusted. They are therefore not suited for detailed investigations of wake development and interaction with the atmospheric boundary layer, however, they are extremely practical and useful in wind farm optimization platforms such as TOPFARM [64]. Some of the popular kinematic models include the N.O Jensen model [54], the PARK model [55] and the G.C. Larsen model [60].

1.2.3.2 Roughness length based models

In the roughness length modeling approach, wind turbines are treated as obstacle elements or 'roughness' elements that impact the logarithmic atmospheric wind profile. Such approach is specifically suited for studying wake losses over large wind farms or farm-to-farm interaction. The Infinite Wind Farm Boundary-Layer (IWFBL) model of Frandsen [38] and its recent extension to include the effect of atmospheric stability in [105] is a commonly used roughness model.

1.2.3.3 Field models

Finally, *field* models refer to Computational Fluid Dynamics (CFD) models that solve the Navier-Stokes equations governing the entire flow field. In wake aerodynamics, four type of CFD models with increasing complexity are typically used: Linearized Navier-Stokes (LNS), Parabolised Navier-Stokes (PNS), Reynolds Averaged Navier-Stokes (RANS) and Large Eddy Simulation (LES). Among these methods, a large number of techniques are involved in the simplification of the Navier-Stokes equation to overcome the turbulence closure problem. Among these techniques we commonly found the eddy-viscosity approach, the two-equation turbulence closure (k-ϵ) and LES.

Eddy-viscosity closure The eddy-viscosity approach was first introduced by Ainslie [5] and successfully applied to wake flow. The approach was further elaborated on by Larsen in [67], [60] and [68] in a semi-analytical wake model where the Prandtl's mixing length closure [109] was combined to an empirical closed form of the wake expansion to model single wind turbine wake. This simple closure technique was later on reemployed by Larsen G.C., Larsen T. and Madsen in [71], [73] and [84] within the DWM. In this approach, the "split in turbulent scales" assumption was proposed, where small scale turbulence, responsible for the wake diffusion, are modeled by the eddy-viscosity technique which are in turn decoupled from the large-scale turbulence in the atmosphere responsible for the wake meandering.

Ott et al. proposed a fast linearized CFD model for wakes (FUGA) [100], where the simple eddy-viscosity closure is adopted. The author motivated his choice by the fact that the eddy viscosity approach well describes the physics of wake diffusion with the surrounding ambient flow, i.e. for process involving eddy size smaller than the wake width. However, the FUGA model lacks to model the large scale features that represent meandering, which, according to [100], may only be possible using a time resolved model that include thermal effects and Coriolis force, such as LES that includes temperature.

The two-equations closure The two-equations turbulence k-ϵ closure detailed in Wilcox [159] is unarguably the most popular turbulence model for industrial applications. However, several studies by Kasmi et al. [35], Rados et al, [110], Réthoré [114], Réthoré et al. [117] among others pointed out the very poor performance of this turbulence model for wake flow. The key issue is that a wind turbine wake in the atmosphere is influenced by turbulence on a very wide range of scales that are not properly captured by this model. Recently, Van der Laan et al. [59] proposed an extension to this model which includes a

flow-dependent $C\mu$ parameter that is sensitive to high velocity gradients, e.g., at the edge of a wind turbine wake. The model validation showed encouraging results for 8 selected test cases with significant improvement compared to the original formulation.

Large Eddy Simulations Large Eddy Simulations (LES), well described in the text book by Pope [108], are typically conducted when large computer resources are available. As opposed to the previous two equations turbulence modeling approach, LES fully resolves the large-scale turbulence eddies while modeling small-scale turbulence using an eddy viscosity model. The most advanced rotor modeling technique makes use of the full blade geometry so that the viscous boundary layer developing at the airfoil is fully resolved. This approach was used in the full rotor simulation studies of Sørensen N. [136], Zahle et al. [162] and [163], Réthoré et al. [118]. As opposed to the full rotor technique, two additional approaches are widely used by the wind energy industry and the research community, to model the turbine rotor in a consistent and efficient manner: the Actuator Disc (AD) and the Actuator Line (AL) approaches.

The Actuator Disc uses equivalent forces to represent the rotor while the surrounding flow field is governed by the Navier-Stokes equations thus requiring much lower grid resolution than the full rotor approach. The generalized Actuator Disc is an extension of the Blade Element Momentum method (BEM) [46], where the aerodynamic forces acting on the rotor are computed from two dimensional airfoil characteristics, typically corrected for three dimensional effects based on a model such as the Bak 3D correction [12], using a blade element approach. The finite number of blades is accounted for by applying a tip correction on the computed forces. This approach have been extensively used in several numerical wake study by Sørensen [53], Amarra et al. [8], Mikkelsen in [94] and [95], Ivanell et al. [51], among others. The main limitation of its initial formulation ([94]) is the assumption of rotationally symmetric flow introduced in the evenly azimuthal distribution of the spanwise dependent forces. It implies that blades are not explicitly represented and thus the influence of tip vortices is not captured. The subsequent model version was improved to account for an azimuthal dependence of the forces acting on the disc. Finally, Réthoré et al. in [114], [119] and [116] extended the AD model to the so-called Actuator Shape (AS) model, which improved the force allocation algorithm and allow the use of the Actuator Disc model on a coarse computation mesh.

In 2002, Sørensen and Shen [134] developed the Actuator Line model. In this approach, the aerodynamic loading is distributed along lines representing the wind turbine blades in a three dimensional domain. This technique was extensively used to study properties of the wake in various type of inflow conditions. Mikkelsen et al. presented AL computations of both isolated turbines in [95] and rows of wind turbines in [96] where body forces introduced in the entire computational domain were used to prescribed a sheared velocity profile. Ivanell et al [52] performed high resolution AL of a single wake to study stabilities property of tip and root vortices in laminar inflow. Troldborg extensively used the AL model to study wake characteristics in uniform inflow and turbulent inflow [144], [147] as well as the wake interaction between two turbines at various inflow conditions in [146]. Recently, Churchfield et al. [29] performed LES-AL simulations of the entire Lillgrund offshore wind farm, requiring about one million processor hours for a full 10 minutes unsteady simulation.

These studies demonstrated that combining Actuator Disc or Line models with LES are excellent research tools to study complex flow structures such as wake interaction of 2 or more wind turbines. When considering computer ressources, the study by Troldborg et al. in [149] revealed that the AD technique is, with respect to the prediction of wake deficits, as accurate as the AL model, and should therefore be of primary use when limited ressources are available.

1.2.4 Wind farm wake interaction modeling

In wind farm environment, upstream turbines generate wakes that interact with downwind machine. This unwanted effect is typically mitigated by farm layout optimization associated to the knowledge of the site specific wind rose, so that the most severe wake situations, i.e. when the mean wind inflow direction is aligned with several downwind turbines, only occurs a fraction of the time. Modeling wake interaction in wind farm is not trivial, mainly because the way velocity deficits and wake generated turbulence physically accumulate at locations where wakes merge is not well understood.

The commonly used approach in wind farm design code is to combined single wake calculations with assumption on superposition to determine the combined characteristics of the merged wake. They key issue in this type of engineering approach, according to Crespo et al. [33], is that the ambient flow in which a downstream wake diffuses is fundamentally different than the one at upstream locations.

A first way to model overlapping wakes is the linear superposition of wake deficits, first introduced by Lissaman in [78]. As argued by Crespo et al. [33], this assumption failed for large perturbations where many upstream wakes are superimposed, as negative velocities may arise.

Contrary, Katic et al. in [55] proposed to apply a linear superposition of the squares of the velocity deficits (quadratic summation rule). Various results are found from the performance assessment of this summation method. Crespo et al. [33] argued that this method is beneficial in the case where many wakes are combined, giving better agreement with experimental results than the linear superposition for a small wind farm.

A different approach for simulating the interaction of several wakes was used by Voutsinas et al. in [155] and [156], where an explicit energy equation was formulated. In this methodology, the energy conservation is adopted to relate the total energy loss of all wind turbines to the energy loss of each individual turbine, and is turn used to calculate the inflow velocity for each turbine, thus capable of predicted their respective power production.

More recently, and based on experimental observation at the modern offshore wind farm Horns Rev, Gaumond [40] argued that the quadratic rule associated to the standard industry wake model N.O. Jensen model [54] using a constant wake expansion rate α is not suitable for large wind farms as it fails to capture properly the physics of merging wakes from neighboring rows of turbine, which occurs at a certain distance downstream of the first rotor. Although these two results may appear contradictory, they are not. The quadratic formulation of Katic at al. was tested for experimental data on a small wind farm, while the effect of neighboring wakes merging occur at a certain downstream

distance only visible on large offshore wind farm as Horns Rev. In the latter observation, the quadratic rule failed to model deep array effects as it reaches an equilibrium state (where the velocity deficit becomes constant) too quickly.

In [40], the author also investigated the performance of the N.O. Jensen model with a linear summation rule instead, on power production along a row of turbines at the Horns Rev offshore wind farm. It appears that the linear summation of wake deficits performs better than the quadratic one, although conditioned to the use of a large value for wake expansion rate, not physically representative for the single wake. This agreement was also conditioned to the use of a 30 degrees wide wind sector for the definition of the power production data.

Instead the results of [40] demonstrated that the linear summation should be used in the so-called InfiniPark model proposed by Rathmann et al [112], where the rate of wake expansion should be decreased each time a new turbine is reached in the wake propagation row. The InfiniPark is essentially increasing the robustness of the N.O. Jensen model for the single wake case, but does not correct the under prediction when narrow wind sectors of 5 degrees are used for the averaging experimental power production data. Such discrepancy for the narrow wind sectors was later on addressed as a consequence of the wind direction uncertainty associated to the validation data. This effect was accounted for in [41].

Most recently, Nygaard presented a comprehensive study of wakes losses in five very large operational offshore wind farm and extended his study to farm-to-farm interaction in [99]. His analysis, was based on the N.O. Jensen model [54] associated with the quadratic summation rule of wake deficits [55] and a wake expansion rate $\alpha = 0.4$. This set up remains today's standard industry model for calculating modern wind farm wake losses despite its initial development 30 years ago in an era with much smaller turbines and wind farms. This summation rule is also the standard implementation of WAsP [89] site assessment and topography package as well as the software WindPRO. The performance of the model was poor for a flow case with low turbulence intensity where wake losses were underestimated dramatically. An improvement of this standard wake model where turbulence intensity is included explicitly or implicitly, such as in the study by Peña [105], may overcome these discrepancies.

As part of the in-house coupling between the Aeroelastic code HAWC2 and the DWM model, overlapping wakes are modeled using the so-called *dominant wake* approach. In this approach, the merged wake at a given location in a wind farm is assumed to be characterized by the most dominant deficit of all upstream wakes contribution. In this way, the most attenuated and expanded upstream wakes contributes to the merged wake deficit more than the conventional quadratic and linear summation. This method proved robust to determine load and power production of a wind farm. The completed description of the method and validation is available in the study by Larsen at al. in [74].

A summary of the current state-of-art of wake superposition assumptions can be made from the work of Crespo et al. in [32]. When considering the superposition of two wakes abreast, it was found that linear superposition of the small velocity deficits in the interference region is performant for predicting the resulting overlapped wake characteristics. However, when considering the situation where two turbines are in a row, the linear superposition assumption overestimates substantially the velocity deficit. This means that large deficit

cannot be summed based on a linear assumption, and instead, the quadratic summation by Katic et al. [55] proved to perform better. This conclusion is also in agreement with the observations made by Gaumond in [40], the semi-empirical superposition law of Smith and Taylor [34] as well as with the engineering model based on momentum conservation by Larsen in [69]. It will therefore be the basic assumption of the first iteration of a new engineering model developed as part of this Ph.D. study.

The present research makes use of high fidelity CFD-LES models combined with Actuator Disc and Lines techniques. These advanced models are capable to simulate the unsteady flow field of overlapping wakes and therefore can be used to assess the performance and further develop lower engineering models.

1.3 The present study

1.3.1 Scope

This PhD project is about detailed non-stationary characterization and modeling of wind farm flow fields, highly relevant for accurate predictions of load and power production of turbines located in wind farm environments. The project in particular focus on interacting wind turbine wakes and aims at a more fundamental understanding of this physical phenomenon. The scientific approach is based on detailed CFD studies combined with analysis of dedicated innovative full-scale recordings.

The full-scale wake measurements are obtained using cutting-edge technologies in wind energy remote sensing such as LiDAR (i.e. WindScanner developed at DTU Wind Energy, WindCube and ZephIR). The goal of the experimental analysis is to characterize the organized flow structures as well as the wake generated turbulence resulting from the interaction of two wakes as function of downstream distance from the wake generating rotors. The characterization of the organized part of the flow field encompasses a generic analysis of the interaction of the two flow structures as well as their downstream attenuation, expansion and transportation. The characterization of the turbulent part includes an analysis of the interaction of turbulence originating from 3 sources - the ambient turbulence and the wake generated turbulence originating from the two wind turbine rotors, respectively.

The numerical study is conducted using the in house EllipSys flow solver, and covers a large range of generic wind turbine operation. Non-stationary flow conditions will be accounted for using the LES approach. A mutual validation between results from experiments and numerical studies is performed. Observation from the validated numerical approach are condensed into a set of proposal serving as basis to the extension of the Dynamic Wake Meandering model from solitary turbines to wind farms. An investigation of the performance of the two previously introduced wake summation rules using a parametric numerical study on multiple wakes is proposed.

1.3.2 The experimental approach

The present experimental approach is heavily based on lidar technologies. In the present section, an introduction to remote sensing in wind energy and the various lidar technologies is proposed. A detailed description of remote sensing for wind energy is available in the collection of paper by Peña et al. [104].

1.3.2.1 Remote sensing in wind energy: a growing interest

Remote sensing in wind energy is a popular topic of research combined with a fast growing industrial development over the last decade. The need for integrating remote sensing devices such as lidars or sodars in the standard wind resource and power performance assessments is easily understood.

Wind turbines are nowadays installed in offshore, hilly, forested areas or complex mountainous terrain. Furthermore, wind turbine size gradually increases and reach higher region of the atmospheric boundary layer flow with little knowledge of the wind resources and turbulence properties.

The traditional method for performing wind resource assessment and power performance measurements at a given site is to mount a calibrated cup anemometer at hub height on a tall meteorological masts, ideally located 2 to 4 rotor diameters upstream of the turbines (IEC 61400-12-1 standard). As wind turbine rotors reach 160 m in diameter (as for the Vestas 8MW-V164), it becomes evident that single point measurements is not representative of the incoming flow over the entire rotor plane. Consequently, multiple measurement locations at multiple heights are required to characterize the wind speed, shear and veer over such rotor planes. Wind lidars are the best solution to answer this problematic at moderate cost.

Similarly, multi-points multi-heights measurement of the wind are of great interest for model validation of wind profile, wind turbine wakes or measurement of the induction zone of a wind turbine. Lidars are also extensively use in wind turbine control research, and may become fully integrated to wind turbines in the future.

1.3.2.2 Continuous Wave and Pulsed lidars

Wind lidars are wind measurement devices able to detect the Doppler shifts in the backscattered light by using light beams. The recorded Doppler shift is proportional to the wind speed in the beam direction (also referred to as line-of-sight direction) in the wind lidar's adjustable measurement volumes. A sketch of working principle is depicted in Fig. 1.4. There are two types of wind lidars available in the market for measuring the mean and turbulent wind characteristics: 1) the Continuous Wave (CW) lidars and 2); the Pulsed lidars.

CW lidars have the particularity to focus a continuous transmitted laser beam at a selected height or horizontal distance (when mounted on the turbine nacelle) and determine also continuously the Doppler shift in the detected backscatter. When measurements at

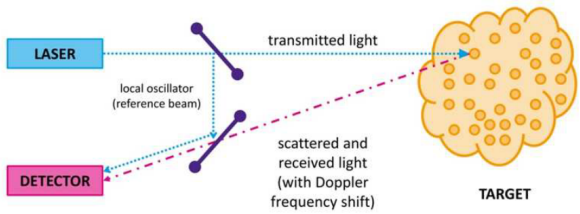

Figure 1.4: Sketch of lidar system. A small fraction of the transmitted light is tapped off by a beamsplitter to form a reference beam. This is superimposed at a second beamsplitter with the weak return scattered from moving aerosols. The detector picks up the resulting beat signal; this undergoes spectral analysis to determine aerosol velocity. Courtesy of M. Harris, from Chapter 4 of [104].

different heights or upstream/downstream distances are required, the CW lidar adjusts the focus of its telescope accordingly. This change in focus distance requires a certain time lapse to complete, depending on the device used. The measurement ranges and the spatial resolution of a CW lidar is directly related to the focal properties of the telescope. Consequently, the shorter the focus distance and the bigger the aperture, the more confine is the line-of-sight measurement volume. Similarly to any telescope, the focal depth increases with the square of distance to the focused measurement point. Therefore, CW lidar have limitations on their range of measurement, typically in the order of 200 m.

Pulsed lidar works with a different scanning approach. They transmit a sequence of many short pulses and detect the Doppler shift in the backscattered light from each pulse propagating at the speed of light. As opposed to CW lidars measuring at one range, pulsed lidar are able to measure the wind speed at several simultaneous ranges. Additionally, the spatial resolution of a pulsed lidar is independent to the measurement range. Instead, the resolution of a pulsed lidar is controlled by its pulse width and the distance the pulse travels while the lidar samples the detected backscatter.

Therefore both technologies have their advantages and disadvantages: while the CW lidar maximum range is conditioned to the increasing averaging volume, the pulsed lidar maximum range is limited to its Carrier-to-Noise ratio. Moreover, a standard CW lidar can typically sample up to 400 individual wind speed measurements per second while a pulsed lidar of similar laser power achieves 2 to 4 wind speeds per second, however, recorded simultaneously at up to 10 different along-beam downstream locations.

1.3.2.3 Lidar application in wind turbine wake research

Most of the lidar assisted wind energy research is orientated towards vertical scanning or 'wind profiling' of the atmospheric boundary later. The use of lidars applied to wake research is relatively new. Bingöl et al. [18] used a nacelle mounted CW lidar to study the 1D wake meandering of the Tellus turbine at the DTU test site, and validate the passive tracer approach of the DWM model. Trujillo et al. [152] extended this work to 2D cross

sectional scanning of the wake and demonstrated the capabilities of lidar to study wake turbulence. Smalikho et al. [132], Aitken et al. [6], Lundquist et al. [80] performed large scale observation of wind turbine wakes on long range lidar on both single turbine and large wind farms. Iungo et al. in [49] and [48] performed 2D field measurements and 3D volumetric scans of wind turbine wakes to study the qualitative effect of atmospheric stability on wind turbine wake.

In the present PhD study, the two technologies previously introduced are used for distinct applications. CW lidar are presently used to investigate detailed flow structures in cross section of a wind turbine wake, allowing characterization of the streamwise turbulent components. Pulsed lidar recordings facilitate the analysis of wake meandering, expansion and transportation due to their ability to scan several downstream cross sections. The used CW lidar is a prototype called *Windscanner* developed at DTU based on the commercially available ZephIR lidar by Natural Powers. The pulsed lidar is a prototype based on the commercial WindCube WLS7 lidar further developed and adapted to wake cross sectional scanning by SWE from the University of Stuttgart.

The lidar used throughout the present experimental work are tested and calibrated using a standard procedure. This process is based on correlating the lidar measured wind speed profile with the one recorded by calibrated cup anemometers on a 125 m tall meteorological mast at DTU Risø campus. Details on the calibration procedure can be found in Wagner at al. [157], where correlation coefficient in the order of ~ 0.99 were found.

1.3.3 The numerical approach

The computation of the unsteady wake flow field is carried out using the EllipSys3D flow solver developed by Michelsen, [92] [93], and Sørensen [135]. The incompressible Navier-Stokes equations formulated in general curvilinear coordinates are discretized and solved using a block structured finite volume approach. The EllipSys3D solver is formulated in primitive variables (pressure-velocity) in a non-staggered grid arrangement. A more detailed description of the numerical scheme is available in [144].

Large Eddy Simulation are used to model the small unresolved length scales of turbulence in the wake flow field. The LES model is based on a spatial filtering of the time dependent governing Navier-Stokes equations, where eddies below a certain size are filtered out. These eddies are subsequently modeled by the simple eddy-viscosity model introduced earlier. In the present numerical approach, the finite volume discretization of the flow equations essentially works as an active filter where scales smaller than the chosen grid spacing are modeled by the sub-grid scale model of Ta Phuoc [141]. This sub-grid scale model both accounts for the energy dissipation and the interaction between small scales responsible for the wake diffusion and large scale driving the wake meandering. Both Actuator Disc and Line modeling techniques are used in the present thesis.

1.3.4 Summary

The present dissertation is organized as followed.

Chapter 2 an 3 are dedicated to a combined experimental and numerical study of the

single wake meandering, expansion and advection.

In Chapter 4, the experimental and numerical work is extended to the study of single wake in non neutral atmospheric boundary layer.

Chapter 5 is dedicated to full scale experimental work and numerical study of the merged wake behind two upstream rotors conducted at two different test site and turbine type.

Chapter 6 makes use of the validated numerical model to study the performance of simple engineering method for wake superposition. This analysis is later on extended to a parametric numerical study based on large eddy simulation with various inflow conditions and turbine spacing. An engineering model for predicting the merged wake deficit from single wake contribution of the upstream turbines is proposed.

Finally, chapter 7 concludes the present thesis with future work and recommendations.

Chapter 2

Wake meandering

2.1 Introduction

This chapter deals with about validation of simple wake engineering models and CFD models using full-scale experimental data obtained from a pulsed lidar system. These validations are facilitated by the recent breakthrough in remote sensing technologies, their increasing reliability and the ease of installation in remote locations such as wind turbine nacelles. Specifically, three main aspects of the wake dynamics are studied in the present work: 1) the wake expansion in the meandering frame of reference, which corresponds to the increase in radial extend of the wake deficit caused by small scale turbulent diffusion and pressure recovery, as it convects downstream; 2) the advection velocity, which is the speed of the downstream transportation of the wake; and 3) the wake meandering, which relates to the continuous change of the lateral and longitudinal position of the wake deficit caused by the large turbulent structures of the atmosphere.

A previous study by Frandsen [39] showed, that wakes have a large impact on the aerodynamic behavior and lifetime of turbines within a wind farm. Therefore, good confidence in wake engineering models is required, so that they can be used extensively to assess and improve the performance of a wind farm layout or a rotor as well as wind farm control strategy.

A measurement campaign, resulting in full-scale wake lidar measurements, was conducted during the spring of 2011 at the DTU Wind Energy Risø campus test site. It involved a WindCube pulsed lidar system with a scanner device developed and adapted by the University of Stuttgart (SWE) to facilitate 2D lidar scan features. The lidar was mounted on the back of the nacelle of a stall regulated 500kW Nordtank wind turbine enabling scanning of the wake flow field simultaneously at different downstream cross sections. As opposed to the study in [83] based on continuous wave lidar technology, where the full-scale

wake measurements are obtained in one particular downwind cross section only, a pulsed lidar offers measurement of the wake expansion simultaneously in a specified number of downstream cross sections.
The meandering path of the wake can be extracted by identifying the wake center for each lidar sweep in all cross sections. It is consequently possible to compare prediction of wake meandering obtained from the Dynamic Wake Meandering model (DMW) [71] with the measured wake meandering in the specified cross sections. Such comparisons are of relevance for model calibration and validation, and provide more insight into the downwind convection of the wake.

Finally, CFD simulations are conducted with atmospheric characteristics and turbine operational conditions identical to a selected 10min time series from the campaign. The simulations are conducted using the Large Eddy Simulation approach for modeling the large atmospheric turbulence scales combined with the Actuator Line technique (AL) to model the rotor. CFD results on average wake expansion in the fixed frame of reference are compared with measurements as well as predictions obtained from simple engineering models.

2.2 Experimental approach

2.2.1 The test set up

The DTU Wind Energy Risø campus test site consists of several turbines and meteorological masts on a nearly uniform and flat land nearby Roskilde Fjord, Denmark. Fig. 2.1 is a sketch of the test site with a description of turbines and met mast with their relative spacing. The present analysis focuses on single wake measurements behind the stall regulated Nordtank 500kW turbine for incoming winds with an inflow direction of 289 °, where the met mast can provide undisturbed inflow measurements to the turbine.

The measurement set up involves a standard pulsed lidar system, Windcube WLS 7, where the scanner device has been adapted. Details on the adaptation and testing can be found in [120]. The raw lidar spectra are post processed by a software developed at SWE and stored in a database at DTU - Risø Campus, together with the data from the met mast and turbine operational sensors. The line-of-sight velocity vectors provided by the lidar system are projected on the main flow direction using the method described in [83]. Time synchronization between lidar and turbine related sensors is performed by the developed post processing software. A robust filtering procedure is implemented, in order to identify erroneous measurements resulting from ground reflection or nearby obstacles. This filtering basically relies on the plausibility of the measured wind speed and the CNR value of the laser beam. During the campaign, two distinct half-opening angle were used. The narrower scanning pattern corresponds to a half-opening angle of approximately 8.5 °, and the wider one has a half-opening angle of 16.7 °. A Cartesian scanning pattern, consisting of a set of 49 measurement target points each spanning 5 planes located at approximately 1,2,3,4 and 5 rotor diameters downstream is used, as depicted in Fig. 2.2. An example of the 10 min average line-of-sight velocities across the 5 scanning planes is shown on Fig. 2.3.

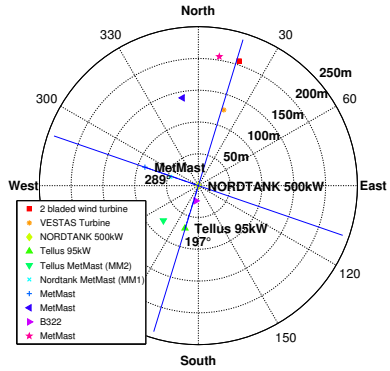

Figure 2.1: Risø test site descriptions, centered around the stall regulated Nordtank 500kW turbine, with a lidar mounted. Concentric circle indicates distance in meter from the Nordtank turbine. The location of a nearby turbine and obstacle have been determined by GPS during a previous campaign. The blue line 289 ° represent the mean flow direction of the present study.

The duration of a single sweep scanning, consisting of 49 measurements over each of the 5 planes, is approximately 7.8s.

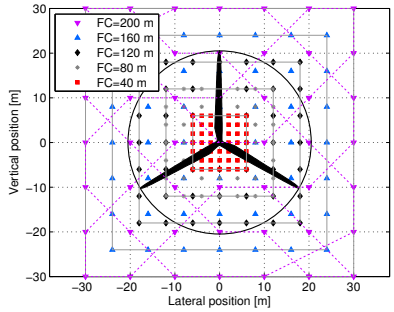

Figure 2.2: Superimposed grid based on the five lidar focus distances with a half-opening angle of 8.5 °. The color points represent measurement locations at different downstream position. The beam trajectory is represented in dash lines for the plane at 200m downstream ($\approx 5D$, D corresponding to the rotor diameter).

2.2.2 Resolving the wake

In this section, the methods used to resolve the wake are detailed. The wake is resolved in two frames of reference: 1) the nacelle frame of reference (also referred as fixed frame of

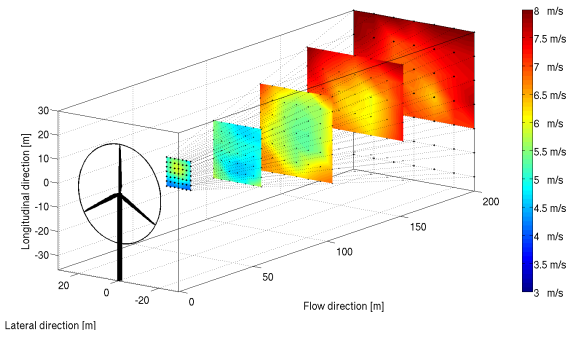

Figure 2.3: Projected view of a 10 minutes average wake flow field scanned by the pulsed lidar in the fixed frame of reference. The black dots are representing cartesian measurement points in the domain. The lower truncation of the 2 most downwind planes is the consequence of ground or obstacles detection. The coordinate system used in this study is right handed with x-axis along the main flow direction, the y-axis directed in the lateral direction, and z-axis vertical and pointing upwards.

reference if we assume no yawing activity of the nacelle); and 2) the meandering frame of reference following the displacement of the wake. In order to determine the unsteady wake in the nacelle frame of reference, i.e. a set of 2D wake profiles corresponding to successive lidar sweeps, a "short term" wake averaging procedure is implemented similarly to that described in [83]. Each lidar sweep volume measurement are assigned into a so-called "wake slice", with release time corresponding to the time average of all measurements within that particular sweep. Thus, "trains" of wake releases are resolved for each focus distance. Each wake slice is re-interpolated over a finer grid in order to handle the changes in grid spacing for each focus plane. The grid spacing of this global refined grid is equal to $1m$, corresponding to half of the grid spacing of the Cartesian scan pattern, at focus distance $40m$. A sketch of this averaging procedure is shown in Fig. 2.4.

The wake deficit is computed for each slice as based on the wake flow field, where the shear contribution is preliminary removed. Two methods are tested for the computation of the sheared inflow. The first one is based on the three sonic anemometer wind speed recorded at the met mast and uses a power law fitting to obtain a mean inflow profile. The second method is to use directly the lidar measurements at the boundaries of the most downwind scanning planes to get an estimate of the shear profile. This latter approach is only used with time series, where the large half opening angle is used, in order to avoid any wake effect on the vertical wind profile. Furthermore, an averaging over a small vertical band of a few meters in horizontal extension is required to reduce the random scatter in the wind profile. Once the shear profile is known, the shear compensated flow is interpolated on the same global grid, in order to facilitate computation of the instantaneous wake deficit. An example, showing the comparison between the shear profile computed from each of the two methods, is shown in Fig. 2.5. It is seen that qualitatively the wind speeds are in fair agreement between the two methods when comparing with the lidar measurements at

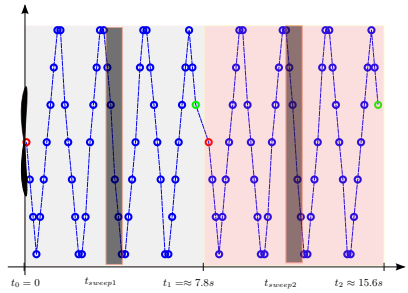

Figure 2.4: Sketch of the sweep averaging procedure seen from the side of the rotor. 2 Lidar sweeps are shown, one in blue and one in red. The 49 measurements points per sweep are shown in blue dots together with the measurement path as function of time. All measurements within one sweep are associated with a "2D wake slice" (dark), where its release time is defined by t_{sweep}, the time average for the relevant sweep.

the two most downwind planes. However, a nearly constant offset along the vertical span in the order of $0.2 - 0.3m/s$ is observed, and the same trend is seen in other investigated datasets. The cause of this mismatch is currently being investigated. It is speculated that the combination of terrain orographic and roughness shift effects at the test site and from westerly winds affects the shear profile downwind, as measured by the lidar. This has to be taken into account in the subsequent wake expansion determination, since it will influence the choice of a suitable free wind speed. In the subsequent analysis, the use of the lidar for determining the shear is adopted. The fair shear gradient agreement seen in Fig. 2.5 gives a good confidence in using this method.

The transformation from the nacelle to the meandering frame of reference is performed by identifying the wake center for each wake slice, and subsequently transform the instantaneous flow field recordings to a Cartesian meandering frame of reference with origin at the wake center. The instantaneous wake center is obtained using an optimization based method similar to the one described in [18].

2.3 Numerical approach

2.3.1 The flow solver and computational domain

The computation of the wake flow field has been carried out using the 3-D flow solver EllipSys3D developed by Michelsen and Sørensen [93], [135]. It solves the discretized incompressible Navier-Stokes equations in general curvilinear coordinates using a block-structured finite volume approach. EllipSys3D is formulated in primitive variables (pressure-velocity) in a non-staggered grid arrangement. The pressure correction equation is solved using the SIMPLE algorithm, and pressure decoupling is avoided using the Rhie/Chow interpolation technique. The convective terms are discretized using a hybrid scheme com-

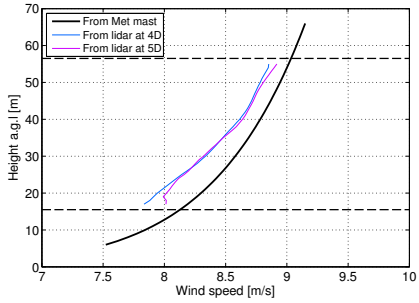

Figure 2.5: Comparison of the shear profile extracted from the met mast and using a power law fit (blue) with the profile measured by the lidar for two downstream cross sections. This profile is averaged over a 3m width band in both the left and the right boundaries of the scanning window. The horizontal dash lines represent the lower and upper part of the rotor.

bining the third-order accurate Quadratic Upwind Interpolation for Convective Kinematics (QUICK) scheme (90%) and the fourth order Central Difference (CDS) Scheme (10%). The LES approach is adopted, employing the mixed sub-grid scale (SGS) model described in [141]. The used mixed SGS viscosity model depends on a filter function and empirically determined constants chosen according to previous work on wake simulations [145].

The wind turbine rotor is simulated using the ACL model developed in [134]. This model combines a three-dimensional (3-D) solver with a technique, in which body forces are distributed radially along lines representing the blades of the wind turbine and smeared azimuthally using a suitable Gaussian smearing function. The standard deviation of the Gaussian function is taken as $3\Delta_x$, where Δ_x is the local grid spacing at the rotor, as based on recommendations from a previous numerical wake study [144]. The body forces are obtained by a look-up table of airfoil data where the local angle of attack is used. In the present study, the blade is discretized using 31 point per radius in the ACL model.

Assuming a homogeneous turbulent field, the modeling of the atmospheric boundary layer (ABL) is done based on the average turbulent intensity and the shear profile as extracted from the measurements. Similarly to [145], the sheared atmospheric mean velocity field is imposed at the inlet of the domain. Additionally, the turbulence field, represented by all three turbulence components of a 3-D incompressible flow field is generated prior to the computation using the Mann algorithm [87], which reproduces homogeneous, stationary, Gaussian and anisotropic turbulence with the same spectral characteristics as observed in the neutrally stratified atmosphere. The Mann spectral tensor is developed using rapid distortion theory combined with a model for eddy lifetime as well as with assumptions of linear shear and neutral stratification. The dimensions of the generated turbulence box is approximately $(Lx, Ly, Lz) = (18R, 18R, 300R)$, where R is the rotor radius, and the number of grid points in the box is $128X128X2048$, resulting in a grid with a resolution corresponding to 7 grid points per rotor radii. The turbulence is introduced in a cross section plane 1.5D upstream of the rotor.

The computational domain has 17.92 million grid points. The dimensions of the grid

used (Lx, Ly, Lz), expressed in terms of rotor radius R, are respectively $(28R, 28R, 36R)$. The grid layout and the boundary conditions are in accordance with previous studies on wake computation [145] and [83]. The inlet of the domain is applied with the desired average wind shear profile as measured at the test site; the outlet has unsteady convective conditions; the ground of the domain has a wall no slip condition; and the top boundary is set to the farfield velocity. The cells are concentrated with a constant spacing of $\Delta_x = \frac{R}{30}$ in the finest resolved wake region in order to resolve and preserve the wake structures. Upstream of the location, where turbulence is introduced, a coarser equidistant region with a spacing $\Delta_x c = \frac{R}{15}$ is used. Finally, stretched regions extend to the inlet and outlet of the domain, respectively. A layout of the computational domain is shown in Fig. 2.6.

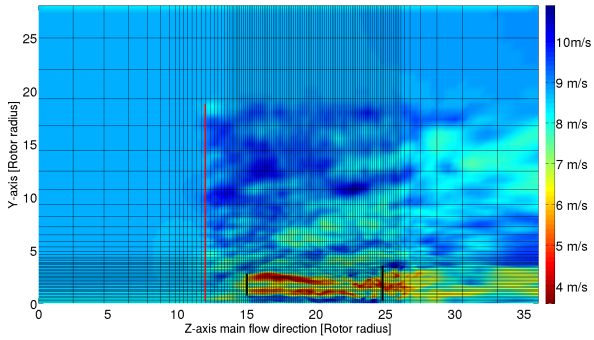

Figure 2.6: Overview of the computational domain. Every 4th cell face is represented. The average streamwise, velocity extracted from a cross section in the middle of the domain ($L_x = 14R$), is shown in a background contour plot. The red line indicates the location of introduced turbulence generated using the Mann model prior to the computations. The locations of the Nordtank turbine is shown in the black line at $L_z = 15R$. The most downwind lidar cross section is shown in black line at $L_z = 24.75R$.

2.3.2 Validation of the numerical model

In this section, a validation of the numerical model is performed. First of all, the ACL model implementation is validated by comparing the measured power curve and thrust curve (derived from two tower bottom bending moment signals) of the Nordtank 500kW with results from the simulations. The measured power curve is determined according to the IEC-61400 standard. The electrical power produced is obtained assuming 7% loss from the available rotor mechanical power, according to [106]. Results of the comparison are shown in Fig. 2.7a.

From Fig. 2.7a, it is seen that the CFD simulations are able to predict fairly well the electrical power produced up to $12m/s$. Above that wind speed, the rated wind speed

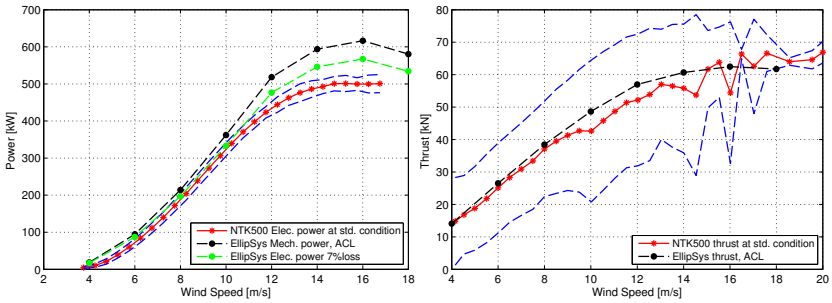

(a) **(b)**

Figure 2.7: Comparison between measured power and thrust curve at standard conditions (TI $< 10\%$, 15^oC and 1013.3mbar) with simulations. (a), Power curve of stall regulated 500kW Nordtank turbine. The overshoot seen in the simulation at high wind speed is due to the stall not being modeled. (b), thrust curve derived from two tower bottom bending moment signals. The blue dash lines represent $\pm\sigma_P$ and $\pm\sigma_T$, the standard deviation of the power and the thrust, respectively.

of the stall regulated turbine is reached, and the separation occurring in the stall region is not properly captured by the model. This, however, has no impact on the subsequent study, since time series with 10 minutes average wind speeds of up to $8.5m/s$ are used in the analysis. Equally good agreement is seen with the thrust comparison.
Secondly, single wake deficit resolved in the meandering frame of reference are compared to measurements for the five available cross sections. The determination of the wake deficit in the meandering frame of reference for the nearest cross section ($1D$ downstream) is not reliable due to the restricted amount of time, where the wake center is located within the scanning area.
Results of the comparison are presented in Fig. 2.8. From Fig. 2.8, discrepancies are observed between the measured and the simulated wake deficit around the wake center, 1D and 2D downstream, respectively. The measured wake deficit at $2D$ is not symmetric and is slightly distorded. This is due to the difficulties for the tracking procedure to identify the wake center for the entire 10 minutes time span. The discrepancies at the wake center tends to disappear with increasing downstream distance, where the reliability of the tracking procedure increases due to the increase of the lidar scanning area in lateral direction. The overall agreement between measurement and simulation is good.

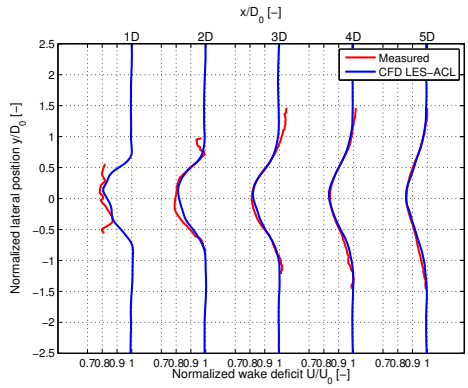

Figure 2.8: Normalized wake deficit at hub height in the meandering frame of reference for all five available downstream cross sections. The top x-axis represents the downstream position in rotor diameters. The bottom x-axis show the normalized wake deficit. The y-axis represents the normalized lateral position. D_0 denotes the rotor diameter and U_0, the average free stream velocity.

2.4 Results and discussion

2.4.1 Single wake meandering dynamics

2.4.1.1 DWM model implementation

The main conjecture behind the Dynamic Wake Meandering model [71] is that the transport of wakes in the atmospheric boundary layer (ABL) can be modeled, by considering the wakes to act as passive tracers driven by the large-scale turbulence structures. In the present study, the DWM model is implemented similarly to [18], where the modeling of the wake meandering relies on a suitable description of the large-scale turbulence structures of the atmospheric boundary layer, as well as of a suitable definition of cut-off frequency.

On one hand, the wake dynamics along the main flow direction is modeled using Taylor's frozen turbulence hypothesis. The downstream advection of the "emitted" wake deficits is assumed to be driven by the constant Taylor advection velocity U_T, which in the present work is computed as the reduced wind speed behind a rotor as initially proposed in the N.O. Jensen's model [54] and summarized in [111]. This simplification decouples the wake along wind deficit profile (and expansion) and the downstream transportation process.

On the other hand, the wake dynamics in the lateral and vertical directions is modeled by considering a cascade of wake elements (also referred previously to as "wake slices") displaced according to the large-scale lateral and vertical turbulence velocities at the position of the particular wake cascade element at each time instant. The transverse velocity field $(v_c(t), w_c(t))$, associated with the large scale part of the turbulence field, recorded by means of 3 sonics anemometers located upstream of the rotor (at $89m$, $\approx 2.2D$), with the mean wind direction aligned towards the rotor, and where large scale filtering is applied using a cut-off frequency corresponding to a spatial scale of two rotor diameter, as based

on previous recommendations by Larsen et. al. [71].

In order to compute a wake displacement at a specific position and time, time synchronization of the various signals is required. Specifically, the signal time lag t_0 caused by the spatial separation between the met tower (sonic signals) and the turbine (thrust derived signals, yaw signals) is determined as specified in Eq. 2.1, whereas a second time lag $t_w(FC)$, representing the time an air particle uses to travel from the rotor to the downstream position FC, is estimated as in Eq. 2.2. Consequently, the total transportation time $t(FC)$ for an air particle to move from the sonic anemometers location to a lidar scanning plane is the sum of both time lags $t_w(FC)$ and t_0 (Eq. 2.3).

$$t_0 = \frac{D_{mr}}{U_0} \tag{2.1}$$

$$t_w(FC) = \frac{FC}{U_{adv}} \tag{2.2}$$

$$t(FC) = t_0 + t_w(FC) \tag{2.3}$$

where D_{mr} is the distance between the mast and the rotor ($\approx 89m$), U_0 is the average free stream velocity, FC is the lidar focus distance, in this case (40,80,120,160 and 200m), respectively, and U_{adv} is the advection velocity computed according to N.O Jensen's model.

In order to compute the wake displacement at a given downstream position (FC) and at a given time, the transverse large scale transverse turbulence velocities (v_c,w_c), the wind directions obtained from the sonic anemometers and the turbine related sensors are expressed in a common time frame $\tilde{t}(FC)$. This common time frame ensure that all sensors are synchronized with respect to the 5 downstream position, and that the relevant time delay is applied to each signal. A sketch representing signal time lines and their corresponding delay is shown on Fig. 2.9.
Thus, following the DWM hypothesis, the lateral and vertical wake meandering dynamics (wake displacements) are determined for all downstream cross sections as:

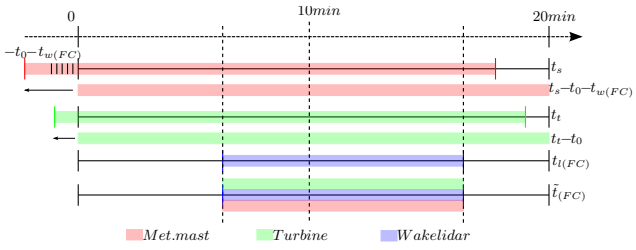

Figure 2.9: Timeline of various measurements. 20 min met mast and turbine measurements are used to cover a 10 minute lidar measurement time series with random start and stop time.

$$y(FC, \tilde{t}) = v_c(\tilde{t}) \cdot \tilde{t}(FC) + h_{yaw}(FC, \tilde{t})$$
$$z(FC, \tilde{t}) = w_c(\tilde{t}) \cdot \tilde{t}(FC) + h_{tilt}(FC, \tilde{t}) \tag{2.4}$$

The tilt contribution $h_{tilt}(FC, \tilde{t})$ is disregarded in the present study since the lidar scanning head was aligned horizontally with the ground and not with the nacelle titled by 2^o. Thus, only the sideways meandering motion of the wake is investigated. The contribution of the turbine yaw misalignment $h_{yaw}(FC, \tilde{t})$ to the wake displacement is taken into account as:

$$h_{yaw}(FC, \tilde{t}) = FC \cdot \tan\left(\theta_s - \theta_{yaw}(\tilde{t}(FC))\right) \tag{2.5}$$

where the misalignment angle is computed from the measurement of yaw position of the turbine $\theta_{yaw}(\tilde{t}(FC))$ and the mean wind direction from the met. mast sonic sensors (average of 3 available heights) θ_s, as detailed in Fig. 2.10.

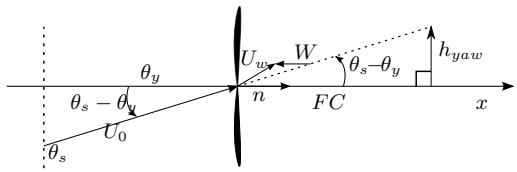

Figure 2.10: Sketch of the wake displacement due to yaw misalignment. The rotor orientation angle θ_y is the reference and is obtained from the absolute yaw position sensor. The misalignment angle is the difference between the wind direction (θ_s) and the absolute rotor position.

2.4.1.2 Comparison of measured meandering with results from DWM

A dataset was selected with the inflow direction aligned along the line connecting the turbine and met mast, a low yawing activity throughout the 10 minutes and a mean free stream velocity of $8.1m/s$. Furthermore, the mean turbulence intensity, defined as the ratio between the standard deviation and the mean of the wind speed, is 11% and the shear exponent obtained from power law fitting of the free wind profile is 0.1. With input from the met mast, the DWM model is used to predict the wake center displacements as function of time using the implementation described in the previous section, whereas the result from the tracking algorithm gives an estimate of the wake center displacements from the lidar measurements. Both results are compared in Fig. 2.11 for a downstream distance of 3 rotor diameters.

The agreement between measured (blue curve) and modeled meandering (magenta curve) is reasonable, however; an offset or "time lag" is seen which is most pronounced between 100s and 140s. In this time interval, the tracking procedure doesn't perform properly due to the restriction of finding the wake center within the measurement area. It seems that

the wake meandering is too large, so that the wake center is outside the lidar scanning area, however, the model is able to predict such large meandering of the wake. The time lag indicates that, in the context of DWM modeling, the use of the reduced wind speed behind a rotor according to the N.O. Jensen's model is not representative for the wake advection velocity, however, the overall fair agreement confirms that it is a good initial guess. Furthermore, the offset can be the consequence of using a constant advection velocity over the considered time span where large scale velocity trends in the mean wind direction is not accounted for. As good agreement can be observed for a given period within a 10 minutes time series, whereas larger deviation can occur elsewhere. This seems to be the most plausible explanation of the local deviation seen in the present comparison.

In order to quantify the time offset, and thus get an estimate of the mean advection time difference, a cross correlation study is performed between measured (W_m) and simulated time series (W_s). The DWM time series is slided in time τ (where τ is approximately ranging as $-600s < \tau < 600s$) relative to the tracked time series, and the cross correlation coefficient is computed for each τ. The time offset τ, that yields the maximum cross correlation coefficient, is the sought time offset.

$$\begin{aligned}\rho(\tau) &= \frac{R(\tau)}{\sigma_{W_s}\sigma_{W_m}} \\ &= \frac{E\left[(W_s(t+\tau)-<W_s>)(W_m(t)-<W_m>)\right]}{\sigma_{W_s}\sigma_{W_m}}\end{aligned} \tag{2.6}$$

where E is the expected value operator, t is the time, σ_W is the standard deviation of the displacement, and $< W >$ refers to the average of the wake center displacement in time. In practice, a cross correlation algorithm doesn't change the characteristics of the time series, as it slides one relative to the other, however, it the context of the DWM, the change in transportation time affect the amplitude of the meandering as seen from Eq. 2.4 and depicted in Fig. 2.11. It is seen, that the amplitude of displacement of the green curves is increasing when increasing the transportation time (which in turn decreases the advection velocity since a longer time is required to reach a particular downstream position). The blue curve represents calibrated DWM result yielding the highest cross correlation. The corresponding mean transportation time lag is in the order of $5.5s$, which is smaller than the sweep averaging time. Results of the analysis are summarized in the following Table 2.1, where the raw DWM results are shown together with the modified advection time and advection velocity obtained from the cross correlation calibration.

Table 2.1: Advection velocities and transportation time at 3D downstream and from the two estimation methods. $U_0 = 8.1$m/s and $t_0 = 11s$. U_w from the N.O Jensen model is computed as: $U_w = \sqrt{1 - CT} \cdot U_0$.

	U_w	t	t_{adv}
DMW Raw	3.4m/s (N.O. Jensen)	46s	35s
DMW Calibrated	4.06m/s	40.5s	29.5s

To conclude, the mean advection velocity of a wake "slice" during its convection from the rotor location to 3D diameters downstream is, in the present case, underestimated by using N.O Jensen model formulation.

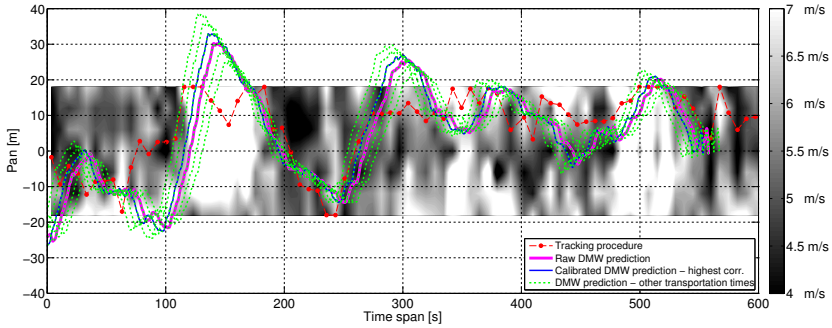

Figure 2.11: Lateral wake meandering analysis at FC=120m ($\approx 3D$). The tracked wake deficit center (using similar technique as in [18]) is shown in red dotted line. The prediction from the DWM model, obtained using the spatially averaged inflow velocity of three sonic anemometers minus the measured nacelle displacement (yaw contribution), is shown in magenta. The background gray density plot represents the measured wake at hub height. Low wind speed is shown in black, and higher wind speed is shown in white. The green dashed lines represent several transportation time lags τ from the cross correlation study. The blue line is the model prediction leading to the highest cross correlation with the tracked wake.

2.4.2 Single wake expansion

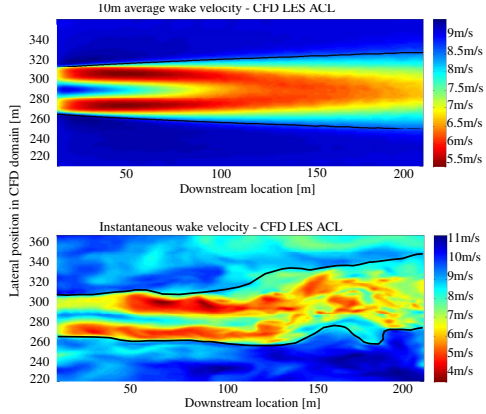

Figure 2.12: Wake velocity field extracted from a slice of the computational domain at hub height and wake width determination from CFD LES ACL. TOP: 10 minute average wake velocity, and BOTTOM: quasi-instantaneous wake velocity. Wake boundaries are shown in black line.

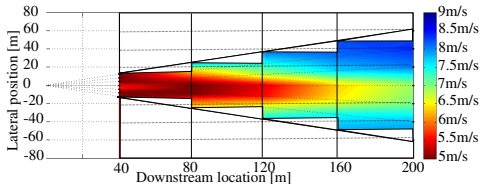

Figure 2.13: Example of wake velocity field extracted from the lidar measurement at hub height and seen from above. 2-D interpolation between the cross sections is performed to obtain the average flow field in the entire measurement region.

In this section, the wake expansion in the fixed frame of reference is computed from a selected dataset representing high rotor thrust coefficient and well resolved wake in all 5 downstream cross sections. The selected dataset has an inflow and operational conditions similar to the previous dataset, i.e., an average free stream velocity of $8.6m/s$, a shear exponent of 0.08 and a turbulence intensity of 13.5%. The large lateral half opening angle of the scanner head of 16.7 ° is used. By operating the lidar at a large opening angle, it is ensured that the full extent of the wake meandering is captured for the expansion study. Typically, the 10 minute average wake width is computed as the extend defined by the lateral coordinates of the intersection between the average wake deficit at hub height and the mean free stream velocity. In practice, the choice of a suitable free stream velocity, giving a realistic wake expansion, is rather challenging. In fact, as discussed previously in the experimental approach section, the observation of several time series shows that the measured free stream velocity at the met mast is often higher than the free stream velocity measured by the lidar around the wake, as depicted on Fig. 2.5.

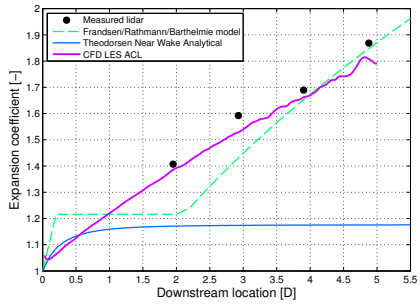

Figure 2.14: Comparison of 10 minutes measured average wake expansion including pressure recovery with a modified Frandsen engineering mode, Theodorsen's near wake analytical solution; and CFD ACL LES simulation. Black dots are measurements.

Results for the wake expansion coefficient, as defined by the ratio of the wake width, at a given downstream position, and the rotor diameter D_0, are compared to the modified wake expansion model of Frandsen in Rathmann et. al. [111], the Theodorsen Near

Wake Analytical solution derived in [142] and implemented in [19], and the present CFD ACL LES unsteady simulation similar to [145] and [83]. The average wake expansion is determined from CFD by computing the wake width from the average streamwise velocity at hub height, as depicted in Fig. 2.12(a). The 10min average streamwise velocity field is obtained in the fixed frame of reference by averaging all instantaneous velocity field (Fig. 2.12(b)), extracted during the computation with a time resolution of 2sec.

The comparison presented on Fig. 2.14 shows good agreement between the measured and the CFD simulated average expansion. Furthermore, Theordorsen's analytical near wake model seems to predict fairly well the near wake expansion, when compared to the results from CFD LES ACL. Larger deviation are seen in the use of the modified Frandsen engineering model for downstream position up to 3 diameters. The agreement becomes more convincing in the far wake.

2.5 Summary

In the present study, single wake characteristics have been studied both experimentally and numerically. The measured wake meandering pattern is obtained from the tracking of the wake center and is compared with the predictions from the DWM model. Good agreement is observed despite of a phase lag due to the uncertainties in using the constant wake advection velocity as predicted in N.O Jensen model. A cross correlation study revealed a time offset of 5.5sec in average between the measured and modeled meandering paths.

The average wake expansion in the fixed frame of reference is determined from the available lidar cross sections and subsequently compared to simple engineering models as well as results from CFD simulations using LES and ACL. Good agreement is observed.

The present analysis is currently being extended to the development of a new wake expansion engineering model and an empirical relationship between the wake deficit magnitude and the advection velocity determined from the available meandering patterns. Moreover, selected consequences of the DWM approach are currently being validated using this pulsed lidar measurement campaign.

Chapter 3

Wake advection and expansion

3.1 Introduction

The study presented in this chapter combines full-scale experimental validation of both wake engineering models and wake CFD models with the development of new empirical models for single wind turbine wake characteristics (i.e. wake expansion and wake advection velocity). This type of analysis is recently facilitated by use of detailed full-scale wind field data obtained from a pulsed lidar. The recent breakthrough in remote sensing technologies, their increasing reliability and ease of installation in unusual locations, such as wind turbine nacelles, allows the research community to benefit from a large amount of high resolution full-scale wake measurements, presenting several advantages when compared to conventional met mast based wake measurements. Specifically, the ability to measure the quasi-instantaneous wake wind field in several downwind cross sections simultaneously is very useful for the study of wake dynamics.

The measurement campaign used in this study was conducted during the spring of 2011 at the DTU Wind Energy Risø campus test site. It uses a WindCube pulsed lidar system equipped with a scanner device, developed and adapted by the University of Stuttgart (SWE), to facilitate 2D spatial lidar scan features. The lidar was mounted on the rear of the nacelle of a stall regulated 500kW Nordtank wind turbine thus enabling scanning of the wake flow field simultaneously at several downstream cross sections. As opposed to the study in [83] which was based on continuous wave lidar technology, delivering the full-scale wake measurements in one particular downstream cross section only, a pulsed lidar offers measurements of the wake characteristics simultaneously in a specified number of downstream cross sections, giving more insight into the advection velocity of the wake, as well as its expansion and recovery.

The present study is a direct continuation of the initial analysis presented in [82]. In [82],

the measured wake meandering obtained from the full scale measurements was shown to agree fairly well with predictions from the DWM model, developed by Larsen et. al. ([71]). However, the uncertainties in the initially specified advection velocity, as derived from N.O. Jensen's model [54], introduced a time lag in the downstream wake transportation. In the present study it is demonstrated, that the use of vortex cylinder theory can improve the advection velocity modeling in the context of wake meandering analysis. In the study in [82], the measured wake expansion determined in the fixed frame of reference, was found in good agreement with predictions from CFD computations using Large Eddy Simulation combined with Actuator Line Technique while in comparison to an existing engineering model [111] significant discrepancies were obtained in the near wake regime.

In this respect, the objectives of the present study are to overcome the inaccuracies in the wake advection velocity estimation found in [82], and to propose a new wake expansion model through an engineering approach based on the basic conjecture of the Dynamic Wake Meandering model. As for advection, a new method to estimate the wake advection velocity is proposed, which relies on a technique involving the cross correlation of the lateral wake meandering time patterns measured in the resolved downstream cross sections. These meandering patterns are obtained from the wake center tracking procedure developed in [152]. This method allows a derivation of an empirical formulation of wake advection velocity as function of the wake velocity deficit, and some analogies with known spherical vortex structures described in [7] are identified. Finally, a new engineering wake expansion model is proposed. This model is based on an initial pressure driven wake expansion in the vicinity of the rotor obtained from theoretical considerations in [65], combined with a spatial expansion gradient in the downstream direction based on the conjecture of the DWM model as well as on the previously obtained empirical formulation of wake advection velocity. The performance of this empirical model is assessed using of 3 datasets representing various inflow conditions and turbine loadings.

3.2 Experimental and numerical approach

3.2.1 The experimental test set up

The DTU Wind Energy Risø campus test site consists of several turbines and meteorological masts on a nearly uniform and flat terrain nearby Roskilde Fjord, Denmark. The instrumented turbine is a Nordtank 500kW stall regulated turbine equipped with 19.1 m long blades manufactured by LM Wind Power. The turbine has a rotor diameter of 41 m. The measurement setup involves a standard pulsed lidar system, Windcube WLS 7, as shown in Fig. 3.1a, where the scanner device has been adapted to facilitate 2D spatial recordings. Details on the adaptation and testing can be found in [120]. Fig. 3.1b presents a sketch of the site layout together with the turbines and met masts. The data sets selected for the subsequent analysis corresponds to westerly inflow directions, in which the met mast provides undisturbed inflow measurements.

The raw lidar spectra are post processed using a software developed at SWE and subsequently stored in a database at DTU - Risø Campus, together with the data from the Nordtank met mast and data from turbine operational sensors. The measured line-of-sight velocity vectors, provided by the lidar system, are projected on the mean flow direction us-

(a) The nacelle mounted Windcube WLS 7.

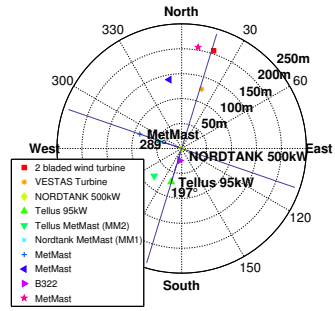

(b) Test site layout.

Figure 3.1: (a) Photography of the nacelle mounted Windcube WLS 7 on the rear of the 500kW stall regulated Nordtank turbine. (b) DTU - Risø Campus test site descriptions, centered around the Nordtank 500kW turbine instrumented with the lidar. Concentric circles indicate distances in meter from the Nordtank turbine. The location of a nearby turbine and obstacle have been determined by GPS during a previous campaign. The blue line in direction 289 ° represents the flow direction for perfect alignment between the instrumented mast and the Nordtank turbine. This flow direction was used for the wake meandering analysis in [82].

ing the method described in [83]. Time synchronization between lidar and turbine related sensors is ensured by the developed post processing software. A robust filtering procedure is implemented, in order to identify and discard erroneous measurements resulting from ground reflection or nearby obstacles. This filtering basically relies on the plausibility of the measured wind speed and the CNR value of the laser beam signal.

During the campaign, two different half-opening angles were used. The narrow scanning regime corresponds to a half-opening angle of approximately 8.5 °, while the wider one has a half-opening angle of 16.7 °. A Cartesian scanning pattern is used that simultaneously covers 5 downstream cross sections at $\sim$ 1, 2, 3, 4, 5 rotor diameters (Fig. 3.2b), each of which contains 49 measurement target points (Fig. 3.2a). The duration of a single scanning sweep is approximately 7.8s, resulting in approximately 77 individual lidar sweeps over a 10 min period.

3.2.2 Resolving the wake

The wake is resolved in two frames of reference: 1) the nacelle frame of reference (also referred to as the fixed frame of reference if we assume no yawing activity of the nacelle); and 2) the meandering frame of reference following the displacement of the wake center. In order to resolve the unsteady wake in the nacelle frame of reference, a “short term” wake averaging procedure is implemented identically to that described in [83] and [82]. Each lidar sweep volume measurement is assigned to a so-called “wake slice”, with release time corresponding to the time average of all measurements within that particular sweep.

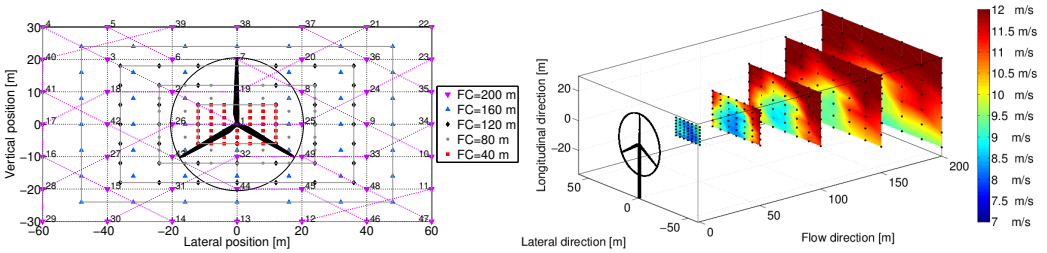

(a) Scanning pattern. **(b)** Measured wake flow field.

Figure 3.2: (a) Superimposed grid based on the five lidar focus distances for the large half-opening angle of 16.7°. The colored grid points represent measurement locations at different downstream position. Beam trajectories are shown/indicated as dashed lines for the plane located 200 m downstream ($\approx 5D$, where D denotes the rotor diameter). The beam trajectory follows the order of the 49 measurements points shown for the plane at the 200 m downstream position. (b), Three-dimensional view of a 10 minutes average wake flow field scanned by the pulsed lidar and shown in a fixed frame of reference, using the large half-opening angle scanning. The black dots represent Cartesian measurement points in the domain. The coordinate system used in this study is right handed with the x-axis along the main flow direction, the y-axis directed in the lateral direction, and z-axis vertical and pointing upwards. The free stream velocity is 12 m/s.

Thus, "sequences" of wake releases are resolved for each focus distance. Each wake slice is subsequently re-interpolated over a finer grid in order to handle the differences in grid spacing between the individual focus planes, as illustrated in Fig. 3.2a.

The instantaneous wake deficit is determined for each wake slice from the wake flow field, after subtraction of the mean wind shear (profile). The mean shear profile is determined directly from the lidar measurements at the boundaries of the two most downwind scanning planes, where wake effects are neglectable. An averaging over a small vertical band a few meters wide in the horizontal direction is required to reduce the random scatter in the wind profile. Once the shear profile is known, the shear compensated inflow is interpolated on the same global grid, in order to facilitate computation of the instantaneous wake deficit.

The transformation from the nacelle to the meandering frame of reference is performed by identifying the wake center in each individual wake slice, and subsequently by mapping the instantaneous flow field on a Cartesian meandering frame of reference with origin at the wake center. The instantaneous wake center is obtained using an optimization based method identical to the one described in [152].

3.2.3 Numerical approach

The numerical computation of the wake flow field has been carried out using the 3-D flow solver EllipSys3D developed by Michelsen and Sørensen [93], [135]. It solves the discretized incompressible Navier-Stokes equations in general curvilinear coordinates using a block-structured finite volume approach. EllipSys3D is formulated in primitive variables (pressure-velocity) for a non-staggered grid arrangement. The pressure correction equation is solved using the SIMPLE algorithm, and pressure decoupling is avoided using the Rhie/Chow interpolation technique. The convective terms are discretized using a hybrid scheme combining the third-order accurate Quadratic Upwind Interpolation for Convective Kinematics (QUICK) scheme (90%) and the fourth order Central Difference (CDS) Scheme (10%). The LES is adopted, employing the mixed sub-grid scale (SGS) model described in [141]. The used mixed SGS viscosity model depends on a filter function and empirically determined constants chosen according to previous work on wake simulations [145]. The wind turbine rotor is simulated using the ACL model developed in [134]. Details on the computational domain layout, the boundary conditions and a validation study of this numerical model are available in [82].

3.3 Single wake advection

In this section, single wake advection is studied using three different approaches: 1) simple theory such as 1D momentum theory and vortex theory; 2) detailed analysis of full scale lidar measurements; and 3) high resolution CFD LES-ACL simulations.

The aim is to improve the accuracy by means of two new *predictive* approaches for the characterization of the wake advection velocity. In the first approach, a closed form expression of the advection velocity is derived from vortex tube theory, thus resulting in a model based on idealized physical first principles. This new approach presents a more

physical variation of the flow velocity passing the rotor. Specifically, the rotor induction decelerating the incoming wind velocity is now taken into account as well as the non linear change of the advection velocity in the flow wise direction.

The performance of this method is tested against the DWM model predictions in [82], and a substantial reduction of the time lag discrepancies observed in [82] is obtained.

The second approach is an empirical approach based on detailed analyses of the full-scale lidar wake measurements. This model assumes that the wake advection velocity relates linearly to the wake deficit magnitude. This type of advection dynamics is also found in spherical Hill's vortex theory [7] and the goal of this study is thus twofold - 1) to validate the conjecture that, under real atmospheric conditions, the transportation process of a wind turbine wake, has advection dynamics that are *qualitatively* similar to that of a spherical Hill's vortex; and 2) to identify the model parameter giving the best possible *quantitative* agreement between model and full-scale observations. To consolidate this result, a set of CFD LES-ACL computations, with similar inflow conditions (mean wind speed, shear and turbulence intensity) as the ones observed during the full-scale experiment, has been performed and subsequently analyzed using the same approach as for the full-scale experiments.

Finally, the quantitative results (i.e. the model parameter estimates) from the full-scale experiments and the CFD computations, respectively, are compared with an analog result derived from spherical Hill's vortex theory. The performance of this later method is tested against the DWM model predictions in [82] together with the advection time obtained from the vortex tube formulation. It is shown that they contribute significantly to the elimination of the time lag.

3.3.1 Advection velocity from 1D momentum and vortex tube theory

A combination of 1D momentum theory relating the axial induction factor, a and the rotor thrust coefficient C_T with the far field wake advection velocity formulation by N.O Jensen's model ([54]), can be generalized to any normalized location $\tilde{x} = \frac{x}{D}$ as:

$$U(\tilde{x}) = U_\infty(1 - a \cdot f(\tilde{x})) \tag{3.1}$$

Where D denotes the rotor diameter. The basic 1D momentum approach for the advection velocity variation of an air parcel across a rotor is to consider the advection velocity equal to the free stream velocity U_∞ upstream of the rotor and equal to $U_\infty\sqrt{1 - C_T}$ in the wake regime. Therefore, the function $f(\tilde{x})$ based on the previous assumption is defined as:

$$f(\tilde{x}) = \begin{cases} 0 & \text{for } \tilde{x} \leq 0 \\ 2 & \text{for } \tilde{x} > 0 \end{cases} \tag{3.2}$$

The vortex tube theory uses the same generalized formulation for wake advection as the 1D momentum (cf. Eq. 3.1), however, with a different expression of the axial induction factor function $f_v(\tilde{x})$:

$$f_v(\tilde{x}) = 1 + \frac{\tilde{x}}{\sqrt{\tilde{x}^2 + 1}} \tag{3.3}$$

A comparison of the normalized advection velocity profile from 1D momentum and vortex tube formulations, respectively, is shown in Fig. 3.3a for locations ranging from 2D upstream to 3D downstream and a high turbine loading corresponding to a thrust coefficient of 0.75. It is obvious, that the advection velocity difference observed in Fig. 3.3a implies a different downstream wake transportation times for the two formulation. For a given start position, x_S, and a given end position, x_E, the advection time difference, ΔT, between the two approaches is derived using the following formulation for the advection time T:

$$dt = \frac{1}{U(x)}dx; \qquad T = \int_{X_S}^{X_E} \frac{1}{U(x)}dx \tag{3.4}$$

In non dimensional time, $\tilde{T} = \frac{TU_\infty}{D}$, the advection time difference is thus given by:

$$\tilde{T} = \int_{\tilde{x_S}}^{\tilde{x_E}} \frac{d\tilde{x}}{\frac{U(x)}{U_\infty}}; \qquad \Delta\tilde{T} = \int_{\tilde{x_S}}^{\tilde{x_E}} \left(\frac{1}{\frac{U(\tilde{x})}{U_\infty}} - \frac{1}{\frac{U_v(\tilde{x})}{U_\infty}} \right) d\tilde{x} \tag{3.5}$$

with $U(\tilde{x})$ being the advection velocity given by Eq. 3.1, with the axial induction factor function $f(\tilde{x})$, defined in Eq. 3.2, whereas $U_v(\tilde{x})$ denotes the advection velocity resulting from the axial induction function $f_v(\tilde{x})$ in Eq. 3.3.

Introducing Eq. 3.1 into Eq. 3.5, we obtain:

$$\Delta\tilde{T} = \int_{\tilde{x_S}}^{\tilde{x_E}} \left(\frac{1}{1 - a \cdot f(\tilde{x})} - \frac{1}{1 - a \cdot f_v(\tilde{x})} \right) d\tilde{x} \tag{3.6}$$

An illustration of the advection time difference as function of the normalized distance to the rotor is shown in Fig. 3.3b. The accuracy of the vortex tube based advection model is subsequently tested against the measured wake advection under real atmospheric conditions.

3.3.2 Advection velocity estimation from wake lidar measurements

A first approach to determine experimentally the measured wake advection velocity is to identify a distinct turbulence structure in the near wake and subsequently tracking it during its downstream transportation. The time resolution of the lidar system, and the number of scan cross sections used in the present campaign do not suffice for this method.

However, alternatively it is possible to take advantage of the passive tracer assumption of the DWM framework, and combine this assumption with the available of 2D lidar cross section recordings to obtain wake advection estimates as function of downstream distance. Within the DWM framework, the meandering patterns, defined as the wake center position time series at a given downstream location, have identical generic shapes. They differ from one downstream location to another only by their amplitude and a phase shift due to the different transportation times. The observed meandering patterns are obtained from the wake center tracking procedure described in [152], resulting in discrete wake center positions as function of time with resolution defined by the sweep time of the lidar system.

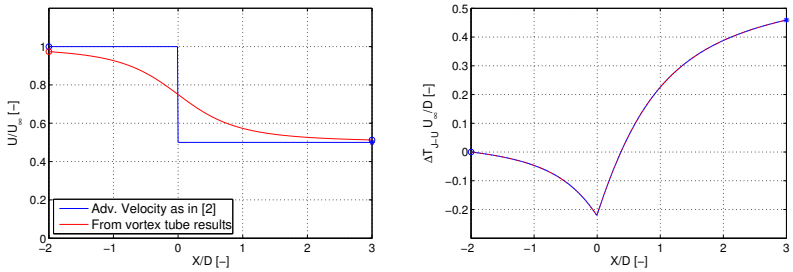

(a) Normalized advection velocity. **(b)** Normalized time difference.

Figure 3.3: (a) Comparison of the normalized advection velocity resulting from vortex tube theory with the N.O Jensen's formulation based on 1D momentum theory. The red curve corresponds to the vortex tube formulation in Eq. 3.3, and the blue curve is the 1D momentum based formulation in Eq. 3.2. The C_T value is 0.75 giving an axial induction factor $a = 0.25$. (b) Non dimensional advection time difference corresponding to an advection distance between 2 rotor diameters upstream and 3 rotor diameters downstream.

Initially, a mapping from the discretely tracked wake center to continuous time distributions is performed using spline interpolation. Due to spatial limitations in the cross sectional scanning area at low focus distances (cf. Fig. 3.2a), the plane at 1D downstream is excluded from the analysis. An example of typical continuous wake meandering patterns is shown in Fig. 3.4 for the remaining 4 cross sections. It is seen, that the wake patterns as expected are strongly correlated, shifted in phase and scaled in amplitude, thus consolidating the validity of using the DWM framework in the present context.

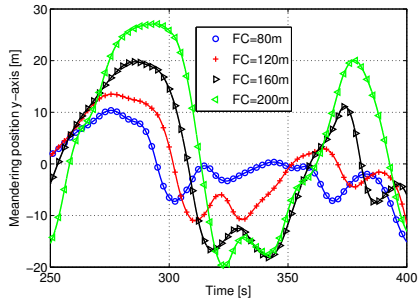

Figure 3.4: Wake center position in the lateral direction as function of time. Four different downstream cross sections are represented. The continuous meandering displacements is obtained from discrete sweep displacement using a spline interpolation.

A quantification of the time lag between the meandering patterns shown in Fig. 3.4 is obtained by performing a cross correlation study between consecutive pairs of meandering paths $(S_k;S_{k+1})$. The maximum of the cross correlation coefficient ρ which, in the present

context, is the advection time estimate, obtained for a specific time shift τ:

$$\rho(\tau) = \frac{R(\tau)}{\sigma_{S_k}}\sigma_{S_{k+1}} = \frac{<(S_k(t+\tau) - S_k)(S_{k+1}(t) - S_{k+1})>}{\sigma_{S_k}\sigma_{S_{k+1}}} \tag{3.7}$$

$< S_k >$ and σ_{S_k} are the average and the standard deviation of the wake center position in cross section k, respectively. With the time shift τ being the sought advection time, a direct estimation of the advection velocity between pairs of cross sections, whose mutual distances are known, is possible.

This cross correlation technique is in turn applied to determine the advection velocity, U_a, as function of the downstream position, which subsequently is compared to the results from the analysis in [82]. For the particular 10 min time series investigated, the tracking procedure fails in finding the wake center in the most downstream cross section plane due to the fast recovery of the wake. Furthermore, and as previously mentioned, the plane, located approximately 1D downstream, is too restricted in size for an effective tracking over a full 10 min period. In fact, the wake center is found within the scanning area only for a limited amount of time. Consequently, the advection time estimation is based on the three remaining planes, respectively $2D$, $3D$ and $4D$ downstream the rotor. Two advection velocities can then be computed. One obtained from the cross correlation study between meandering patterns using the advection distance ($2D \rightarrow 3D$), and the second using the advection distance ($3D \rightarrow 4D$). The results are summarized in Table 3.1.

Table 3.1: Advection velocities and transportation times 3D downstream based on the various estimation methods. $U_\infty = 8.1$ m/s.

	U_a	t	t_{adv}
DMW Raw (from [82])	3.4 m/s (NO Jensen)	46 s	35 s
DMW Calibrated (from [82])	4.06 m/s	40.5 s	29.5 s
Vortex tube theory	4.21 m/s	39.2 s	28.5 s
Meandering patterns method	80-120 m: 3.95 m/s	41.4 s	30.4 s
	120-160 m: 4.49 m/s	37.7 s	26.7 s
	$< U_a >$: 4.22 m/s	39.4 s	28.4 s

The results in Table 3.1 seems to confirm the trend obtained in [82], where the actual wake transportation time from the rotor plane to a location 120 m downstream is approximately 5 s less than the DMW predictions based on 1D momentum theory and the simple advection model. The advection velocity is seen to increase as the wake convects downstream, in accordance with classical theory on wake recovery. Also, the estimate emerging from the meandering pattern method agrees very well with the prediction from the vortex cylinder theory.

3.3.3 Empirical relation between advection velocity and maximum wake deficit.

The previously introduced cross correlation based method to estimate a measured wake advection velocity directly showed good agreement with vortex tube theory for the se-

lected time series. In this section, this method is applied to a larger set of data, in order to investigate the relation between wake advection velocity and wake deficit magnitude (located at the wake center). The study is based on both experimentally and numerically derived wake properties. Further, a possible link to results following from spherical vortex theory is investigated.

General formulation for CFD and measurements

In Fig. 3.5, the measured wake deficit profiles associated with each of the 5 pulsed lidar cross sections, and resolved in the meandering frame of reference, are shown. For the most downstream profile, the maximum wake deficit, located at the wake center, and denoted Δu is indicated. Additionally, the wake advection velocity, U_a and the mean self induced velocity, U_i are also represented. These last two quantities are related as:

$$U_a = U_\infty - U_i \tag{3.8}$$

where U_∞ denotes the mean free stream velocity. We assume the maximum deficit Δu to be related to the wake self induced wake velocity U_i as:

$$U_i = c\Delta u \tag{3.9}$$

where c is a constant to be determined empirically. This determination is performed using the knowledge of the advection velocity as function of downstream position, obtained from the cross correlation analysis described in the previous section, and the measured wake deficit magnitude. In dimensional and non dimensional forms, Eq. 3.8 and Eq. 3.9 reduce to respectively:

$$U_a = U_\infty - c\Delta u; \qquad \frac{U_a}{U_\infty} = 1 - c\frac{\Delta u}{U_\infty} \tag{3.10}$$

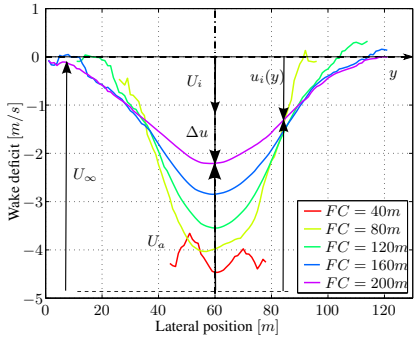

Figure 3.5: Sketch of the measured wake deficit in the meandering frame of reference, its self induced velocity and the free stream velocity. The maximum wake deficit yielding the minimum wake wind speed is located at the wake center.

The mean advection velocity obtained from the cross correlation study is associated to the mean downstream location of the 2 cross sections (sections S_k and S_{k+1}) used for its calculation. However, the maximum wake induced velocities are measured directly at a specific section S_k.Consequently, they are linearly interpolated to the same location the

advection velocities are ascribed.

Spherical vortex theory

From the general vortex theory by Akhmetov in [7], an expression for the constant c in Eq. 3.9 can be obtained by approximating the wake deficit with a Hill's spherical vortex. Such vortex structures of radius a have a self induced stream wise velocity, U_i, of the flow velocity inside the sphere. In a fixed coordinate system attached to the vortex itself and in an uniform flow characterized by velocity U_0 in a direction of the negative x-axis:

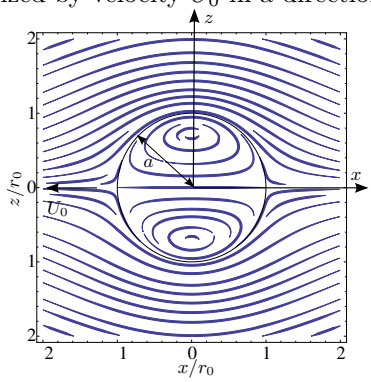

Figure 3.6: Streamline pattern of a Hill's spherical vortex, with a radius $a = 1$ and coordinate system with vertical z and horizontal x axis. This streamline pattern was computed from the expression of U and V velocity components in [7].

$$U_i(x, z, a) = \frac{3}{2} U_0 \left(1 - \frac{2z^2 + x^2}{a^2}\right) \tag{3.11}$$

Similarly, the flow velocity outside the sphere ($z^2 + x^2 > a^2$) is derived from Hill's stream function formulation as:

$$U_i(x, z, a) = U_0 \left[\left(\frac{a^2}{x^2 + z^2}\right)^{\frac{5}{2}} \frac{2x^2 - z^2}{2a^2} - 1\right] \tag{3.12}$$

An illustration of the streamline pattern of Hill's vortex is shown in Fig. 3.6 together with a definition of the corresponding coordinate system.

The velocity at the center of the vortex sphere (Eq. 3.11) ($x = 0, z = 0$), expressed in the same fixed coordinate system, is:

$$U_i(0, 0, 0) = \frac{3}{2} U_0 \tag{3.13}$$

The velocity outside the sphere for $x = 0$ and $z \to \infty$ is obtained from Eq. 3.12 as:

$$U_i(0, \infty, a) = -U_0 \tag{3.14}$$

The maximum vortex structure deficit Δu therefore reduces to:

$$\Delta u = U_i(0,0,0) - U_i(0,\infty,a) = \frac{5}{2}U_0 \tag{3.15}$$

In the fixed coordinate system, the corresponding advection velocity is $U_a = -U_0$, which corresponds to the induction at the center of the vortex structure. Therefore, when the vortex structure is advected at a velocity equal to the free stream velocity ($U_\infty \neq 0$), the advection velocity in absolute coordinates becomes:

$$\begin{aligned} U_a &= U_\infty - U_0 \\ &= U_\infty - 0.4\Delta u \end{aligned} \tag{3.16}$$

An expression for the advection velocity of a Hill's spherical vortex is thus obtained as:

$$\frac{U_a}{U_\infty} = 1 - 0.4\frac{\Delta u}{U_\infty} \tag{3.17}$$

Results

An empirical analysis is now conducted using a wide range of datasets representing the various inflow conditions occurring during the measurement campaign, as listed in Table 3.7b. In addition, 5 full 10 minutes unsteady CFD LES-ACL computations with sheared inflow and atmospheric turbulence are conducted, which are also listed in Table 3.7b. Results of the comparison are shown in Fig. 3.7a.

The assumption/hypothesis stating that the maximum wake deficit is related to the wake induction by a constant c is confirmed, since all measurements display a fairly linear relationship. From Fig. 3.7a, it is further seen, that both measurements and CFD results are in good agreement. However, their respective linear slopes, c, are larger than the one obtained from Hill's spherical vortex theory. The scatter of the measurements is larger than the scatter obtained from the CFD simulations, which may be due to general uncertainties of lidar based full scale measurements associated with e.g. the inflow wind profile, the lidar averaging procedure and the unavoidable velocity projections. Furthermore, the meandering tracking procedure is more challenging to operate on the measured wind field as compared to the CFD generated flow fields, since the lidar spatial resolution is much coarser than the resolution provided by the CFD results.

3.4 Single wake expansion

Initially, an investigation of the single wake expansion in the fixed frame of reference is conducted. A comparison is performed between the measured wake expansion from the pulsed lidar recordings, the numerical results from the CFD LES-ACL computations and Frandsen's empirical expansion model, as implemented by Rathmann et al in [111]. This study is conducted for two selected datasets with different turbulence intensities and mean wind speeds, and discrepancies are discussed both in the near and the far wake regime.

Subsequently, a new empirical expansion model is proposed taking advantage of the DWM framework. One of the strengths of using the DWM formulation for wake expansion

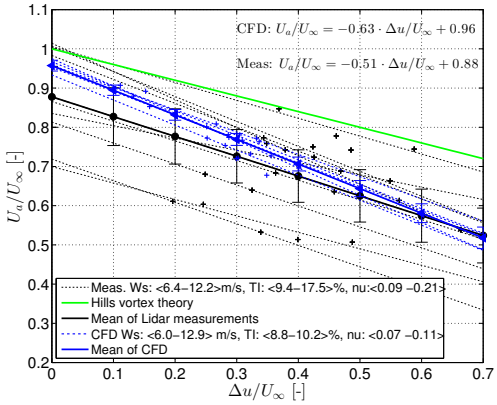

(a) Empirical analysis.

	#	WS [m/s]	TI [-]	CT [-]	α [-]	U_a [m/s]	Pow. [kW]
Measurements	1	6.4	0.09	0.83	0.18	2.63	75.9
	2	6.7	0.17	0.81	0.21	2.93	134.0
	3	8.1	0.13	0.71	0.09	4.37	211.7
	4	8.2	0.14	0.70	0.14	4.40	181.9
	5	8.5	0.12	0.68	0.07	4.79	200.9
	6	8.9	0.14	0.64	0.16	5.34	241.1
	7	9.1	0.14	0.62	0.14	5.67	258.5
	8	9.7	0.18	0.56	0.15	6.50	299.3
	9	12.2	0.16	0.44	0.11	9.15	437.3
CFD	1	6.0	0.08	0.89	0.11	1.99	72.0
	2	8.3	0.09	0.75	0.07	4.19	196.5
	3	8.6	0.10	0.70	0.07	4.70	208.9
	4	10.0	0.08	0.57	0.11	6.56	326.7
	5	12.9	0.10	0.45	0.01	8.93	451.3

(b) Selected datasets.

Figure 3.7: (a) Empirical relationship obtained from linear fitting of observations from full-scale measurements and from CFD respectively. A comparison with the theoretical spherical vortex solution is also shown. Dash lines represent linear fit of the measurements points (crosses). The mean of the lidar measurements and the CFD results are also shown together with their respective error bars. The following empirical constants are obtained: $c_{CFD} = 0.63$, $c_{meas} = 0.51$. (b) List of selected datasets. U_a is the simple theoretical advection velocity equal to $U_\infty\sqrt{1-CT}$, and α is the mean wind shear exponent. All quantities are 10 minutes averages.

modeling is that the influence of ambient turbulence is included in the modeling primary through the relation between the magnitude of meandering and the intensity of the large scale turbulence. In this analysis, the far wake expansion is assumed to be dictated by the Gaussian distributed lateral wake meandering, whereas 1D momentum theory gives valuable insight into the wake expansion in the vicinity of the rotor. Both conjectures are validated in the present analysis. Time series where large wake deflections (i.e. significant meandering) occur are used in order to facilitate the validation.

Several formulation of the wake expansion gradient are investigated using different normalization and scaling of the lateral velocities. The most advanced gradient formulation makes use of the previously developed empirical wake advection model. The accuracy of the different formulations are tested using three selected full-scale datasets representing different inflow conditions.

3.4.1 Measured and modeled wake expansion.

The wake expansion in the fixed frame of reference is determined from two selected datasets representing different mean wind speeds. The first dataset (labeled #5 in Table 3.7b) represents a situation with moderate rotor thrust coefficient (0.63) and mean wind speed (8.5 m/s) resulting in pronounced wakes in all 5 downstream cross sections. The inflow turbulence level is moderate for this onshore wind turbine site (12%). The second selected dataset (labeled #9 in Table 3.7b) has a lower thrust coefficient (0.44), a larger mean wind speed (12.2 m/s), and a higher stream-wise turbulence level of 16%.

The two selected datasets are recorded using the large lateral half opening angle of the scanner head of 16.7°. By operating the lidar at a large opening angle, it is ensured that the full extent of the wake is captured for the expansion study of the three most downwind cross sections. However, the recording area for the first and second cross sections may not extend sufficiently to measure the entire wake span for some datasets.

In addition, numerical simulations are conducted with inflow characteristics closed to the ones observed in the measurements and labeled #2 and #5, respectively in Table 3.7b. More specifically, these simulations are CFD ACL LES unsteady simulations similar to those described in [145] and [83].

For both measurements and CFD results, the 10 min average wake width is obtained as the vector length defined by the two points intersection between the average wake deficit and the mean free stream velocity.

Results from full-scale measurements and CFD simulations are compared to the wake expansion model of Frandsen in Rathmann et. al. [111]. In the adaptation of Frandsen's expansion model in Rathmann et. al. [111], the wake expansion, E_F, is expressed as function of downstream distance:

$$E_F(x) = D_0 \, max \left[\beta, \alpha \frac{x}{D_0} \right]^{\frac{1}{2}} \tag{3.18}$$

where $\alpha = 0.7$ is an empirical constant determined in [111], D_0 is the rotor radius, and β

is defined by:

$$\beta = \frac{\frac{1}{2} - \frac{1}{2}\sqrt{1 - C_T}}{\sqrt{1 - C_T}} \tag{3.19}$$

where C_T is the rotor thrust coefficient.

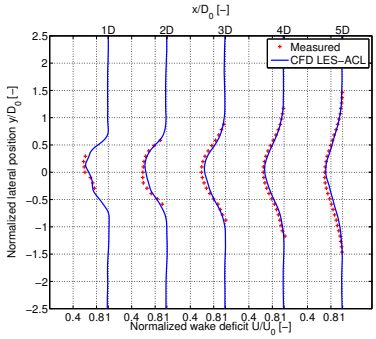

(a) Deficit: meas. (dataset #5) and CFD (dataset #2).

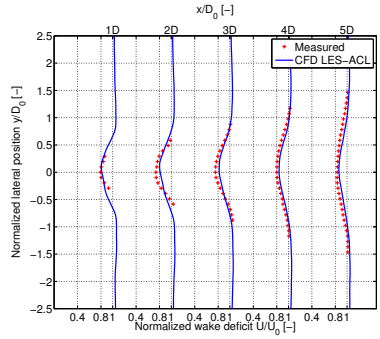

(b) Deficit: meas. (dataset #9) and CFD (dataset #5).

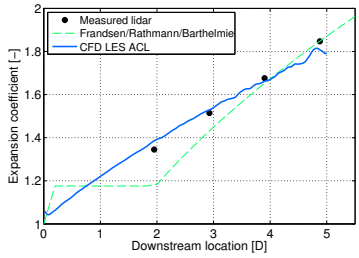

(c) Expansion: meas. (dataset #5) and CFD (dataset #2).

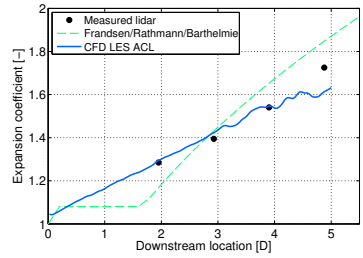

(d) Expansion: meas. (dataset #9) and CFD (dataset #5).

Figure 3.8: (a) and (b) Normalized wake deficit in the meandering frame of reference from measurements and CFD simulations ; (c) and (d) comparison of measured 10 min mean wake expansion with predictions from Frandsen's engineering model as well as with CFD ACL LES simulations for the same datasets. The α value in the empirical formulation in Rathmann et. al. [111] is 0.7.

The comparison presented in Fig. 3.8 shows good agreement between the measured and the CFD-simulated average expansions. Larger deviations are seen between measurements and the modified Frandsen engineering model, especially for downstream positions up to 3 diameters where pressure recovery is dominant relative to the turbulent diffusion. The agreement becomes more convincing in the far wake. This is in agreement with the limitations of Frandsen's model, which is empirical and based on met mast far wake measurements. Whereas the empirical value of $\alpha = 0.7$ shows good agreement with the lidar data in the far wake of moderate wind speed dataset (Fig. 3.8c), the agreement is

less convincing for the high wind dataset (Fig. 3.8d), revealing a lack of accuracy for high turbulence intensity cases.

3.4.2 Verification of a DWM model assumption.

The time lag between each of the meandering patterns obtained from the cross correlation study performed in Sec. 3.3.2 are used to "de-lag" the wake center positions recorded at different downstream cross sections, as illustrated in Fig. 3.9a.

By removing the time lag, a direct visualization of the "trace" of an imaginary air parcel advected in the wake and following the wake center is facilitated. This allows validation of a DMW consequence, namely that the characteristic lateral displacement velocities in the *near wake* are approximately constant for each deficit "release". This consequence is first verified graphically in Fig. 3.9b where the wake center displacements, for a random set of sweeps selected within a dataset, are plotted against the downstream location. It is observed, that the wake centers are lying approximately on a straight line through the 4 investigated cross sections, thus indicating constant lateral velocities in the *near wake* as predicted by the DWM model.

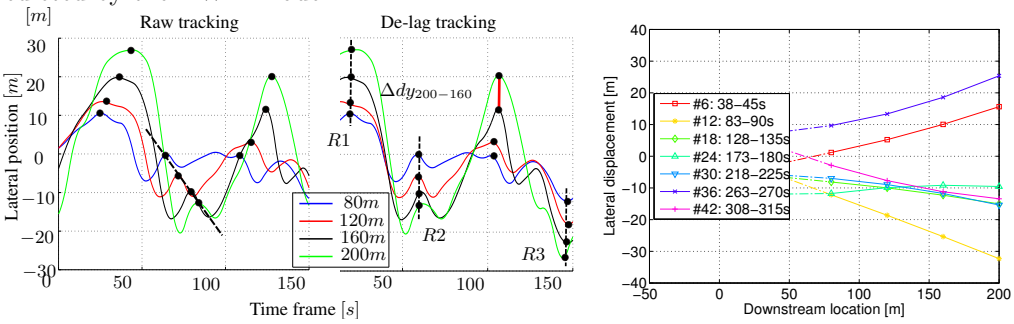

(a) Meandering patterns.

(b) Lateral wake displacements.

Figure 3.9: (a) Wake center lateral motion for four downstream cross sections recorded during a period of 2.5 min. On the left figure, the raw signal is shown, and on the right figure the signals with the relative time lag eliminated is shown. The red vertical segment on the right figure represents the lateral deflection of an imaginary particle following the wake center between two consecutive cross section scanning planes. R1, R2 and R3 denote regions, which are used to verify the DWM consequence in focus. (b) Tracked wake center positions as function of downstream position. Specific lidar sweep measurements are numbered and selected randomly from the 10 min dataset.

The meandering patterns shown in Fig. 3.9a are used to compute the *lateral* velocities v_{S_k} at a cross section, S_k, based on the knowledge of the mean advection time between two cross sections obtained from the previous section. This analysis is first performed on three imaginary air parcels over a time span of 20 s. The air parcels, denoted R1, R2 and R3 respectively, correspond to regions where the wake deflections are large, hence

facilitating the validation locally. Finally, the entire 10 min dataset is used. The average lateral velocity $< v_{S_k} >$ over a region R_k is then obtained as:

$$< v_{S_k} >= \frac{< d_{y(S_{k,t})} >}{\tau(S_k)} \tag{3.20}$$

where $d_{y(S_{k,t})}$ represents the time dependent lateral displacement of the wake center, and $\tau(S_k)$ is the time used for an air parcel to travel from the rotor to a given cross section S_k. Results are summarized in the Table 3.2.

Table 3.2: Lateral velocities derived from three test regions as well as the average over the entire dataset span as function of downstream cross sections. The advection time is the time a 'wake slice' used to travel from the rotor to the corresponding downstream scanning plane.

Downstream location [m]	Adv. time τ [s]	v_{S_k} at $R1$ [m/s]	v_{S_k} at $R2$ [m/s]	v_{S_k} at $R3$ [m/s]	10 min [m/s]
80	27.0	0.31	-0.23	-0.28	-0.17
120	39.2	0.33	-0.27	-0.25	-0.14
160	49.9	0.36	-0.32	-0.28	-0.14
200	59.2	0.41	-0.28	-0.32	-0.12

The results in Table 3.2 confirm that the lateral velocities are reasonably constant throughout the entire dataset, with a maximum deviation of 0.05 m/s and a tendency to decrease slightly in magnitude with respect to the distance from the rotor. This is most likely associated with deviations from the *near wake* assumption.

3.4.3 Wake expansion derived from the measured wake center tracking

In Sec. 3.4.1, the measured expansion coefficient is obtained from an analysis of the recorded 2D cross sections in the wake flow field. The subsequent analysis focuses on the development of a method, where the wake expansion in the far field is determined from the measured wake center displacements only. A linear extrapolation of the expansion in the *far wake* regime into the *near wake* regime and ultimately to the rotor position is performed. This in turn determines an imaginary initial expansion just after the rotor plane, where pressure recovery drives the wake flow field. This initial expansion is subsequently compared to the theoretical formulation by Larsen et al. [65].

Analysis of expansion gradients from full-scale measurements. The positive and negative gradients of the wake center position expansion in the fixed frame of reference, at a downstream distance k, denoted respectively $\alpha^+(k,t)$ and $\alpha^-(k,t)$, are depicted in Fig. 3.10. They can be computed as the ratio between the time dependent lateral displacement $d_y(k,t)$ and the downstream position $d_x(k)$, where $d_y(k,t)$ refers to the instantaneous lateral wake center position. Physically, these slopes can be directly related to the expansion of the wake due to wake meandering. Two types of gradients are defined: 1) the so-called global gradients, defined from the rotor plane location to each downstream cross section; and 2) the local gradients defined as the ratio between the displacement increment and the

downstream distance between the k^{th} and the $(k^{th}-1)$ plane (Eq. 3.21). These gradients are sketched in Fig. 3.10 (left).

$$\alpha_{local}(k,t) = \frac{d_y(k,t) - d_y(k-1,t)}{d_x(k) - d_x(k-1)}; \qquad \alpha_{global}(k,t) = \frac{d_y(k,t)}{d_x(k)} \tag{3.21}$$

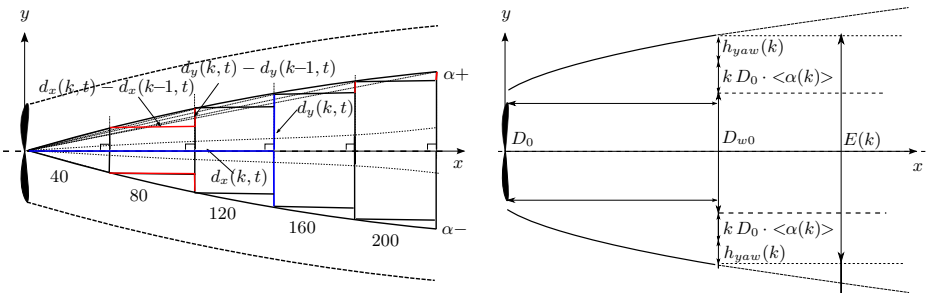

Figure 3.10: (Left) Sketch of the expansion gradients expressed in the fixed frame of reference. Each individual gradients is computed for every available instant, t, and the results are time averaged to obtain the mean expansion gradient. Furthermore, the maximum displacement is also extracted, which eventually defines the wake envelope. (Right) Decomposition of the contributions to the total expansion coefficient at a given downstream cross section k.

The average wake center displacement gradient, $< \alpha_{(k)} >$, is the average of the *absolute value* of all negative and positive gradients. This implies, that large and small excursions from the mean displacement are equally weighted. The normalized average gradient is denoted $\tilde{\alpha}(k)$, and two normalization constants K are investigated:

$$\tilde{\alpha}(k) = \frac{< \alpha_{(k)} >}{K} \tag{3.22}$$

The first option is defined by $K_a = \sigma_v / < U_a >$, where $< U_a >$ is a mean characteristic advection velocity of the wake (obtained from averaging the downstream-dependent known advection velocities), and σ_v is the standard deviation of the lateral velocities obtained from three sonic anemometers recording the undisturbed *inflow* characteristics. The second option is defined by $K_b = \sigma_{v_c} / < U_a >$, where σ_{v_c} denotes the standard deviation of the large scale lateral velocity fluctuations. v_c corresponds to the low frequency content of the lateral velocity power spectrum, as detailed in [82] and [71]. Similarly, the maximum wake center displacement gradient $\alpha_M(k)$ is defined as the average of the maximum positive and the absolute value of the minimum negative gradient and normalize with the two expressions for the constants, K_a and K_b, defined previously. To summarize, there are 4 non-dimensional average gradients (one local, one global with two dimensional constants each) plus the maximum global slope.

The non dimensional values of these 5 gradients are computed for the time series labeled #5 in the table in Fig. 3.7b, and the results are shown in Fig. 3.11a. The normalized gradients are compared to two constants: 1) the mean absolute deviation (MAD) which is defined

as the mean of an absolute deviation of a set of data about the data's mean or median, and for a standard normal distribution equal to $\sqrt{2/\pi}$; and 2) the normalized gradient equal to 1. Thus, for the normal distribution, the MAD is about 0.8 times the standard deviation. From Fig. 3.11a, it is seen that the choice of global or local determination of the gradient has hardly any impact on the results. However, local slopes are typically more sensitive and less accurately determined, since the lateral displacements scales are smaller than the ones for the global slopes. Furthermore, it is seen, that the normalization based on all lateral velocities gives a gradient of $\sqrt{2/\pi}$, whereas the normalization based on the large scales only gives a gradient of 1. This last normalization factor will be used in the formulation of the subsequent engineering model.

Finally, the normalized maximum gradient shown in Fig. 3.11a has a value ranging 3.1 from 3.4, depending on the downstream distance. For the present meandering stochastic process, the most likely extreme within a specified time span T and normalized with the process standard deviation is known as the peak-factor, k_p. Following the analysis in [25], the peak-factor for a Gaussian process, illustrated in Fig. 3.11b can be expressed as:

$$k_p = \sqrt{2\ln(\nu T)} + \frac{\gamma}{\sqrt{2\ln(\nu T)}} \tag{3.23}$$

where γ is the Euler constant, and ν is the zero crossing frequency of the process given by $\nu = \sqrt{m_2/m_0}$. The spectral moments, m_i, are in turn defined as:

$$m_i = \int_0^\infty n^i S(n) dn \tag{3.24}$$

in which n denotes a frequency, and $S(n)$ is the (single sided) power spectrum of the process. For a wind speed process, k_p is typically in the range of $[2.5; 3.5]$ for a time span of 10 minutes.

In the present study, the peak factor has been determined using three different types of input: 1), the meandering path time series as depicted in Fig. 3.9; 2), the *full* lateral turbulence component v of the undisturbed flow and 3), the *low pass filtered* lateral component v_c of the undisturbed flow. The calculated peak factors are listed in Table 3.3. It is seen in Table. 3.3 that the peak factor associated to the large scale lateral turbulence component is as expected lower than the one obtained from the "full" lateral velocity component, due to the attenuation of extrema by the low pass filtering. It is further seen in Table. 3.3 that the peak factors obtained from the measured meandering path time series are in good agreement with the normalized maximum wake deflection depicted in Fig. 3.11a, and with the theoretical peak factor of a Gaussian process. This result will be subsequently used to define the wake expansion envelop.

Formulation of wake expansion from full-scale measurements. The measured wake expansion E_t, as introduced in Sec. 3.4.1, is now assumed to be the sum of two contributions: the expansion caused by the wake meandering and the yaw contribution to the lateral wake displacement. The wake expansion as function of downstream cross section location ($k = 2, .., 5$), as depicted in Fig. 3.10 (right), is thus defined as:

$$E_t(k) = D_0 + 2\,k D_0 < \alpha(k) > + 2\,h_{yaw}(k) \tag{3.25}$$

Table 3.3: Peak factor k_p of the wake meandering Gaussian processed, using three different inputs.

Input	Peak factor k_p
Large scale lateral turbulence component v_c	2.79
"Full" lateral turbulence component v	3.57
Meandering path time series (function of downstream position)	2D: 3.04 3D: 3.00 4D: 3.25 5D: 3.24

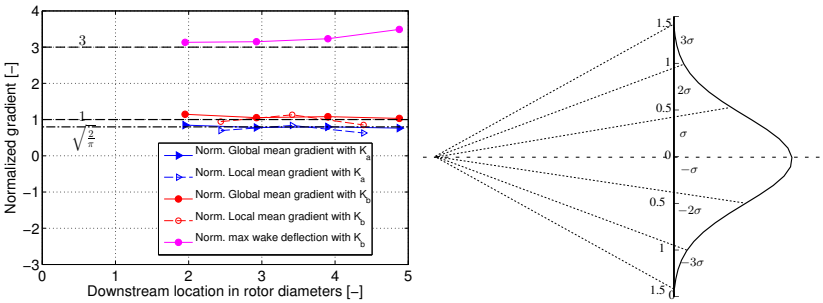

(a) Normalized gradients. **(b)** Sketch of a Gaussian distribution.

Figure 3.11: Normalized gradient investigation and relation to normal distribution characteristics. (a) Mean and maximum of the expansion gradient of the wake center lateral displacements computed for each cross sections normalized using all lateral velocities and the large scale lateral velocities, respectively; and (b), example of normal distribution with zero mean and standard deviation of 0.5 with illustrated confidence intervals.

In Eq. 3.25, the wake expansion has three terms. The first term is the rotor diameter D_0, the second term corresponds to the linear wake expansion due to wake meandering in the turbulent diffusion dominated regime of the wake, and the third term represents a fictitious wake expansion contribution caused by turbine yaw misalignment. The latter contribution is an artifact of the lidar being mounted on the rear of the turbine nacelle. The determination of the mean yaw misalignment contribution, h_{yaw}, is described extensively in [82]. The corresponding standard deviation of the directly observed wake expansion is defined as:

$$\sigma_{E_t(k)} = 2\sqrt{var\left(h_{yaw}(k)\right) + k^2 D_0^2\, var\left(\alpha(k)\right) + 2k^2 D_0\, cov\left(h_{yaw}(k), \alpha(k)\right)} \tag{3.26}$$

The calculated covariance between the mean yaw contribution $h_{yaw}(k)$ and the lateral meandering displacement contribution to the expansion coefficient $\alpha(k)$ is very close to zero; therefore the involved stochastic quantities are assumed to be independent, and the covariance term in Eq. 3.26 is consequently dropped.

A comparison between the expansion as defined by Eq. 3.25 with the results from CFD simulations and the pulsed lidar measurements is shown in Fig. 3.12, where an expansion

coefficient, $\tilde{E}_t(k)$, defined as $\tilde{E}_t(k) \equiv E_t(k)/D_0$ is shown. For all 4 downstream locations, very close agreement is seen between the expansion obtained from Eq. 3.25 and the CFD results. Furthermore, a slow-down in wake expansion is observed for the cross section with the largest distance from the rotor. The origin of this decrease is investigated by removing the yaw misalignment contribution from Eq. 3.25. As the same slow-down magnitude still appears, it is believed that this clear gradient decrease of the expansion may be related to an acceleration of the wake recovery, or simply an artifact associated to the uncertainty of the present analysis.

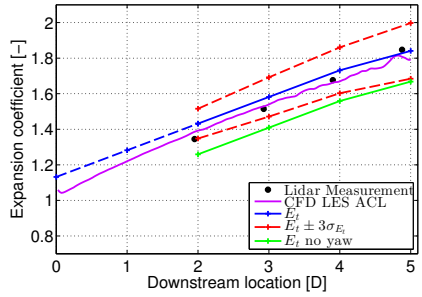

Figure 3.12: Expansion coefficient obtained from Eq. 3.25 compared to the one obtained from CFD and lidar measurements. The linear extrapolation cross the origin at $\tilde{E}_{0,t} = 1.13$. The wake expansion coefficient envelope is shown in dash red lines.

Finally, a linear extrapolation from 80 m (i.e. approximately $2D$) to the origin is performed using the local slope at 80 m. It intersects the origin axis at $\tilde{E}_{0,t} = 1.13$. The previously obtained initial expansion coefficient in the vicinity of the rotor is compared to the theoretical work conducted by Larsen et. al [65] describing wake expansion caused by pressure relaxation. Typically, the pressure close to the rotor is lower than the ambient pressure. In the current engineering approach, by performing a linear extrapolation from 0 to 2 rotor diameters, it is implicitly assumed that the pressure recovers 2D downstream, and it is known from theory ([65]), that a simple relationship between the rotor thrust and the expansion due to pressure recovery can be described as:

$$D_{w0} = D_0\sqrt{\frac{1}{2} + \frac{m}{2}}; \qquad m = \frac{1}{\sqrt{1 - C_T}}; \qquad \tilde{E}_{0,t} = \frac{D_{w0}}{D_0} \tag{3.27}$$

Using the mean thrust coefficient of 0.67, derived from the bending moment load at the tower bottom and the rotor diameter $D_0 = 41$ m, the initial wake radius is $D_{w0} = 48.0$ m giving an initial wake expansion coefficient of $\tilde{E}_{0,t} = 1.17$. The initial expansion as predicted from theory and the pressure driven initial expansion obtained from the measurements in Fig. 3.12 are therefore in good agreement, with a dimensionless deviation of 0.08 corresponding to a difference in wake expansion of about 1.6 m. The wake expansion obtained from the wake center measurement as function of the cross section plane index $k = 2, .., 5$ is reformulated as:

$$E_t(k) = D_{w0} + 2\,k\,D_0 < \alpha(k) > +2\,h_{yaw}(k) \tag{3.28}$$

3.4.4 Engineering model for wake expansion

Introduction

In this section, a new engineering wake expansion model is proposed and validated. The model takes advantage of the framework of the DMW model described in [71]. As extensively described in [5], the single wake expansion in a fixed frame of reference is the result of: 1) the wake meandering attributed to the large turbulent scale of the wake flow; 2) the near field pressure recovery; and 3) the turbulent diffusion taking place after two to three diameters downstream of the rotor and associated with the small turbulent scale of the wake flow. In Sec. 3.4.3 , it was demonstrated, that the *initial expansion* relation formulated in terms of rotor thrust coefficient has proven accurate. Consequently, this will be the basis of a new expansion engineering approach conserving the treatment of the near wake expansion. It is also demonstrated in Sec. 3.4.3, that the non dimensional expansion scales with the large scale lateral velocity fluctuations and a characteristic mean advection velocity obtained as in Sec 3.3.2. Furthermore, the distribution of lateral wake displacements is assumed to be a zero mean Gaussian process. However, as indicated in Fig. 3.13a, and confirmed by a Kolmogorov-Smirnov test, a distribution based on a 10 min time span may not always be Gaussian and symmetric around the origin. Since the focus is on large scale behavior, longer time series are required to validate or reject the assumption. As seen in Fig. 3.13b, showing the normal distribution fitting based on 90 min time series, the use of longer time series is much more convincing. Furthermore, the yaw misalignment has a direct impact on the center of the lateral displacement distribution for short observation times, as it can be seen from the asymmetric distribution in Fig. 3.13a.

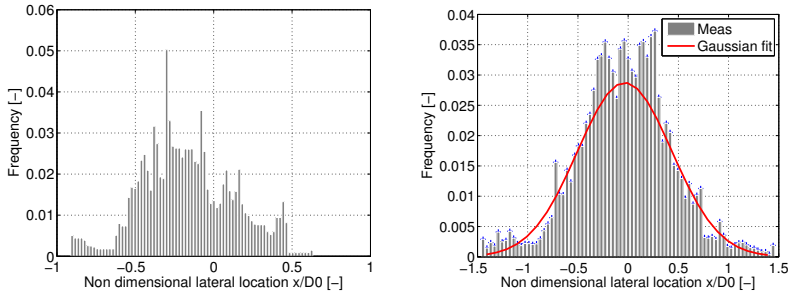

(a) 10 min observation **(b)** 90 min observation

Figure 3.13: Frequency histogram of the non dimensional lateral displacement of the wake center at FC=160m (approximately $4D$), with the number of bins corresponding to the number of complete sweeps within a 10 min lidar scanning. (a) using a 10 min time series and (b) using a 90 min time series. D denotes the rotor diameter. A Gaussian fit of the distribution is plotted, with the fitted mean $\mu = -0.03$ and a standard deviation of $\sigma = 0.47$.

Gradient investigation

In the present engineering approach, the wake expansion coefficient $\tilde{E}(k)$, is defined in its general form as the wake width at a given downstream lidar cross section k divided by the rotor diameter D_0. Based on the previous qualified assumptions, the proposed engineering model is composed of a theoretical initial expansion D_{w0} in the vicinity of the rotor and a downstream expansion defined by the expansion gradient α_t, where t is an index corresponding to a tested expansion gradient. It is thus expressed as:

$$E(k) = D_{w0} + 2kD_0\alpha_t \tag{3.29}$$

where α_t is the expansion gradient, D_{w0} is the initial wake diameter defined according to Eq. 3.27, and $k = 2, .., 5$. Several wake expansion gradients (α_t) are tested, as listed in Tab. 3.4.

Table 3.4: List of the various expansion gradients investigated for the development of an engineering expansion model.

t:	Expansion angle α_t:	Description:
1	$\alpha_1 = \frac{\sigma_v}{< U_a >}$	Constant advection velocity
2	$\alpha_2 = \frac{\sigma_{\tilde{v}c}}{< U_a >}$	With cut-off length scales of $1D$, $2D$ and $3D$, respectively. Constant advection velocity
3	$\alpha_3 = \sqrt{\frac{2}{\pi}} \cdot \left(\frac{\sigma_v}{< U_a >}\right)$	Verify similarity with α_2 at 2D. Constant advection velocity
4	$\alpha_4(k) = \tilde{\sigma}_{v_c} \cdot \frac{\tau(k)}{b_{meas} \cdot U_\infty \cdot \tau(k) + c_{meas} \cdot \int_0^{\tau(k)} D(\tau(k)) d\tau(k)}$	$b_{meas} = 0.88, c_{meas} = -0.51$ from Fig. 3.7a. Variable advection velocity. Cut off length scale is 2D.

In Tab. 3.4, $\tilde{v_c}$ represents the large scale fluctuations of the lateral wind velocity, v, at various cut off length scales. $< U_a >$ is the *average* wake advection velocity. $\tau(k)$ is the transportation time as function of the downstream section k obtained from the cross correlation technique detailed in Sec. 3.3.2, $D(\tau(k))$ is the maximum of the wake deficit as function of transportation time directly obtained from the measurement, and c_{meas} and b_{meas} are two constants obtained empirically in Sec. 3.3.2 and equal to 0.51 and 0.88, respectively.

While the 3 first gradient expressions are directly related to the analysis in Sec. 3.4.3 and have a constant expansion gradient, the last formulation makes use of the empirically-determined non constant advection velocity derived in Sec. 3.3.3. It therefore includes more physics by treating the advection as a deficit-dependent quantity, which is in turn dependent on the distance from the wake emitting rotor . $\alpha_4(k)$ is formulated using the

expression derived for the advection velocity in Sec. 3.3.3 as:

$$\begin{aligned}\alpha_4(k) &= \frac{\tilde{\sigma}_{v_c}\tau(k)}{b_{meas}\cdot\int_0^{\tau(k)} U_\infty d\tau + c_{meas}\cdot\int_0^{\tau(k)} D(\tau(k))d\tau(k)} \\ &= \frac{\tilde{\sigma}_{v_c}\tau(k)}{0.88\cdot U_\infty\cdot\tau(k) - 0.51\cdot\int_0^{\tau(k)} D(\tau(k))d\tau(k)}; \quad k=2,3,4,5. \end{aligned} \tag{3.30}$$

where the empirical relation obtained in Fig. 3.7a i.e. $b_{meas} = 0.88$ and $c_{meas} = 0.51$, has been introduced.

Results of the gradient investigations are shown in Fig. 3.14 for the dataset labeled #5 in the table in Fig. 3.7b.

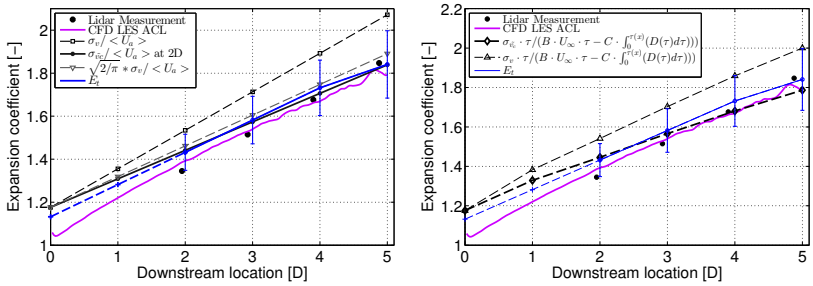

(a) Expression #1, #2 and #3 of Tab. 3.4

(b) Non constant gradients defined by expression #4 of Tab. 3.4

Figure 3.14: Expansion gradients investigation. Comparison of expansion coefficient obtained from CFD, full-scale measurements, and model predictions with the investigated gradients.

It is seen in Fig. 3.14a that the slope α_2 associated with a cut-off length scale of 2D, seems to agree best with the lidar measurements, the CFD computations and the expansion from the wake center tracking procedure. As depicted in Fig. 3.11a, and confirmed with the comparison shown in Fig. 3.14a, the expansion taken as $(\sqrt{2/\pi})\sigma_v/ < U_a >$ and $\tilde{\sigma}_{v_c}/ < U_a >$ are almost identical. An excellent agreement with the the slope $\alpha_4(k)$ is observed in Fig. 3.14b. However, a more thorough validation is needed to verify the accuracy of the model with different turbulence intensity and turbine loading.

General formulation

The empirical formulation of the single wake expansion coefficient in Eq. 3.30 is generalized to any downstream location x. Expanding the initial wake expansion at the rotor location from Eq. 3.27, the final expression takes the following form:

$$E(x) = \frac{1}{D_0}\left(D_0\sqrt{\frac{1}{2}+\frac{\frac{1}{\sqrt{1-C_T}}}{2}} + m\cdot 2x\cdot\left(\frac{\tilde{\sigma_{v_c}}\cdot\tau(x)}{b_{meas}\cdot U_\infty\cdot\tau(x)+c_{meas}\cdot\int_0^{\tau(x)}D(\tau(x))d\tau}\right)\right) \tag{3.31}$$

where m is a factor equal to 1 when determining the average wake expansion and equal to k_p (the Gaussian process peak factor in Sec. 3.4.3) when determining the maximum wake envelop. The accuracy of the new expansion model is tested on 3 selected datasets representing different rotor loadings and turbulence intensities of the ambient flow. The results are shown in Fig. 3.15. In Fig. 3.15a, the deviation between the CFD results and the empirical formulation is rather large in the near wake regime for the dataset with high thrust coefficients, possibly because pressure recovery is not taking place "instantaneously" in real life, and gradually reduces further downstream. Another important factor, which can lead to deviation in the near wake regime is the uncertainty of the CFD model due to lack of nacelle modeling. An increased blockage due to the presence of a nacelle may contribute to an increase in wake diameter close to the rotor. This deviation is less severe for the lower thrust coefficient datasets (Fig. 3.15b and Fig. 3.15c). The agreement with the measurements remains excellent in the far wake, for all three cases.

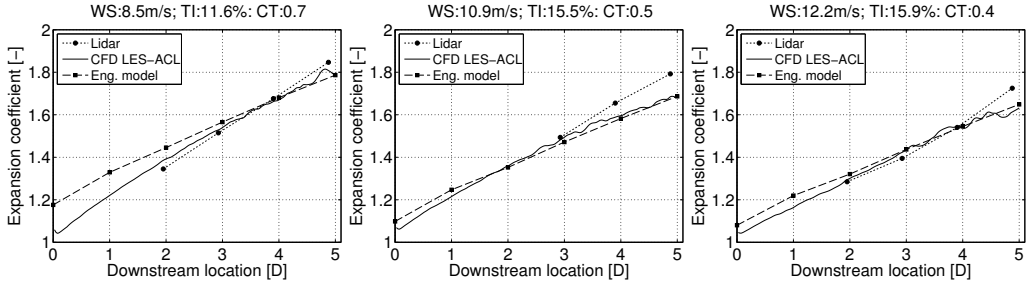

(a) High thrust. **(b)** Moderate thrust. **(c)** Low thrust.

Figure 3.15: Validation of the new expansion engineering model against CFD LES-ACL simulations and pulsed lidar measurements. The overall agreement is good for all three different turbine loading cases in the far wake. The case with high thrust coefficient (a) shows, however, larger discrepancies in the near wake.

3.5 Summary

In the present chapter, single wake advection and expansion have been studied both experimentally using pulsed lidar measurements and numerically using CFD LES-ACL simulations. As a spin off, basic consequences of the Dynamic Wake Meandering modeling are validated from the present experiment. The advection velocity is estimated from experimental full-scale data using a method based on cross correlation of the meandering patterns, defined by the discrete wake center lateral positions as function of time at par-

ticular cross sections. Vortex tube theory is used to overcome limitations of N.O Jensen's advection velocity formulation and was shown to compare well with results from the experiment.

Further, an empirical model, relating the maximum wake deficit at the wake center to the wake advection velocity, is developed and linked to characteristics of Hill's spherical vortex structures.

Finally, a new empirical model for single wake expansion is proposed, based on an initial wake expansion in the near field derived from 1D momentum theory, and a far wake expansion gradient formulated within the DWM framework, making use of the presently obtained empirical advection model. This model has been found accurate when benchmarked against 3 selected datasets representing various inflow conditions.

Chapter 4

Wake in the non-neutral atmospheric boundary layer

4.1 Background

Throughout the last decades of wind energy research, wind turbine wakes have always played an important part of investigations, since wakes are not only of concern in the design stage of a wind turbine (load cases calculations and structural design) but also in the design and operating stage of the entire wind farm (micro sitting, park performance and wake losses). Therefore, large efforts have been made to develop powerful and accurate wake models with different levels of complexity and practicability.

Today, most wake models are able to predict with a good degree of accuracy (depending on their complexity) the average wind speed deficit caused by each of the turbines clustered in a wind farm under neutral atmospheric conditions, giving a fairly reliable estimate of the annual energy production (AEP). This fair performance, discussed by Pena et al. in [105], is attributed to the fact that, when considering long term observations, most atmospheric static stability conditions at typical European onshore sites are generally close to neutral, slightly biased to stable side over land and to unstable side over water. However, the modeling of wind turbine wakes in neutral atmosphere may not be relevant in the context of short term forecasting of power production, highly relevant for wind farm operators, as the state of the atmosphere can change rapidly at a given site, as seen in the study by Vincent at al. in [154]. Furthermore, Sathe et al. [127] argued that the neutral condition, in which buoyancy effects have negligible influence on the vertical turbulence, is only experienced a fraction of the time in the atmosphere.

The qualitative effect of atmospheric stability on wind farm production is now better understood, as high quality experimental data from operating onshore and offshore wind

farms become available. Larsen et al. [62] attributed the influence on atmospheric stability on wake meandering as the main effect on wind farm power production. He conjectured that stable conditions are characterized by a decrease of energy content in the low frequency part of the turbulent spectrum of velocity fluctuations and thus by an attenuation of the wake meandering. For a downstream turbine perfectly aligned with the 10-minute mean wind direction of the wake generating turbine, this will lead to a more pronounced mean wake deficit and therefore to an increase in mean production loss. Conversely, unstable conditions lead to an increase in the energy content of the low frequency part of the turbulent spectrum, leading to more intense wake meandering compared to the neutral situation. The downstream turbine experiences an attenuated mean wake and thus lower power deficit. These effects are captured by the Dynamic Wake Meandering model [71], and further elaborated on in the study by Keck at al. [56].

Similar observations where made by Barthelmie et al. in [16], where they found that the Nysted offshore wind plant in the Baltic sea under-produced during stable conditions, due to decreased turbulence intensity and more gradual wake mixing and recovery further downstream. Other experimental studies have also documented the effects of atmospheric stability on turbine loads and power production: Hansen et al. [44], Wharton et al. [158], Chamorro et al. [26].

The work presented in this paper aims to understand the fundamental nature of wakes and wake dynamics under flow conditions different from neutral, and to validate the in-house EllipSys3D flow solver and specifically its newly developed extension which includes buoyant forces. The validation data are obtained from a full-scale experiment based on a setup, where a pulsed lidar device is mounted on a 500kW stall regulated Nordtank turbine, located at the site of DTU Wind Energy, Risø campus.

In the present context, the use of lidar technologies is of great benefit for model validation, since it allows full scale measurement of wake velocities remotely and offers a much greater spatial resolution and less flow disturbance than point measurements delivered by conventional cup or sonic anemometers mounted on meteorological masts, as observed in previous met mast-based wake measurement campaign such as Sexbierum [30] and ECN WTW farms [128]. The use of lidar for studying wake dynamics under non neutral atmospheric conditions has been increasingly popular in the recent years, as seen in the comprehensive studies by Iungo et al. [48] and Aitken et al [6]. The present lidar measurements are supplemented with a highly instrumented meteorological mast, among other sensors equipped with three 3-D sonic anemometers at different heights, facilitating the characterization of the atmospheric stability and the turbulence characteristics of the incoming wind.

A limited amount of 10 min time series from the present measurement campaign have already been used for the investigation of advection, expansion and meandering characteristics of the wake under neutral stratification by Machefaux et al. [82] as well as for the development of a new wake expansion empirical model [81]. The present analysis makes use of the entire campaign recordings in order to gather a sufficient amount of data for performing bin averaging of wake profiles under several atmospheric stability and inflow wind speed conditions.

As part of the experimental analysis, three different atmospheric stability classification approaches are investigated: 1) using the definition of the Monin-Obukhov length scale

L and the corresponding classification found in the study by Pena et al. [103]; and 2) the classification based on the Bulk-Richardson number as used in [44], and based on the empirical derivation in [42]; and 3) the Froude number approach similar to the study of flow over complex terrain in [122]. The combined effect of non flat terrain and very stable conditions is further analyzed experimentally, especially the impact on the wake meandering. Three test cases of various stability and characterized by similar mean wind speeds are selected from the available datasets.

The numerical validation is conducted with the EllipSys3D flow solver using Large Eddy simulation (LES) and Actuator Disc to model both wind turbine rotor and nacelle. In this approach, we commonly superpose turbulence generated from the neutral spectral tensor models developed by Mann [88] onto a neutral logarithmic inflow profile, similarly to the work of Ivanell et al. [50] and Troldborg et al. ([144], [146]). In order to account for the change of turbulent structures in the atmosphere for stable and unstable stratification, a newly developed generalization of the Mann model [27] is adopted, and combined with Monin-Obukhov similarity [98] theory for the modeling of the mean inflow profile as well as a precursor diurnal cycle simulation for the determination of the inflow temperature profile. Finally, thermal and Coriolis effects are explicitly added as external force terms in the momentum equations as described subsequently and based on the work of Koblitz et al [58]. The LES model uses a mixed subgrid scale model developed by Ta Phuoc [141] regardless of the simulated atmospheric stability, and the solver parameters are identical to previous work in [146].

The generation of turbulence in the present approach fundamentally differs from other more fundamental and computationally expensive techniques as the one developed by Churchfield et al. [29]. In their study, the turbulent atmospheric inflow fields for unstable stratification are generated by precursor LES simulations conducted on a much larger domain and for a longer simulation time. Furthermore, the Smagorinsky model [131] is used to model the subgrid-scale (SGS) turbulent fluxes of momentum and heat.

Stoll and Porté-Agel [137] developed a more sophisticated dynamic subgrid-scale model for modeling the stable boundary layer (SBL), and Lu et al. applied it to LES simulations of very large wind farms under stable conditions in [79]. Such scale-dependent dynamic models proved to better resolve the flow statistics near the surface than traditional scale-invariant dynamic models.

In this respect, the present numerical approach can be regarded as a simpler extension of the neutral LES simulations where focus is rather on the adaptation of the length and velocity scale of the superimposed synthetic turbulence and thermal effects are accounted for in a consistent manner with regard to the superposed flow.

4.2 Experimental approach

4.2.1 The test site

The measurement campaign was conducted from June 2011 to early January 2012 at the DTU Wind Energy, Risø Campus test site located in the south-east end of Roskilde Fjord in Denmark.

This onshore site is mainly characterized by farm land, grass and nearby buildings and trees. It has a moderate to high inflow turbulence intensity typically ranging from 9 to 15% thus associated with a roughness length of approximately 10 cm. Furthermore, a constant downhill slope of $\approx 0.3\%$ is observed from the base of the installed Nordtank turbine towards the fjord corresponding to inflow directions from the sector $120 - 150°$. Despite its low magnitude, this terrain effect will have some impact on the wake measurements especially under very stable condition as will be discussed subsequently.

4.2.2 The measurement set up

In this campaign, a Nordtank 500 kW turbine was equipped with a pulsed lidar mounted on a platform at the rear of the nacelle, with its laser pointing downstream. The Nordtank is a stall regulated turbine with a hub height of 36 m and a rotor diameter of 41 m, equipped with LM 19.1 m blades. The wind turbine is instrumented with a data acquisition system for recording meteorological properties (wind speed, wind direction, air temperature, atmospheric pressure and rain) from the 57 m tall meteorological mast located nearby in direction 283° from the turbine.

Additional wind turbine operational parameters (electric active power, generator torque, rotor azimuthal position) and structural loads measured by strain gauges are also acquired by a PC based data acquisition system.

The installed pulsed lidar is based on a Windcube WLS 7 lidar (as shown in Fig. 4.1a), where modifications of the scanner device have been performed to facilitate 2D cross sectional recordings ([120] and [121]).

The lidar scanning strategy is based on a Cartesian pattern consisting of 49 measurement points over 5 simultaneous downstream cross sections ranging from approximately 1 to 5 rotor diameters. A complete description of the lidar scanning capabilities as well as the post processing of the raw data is presented by Machefaux et al. in [82] and [81]. An assessment of the measured wind resources from the sonic anemometer at 34.5 m altitude is performed. This analysis is conducted on time series where the lidar data are considered fully valid, based on a filtering procedure described in [129]. This analysis revealed that the dominant wind sector observed during the measurement period is a south east sector associated with mean inflow directions between 120° and 150°. In this sector, the wind speed distribution above cut-in wind speed includes bin ranges from 4 to 12 m/s, with approximately 900 datasets available.

4.2.3 Data availability and validation

The campaign was initiated on the 8th of June 2011, and terminated on the 6th of January 2012. During the 212 days of measurements, the lidar was operating 22% of the time. This low data availability is due to several user interactions on the system, maintenance schedules on the turbine and the lidar, and updates of the base software of the lidar system. As a result, around 4000 sets of 10 min long datasets of raw measurements were collected during the campaign for different purposes: i.e. wake measurement as well as

(a) Photography of the lidar **(b)** Test site

Figure 4.1: (a) Photography of the nacelle mounted Windcube WLS 7, on the rear of the 500kW stall regulated Nordtank turbine. (b) Wind rose showing the frequency distribution of wind direction at 34.5 m altitude from the wind vane and the corresponding wind speed distribution at the same height from the sonic anemometer. The bin width is 15°. The dominant sectors between 120° and 150° are selected for the subsequent wake study. The background picture is a Google Earth satellite picture of the test site centered at the Nordtank turbine. The met mast (M.M) is not ideally located to the west of the Nordtank turbine for these inflow directions. Source: Google Maps, coordinates: $55°41'4.29"N$, $12°5'47.72"E$ for the determination of the Coriolis parameter. *Google and the Google logo are registered trademarks of Google Inc., used with permission.*

lidar validation and calibration.

Additional exclusion of data points as well as entire 10 min blocks were further conducted on this database. Data points are excluded for several reasons: bad synchronization, bad Carrier Noise Ratio (CNR) or hard target detection, as described in [129].

4.3 Experimental analysis

4.3.1 Atmospheric stability classification

In the context of full-scale measurements, the classification of the atmospheric stability is not trivial, as it requires a precise knowledge of the physical and thermodynamic state of the ambient air throughout the experiment. Specifically, measurements of absolute atmospheric pressure, skin surface temperature, specific humidity and potential temperature fluctuations at several heights within the surface layer are often required for obtaining a reliable atmospheric stability characterization. The measurement quality of such thermodynamical properties depends critically on the use of proper and well calibrated sensors. Therefore, three dimensional sonic anemometers, when available, are often used for stability classification, since they offer recordings at high sampling frequency of the relevant turbulent co-variances involved in the determination of the Obukhov length and the heat flux.

Three classification methods are tested in the present analysis. The first method uses the classical definition of the Monin-Obukhov length and its relation to 7 commonly defined stability classes. In this approach, the recordings from the sonic anemometers are used to determine directly the kinematic heat flux at a given height.

The second method, entitled the Bulk-Richardson approach, is based on a combination of wind speed and temperature gradients. The Bulk-Richardson number Ri_b is in turn related to the Monin-Obukhov length number L through empirical relationships. Compared to the first method, this approach is typically more sensitive to the quality of the wind speed, temperature and pressure sensor recordings.

The last method uses an approach adapted from the study of idealized flows over hills, presented in a textbook by Stull [139]. This classification makes use of the *internal Froude number*, defined in the present context as the ratio of natural wavelength of the air to the effective wavelength of an obstacle. The possible adaptation of this method from flows over hills to flows across wind turbine rotor is investigated presently.

4.3.1.1 The Obukhov length approach

This first approach was initially derived by Monin and Obukhov in [98]. They introduced what has become the most commonly used quantity to characterize atmospheric stability, the Obukhov length L; this loosely represents the height at which the production of turbulent energy from buoyancy is equal to the shear induced turbulent production.

Experimentally, this quantity is easily determined by means of three dimensional velocity

and temperature measurements. The Obukhov length, at a given height H, is defined as:

$$L_H = -\frac{u_*^3 \overline{\theta_v}}{\kappa g \left(\overline{w'\theta_v'}\right)_H} \tag{4.1}$$

In Eq. 4.1, $(\overline{w'\theta_v'})_H$ is the mean virtual potential temperature flux at the height H directly measured by the sonic anemometer, g is the gravitational constant, κ is the Von Karman constant ~ 0.4, and $\overline{\theta_v}$ is the mean potential temperature. The friction velocity, or turbulence velocity scale u_*, is presently calculated via $u_* = |\overline{u'w'}|^{1/2}$. The measured Obukhov length is then attributed to one of the 7 stability classes outlined in [103]: $-100 \leq L \leq -50$, very unstable (VU); $-200 \leq L \leq -100$, unstable (U); $-500 \leq L \leq -200$, near unstable (U); $|L| \geq 500$, neutral (N); $200 \leq L \leq 500$, near stable (NS); $50 \leq L \leq 200$, stable (S); $10 \leq L \leq 50$, very stable (VS). The Monin-Obukhov similarity theory is only valid in the surface layer, which typically represents the first tenth of the total atmospheric boundary layer height. Therefore, in the case of very stable stratification, the sonic anemometer at 16.5 m a.g.l. should be primarily used, as the higher sensors may not be located in the surface layer when highly stable stratification occurs.

The impact of the sensor height is presently investigated. In Fig. 4.2a, the distribution of z/L values as function of the mean wind speed for the selected inflow sector 120° - 150° is shown for the three available sonic anemometers. For the present dataset, it is seen that the measurements associated with low wind speeds are typically on the stable side, becoming progressilvely unstable for the bin 7-8 m/s. Asymptotically, the mean atmospheric stability for higher wind speeds approach near neutral conditions. This is a consequence of an increased shear production due to higher mean wind speeds that progressively balance the buoyant forces, thus characterizing a neutrally stratified atmospheric boundary layer. As expected, the most notable difference between the three tested sensor height is found for the stable atmosphere situations, while remaining fairly insensitive elsewhere.

In Fig. 4.2b, the z/L distribution of 33 *very stable* datasets (determined as based on the 16.5 m sensor), which corresponds to less than roughly $\sim 1/3$ of stable cases (Kelly et al. [57]) and for the wind speed bin 6-7 m/s is investigated. The corresponding Obukhov length derived for the two sonic anemometers at higher altitude shows a much wider spread, and a drift of the observations towards stable conditions. This reveals the large sensitivity of the measuring height on the stability class quantification.

4.3.1.2 The Bulk Richardson approach.

The atmospheric stability condition within the surface layer can be determined from an empirical relation relating the Richardson number to the corresponding Obukhov length. The current approach follows the work by Larsen et al. described in Appendix A of [62].

The Bulk-Richardson number Ri_b has the advantage over the classical Richardson number Ri to be based on single height wind speed and temperature measurements, thus avoiding the introduction of summation errors from multiple sensors. It is determined from the specific humidity q, the temperature gradient ΔT, the surface temperature T_0, the velocity

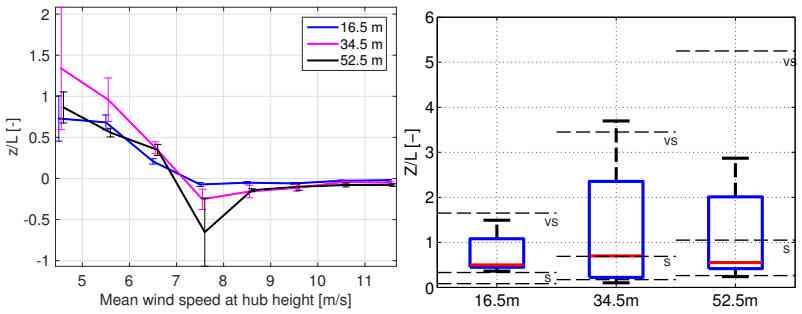

(a) (b)

Figure 4.2: (a) Stability analysis of the selected datasets from the wind sector 120° - 150° using the three available sonic anemometers at different heights. The wind speed range from 4 to 11 m/s with a bin width of 1 m/s. One standard deviation of the integer stability class is also indicated in error-bars. (b) Box plot of Obukhov length distribution for the very stable stability class determined at 16.5 m height. The red line indicate the median, the edges are the 25th and 75th percentiles, and the whiskers are the non outliers extreme data points.

u at height z_2 (where the Ri_b is estimated from) as:

$$Ri_b \approx \frac{g\left(\Delta T \Delta z - \frac{(1-q)(\Delta z)^2}{1-0.1q} \cdot 0.01\right)(1+0.61q)}{T_0(\overline{u(z_2)})^2} \tag{4.2}$$

Businger, Dyer, Pandolfo derived an empirical expression based on full-scale measurements in [23] and [101] which relates the Obukhov length to the Bulk-Richardson number as:

$$\frac{z_2}{L} = 10Ri_b \text{ for unstable stratification ;} \qquad \frac{z_2}{L} = \frac{10Ri_b}{1-5Ri_b} \text{ for stable stratification} \tag{4.3}$$

The calculation of the Bulk-Richardson number is, in the present study, not straightforward due to the lack of reliable sensors at the surface. As demonstrated in the work of Sathe at al. [126], the Bulk-Richardson classifiation often fails at characterizing atmospheric stability. The first source of uncertainties comes from the definition of T_0, the surface temperature. The sensor located the closest to the ground (1 m a.g.l.) displayed some inconsistent temperature values throughout the campaign and was therefore disregarded. The most reliable surface temperature available is determined from a temperature difference sensor between 10 m and 54 m and an absolute temperature recording at 54 m. The derived temperature at 10 m is then extrapolated to the surface ($z = 0$) using the local temperature gradient between 10 m and the 16.5 m temperature recordings, where the 16.5 m recording originate from the lowest located of 3 three dimensional sonic anemometers.

Due to the use of two different sensor closely spaced in height, this technique is associated with a high degree of uncertainties.

The mean velocity at height z_2 is obtained from the sonic anemometer at 16.5 m. Finally, the specific humidity q is not known with the available equipment. In turn, we assume a mean relative humidity of 65%, which corresponds to the humidity typically observed in Denmark during the season where the campaign took place. The specific humidity q is then computed following the procedure described in Appendix A of [62]. The use of a constant relative humidity is an acceptable guess, as it does not affect the Ri_b value significantly. However, the determination of a proper temperature gradient and surface temperature condition impacts the quality of this classification.

By using the sonic anemometer at 16.5 m for the Ri_b calculation, it is ensured that the previous empirical relationships, only applicable in the surface layer (i.e. the first 10% of the ABL height), are also valid for very stable stratification where the total ABL height is greatly reduced as compare to a neutral atmosphere. The stability determined from the Obukhov approach is used to guide the choice between the stability dependent Richardson number from Eq. 4.3.

4.3.1.3 The Froude number approach

The method behind the present stability classification is an adaptation of the IEA Task 31 "Wakebench" study of Rodrigo in [122] and [125] . In this work, the complex flow over the hill of Alaiz is studied experimentally using several highly instrumented masts located on the top and downstream of the hill. The measurements collected are used to verify models of flow in complex terrains under different stability conditions. The atmospheric stability classification proposed in [122] is based on the theory described in [139], however, including empirical adjustments as based on observations. The present adaptation first considers the turbine itself as a flow disturbance similarly to a terrain obstacle, and the subsequent analysis investigate the validity of this assumption for performing a robust stability classification.

In stable conditions, a perturbed air parcel, i.e. an air parcel of given temperature displaced vertically into different temperature, oscillate vertically at the Brunt-Väisälä frequency, N_{bv}. This oscillating air parcel, when advected in an air flow of mean wind speed $\overline{U}$, create a wave trace. The wavelength of this oscillation is proportional to $2\pi\overline{U}/N_{bv}$, its natural air wavelength. The length scale of an obstacle disturbing the flow is denoted W_T, and its effective wavelength is $2W_T$. The internal Froude number is then defined as the ratio of the natural air wavelength to the effective obstacle wavelength as:

$$Fr = \frac{\pi\overline{U}}{N_{bv}W_T} \tag{4.4}$$

where the Brunt-Väisälä frequency is defined as:

$$N_{bv} \equiv \sqrt{\frac{g}{\theta_0}\frac{\partial\theta}{\partial z}} \tag{4.5}$$

where θ_0 is the potential temperature at or near the ground, g is the gravitational constant, and $\frac{\partial\theta}{\partial z}$ is the gradient of potential temperature with height.

For $Fr << 1$, the flow is very stable ([139]) and therefore goes rather around the hill than above, and when $Fr >> 1$, the flow is considered neutral. At the resonance, i.e. $Fr \sim 1$, *lee waves* or *mountain waves* are formed behind the hill. Observations at the Alaiz test site revealed that a maximum in wind shear, characterizing a stable stratification, is observed and arbitrary assigned to $Fr = 1$. This way, the length scale of the obstacle W_T is inferred. In unstable conditions the characterization of W_T is more challenging and the sign of the potential temperature gradient is used instead to differentiate the unstable and stable regime. Therefore, Eq. 4.5 becomes:

$$N_{bv} \equiv \text{sign}(\frac{\partial\theta}{\partial z})\sqrt{\frac{g}{\theta_0}|\frac{\partial\theta}{\partial z}|} \tag{4.6}$$

An application of the stability classification of the Alaiz test case in [125] in the present experimental context is attempted. We consider the characteristic velocity to be the hub height wind speed. The potential temperature gradient $\frac{\partial\Theta}{\partial z}$ is obtained from a differential absolute temperature sensor between 10 and 54 m. The reference temperature Θ_0 is assumed to be the mean of the two previous mentioned temperature levels. The absolute atmospheric pressure sensor located at the bottom of the met mast is used to determined the potential temperature gradient.

The characteristic obstacle length scale W_T is determined by investigating the Froude number as function of the wind shear exponent based on two assumptions: the first approach assumes the obstacle length scale to be equal to the rotor diameter, whereas the second approach assumes the obstacle length scale to equal the wind turbine height H, similarly to [125]. As depicted in Fig. 4.3a, a peak in the wind shear assigned to a Froude number of 1 is observed for a value $W_T = H$. This value of W_T also displays a better distribution among the stability classes defined in [125], as opposed to the distribution using the lower length scale. However, both approaches suffer from a very limited number of unstable, very unstable and very stable datasets. As seen in Fig. 4.3b, an inverse Froude number of 1 is associated to low turbulence intensity, typically characterizing a stable atmosphere. However, since this method is for the first time adapted to wind turbines, it is not possible to verify whether the chosen obstacle length is site-dependent or turbine dependent.

4.3.2 Wake bin averaging

Bin averaging of the lidar measurements is performed using mean wind speed bins of 1 m/s width ranging from 4 to 12 m/s, over the 7 stability classes. The stability bins are obtained from the classification approach based on the Obukhov length determined at 16.5 m a.g.l., which is justified in the next section.

A test case matrix of 8 (mean wind speed bins) by 7 (stability bins) is then defined. These narrow bins are a trade off between large enough number of observations within individual bins to obtain statistically converged mean wake profiles while remaining short enough to limit ensemble variability. As a result, the 625 lidar datasets collected from the selected inflow sector, does not fill up the entire test matrix.

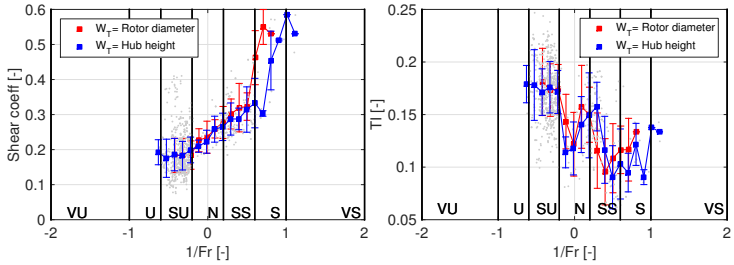

(a) Inflow shear exponent ν **(b)** Hub height turb. intensity

Figure 4.3: (a) Influence of the characteristic obstacle length scale on the Froude number based stability classification as function of inflow shear exponent. The length W_T is inferred to H where a distinct peak is observed in the wind shear for a Froude number of 1. The atmospheric stability classes are derived from the classification introduced in the study [122]. (b) Mean hub height turbulence intensity as function of the Froude number derived stability classes. Stable cases have a turbulence intensity of the order of 9%, whereas unstable cases are associated to turbulence intensities in the order of 17%.

Three test cases from the previously defined test matrix are selected for the subsequent experimental and numerical analysis: 1 neutral, 1 unstable and 1 very stable case all with similar mean inflow velocities. An overview of these test cases and their respective ambient parameters is available in Table A.1. The mean speed at hub height are obtained as the mean of all individual 10 min average velocities within that particular stability bin. The hub height velocity presented in Table A.1 is based on the velocity recorded at 34.5 m a.g.l at the mast location, corrected to account for the relative height difference between the instrument and the actual hub height of the turbine (36 m) as well as the elevation different of approximately 2 m between the ground level at the turbine and the mast location. This correction is based on the evaluation of the mean wind speed at corrected height based on a fitted logarithmic profile.

All datasets are, prior to performing the bin averaging, normalized by the mean free stream velocity at hub height. Several techniques for determining the normalization wind speed are considered in the present study: 1) the use of the mean power produced and the standard turbine power curve also referred to as PTC method in [115]; (2) the use of sonic or cup anemometer measurements of the free stream velocity near the turbine at hub height; and 3) the direct use of the wind speed lidar measurements recorded outside the wake at the most downwind cross section.

An independent sanity check of each of these techniques revealed that the latter method is the most accurate with the limitations of the experiment, as it provides a direct measurement of the free stream velocity with the best possible spatial correlation with the lidar measurements as opposed to the nearby mast. Contrary, the two first techniques displays more variability resulting in occasionally large discrepancies for highly turbulent datasets.

Finally, the test site roughness length z_0 is determined from the empirical approach described in [102], which consists in solving the following equation for z_0 for all test cases

Table 4.1: Main parameters of the test cases with similar inflow velocities. Each quantities are obtained as the mean of all individual 10 minutes time series of each test case. The values in parentheses correspond to wind speed standard deviations and the standard deviation of the bin stability measure, respectively. The shear exponent is obtained from a power law fitting to the 3 heights sonic measurements of the average test case profile.

Test case index	Stability class and bin limits	Obukhov length 16.5m a.g.l. [m]	3D inflow velocity at hub height [m/s]	3D turb. intensity at hub height I_{ref} [-]	3D turb. kinetic energy $[m^2/s^2]$	Measured thrust coefficient [-]	Measured Elec. power [kW]	Shear exponent ν [-]	Dataset length [h]
#1 (N)	Neutral $\|(L)\|\geq 500$	1677.7 (362.9)	7.03 (0.97)	0.14	1.42	0.75	125.61	0.19	3.2
#2 (U)	Unstable $-200 \leq L \leq -50$	-84.8 (19.2)	6.82 (1.02)	0.15	1.55	0.71	120.25	0.16	3.3
#3 (VS)	Very stable $10 \leq L \leq 50$	29.0 (11.3)	6.76 (0.70)	0.10	0.73	0.83	96.44	0.26	5.5

with the test matrix (function of the hub height wind speed U_H and the Obukhov length L):

$$TI_{16.5m}(U_H, L) = \frac{1}{\log(\frac{16.5}{z_0})} \tag{4.7}$$

Based on the streamwise turbulence level recorded by the 16.5 m a.g.l. sonic anemometer, the mean roughness length is estimated to 9.5 cm with an uncertainty of ± 3 cm.

4.3.3 Wake deficit and stability classification method

The impact of the atmospheric stability on the wake profile is presently investigated for the wind speed bin including measurements in the range 6-7 m/s and for both the stable and unstable cases. A comparison of the normalized wake deficit, as function of downstream distance from the rotor is for the three classification methods shown in Fig. 4.4a and 4.4b for the stable and unstable case, respectively. Additionally, the frequency distribution of datasets within each of the 7 stability classes is shown in Fig. 4.4c.

It is seen in Fig. 4.4a that the wake profile is fairly invariant to the classification method for the stable case. The only notable disagreement is observed for the Froude based profile, which display a deeper deficit in the left side of the wake when facing the rotor. The impact of the stable atmosphere is clearly seen at the most downwind location in Fig. 4.4a, where the unstable profile displays a fully recovered wake as opposed to the deep deficit of the stable wake profile.

The agreement among classification approaches is less pronounced for the unstable case in Fig. 4.4b. The Obukhov length approach seems to be the only method showing a faster wake recovery, typically characterizing an unstable atmosphere. As seen in Fig. 4.4c, the Froude number classification shows a large frequency of unstable cases, which is not seen with the other methods. This may be a consequence of the definition of the stability bin

limits proposed in [125], determined empirically for a different site. Fig. 4.4c therefore indicates that the Froude number intervals, defining the different stability classes, should be reconsidered to obtain a better agreement with the classical approaches.

Based on the above observations, it was decided to classify the wake validation data from the Obukhov length approach at 16.5 m a.g.l. This further ensures that the observation height is inside the surface layer even for a very stable atmosphere.

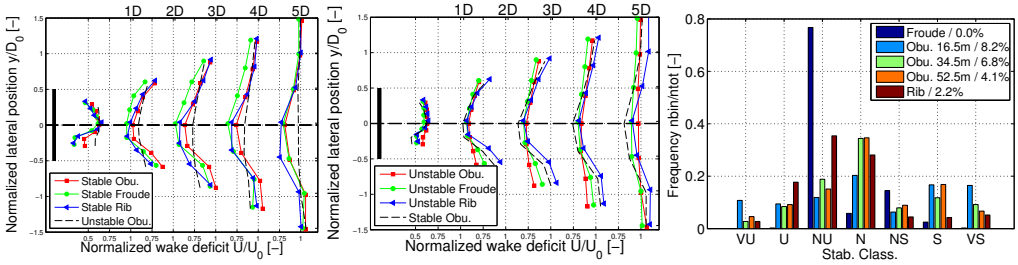

(a) Very stable case **(b)** Unstable case **(c)** Distribution among classes

Figure 4.4: Sensitivity analysis of the stability classification method on the ensemble averaged wake profile for the wind speed bin 6-7 m/s. (a) Normalized wake velocity expressed in the fixed frame of reference (FFoR) as function of the downstream distance for the stable atmosphere. The corresponding unstable profile is also shown for a better appreciation of the stability impact. The profile determined from the Froude number approach is obtained from combining the bins (U-NU) and (NS-S) respectively, due to the lack of data in the target bin U and S bins. (b) Similar analysis for the unstable case. (c) Frequency distribution of the 625 selected datasets among the stability classes determined from the 3 methods. The percentage indicates the amount of bins not included in any class.

4.3.4 Wake meandering and stability

As based on the assumption of the 'split in scales' in the DWM model [71], the ambient turbulence can be decomposed into two parts: the large scale turbulence (with length scales $\geq$ 2D), assumed to be responsible of the wake meandering; and the small scale turbulence ($\leq 2D$) dictating on the wake deficit evolution in the meandering frame of reference. As further discussed in [56], the stable atmosphere has a lower amount of energy in scales larger than 2D and a larger energy on the diffusive scales as compared to the unstable atmosphere. With the present experimental approach, the validity of this assumption can be assessed by resolving the wake in both fixed and meandering frame of reference (FFoR and MFoR).

By removing the meandering contribution to the wake profile, all three stability cases display a similar wake expansion and thus deficits in MFoR as depicted in Fig. 4.5.

The obtained wake profiles are almost invariant to atmospheric stability, where the only notable difference is the larger deficit seen for the stable profile. This can, at least partly, be explained by the variation of the thrust coefficients among the test cases, where the rotor loading is the highest for the stable case.

In Fig. 4.5a , the inverted shape of the profile at 1D downstream corresponds to measurement of the inner part of the double bell near wake shape characterizing the unloaded inboard part of the rotor. This wake characteristic is not observed in the MFoR in 4.5b, as the 2D Gaussian tracking algorithm fails to capture the real wake center and instead typically uses the largest deficit peak to perform the fit. With that respect, near wake profile at 1D in the MFoR are not reliable and a new tracking procedure will be develop in the future based on an adapted fitting function for the near wake.

This analysis demonstrates that the effects of atmospheric stability can be modeled by adapting the length and velocity scale of the atmospheric turbulence, and that the wake large scale dynamics can be decoupled from the wake deficit evolution, as assumed in the Dynamic Wake Meandering (DWM) model ([62]), and further elaborated on in [56]. This findings were used in the recent study by Larsen et al. [63] to validate the extension of the DWM model to non neutral atmosphere.

Unstable stratification enhances lateral and vertical wake meandering thus attenuating the mean deficit in the FFoR as opposed to stable atmosphere. An illustration of this is depicted in Fig. 4.5c, where the magnitude of wake meandering, determined as the standard deviation of the wake center position, is plotted against the various stability class. For a very unstable atmosphere, the lateral meandering displacement standard deviation is almost doublet compared to the same metric for a very stable atmosphere. A validation of the empirical model for wake expansion in [81] will be conducted using the present non neutral datasets.

4.3.5 Terrain effect and stability

The lidar measurements collected from the selected inflow section are performed with the scanning head horizontally leveled. However, the test site terrain has a downhill slope characterized by a height difference of 5.5 m (determined from STRM based terrain data) from the rotor location to the most downstream cross section.

This configuration facilitates the study of the impact of the terrain on the wake measurements for varying atmospheric stability. The present investigation is done by extracting the mean vertical skew angle of the wake χ_z, which is defined as the angle between the horizontal plane and the mean vertical displacement of the wake center as function of downstream position, as depicted in Fig. 4.6a. The time series of the vertical wake center position are, for all available downstream cross sections, determined from an optimization algorithm described in [152], based on a 2D Gaussian profile fitting of the cross sectional unsteady wake measurements. The effect of wind veer on the vertical wake center position is presently neglected due its small magnitude over the extent of the rotor: (very unstable: 0.5°; neutral: 1.8° and stable: 2.5°), as determined from the sonic anemometers at 16.5

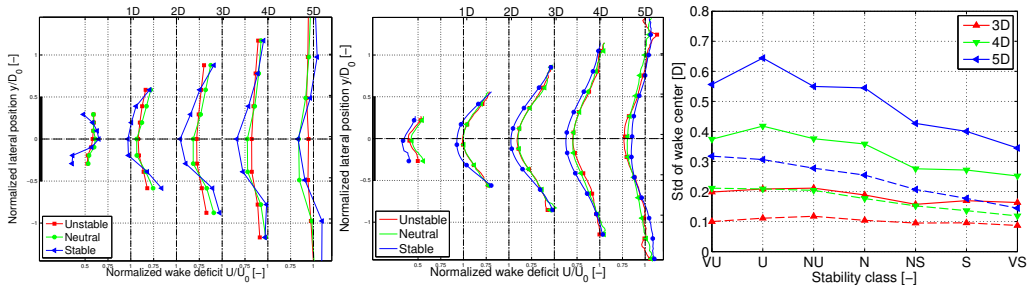

(a) FFoR **(b)** MFoR **(c)** Wake meandering intensity

Figure 4.5: Wake resolved in (a) the fixed and (b) the meandering frame of reference. The impact of stability is strongly diminished in the MFoR. (c) Wake meandering intensity characterized by the standard deviation of the wake center displacement for three downstream positions as function of the atmospheric stability. The dash lines show the vertical components and the full lines show the lateral components of wake center displacement.

and 52.5 m. The average vertical wake skew angle is then defined as:

$$\chi_z(FC) = \arctan(\overline{d_z}/FC) \tag{4.8}$$

where FC denotes the focus distance, $\overline{d_z}$ is the 10 min average vertical position of the wake center.

In Fig. 4.6b, the average wake skew angle is shown for different atmospheric stabilities. Fig. 4.6b shows an experimental evidence that the wind turbine wake has a strong tendency to 'follow' the terrain for stable and very stable conditions, as revealed by the very close agreement between the terrain slope angle and the vertical wake skew angle. This effect is not observed for the wake measurements under unstable stratification where the downstream transportation of the wake follows the horizontal plane.

This is in accordance with classical theory of atmospheric turbulence, where a stable stratification is characterized by a strong downward buoyancy force acting as a 'lid' on the wake flow field. This is characterized by a strong correlation between velocity field streamlines and the terrain irregularities. Such effect are important when subsequently comparing vertical measured wake profiles with numerical simulation conducted on perfectly flat and homogeneous domain, as the height at which the velocity field is extracted is then stability dependent.

4.4 Numerical simulations

Previous wind turbine wake simulations using the EllipSys3D flow solver, ([91], [135] and [93]), were carried out under neutral atmospheric conditions only, where neutral turbu-

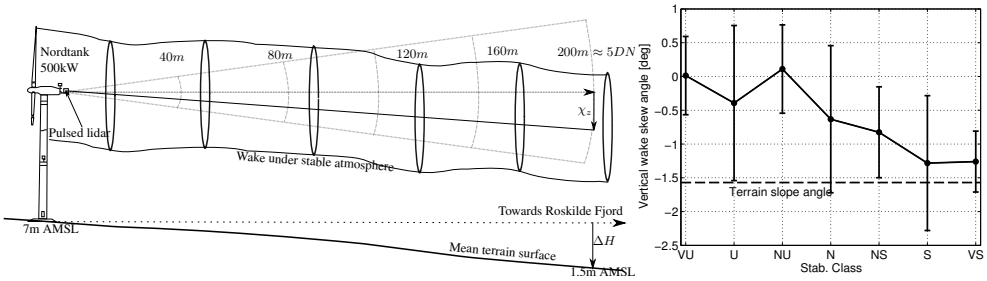

(a) Sketch of vertical wake skew angle for a stable stratification

(b) Skew angle function of stability

Figure 4.6: (a) Sketch of the vertical motion of the wake under stable atmosphere. The wake skew angle χ_z is indicated. (b) Investigation of the wake center vertical position as function of the atmospheric stability. The y-axis represents the mean vertical wake skew angle, defined as the angle between the vertical position of the wake center and a horizontal plane. The dash line shows the terrain slope angle. This analysis reveals the wake tendency to follow the surrounding terrain for stable stratification.

lence generated from the Mann spectral tensor, ([86]), is introduced in a cross section upstream of the rotor ([144], [83], [147]). In these numerical studies, based on Large Eddy Simulations, the rotor was modeled with either an Actuator Line [144] or an Actuator Disc technique [94], and the mean sheared inflow was typically imposed at the inlet of the computational domain using a logarithmic law.

The present work aims to extend the previous modeling approach of wind turbine wakes to non neutral atmospheric stratification. There are several aspects that differentiate the wake flow modeling under neutral and non neutral atmospheric conditions, respectively. A non neutral atmospheric boundary layer (ABL) enhances (unstable) or attenuate (stable) turbulent fluctuations through the magnitude of *buoyant forces*. Furthermore, Peña et al. [103] argued that modeling a non neutral atmosphere requires proper characterization of the shifts *in length and velocity scales* of the turbulence. Finally, stable and unstable stratification have different effects on the mean wind profile, which makes the corresponding wind shears differ from the typical logarithmic profile of the neutral ABL.

In the present numerical work, the three test cases described in Table A.1 are simulated using two numerical approaches described subsequently.

4.4.1 The "classical" approach

The first (classical) approach is based on the EllipSys3D flow solver using Large Eddy Simulation. Both the rotor and the nacelle are modeled by two permeable Actuator Discs. This model, based on the Actuator Shape model [116], makes use of both 3D corrected airfoil data and the local flow conditions at the discs to determine the aerodynamic loading

acting on a blade element, [119]. The nacelle is modeled as a disc with a diameter of 3 m normal to the incoming flow. The force distributed over the disc area is equal to the total drag force of a bluff body with a cylindric shape. The drag coefficient was set to 0.95, according to the definition in [35]. As was observed in [20], the contribution of the nacelle on the near wake deficit is fairly small. Both rotor and nacelle are represented on two 2D polar grids with 90 radial and 180 angular elements.

Synthetic inflow turbulence are generated from the Mann model ([88]) with the three input parameters obtained from a spectral fitting of the 3D sonic anemometer measurements. These three model parameters are: 1) a parameter linking mean wind shear magnitude with eddy life time (Γ) 2), the turbulence length scale (L) and 3), the viscous dissipation of turbulent kinetic energy ($\alpha\epsilon^{2/3}$). Although the Mann model does not include buoyancy effects, it has occasionally been used to model wind spectra of a non neutral atmosphere as in [103], [62] and [127]. The validity of this approach is re-assessed in the present study.

The computational domain and boundary conditions are set according to Fig. 4.7. The inlet profile is modeled by a logarithmic law when neutral atmospheric condition is simulated. It is obtained from a least-square fit procedure where the friction velocity value is varied to obtain the best agreement with the measured averaged wind profile. In this fitting routine, the empirically defined site roughness $z_0 = 9.5$ cm is kept constant.

The $\phi-$function from Monin-Obukhov similarity theory summarized in [160] is used for modeling the mean wind profile of the non neutral atmosphere. A good agreement between the wind speed profile measured at the met mast and the modeled inflow was observed for the unstable test case. However, a large discrepancy was observed for the stable case, where the modeled MO inlet was much more severely sheared as compared to measurement, as a consequence of the very low measured Obukhov length. In this case, a power law was used instead. Due to the restriction on computational resources, the unsteady LES computations are performed for only 10 min after the rotor wake has reached for the first time the end of the computational domain, i.e. that transient phenomena does not appear in the solution.

The performance of this approach was reassessed as part of this analysis on three neutrally stratified dataset representing various inflow mean wind speed ranging from 6 to 10 m/s. The observed agreement was excellent for downstream distance of 2 diameters and above, however displaying an underestimated deficit at the very near wake. Results are available in Appendix A.3.

4.4.2 The extended model

The second approach is an extension of the classical approach accounting consistently for thermal effects. It makes use of the same rotor / nacelle modeling technique based on the two Actuator Discs, and computations are carried out on the same computational domain. The adaptation of the governing Navier-Stokes equations inside the EllipSys3D flow solver is done by adding up explicitly thermal and Coriolis effects as external force terms in the momentum equations. A complete description of the ABL flow model and its implementation in the EllipSys3D flow solver is available in [58].

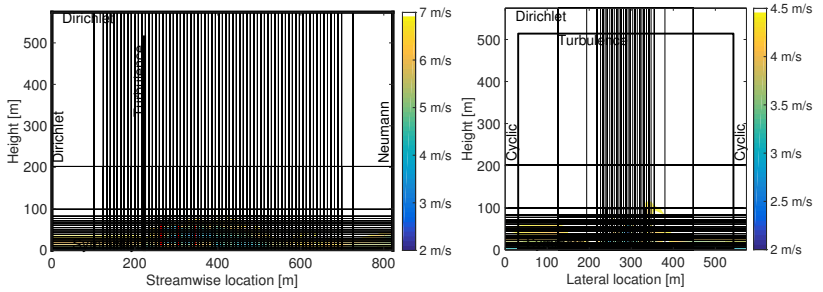

(a) Side view of the domain. **(b)** Front view of the domain.

Figure 4.7: Overview of the non uniform Cartesian mesh, in a coarser representation. The dimensions are ($L_x = 20D_N$, $L_y = 14D_N$, $L_z = 14D_N$) where x, y and z denotes the streamwise, lateral and vertical coordinates, respectively, and D_N denotes the Nordtank turbine rotor diameter. The boundary conditions are shown on the sketch. The domain has a total of 19.9 millions cells. The fine region in the near wake has a grid spacing equivalent to $dx = D_N/60$,$dy = D_N/60$,$dz = D_N/41$.

4.4.2.1 Modeling synthetic turbulence for non neutral atmosphere

The synthetic turbulence is generated using a newly developed generalization of the classical Mann model, which includes the effect of non neutral stratification on the turbulence structure ([27]). In addition to the three parameters describing the classical Mann spectral tensor, this model has two parameters: the gradient Richardson number, Ri, and the rate of destruction of temperature variance n_θ.

These parameters may be determined by fitting the non-zero model spectra to their measured analogues - i.e. the u-, v-, w- and θ auto-spectra as well as the uw-, $u\theta$- and $w\theta$-co-spectra. However, primarily due to large scatter in the temperature auto- and co-spectra, it turned out to be challenging to obtain satisfactory fits to all available spectra simultaneously.

Therefore an alternative strategy was applied. The present study requires only simulation of the turbulent velocities, whereas the temperature fluctuations are only indirectly relevant. Therefore, it was decided to fit the generalized spectral tensor only to the velocity spectra, and thus omit the measured temperature related spectra. This is possible due to the inherent flexibility of the generalized spectral tensor which allow to perform a consistent velocity spectra fit for non neutral stability conditions without introducing additional uncertainties caused by scattered temperature spectra. The fitting was performed using a Chi-Square approach, in which the spectra are variance normalized, reflecting that the (u,v,w) turbulent fluctuations are considered of equal importance for the CFD simulations. To initiate the fitting optimization procedure for the 5 generalized tensor parameters, it was found appropriate to first fit the classical Mann spectral tensor to the measured spectra, and then subsequently to use the result of this fitting as start values. For both type of fittings suitable high pass filtering was initially performed, since the very

low wave numbers, which hardly relates to conventional turbulence, are without interest for the present study and therefore essentially acts as a source of increased inaccuracy for the subsequent turbulence simulation.

The cut-off wave number was defined as $k_{cut} = 0.1/z$, where z denotes the altitude at which the measurements were performed. It should, however, be noted that for strongly unstable conditions this prescription may give slightly too large cut-off wave numbers since, if the ABL depth is large enough, the peak of the u-spectrum tends to go as the inverse of the boundary layer depth. However, as mentioned above, a counter argument is that the buoyant RDT is not meant to model/capture what is going on at those large scales, where there are organized motions/rolls. Once the spectral fitting is completed, the fitted generalized tensor parameters are in turn used as input to a turbulence generator, which is then analog to the procedure based on the neutral Mann model.

4.4.2.2 Modeling the ambient conditions

The mean potential temperature and velocity profiles imposed at the inlet of the computational domain are determined from a transient precursor computation, which simulates the time-varying vertical structure of the whole ABL. The complete description of the precursor simulation is available in Chapter 3.6 of [58]. The simulated diurnal cycle is based on the test case *GABLS2*, where the experimental data were collected as part of an experiment performed in Kansas [140]. The time selection of the diurnal cycle for each of the 3 test cases is done by seeking the best agreement with both the measured average velocity and the profile of potential temperature. The simulated temperature profile is presently normalized with the surface temperature θ_0. The obtained temperature gradient is in turn compared to the measured temperature gradient, as based on the two sonics sensors at 16.5 m and 52.5 m a.g.l., respectively. Results are shown in Fig. 4.8d. Because of the lack of surface temperature measurements, the measured potential temperature is normalized with the lowest sonic measurements θ_s at 16.5 m. To compensate for the difference in absolute surface temperature between the two geographically distant experimental sites, the measured gradient is adjusted to the simulated one by forcing the two absolute temperatures at 16.5 m a.g.l. to collapse with each other.

Because the lidar campaign took place at a test site with different characteristics compared to the Kansas site, on which the precursor simulation is based (higher roughness due to nearby vegetation, terrain and nearby fjord), it is in practice impossible to obtain a full agreement between the combined temperature and velocity profiles. In the present numerical approach, we focus on obtaining the best possible agreement with the potential temperature gradient for the three selected test cases in Table A.1)).

As seen in Fig. 4.8d, the measured potential temperature gradient has a fair agreement with the selected diurnal cycle time for all three test cases and is further in accordance with the mean time where the measurements were collected, 06:15, 12:40, and 16.10, respectively. However, as seen in Fig. 4.8c, the agreement is rather poor when considering the wind profile for all three test cases. The stable case shows a rather large shear compared to the measurements, whereas the neutral wind profile is even further off.

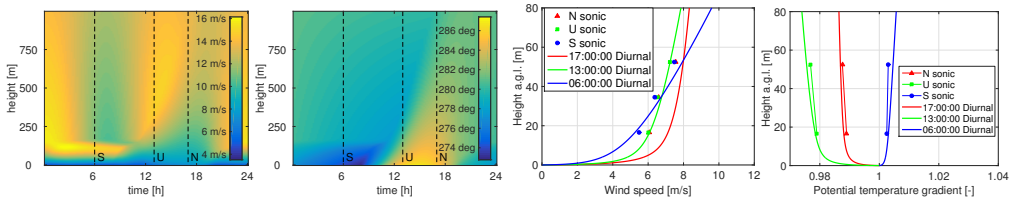

(a) Diurnal cycle: WS **(b)** θ **(c)** ASL: WS **(d)** ASL: θ gradient

Figure 4.8: Diurnal precursor simulations. (a) shows the diurnal cycle of wind speed profile. (b) shows the diurnal cycle of the potential temperature profile. Dash lines in (a) and (b) indicates the selected time instant for the subsequent numerical simulation and is done as a compromise between day time agreement with the test case measurements and good agreement with the potential temperature gradient in (d). Due to local test site effects, the wind profile depicted in (c) shows rather larger discrepancies with the simulated one. ASL denotes the atmospheric surface layer. WS denotes the wind speed.

4.4.2.3 Model limitation and discussion

In order to perform simulations with wind condition similar to the measured ones, we disregard the precursor simulated wind profile and used only the transient temperature profile. The wind profile is identical to the classical approach, i.e. logarithmic profile for neutral stability and the Monin Obukhov ϕ-function for the non neutral stability.

The model currently doesn't take into account roughness effect at the bottom of the domain, but uses instead a simpler slip wall conditions. This clearly doesn't capture the true behavior of the flow near the ground, as the flow tends to accelerate due to the lack of friction. This does not introduce a major issue in the analysis, as the focus is given on the wake characteristics and not the entire surface layer flow. The implementation of a rough wall in LES will be performed in the near future, as based on the PhD thesis work of Andreas Bechmann, [17].

Another point of discussion originates from the insertion of the synthetic turbulence. The turbulence from the kinetic models is in general not in balance with the flow in which it is inserted, which causes distortion of turbulence properties in the computation. An amplification of the turbulence fluctuations is therefore performed before hand to compensate for this distortion and to adjust the total turbulence intensity to the one measured at the test site.

An improvement of the current numerical approach would be to perform a complete 3D transient precursor simulation with a mesh generated from the terrain data, and subsequently extracting the diurnal cycle at the exact location of the met mast.

4.5 Results and discussions

In this section, the ambient flow properties and the turbine production are mutually compared between measurements and simulations, respectively, to validate the present numerical approach. The modeled turbulence characteristics is further compared to velocity spectra resolved by the CFD simulations. The wake properties, in terms of mean horizontal and vertical velocity deficit, and the wake meandering intensity are also analyzed for the selected atmospheric stability cases.

4.5.1 Flow field properties

4.5.1.1 Mean ambient conditions

The key ambient condition parameters, turbine thrust and power production are mutually compared between the measurements and the two tested CFD models. Results of this comparison are shown in Tab. 4.2.

As seen in Tab. 4.2, the overall agreement is fair for the three selected test cases. The agreement in the hub height turbulent properties was reached after several simulation attempts, where the amplification factor of the inserted turbulence was tuned to best fit the measured turbulent properties of the test cases. The observed deviations with the simulation was found in the order of $\pm 5\%$. This agreement is far worse when considering wind fluctuation at the lowest altitude of 16.5 m, due to the lack of wall modeling in the simulation. The average wind profile agrees within $\pm 3\%$ with the measured one for all simulations. The model prediction accuracy for the thrust coefficient and power production is acceptable when considering the typically large uncertainties on the strain gauges based thrust measurements and the definition of turbine efficiency for the conversion from mechanical to electrical power.

4.5.1.2 Turbulence characteristics

The simulated turbulence from the two CFD models is compared to the spectral tensor model input as well as the measured spectra by the sonic anemometers. This comparison aims to validate the turbulent properties of the simulated flow. This analysis is performed on a cross section upstream of the rotor and downstream of the insertion of the synthetic turbulence. Results of this analysis are shown in Fig. 4.9.

The spectral bandwidth of the LES simulations is restricted to both the large scales and the small scales side due to the relatively low simulation period and limitations on the cell spacing, respectively. A contamination of the spectra is seen in the high frequency range towards a wavenumber of 1 m^{-1}, corresponding to the lowest resolved wavenumber in the simulations. However, in general the agreement is fair between the modeled turbulence and the resolved turbulence for all three test cases, thus strengthening the robustness of the subsequent near wake deficits comparison

Table 4.2: Ambient parameters associated with the measured and modeled test cases. "LES" refers to the "classical" modeling approach and "LES-ABL" refers to the extended model both described in Section 4. The percentage error between modeled and measured quantities is added in parentheses. The turbine efficiency was set to 0.93 in the conversion from mechanical to electrical power according to the specification in [106]. 'HH' refers to as hub height in the present table.

Definition	Neutral #1			Unstable #2			Stable #3		
	Meas	LES	LES-ABL	Meas	LES	LES-ABL	Meas	LES	LES-ABL
Nb. of 10 min sets	19	1	1	20	1	1	33	1	1
$< U_{16.5m} >$ **(m/s)**: $\sqrt{u_{16.5}^2+v_{16.5}^2+w_{16.5}^2}$	6.06	6.14 (+1.3%)	6.04 (-0.3%)	6.02	6.14 (+2.0%)	6.16 (+2.3%)	5.49	5.51 (+0.4%)	5.49 (+0.1%)
$< U_{HH} >$ **(m/s)**: $\sqrt{u_{HH}^2+v_{HH}^2+w_{HH}^2}$	7.03	6.93 (-1.4%)	6.91 (-1.7%)	6.82	6.93 (+1.6%)	6.87 (+0.7%)	6.76	6.65 (-1.6%)	6.64 (-1.8%)
$< U_{52.5m} >$ **(m/s)**: $\sqrt{u_{52.5}^2+v_{52.5}^2+w_{52.5}^2}$	7.55	7.39 (+2.1%)	7.35 (+2.6%)	7.24	7.37 (+1.8%)	7.40 (+2.2%)	7.47	7.46 (+0.1%)	7.45 (+0.3%)
$\sigma_{U16.5}$ **(m/s)**: $\sqrt{\frac{1}{3}(<u_i'u_i'>_{16.5m})}$	0.86	1.04 (+21.0%)	0.99 (+15.2%)	0.98	1.23 (+25.6%)	1.02 (+4.2%)	0.53	0.68 (+29.2%)	0.72 (+36.8%)
σ_{UHH} **(m/s)**: $\sqrt{\frac{1}{3}(<u_i'u_i'>_{HH})}$	0.97	1.03 (+5.8%)	0.98 (+0.7%)	1.02	1.07 (+5.0%)	1.06 (+3.8%)	0.70	0.66 (-5.6%)	0.66 (-4.9%)
$\sigma_{U52.5}$ **(m/s)**: $\sqrt{\frac{1}{3}(<u_i'u_i'>_{52.5m})}$	0.92	1.16 (+26.5%)	0.94 (+2.5%)	0.92	1.04 (+12.6%)	0.99 (+7.1%)	0.56	0.74 (+31.3%)	0.62 (+10.0%)
TKE (m^2/s^2): $\frac{3}{2}\sigma_{U_{HH}}^2$	1.42	1.59 (+12.0%)	1.44 (+1.4%)	1.55	1.71 (+10.3%)	1.67 (+7.7%)	0.73	0.65 (-11.0%)	0.66 (-9.6%)
Iref (-): $\sigma_{U_{HH}}/\overline{U_{HH}}$	0.14	0.15 (+7.3%)	0.14 (+2.5%)	0.15	0.15 (+3.4%)	0.15 (+3.0%)	0.10	0.10 (-4.1%)	0.10 (-3.2%)
CT (-): Strain gauges / Act. Disc	0.75	0.80 (+6.7%)	0.78 (+4.0%)	0.71	0.81 (+14.1%)	0.83 (+16.9%)	0.83	0.80 (-3.6%)	0.83 (-0.1%)
Power Elec. (kW): SCADA / Act. Disc	125.6	127 (+1.4%)	119 (-5.2%)	120.3	119 (-0.9%)	127 (+5.8%)	96.4	108 (11.7%)	117 (+20.9%)
Shear coeff.: α **(-)** Power law fit	0.19	0.17	0.18	0.16	0.18	0.18	0.26	0.27	0.27

4.5.2 Near wake deficits

The normalized wake velocity obtained from the simulations is compared to the lidar measurements for both the vertical and the horizontal wake profile and for all three types of stratification. Results of this analysis are shown in appendix A.4.

For the very stable cases, and as motivated in section 4.3.5, the CFD results are extracted at a different altitude (as function of the downstream position) than the horizontal plane, to compensate for the absence of terrain modeling in the simulation.

It is seen in Appendix A.4a that the agreement is excellent at downstream distance of $4D$ and further downstream. In the vicinity of the rotor, the simulated profile shows a lack of wind deficit close to the rotor centerline, which progressively disappear from $3D$ downstream. This disagreement is probably a combination of modeling issues and

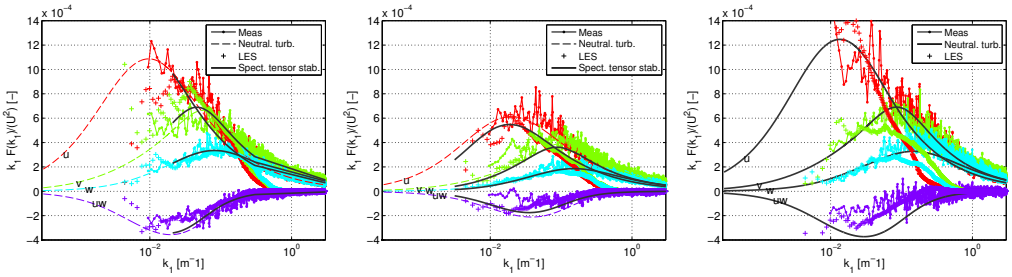

(a) Unstable case **(b)** Very stable case **(c)** Neutral spectral fit

Figure 4.9: Spectral analysis of the turbulence field. For each test case, the resolved turbulence upstream of the rotor by the LES model is compared to the measured turbulence by the sonic anemometer, the model input of the neutral spectral tensor and the non neutral spectral tensor. The red, green, light blue and purple line and crosses represents the u-, v-, w- and uw- component of the velocity, respectively.

experimental uncertainties.

On the modeling side, a bad representation of the nacelle, the lack of tower modeling or uncertainties related to the airfoil data in the actuator disc modeling may explain the observed discrepancies.

On the experimental side, the normalization of the very near wake wake profile using the mean wind speed measured at $5D$ downstream may explain the observed discrepancies as the mean wind speed may not be well correlated in the far wake due to the inhomogeneous terrain. The latter seems the most plausible cause of the observed disagreement.

In Appendix A.4b, the discrepancies observed near the bottom of the domain are a consequence of the slip wall boundary conditions. A further implementation of the model will include a consistent rough wall formulation which will enhance agreement near the surface.

The unstable case shows a rather well preserved wake in the simulations as opposed to the measurements at the most downstream position. This indicates a possible underestimation of the wake meandering intensity leading to a too slow wake recovery. A more thorough analysis of the magnitude of wake meandering will be subsequently performed.

There are no major difference on the wake deficit predictions between the classical approach and the extended model for the two non neutral cases. This can be explained by the relatively small length scales involved in this experiment both from the turbine (total height of approx 60 m) and from the investigated wake downstream transportation distance (up to 5D). A qualitative representation of the stability effect on the mean and instantaneous wake velocity and potential temperature contour is shown in Fig. 4.11.

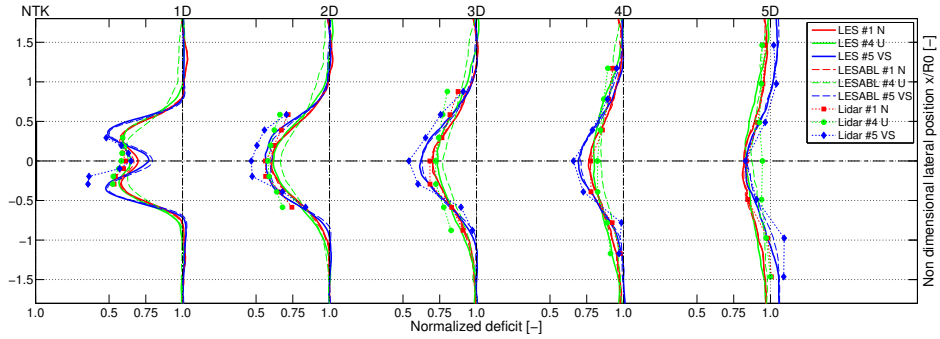

(a) Wake deficit at hub height.

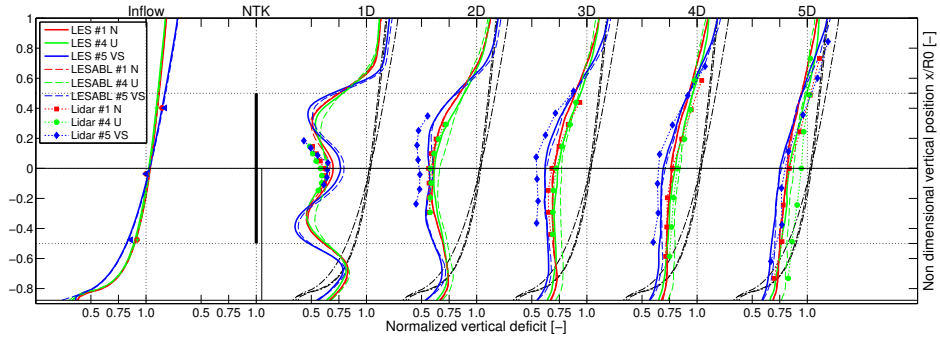

(b) Vertical wake deficit profile.

Figure 4.10: Comparison of measured and modeled wake velocity in the near wake of the Nordtank turbine under three different atmospheric stability conditions.(a) represents the wake deficit at hub height and seen from the top. (b) is the corresponding vertical profile along a vertical axis aligned with the turbine tower. Dash lines indicates the mean inflow profile.

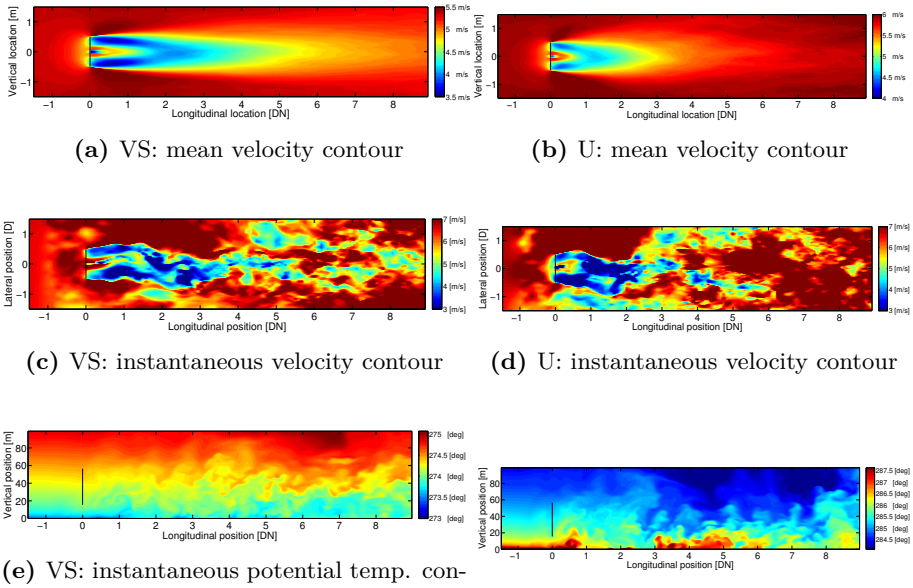

(a) VS: mean velocity contour

(b) U: mean velocity contour

(c) VS: instantaneous velocity contour

(d) U: instantaneous velocity contour

(e) VS: instantaneous potential temp. contour

(f) U: instantaneous potential temp.

Figure 4.11: Contour plot of the 10 min average mean wake velocity at hub height and seen from the top (a: very stable), (b: unstable); and the corresponding instantaneous wake flow field in (c: very stable), (d: unstable). The potential temperature contour plot is shown in (e: very stable) and (f:unstable).

4.5.3 Near wake dynamics

The magnitude of wake meandering, understood presently as the standard deviation of the wake center position as function of the downstream position, is investigated. The goals of this analysis is to validate the dynamic behavior of the wake in the CFD simulations, relevant for a future analysis on load and power prediction under non neutral stratification. As seen in Fig. 4.12a, the meandering magnitude increases with instability, similarly to the observation in the numerical study by Abkar et al. in [2]. The apparent difference in meandering magnitude with the later study is explained by the large sampling time required by the pulsed lidar to complete a lidar sweep as opposed to the high resolution of wake meandering in [2]. Additionally, a fair agreement between the measured dynamic by the pulsed lidar and the CFD model is observed.

The sudden gradient change in the lateral meandering at $5D$ downstream for the unstable stratification confirms the lack of lateral wake meandering and the poor agreement in Fig. A.4.

When resolving the wake deficit in the meandering frame of reference (MFoR), the wake deficit is fairly invariant to stability conditions for downstream location above 3D (Fig. 4.12b), as similarly observed in the experimental analysis.

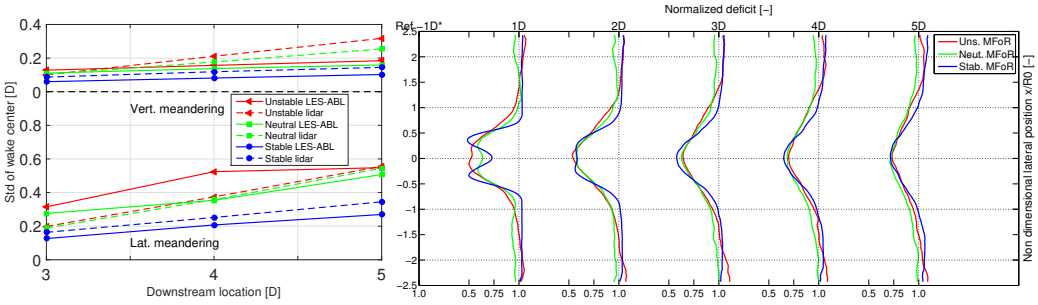

(a) Meandering magnitude **(b)** LES-ABL in MFoR

Figure 4.12: (a) Analysis of the simulated wake meandering in the EllipSys3D LES-ABL model compared to the measured one. The discrete wake center position are determined at the same sampling time as the one the lidar performs. (b) Results of the LES-ABL computations in the MFoR.

4.6 Summary

In the present chapter, single wind turbine wake were analyzed under varying atmospheric stability conditions both experimentally using full-scale pulsed lidar measurements and numerically using Large Eddy Simulation based on the EllipSys3D flow solver.

The numerical set-up involved a simple approach where the modeled terrain, as opposed to

the one of the experiment, is assumed flat and homogeneous. A validation of the numerical model is performed on three datasets of similar incoming mean wind speed, where the superimposed synthetic turbulence is generated from a newly developed spectral tensor which include buoyant effects.

A fair agreement is seen for the wake deficit profile for downstream distances of 3 rotor diameters and above. The poor agreement in the near wake is suspected to be a consequence of the lidar measurement normalization procedure, where the used wind speed at the most downstream location is not well correlated with the near wake due to inhomogeneity of the terrain. Moreover, a reasonable agreement between the wake meandering magnitude and key ambient and turbine parameters is observed, taking into account the uncertainties inherent to one-to-one mapping of lidar measurements with LES models.

As part of the model benchmark, the extended LES-ABL model with buoyant forces displayed comparable results and performance with the classical LES approach which do not model atmospheric stability. It is however expected that the use of the LES-ABL model is beneficial when simulating on a larger domain a real wind farm involving multiple wakes.

Experimental evidence that the wake under very stable conditions tends to follow the terrain during its downstream transportation as opposed to the quasi-horizontal advection in unstable stratification was found. This will be further investigated by analyzing the streamlines path from a terrain simulation and correlate it to the wake path.

The present analysis further validated the main conjecture of the engineering Dynamic Wake Meandering model when applied in stability condition's different from neutral, namely that a wind turbine wake profile is virtually invariant to atmospheric stability when observing from the moving frame of reference.

This numerical model is the initial step of an on-going development, where new numerical techniques will be implemented and tested in the near future. The surface boundary condition will be replaced by a consistent formulation of the rough wall, and simulations will be conducted on a similar terrain as the one of the experiment. This numerical approach will further be used for a parametric study of overlapping wakes, aiming at developing a simpler engineering model of practical relevance.

The measurements presented in this paper are formulated as a new test case for the IEA - Task 31 "WakeBench" framework, where all relevant informations required for reproducing the present results are available. A benchmark will be conducted in the near future using advanced CFD models such as NREL's CFD model [29].

Chapter 5

Multiple wake dynamics

5.1 Introduction

As the capacity of wind farm exceeds 300MW with more than 100 turbines as in Walney, Anholt and the London Array, the financial uncertainties in relation to the overall wind farm performance become proportionally larger. It is therefore vital for a wind farm developer to rely on accurate wind farm flow models in order to lower the uncertainty on both the energy production and the turbine loading at the design stage and consequently lower the cost of energy.

One of the main research areas connected to lowering the cost of energy is the alleviation of wind farm wake loss. The research community can now benefit from several years of operational data from modern offshore wind farms such as Horns Rev, Nysted and Lillgrund. These long term observations have been extensively used to assess the performance of standard engineering models used by the industry [14], or to understand key parameters affecting the wind farm performance and wake losses [45]. Recently, the focus shifted towards wake effects in very large wind farms, known as deep array effects and interaction between large wind farms. Nygaard et al. [99] studied these effects using the Jensen model [54] coupled with a quadratic overlapping wakes model and showed clear limitation in the wake losses prediction and thus a necessity to extend the industry standard models to remedy over and underestimation of wake losses inside large arrays. This can only be achieved by a better understanding of the physical phenomenon of overlapping wakes and deep array effects within wind farms.

Today, the model of Frandsen [39] is used in the design standards for wind turbines in wind farms. In this model the power production of turbines in a wind farm is predicted based on 1D momentum considerations similar to the work of Jensen [54], while the fatigue loading is based on the so-called effective turbulence intensity, [39]. The model of Frandsen works

in general well but occasionally reveals discrepancies when compared to measurements.

Recently Ott et al. developed the FUGA model [100], which is a very fast linearized CFD model tool for simulation of wind farm wakes. This model was used to predict the power output from the Horns Reef and Nysted wind farms and revealed good agreement when compared with measurements. However, because FUGA is a steady state model, it is not well suited for predicting loads.

In order to formulate a fast unifying theory that account for both power production and loads on wind turbines in wind farms, Larsen et al. developed a "poor man's" LES, i.e. the unsteady Dynamic Wake Meandering model [71], where the main assumption is, that the wake meandering is governed by large scale turbulence structures in the atmosphere. This interpretation is supported by lidar measurements by Bingöl et al. [18] as well as by hot wire and PIV measurements in a boundary layer wind tunnel conducted by España et al. [36]. The DWM model has previously proven accurate for predicting single wake development [84], but recently also for predicting power output and loads of a whole wind farm when combined with the aero-elastic code HAWC2 and suitable assumptions about merging wakes, [72]. Despite the promising results of the DWM model there is still room for improvements in terms of wake deficit and turbulence characteristics, which are derived assuming axisymmetry of the wake. For future improvement, a better understanding of the characteristics of merged wakes is necessary.

With the newest remote sensing technology such as lidars, both industry and research community can now benefit from detailed full-scale measurements of wakes, giving a large and valuable source of knowledge for deeper analysis and model validation of wake generation, development and interaction. Specifically, two-dimensional lidar scanning of wakes have been conducted by Larsen et al. [66] on a stall regulated 95kW Tellus turbine at Risø and on a 2MW wind turbine at the Tjæreborg site to characterize the wake meandering as well as the quasi-steady wake deficit and wake turbulence under real atmospheric conditions.

Wake interaction and characteristics have also been studied extensively using computational fluid dynamic. Fletcher and Brown [37] simulated the aerodynamic interaction between two wind turbines operating in uniform flow conditions using a lifting line technique. Troldborg et al. [145], Storey et al. [138] and Lee et al. [75] used the actuator line model to simulate wake interaction between two turbines operating in the atmospheric boundary layer. In the latter study the influence of both roughness and atmospheric stability was investigated and shown to be of major importance for turbine loads and power production. Simulations of a whole wind farm have been carried out by Ivanell [50] using the actuator disc method as well as by Churchfield et al. [28] using the actuator line model. Such simulations provide valuable information about wakes and can be used to calibrate simpler engineering models [84].

The first part of the present chapter is a continuation of the study of Troldborg et al. [145]. It aims to contribute to the overall understanding of two interacting wakes, also referred to as double wake, by the use of lidar measurement recorded from the nacelle of a modern 2MW turbine combined with a numerical study of the same turbine exposed to similar external flow field conditions. This numerical study, similar to the one conducted in [145], uses the Risø DTU in-house 3D Navier-Stokes solver EllipSys3D. Analysis and comparison of merged wake characteristics is performed for two different turbine spacings and inflow conditions. It is a one to one mapping of experimental results on numerical

predictions.

The second part of this chapter aims at investigating the simplest possible wind farm configuration and attempts to characterize the wake interaction generated by two aligned turbines using both an extensive full-scale experiment and CFD LES. The experiment involves 3 scanning lidars, a fully instrumented meteorological mast and two stall regulated turbines, located at the DTU Wind Energy, Risø campus test site. This test site has hosted several lidar measurement campaigns in the past decade. In the study by Bingöl et al. [18] and pursued by Trujillo et al. [152], a prototype ZephIR Continuous Wave (CW) lidar was installed on the back of a Tellus 95 kW stall regulated turbine to study 1D and 2D cross sectional wake measurements. In these two studies, instantaneous wake deficits of wind turbines were, for the first time, measured and analyzed in one- (1D) and two dimensions (2D). More recently, a study by Machefaux et al. [81] made use of the nearby Nordtank 500 kW turbine equipped with a pulsed lidar system to characterize single wake meandering, advection and expansion. The numerical work combines CFD LES of the flow and actuator disk modelling of the rotor. As part of a mutual validation of the measurements and computations, the wake deficit and the wake generated turbulence as well as the power and rotor thrust was compared for a selected time series under near neutral atmospheric stratification. Through this comparison, the capability of CFD LES and advanced wake lidar measurements to accurately capture flow characteristics of an overlapped wake is demonstrated.

With the increasing growth of computational capacity, properly validated CFD tools can be used to develop and validate simple engineering models for overlapping wakes based on parametric studies, and also to understand the physics of deep array effect in large wind farms, similarly to the work by Calaf et al. [24].

5.2 The Tjæreborg experiment

The experimental data were obtained from a full-scale experiment conducted at Tjæreborg Enge wind farm, as part of the EU-TOPFARM project [64]. It is an onshore wind farm located south of the city of Esbjerg and approximately 15km from the west coast of Denmark. The site is open land with low roughness; it has thus typically low shear and low turbulence for the prevailing westerly winds. The layout of the wind farm is sketched in Figure 1. During the measurement campaign, the NEG MICON NM80 wind turbine denoted WT3 was instrumented with a nacelle mounted lidar, which scanned 2D flow fields in its wake at different downstream cross sections. A ZephIR Continuous Wave lidar system manufactured by QinetiQ was adapted to comply with the specific project needs and details of this equipment and its adaptation can be found in [18]. The level of uncertainties associated with lidar anemometry has been studied by Lindelöw-Marsden [77], and it is likely that a ZephIR equipment can extract the wind velocity with a deviation of $\pm 2\%$ when compared with cup anemometers. The lidar measurements were synchronized with simultaneous 20 Hz wind field measurements from the nearby 93 m high intensively instrumented reference mast (M1), as well as with 1 Hz measurement on WT3 of various operational conditions (yaw, power, rotor speed and pitch).

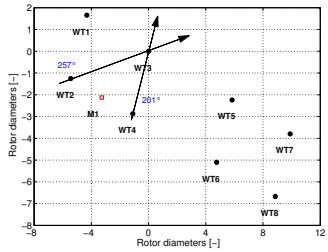

Figure 5.1: Tjæreborg wind farms and selected main wake directions. The graphic is scaled based on rotor diameters (80m). The wind farm consists of 3 Vestas V80-2MW and 5 NEG MICON NM80 turbines owned by DONG Energy A/S and Vatenfall AB, respectively.

As a part of the experimental analysis, the rotor wake longitudinal flow field is discretized by associating lidar cross sectional recordings with non-overlapping grid cells of $2 \times 10m^2$ from a particular laser beam sweep. By averaging all measurements within a cell for each "passage", the flow field statistics will appear on a regular grid. The lidar is averaging the velocities along the beam over a distance which depend on the range. This distance ($\approx$ 50m at focus distance of 200m) is significantly larger than the grid cells, thus in turn justifying the applied cell averaging. An illustration of a typical lidar sweep pattern and the corresponding averaging grid is shown on Fig. 5.2a. Fig. 5.2b shows the measurements spherical envelop defined by the lidar focus distance, viewed from the top.

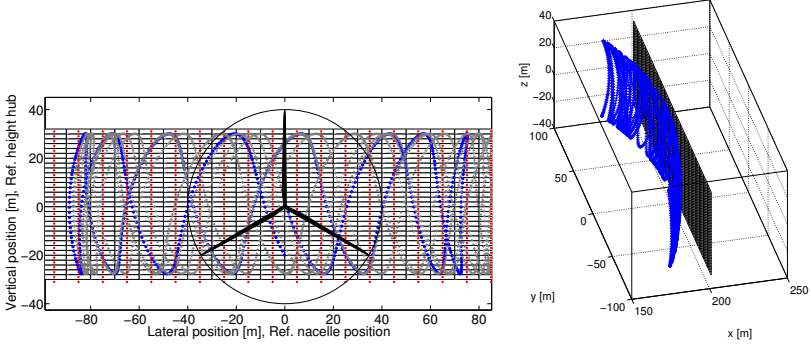

(a) **(b)**

Figure 5.2: (a) lidar wake resolving grid at a focus distance of 200m ($\approx 2.5D$). The blue dots represent one sweep pattern, the gray crosses are consecutive sweeps. The superposed resolving grid is also shown with its cell centers in red circle. (b) View from the top and expressed in the lidar axis coordinate (x-axis is the flow direction)

The subsequent analysis involves 2 merged wake situations: 1) the double wake from wind turbines WT2/WT3 with a large turbine spacing ($\approx 5.5D$); and 2) the double wake from wind turbines WT4/WT3 with a lower turbine spacing ($\approx 3D$). The comparison is

conducted using 10-minute averaged time series associated with a 200m downstream focus distance. In order to mimic the experimental conditions, the computed data are obtained using specific measured ambient conditions as listed in Table 5.1 (cf. Section 5.3). Both 10-minutes measurements have a neutral atmospheric stability class (obtained with the use of temperature sensors and computed with the Monin-Obukhov similarity theory). Finally, the 10-minutes average wind direction is equal to the ideal full wake direction, and its standard deviation does not exceed 5° in both cases.

Table 5.1: Case study 10min average quantities

Site measurements	WT2-WT3	WT4-WT3
Wind speed [m/s]	8.50	7.24
Shear coef. [-]	0.14	0.08
Inflow turbulence level [-]	0.05	0.03
RPM upstream [-]	15.00	15.90
RPM downstream [-]	13.15	12.22
Turbine separation [m]	446	246
lidar Focus distance [m]	200	200

In order to perform a fair comparison between the main flow direction component U from the computations and the line of sight velocity (U_{los}) from the laser beam, an additional correction is proposed. The angle between the laser beam and the main flow direction (z-axis) can increase significantly outside of the wake core. We denote the instantaneous flow velocity vector expressed in the fixed frame of reference by:

$$(v(t), w(t), U + u(t)) \equiv \underline{U(t)} \tag{5.1}$$

where U is the mean streamwise velocity in the wake, u(t) is the fluctuating longitudinal part, v(t) is the fluctuating lateral part, and w(t) is the fluctuating vertical part. Similarly, we denote the instantaneous flow velocity vector expressed in the lidar beam frame of reference by:

$$\left(\tilde{v}(t), \tilde{w}(t), \tilde{U}(t) + \tilde{u}(t)\right) \equiv \underline{\tilde{U}(t)} \tag{5.2}$$

As previously shown on Fig. 5.2a(a), the lidar beam is moving with 2 degrees of freedom in the fixed frame of reference. The pan angle, denoted θ_P, represents the beam angle resulting from the rotation around the x-axis (illustrated in Fig. 5.3), whereas the tilt angle θ_T is the rotation angle around the y-axis.

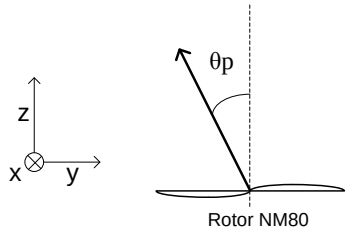

Figure 5.3: Representation of the pan angle of the laser beam in the fixed frame of reference.

The transformation matrix defining a panning, $\theta_P(t)$, of the fixed frame of reference is:

$$\underline{\underline{T}}_P \equiv \begin{pmatrix} 1 & 0 & 0 \\ 0 & \cos\theta_P(t) & -\sin\theta_P(t) \\ 0 & \sin\theta_P(t) & \cos\theta_P(t) \end{pmatrix} \tag{5.3}$$

Similarly, the transformation matrix associated with tilting the fixed frame of reference is:

$$\underline{\underline{T}}_T \equiv \begin{pmatrix} \cos\theta_T(t) & 0 & \sin\theta_T(t) \\ 0 & 1 & 0 \\ -\sin\theta_T(t) & 0 & \cos\theta_T(t) \end{pmatrix} \tag{5.4}$$

with $\theta_T(t)$ denoting the tilt angle. The velocity vector $\underline{U}$ can be transformed to the lidar beam frame of reference by calculating the product $\underline{\tilde{U}} = \underline{\underline{T}}_P \underline{\underline{T}}_T \underline{U}$:

$$\underline{\tilde{U}} = \begin{pmatrix} w(t)\cos\theta_T(t) + (U+u(t))\sin\theta_T(t) \\ v(t)\cos\theta_P(t) + w(t)\sin\theta_P(t)\sin\theta_T(t) \\ \qquad \cdots - (U+u(t))\sin\theta_P(t)\cos\theta_T(t) \\ v(t)\sin\theta_P(t) - w(t)\cos\theta_P(t)\sin\theta_T(t) \\ \qquad \cdots + (U+u(t))\cos\theta_P(t)\cos\theta_T(t) \end{pmatrix} \tag{5.5}$$

The line-of-sight velocity U_{los} is expressed as:

$$\begin{aligned} U_{los} &\equiv \tilde{U}(t) + \tilde{u}(t) \\ &= v(t)\sin\theta_P(t) - w(t)\cos\theta_P(t)\sin\theta_T(t) \\ &+ (U+u(t))\cos\theta_P(t)\cos\theta_T(t) \end{aligned} \tag{5.6}$$

For moderate tilt and pan angles and for a conventional atmospheric boundary layer, the following conditions apply:

1. $v(t)\sin\theta_P(t) \ll (U+u(t))\cos\theta_P(t)\cos\theta_T(t)$
2. $w(t)\sin\theta_T(t) \ll (U+u(t))\cos\theta_T(t)$

Thereby, the z- component of Eq. 5.5 reduces to:

$$\begin{aligned} U_{los}(t) &\simeq (U+u(t))\cos\theta_P(t)\cos\theta_T(t) \\ (U+u(t)) &\simeq U_{los}(t)\cdot\frac{1}{\cos\theta_P(t)\cos\theta_T(t)} \end{aligned} \tag{5.7}$$

To conclude, the projection of U_{los} along the streamwise velocity in the fixed frame of reference is computed as:

$$U_{lidar}(t) = U_{los}(t)\cdot\frac{1}{\cos\arcsin\left(\frac{Y}{FC}\right)\cos\arcsin\left(\frac{X}{FC}\right)} \tag{5.8}$$

where X and Y are vertical and horizontal position of the beam, respectively, and FC is the lidar focus distance. A 2D representation of the correction for the pan angle is shown on Fig. 5.4.

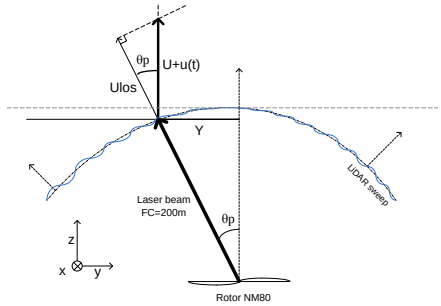

Figure 5.4: Velocity triangle for a lidar measurement. The line of sight velocity (U_{los}) is projected on the main flow direction for comparison with numerical computations.

Finally, as opposed to the analysis conducted in [61], the present analysis of the wake is done in a fixed frame of reference to simplify matters, due to the complexity of implementing a meandering tracking algorithm for merged wakes.

5.3 Numerical approach

The computation of the flow field has been carried out by LES approach using the 3D flow solver EllipSys3D developed by Michelsen and Sørensen [93], [135]. The wind turbine rotor is simulated using the actuator line model developed by Sørensen and Shen [134]. The modelling of the atmospheric boundary layer (ABL) is done in two parts: a model for the sheared atmospheric mean velocity field and a model for the ambient turbulence. The mean velocity field is imposed using a technique where steady body forces are initially computed and applied to the entire domain, while synthetic turbulent fluctuations are introduced in a cross-section upstream of the rotors by using an unsteady actuator.

The turbulence field is generated prior to the computation using the Mann algorithm [87], which produces homogeneous, stationary, Gaussian and anisotropic turbulence with the same spectral characteristics as observed in the neutral atmosphere. The unsteady computation are performed until at least 10 minutes average statistic of the wake flow can be extracted and compared to the measurements.

Two Cartesian computational domains have been used in the present study: one for the case with $3D$ spacing; and one for the $5.5D$ spacing. The grid layout and boundary conditions are in accordance with previous studies on wake computation [145], where the inlet is applied with the desired wind shear profile; the outlet has unsteady convective conditions; the ground of the domain has a wall no slip condition; and the top boundary is set to the farfield velocity. The dimensions of the grid used for the $5.5D$ spaced turbines is (L_x,L_y,L_z): (24R, 24R, 37.4R) while the one for the $3D$ spacing is (24R, 24R, 31.8R), where L_z denotes the length in flow direction, L_y the domain height, and L_x the domain width, and R is the rotor radius. The two grids have 3.981 and 2.949 millions cells,

respectively. The cells are in both grids concentrated equidistantly with a spacing of 0.04R in the region around and between the turbines in order to resolve and preserve the wake structures. An overview of the computational domain is shown in Fig. 5.5a for the y-z plane and in Fig. 5.5b for the x-y plane. Note that only every 16th cell boundary is shown in the Figures.

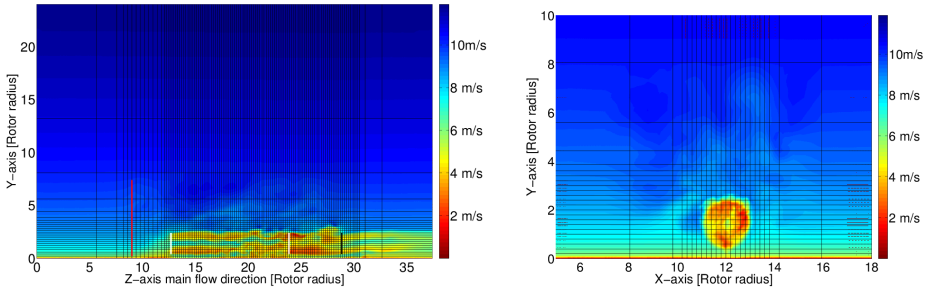

(a) **(b)**

Figure 5.5: (a) Average streamwise velocity field extracted from a cross section in the middle of the domain ($L_x = 12R$). The red plane ($L_z = 9.2R$) indicates the location of introduced turbulence generated using the Mann model prior to the computations. The location of the two turbines are symbolized by the white planes. Finally the location of the lidar recording plane is shown in black. (b) Average streamwise velocity field extracted from a reduced size cross section ($L_z = 24R$).

5.4 Results and discussion

5.4.1 Merged wake at 2.5D downstream for 3D turbine spacing

The average wake characteristics at hub height 2.5D downstream of WT3 when operating fully in the wake of WT4 (i.e. 3D spacing) are shown in Fig. 5.6a. A first computation conducted with the same parameters as measured on the mast M1 showed poor agreement with the measured deficit as seen on Fig. 5.6a(a). The streamwise wake velocity extracted from the computation is everywhere larger than the measured one, which might be a consequence of a possible over estimation of the inflow wind speed. Moreover, the computed power of both turbines is not consistent with neither the NM80 power curve nor their respective measured power. This confirms that the wind speed measured at the mast is not representative for the actual upstream rotor wind speed, which explains the discrepancies previously observed on Fig. 5.6a. Additionally, the RPM of the upwind turbine is not known accurately, due to the fact that only integer variables were used for this sensor recording in the database.

Consequently, a sensitivity analysis is performed where RPM, turbulence level and inflow velocity are slightly changed around the measured values. For each case, the relative

error on the power production (as defined by Eq. 5.9) is investigated, and the results are summarized in Table 5.2.

Table 5.2: Relative error on power production

TI [%]; U0 [m/s]; RPM [-]	**Rel. error WT4 [%]**	**Rel. error WT3 [%]**	**Rel. error power ratio [%]**
5%; 8.5m/s; 15 (measured)	13.20	18.34	5.92
10%; 8.5m/s; 15	5.52	35.16	31.37
5%; 7.0m/s; 15	-56.03	-47.60	5.41
5%; 7.0m/s; 17	-47.04	-34.74	8.37
5%; 8.5m/s; 17	9.14	19.10	10.97
5%; 8.0m/s; 15	-2.84	3.43	6.09

$$\epsilon = 100 \cdot \frac{P_{EllipSys3D} - P_{meas}}{P_{EllipSys3D}} \tag{5.9}$$

With reference to Fig. 5.6a, it is seen that the best wake velocity and turbulence level agreement obtained for computations with a free stream velocity of 7.0 m/s. However, for the two RPM-cases associated with this wind speed, large deviations of around 50% are observed on the power production, as seen in Table 5.2. This emphasizes the sensitivity of the power production with respect to a change in wind speed, since the power is function of the cube of the free-stream velocity.

The minimum wake wind speed has the best agreement with the computation performed at 8.0 m/s under the same RPM and turbulence level setting as measured. Also both mechanical power and power ratio have a deviation of less than 4% from the measurement. For this case, the agreement remains less convincing outside the core of the wake, where the wind speed recovery is less abrupt in the measurement. The measured wake center location deviates from the computed one with a lateral offset of magnitude 10-12m. The analysis suffers from the lack of knowledge of the measured wind speed outside of the wake, due to the limitations in the lidar spatial coverage. This deviation may be a consequence of the influence of a nearby turbine, uncertainties of the yaw misalignment of the turbines, or other mounting issues. Moreover, it must be stated that discrepancies exists while comparing only one 10-minute timeserie with another, due to natural variability. Finally, it is also possible that the meandering of the wake in the LES computations is too low due to the "limited" size of the turbulence box in the lateral direction. In the work conducted by Madsen et al. [84], the turbulence box is extended to several kilometers.

Additionally, contour plots of the measured and computed streamwise wake velocities (corresponding to $U_0 = 8.0m/s$) are shown on Fig. 5.7a, and similarly the turbulence level are shown on Fig. 5.8a. It is seen on Fig. 5.7a, that the measured wake has a more rapid transition into a bell shaped form and is more asymmetric than the computed wake for the given downstream position. Finally, the measured wake has a larger expansion, maybe due to meander, which is clearly seen in Fig. 5.6b.

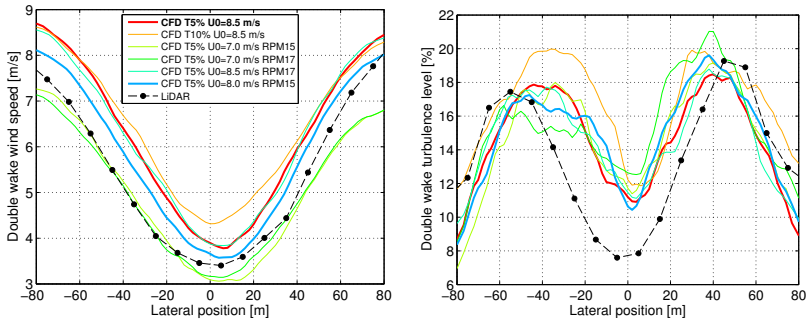

(a) **(b)**

Figure 5.6: Comparison of (a) measured (lidar) and computed (CFD) stream wise wake velocity; and (b) turbulence intensity at hub height for the double wake situation generated by WT4 and WT3. The bold text in the legend corresponds to the computation using the measured ambient condition which shows poor agreement with the full-scale flow recordings. The dots represent full-scale measurements.

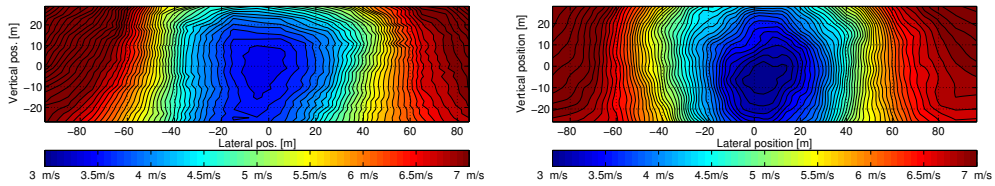

(a) **(b)**

Figure 5.7: Comparison of (a) measured (lidar); and (b) computed (CFD) contour plot of streamwise wake velocity for the double wake situation generated by WT4 and WT3.

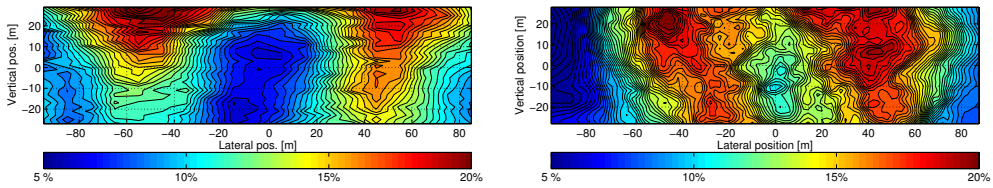

(a) **(b)**

Figure 5.8: Comparison of (a) measured (lidar); and (b) computed (CFD) contour plot of wake turbulence level for the double wake situation generated by WT4 and WT3

5.4.2 Merged wake at 2.5D downstream for 5.5D turbine spacing

Similar analysis is conducted for the wake interaction of turbines WT3 and WT2 as shown on Fig. 5.9a. In this case, the recorded overall wake wind speed and turbulence level shapes are in very good agreement with the computations as is the power produced. Once again, a lateral offset is clearly seen in the mean profile. At 200m downstream, this offset is of the order of 10 to 15m in both cases, corresponding to an angle of 2.9 ° to 4.2 ° at the nacelle. Because of the moderate magnitude of this angle, the observed offset could realistically be the consequence of a small mounting misalignment of the lidar beam axis to the nacelle axis.

The comparison of contour plots of wake velocity and turbulence profile shows similar discrepancies as observed for the lower turbine spacing case; i.e. the measured wake has a larger expansion and more pronounced asymmetry as compared to the computed one. In both cases, the turbulence profile seen on Fig. 5.6a and Fig. 5.9b, respectively, has a non symmetric profile, which most likely relates to the combined wake rotation and shear, as described in the study by Zahle and Sørensen [161]. The turbulence level around the wake core is less than the computed one, and this could be the consequence of the spatial averaging of the lidar.

A quantitative measure of the previous comparisons is given by the cross correlation coefficient R with respect to the lateral position X denoted $R(X)$. When considering deficit and turbulence profiles as data series, the normalized cross correlation coefficient, ρ, of the two random variables $(D_m;D_p)$ representing the measured and predicted wake velocity, is given by:

$$\begin{aligned}\rho(X) &= \frac{R(X)}{\sigma_{D_m}\sigma_{D_p}} \\ &= \frac{E\left[(D_m(x+X)-<D_m>)(D_p(x)-<D_p>)\right]}{\sigma_{D_m}\sigma_{D_p}}\end{aligned} \tag{5.10}$$

The formulation is similar in the case of the turbulence level represented by an analog couple of "random variables" $(T_m;T_p)$. E is the expected value operator, X is the lateral

position in meter, σ_D is the standard deviation of the deficit, $< D >$ refers to the average of the deficit in space, and subscripts m and p refer to measured and predicted, respectively. For each case, the maximum normalized cross correlation coefficient is found at a particular lateral offset. The results of this analysis are summarized in Table 5.3. From Table 5.3, it is seen that the magnitude of the lateral offset is nearly constant for the two cases, reinforcing the conjecture of having a combination of yaw and lidar mounting misalignment. The cross correlation coefficient is very close to 1, indicating a high correlation between the data series analyzed and therefore good agreements in the comparison.

Table 5.3: Normalized cross correlation coefficients and corresponding lateral offsets.

	Turb. WT4-WT3	**Turb. WT4-WT3**	**Ws WT2-WT3**	**Ws WT2-WT3**
$\rho(X)$ [-]	0.979	0.982	0.984	0.988
X [m]	5	6	6	7

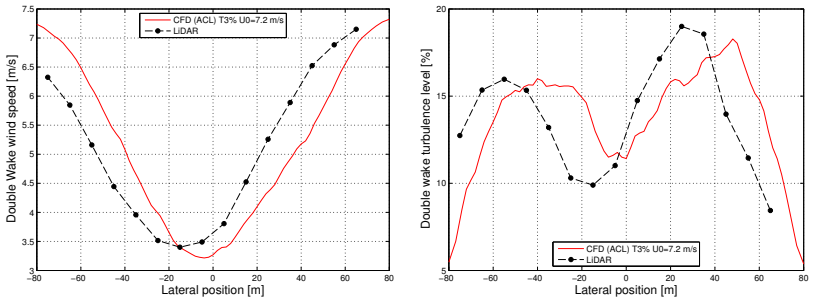

(a) **(b)**

Figure 5.9: Comparison of (a) measured (lidar) and computed (CFD) stream wise wake velocity; and (b) turbulence intensity at hub height for the double wake situation generated by WT2 and WT3. The dots represent full-scale measurements.

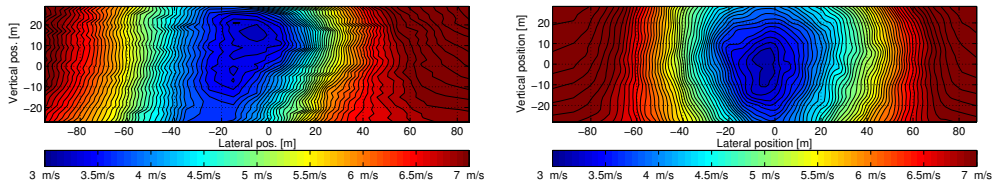

(a) **(b)**

Figure 5.10: Comparison of (a) measured (lidar); and (b) computed (CFD) contour plot of streamwise wake velocity for the double wake situation generated by WT2 and WT3.

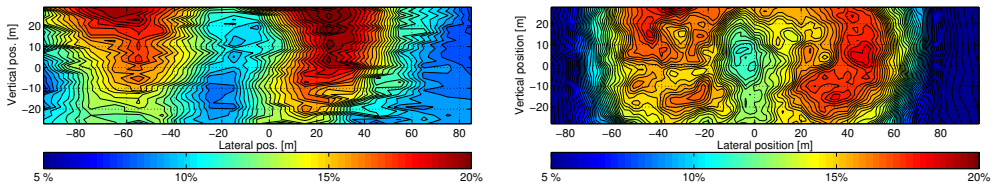

Figure 5.11: Comparison of (a) measured (lidar); and (b) computed (CFD) contour plot of wake turbulence level for the double wake situation generated by WT2 and WT3.

5.5 Summary from the Tjæreborg lidar experiment

In the present analysis, two wind turbine double wake cases are investigated using full-scale experimental data and CFD LES ACL computations on a NM80 turbine in the Tjæreborg wind farm. A sensitivity analysis is performed to enhance agreement and to overcome the uncertainties related to the recording of ambient wind field conditions and turbine sensors. A lateral offset between the wake variance profiles is observed, which may be a consequence of either a calibration issue on the yaw sensor or a misalignment of the lidar mounting with respect to the nacelle. In one of the two cases, larger deviations are seen in the turbulence level around the wake core. The reason of this discrepancy is not fully understood yet, but it is expected to be the consequence of the averaging procedure of the lidar, potentially attenuating in particular the small scale fluctuating part of the wind velocity, thus reducing the turbulence level around the wake core. However, the wake characteristics is very close to the computations, giving high confidence in both the measuring techniques and the CFD LES ACL model.

A subsequent analysis of merged wakes, as part of the DSF FlowCenter project, will comprise a set-up where both up and downstream turbines are mounted with synchronized lidar's and where the downstream lidar has a very high spatial and temporal resolution with a laser pattern optimized for wake measurement. Thus this analysis will not only benefit from the overall increased resolution, but the use of an additional upstream lidar system will give detailed knowledge of the single wake inflow to the downstream turbine. In the context of full wakes, it would be then possible to investigate the added wake turbulence and deficit generated by the downstream turbine. It will also be possible to investigate the merged wake deficit in more details.

5.6 The Risø campus full-scale experiment

In this section, a detailed description of the Risø full-scale experimental setup is given. It starts with a brief overview of the Risø test site and the operating turbines, supplemented by a more detailed description of the remote sensing devices, specifically their technical functionality and scanning capabilities.

5.6.1 The Risø test site

The Risø test site is located by the Roskilde Fjord, on the Risø campus of the Technical University of Denmark. It is an onshore test site with moderate to high inflow turbulence intensity typically ranging from 9% to 15% depending on the flow direction, and a $1.5-2\%$ fairly constant slope extending from the fjord towards the eastern inland. Primary inflow directions are from westerly winds, where an internal boundary layer (IBL) develops due to the sudden change of surface roughness in the transition between water and land. The primary merged wake inflow direction, of interest in the present study, is winds coming from a south-southwesterly wind direction around 197°.

Two stall regulated wind turbines are used for the merged wake experiment; a Nordtank 500 kW [106] and a Tellus 95 kW [85]. The Nordtank turbine is equipped with LM 19.1 m blades and has a total rotor diameter of 41 m and a hub height of 36 m. The Tellus, mounted with 9.5 m LM Wind Power blades and a lattice tower with a height of 29.3 m, is an anti clockwise rotating rotor as opposed to the clockwise rotation of the Nordtank rotor. Their respective rotational speed are 27.1 rpm and 36 rpm.

A satellite photograph of the test site is shown in Fig. 5.12. A Vestas V27 turbine located 3 rotor diameters north of the Nordtank turbine, was not operating during the campaign. Additionally, nearby office buildings are located north of the test site at a distance of about 270 m from the Nordtank turbine and thus, do not affect the wake measurements. Finally, the technical control room, seen between the two turbines in Fig. 5.12, has a height of only 2.5 m, and thus, do not present a major obstacle to the wake flow.

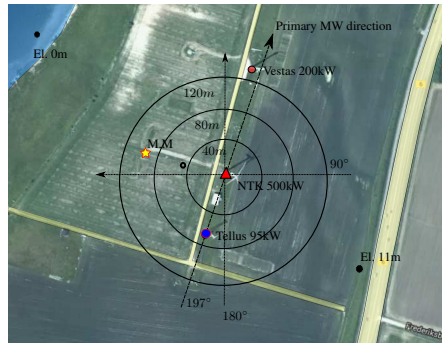

Figure 5.12: Satellite picture of the DTU Wind Energy, Risø Campus test site, centered around the Nordtank turbine. The nearby fjord in blue is located West / Northwest of the Nordtank. Concentric circles, representing the distances in rotor diameter from the Nordtank rotor, are drawn. The main meteorological mast (met. mast) is indicated as "M.M" (yellow star), whereas the lidar mounted Nordtank and Tellus turbines are indicated with red triangle and blue dots, respectively. The primary merged wake inflow direction of 197° is also indicated. Source: Google Maps. *Google and the Google logo are registered trademarks of Google Inc., used with permission.*

5.6.2 The test set-up

A sketch of the test set-up in a merged wake situation is depicted in Fig. 5.13. A meteorological mast located 92 m to the west of the Nordtank turbine is used for characterizing the ambient conditions of the experiment. It is equipped with several cup anemometers, wind vanes, three-dimensional sonic anemometers, absolute and differential temperature sensors as well as absolute atmospheric pressure sensors. These recordings are synchronized with the Nordtank turbine operational sensors, strain gauges, power production and rotational speed among others, and stored in a database. The Tellus turbine does not have standard operational sensors, and was not specifically instrumented for this experiment.

Three lidars are used in this full-scale experiment: two of them are mounted on the nacelle of the Nordtank turbine and one is located at the back of the Tellus turbine nacelle. One of the Nordtank lidars is directed towards the incoming wind, whereas the second one, installed on a platform on the back of the nacelle, sensed the velocity in the wake. All lidars and met. mast sensors are time synchronized using a time stamp delivered by the DTU Wind Energy server. In a merged wake event, occurring for an inflow direction close or equal to 197°, the Tellus lidar perform recordings of the so-called *reference wake affected inflow (RW)* advecting downstream towards the Nordtank turbine. Accordingly, the downstream scanning Nordtank WindScanner measures the wind speed within the so-called *merged (double) wake (DW)*.

The measurement campaign took place from October 2012 to the end of May 2013. The first four months were dedicated to testing of the lidar equipment. During this phase, the lidars were not operating continuously and not simultaneously. Several technical problems with the downwind scanning lidar systems delayed the beginning of the merged wake measurements phase to mid-February 2013. The failures on the Nordtank wake lidar were mainly occurring on the moving mechanism under high duress due to the very high speed of the scanner. Other failures occurred on the Tellus wake lidar, where deteriorated optical cables needed to be replaced. Finally, some of the Nordtank turbine related operational sensors were malfunctioning or upgraded during the testing phase. In total, about 10 major maintenance operations were needed in the testing phase, revealing the challenge faced by the technicians to operate this ambitious experiment. This resulted in the collection of approximately 1600 10 min time series where both wake lidar are fully operating. However, due to the low occurrence of southerly wind, only about 2 hours of merged wake event were recorded.

5.6.3 The remote sensing devices

5.6.3.1 The reference wake lidar

The reference wake lidar, mounted on a small platform on the back of the Tellus nacelle as depicted in Fig. 5.14a, has a set-up as described by Bingöl et al. [18]. It is a Continuous Wave (CW) lidar built from a copy of the first prototype of the ZephIR instrument manufactured for DTU by QinetiQ in 2004. Initially designed for vertical scanning focusing between 10 and 200 m, the equipment went through several hardware upgrades in 2005 to adapt it to line-of-sight projected wind velocity measurements in a 2D scan plane. Each

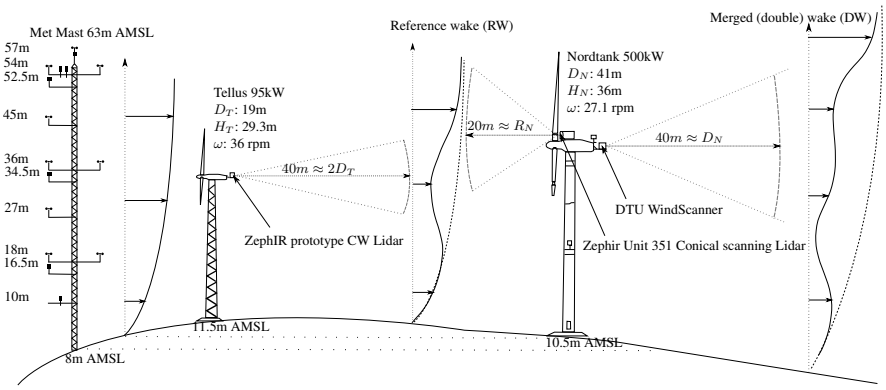

Figure 5.13: Principle sketch of the experimental set-up in a merged wake event, where the inflow wind comes from the left side (southerly winds). The met. mast is, in this sketch, located to the left of the Tellus for the sake of clarity, which differs from its real location to the west of the Nordtank turbine, as seen in Fig. 5.12. The spatial locations of the lidar recordings, lying along an arc in this 2D representation,represents a typical focus distance set-up for merged wake recordings. D_T, D_N and R_N denotes the diameter and radius of the Tellus and Nordtank turbine, respectively. *AMSL* denotes "above mean sea level".

line-of-sight projected wind speed is obtained from a centroid peak detection technique [21], applied to the mean Doppler spectrum obtained from the averaging of 256 individual spectra. The quality of the reference wake lidar has been assessed by Branlard et al. [21] and Smith et al. [133] by measuring vertical wind profiles and documenting good agreement with corresponding Risø cup anemometer measurements. In [133], the correlation coefficient ranged from 0.96 at 40 m to 0.98 at 100 m above ground.

The prototype ZephIR has an optical wedge which, associated with an oscillating mechanism, generates a vertical movement of the lidar beam. This tilting movement is in turn combined with a mechanically generated panning movement. The whole system is installed on the back of the turbine nacelle thus allowing for 2D cross sectional scanning of the Tellus turbine rotor wake.

For this campaign, the half-opening angle of the pan mechanism θ_p, defined as the lateral movement on each side of the axis center, was set to 25.8°, whereas the half opening angle of the tilt displacement is $\theta_t = 8.2°$. The prototype lidar sampling rate of wind speeds were 348 samples/s, and since the focus distance was kept constant the scanning pattern followed a *sphere scan mode* [18, 83], which corresponds to a small patch of a spherical surface. As motivated in [83], we presently assume that spherical effect is not significant and that its effect is taken into account in the line-of-sight projection technique described in Sec. 5.7.1.1. A typical scanning pattern is illustrated in Fig. 5.14b and presents a spatial distribution of measurement points that is intended for a fairly accurate reconstruction of a complete 2D cross section of the "quasi-instantaneous" flow field.

The speed of the lateral beam movements defines the *sweep time*, i.e. the time required

for the mechanism to complete a 2D scan. For the present measurement campaign, the sweep time was approximately 6 seconds, thus giving about 100 2D cross sectional scans for a 10 minutes time series. Furthermore, a technical problem, with the wedge translation mechanism, which is responsible for the tilting of the beam, occurred in the middle of the merged wake campaign and was unfortunately not detected before the measurement campaign finished. This caused the tilting movement to be several times slower than the design speed and as depicted in Fig. 5.14b lowered the spatial resolution significantly. Whereas the intended configuration gives around 15 tilting cycles per lidar sweep, only one cycle is observed in the faulty mode. However, the data sampling rate was not affected by the technical problem with the mechanical scanner motion and because the scanning pattern continuously change from one sweep to another, the faulty scan pattern was still capable of covering a fair extent of the wake when more than one lidar sweep were considered, as shown in Fig. 5.14b. The consequence of using several lidar sweeps and thus a longer scan averaging period for resolving the quasi-instantaneous wake profile is investigated in section 5.7.3.

(a) The prototype ZephIR lidar

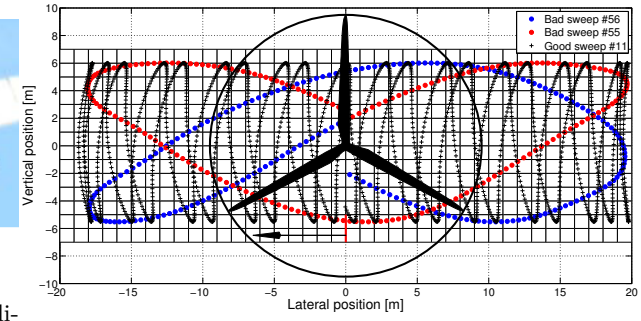

(b) Scanning patterns.

Figure 5.14: (a) Photo of Tellus prototype ZephIR lidar, taken from an earlier experiment [18]. (b) Sketch of the lidar measuring pattern for a focus distance of 40 m ($\approx 2D_T$). The blue and red dots are two consecutive faulty scanning patterns where one every 10 recordings are shown. The black crosses show all measurements location obtained from the standard pattern. The arrow represent the location of a lidar sweep start. The background grid is used to discretize the wake line-of-sight projected wind speed.

5.6.3.2 The forward scanning lidar

The lidar Unit 351 is a prototype ZephIR Dual Mode (DM) CW lidar. The standard ZephIR DM operates a single beam-diverting rotating prism that scans the lidar beam around a conical scan pattern. In this experiment, it was mounted on the top of the Nordtank turbine nacelle at a height of 37.5 m AMSL (above sea level) and scans the incoming wind through the rotor, as shown in Figs. 5.15a and 5.15b. The delay of acqui-

sition between two averaged spectra is 20.48 ms, giving a 48.8 Hz line-of-sight wind speed assessments on the conically scanned circle. As a result approximately 49 measurements of the line-of-sight projected wind speed is measured per full revolution cone scan every second. The wind speed estimation is performed using the proprietary ZephIR program Waltz and is based on a large number of collected spectra (typically 4000 spectra per wind estimation). A complete description of the Continuous Wave ZephIR conical lidar and the post processing algorithms is provided in the Chapter 4 of Peña et al. [104].

For this experiment, the forward scanning lidar was operated with two standard configurations: 20 m and 91 m constant set focus distance, respectively. The first set-up was used during merged wake events, in order to provide redundant measurements on the reference wake. The second focus distance was used for validation, where a direct comparison with the met. mast measurement is facilitated.

As part of the data analysis, a sanity check based on two datasets of moderate and high mean wind speeds is conducted. The comparison showed good agreement between the mean wind profile obtained from the met. mast and the forward scanning lidar, as depicted in 5.15c.

(a) Front view **(b)** Top view **(c)** Forward scanning validation

Figure 5.15: (a) - (b) Photo of the ZephIR 351 Unit mounted on the top of the Nordtank nacelle while conically scanning forward through the rotor. The aerial film drone photos are taken by Rune Mikkelsen (OpenHouse.dk). (c) Comparison of the average lidar wind profile of two 10 minutes average datasets (low and high mean wind speed) against the cup anemometers measurement mounted on the met. mast. The gray dots represent the line-of-sight recordings filtered from blade detection. The projected streamwise velocity is obtained from the technique described subsequently in Eq. 5.11 and developed in [83].

5.6.3.3 The merged wake lidar.

In order to capture the merged wake characteristics with high detail, a newly developed prototype lidar with a high spatial and temporal resolution is mounted on a platform

extending from the back of the Nordtank 500kW nacelle. The so called "spinner lidar", is a new 2D scanning device developed by DTU Wind Energy in collaboration with ZephIR. It includes two rotating prisms with a fixed ratio of the rotation speeds integrated on the top of a modified ZephIR 300 CW coherent Doppler lidar, [130].

A selectable rate of up to 500 measurements per second is achievable with the current set-up. For the major part of the campaign, the adjustable scanning speed was set so that a complete two-dimensional scan pattern (or *lidar sweep*) is achieved in only 2 seconds corresponding to a rate of 312.5 measurements per second. In this way, the lidar operates at a very high speed while still operating far from its design limits to allow for long term recordings and reduce over-heating risks. The fastest configuration was tested for a short period at the end of the campaign to provide high spatial and time resolved single wake measurements.

The selected scanning pattern is an optimized distribution of points in space for wake measurements. It is obtained from the two rotating prisms that deflect the laser beam direction by 15° each, resulting in a full opening angle θ_s of 60°. Similarly to the reference wake lidar, the obtained scanning geometry is a spherical patch. An illustration of the 2D scanning pattern is shown in Fig. 5.16a, whereas an example of a 10 minutes average wake flow field is shown in Fig. 5.16b. The absolute measurement positions are calculated from the instantaneous positions of the two optical prisms.

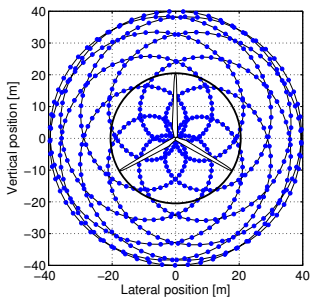

(a) The spinner lidar scanning pattern.

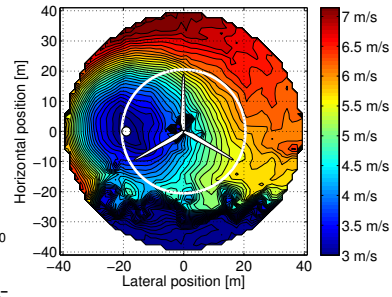

(b) Mean line-of-sight velocity

Figure 5.16: (a) Sketch of the wake lidar scanning pattern at a focus distance FC of approximately $2D_N$. (b) Example of 10 min average line-of-sight velocities in high yaw misalignment situation (−10°). The black areas at the center of the scanning area are disturbances caused by laser reflection of the incident beam by the exit window. The blue area in the bottom are low wind speeds recorded near the ground that are below 3 m/s. The black dot shows the mean wake center (y=-19 m, x=0 m). The "stairs" effect at the edge of the scanning domain is an artifact of the wake resolving procedure described in Sec. 5.7.1.1

.

5.7 Analysis of measurements

In a wind tunnel based experiment, the ambient conditions is carefully monitored and tailored to a specific test, in which all parameters related to the test section geometry are accurately characterized by means of high precision measuring equipment and thorough monitoring.

Such precise control of experimental conditions is not achievable in a full-scale experiment. Larger uncertainties are typically caused by the bigger experimental scale which relate to both geometrical (turbine separation, rotor diameter) and environmental (terrain, atmospheric turbulence, flow homogeneity and variability effects). It is critical to characterize these quantities as well as possible for subsequent numerical comparison with measurements.

In the present extensive campaign, the use of two turbines combined with a meteorological mast and 3 nacelle mounted remote sensing lidars present a challenge for estimating the key parameters characterizing a merged wake situation in both the fixed and the meandering frame of reference. These issues are addressed in the present section, after the description of the key lidar post processing techniques.

5.7.1 Lidar post processing techniques

5.7.1.1 Resolving the reference wake

In order to derive the unsteady wake from the reference lidar measurements, the quasi-instantaneous line-of-sight velocity in the wake is initially extracted. The quasi-instantaneous wake is defined as the collection of all individual recordings during one lidar sweep. A *lidar sweep* starts when the laser crosses the lateral center of the scanning region and stops the next time the laser crosses this origin in the same direction.

Thus, a short-term averaging is performed, where the recordings during one lidar sweep are assigned to one *wake slice* or snapshot of the unsteady wake as described by Machefaux et al. [82]. This method is only valid as long as the sweep time is small enough to ensure that individual measurements within a sweep are time correlated.

Once the wake slices are determined, the line-of-sight velocity field in the wake is discretized by representing lidar cross sectional recordings with a spatial resolution corresponding to non overlapping cells of $1 \times 1\ m^2$ for each lidar sweep as described by Machefaux et al. [83]. Subsequently, an interpolation method based on the Delaunay triangulation is used to interpolate linearly wind speeds in between the irregularly distributed measuring points of the lidar. This allows the reconstruction of a full 2D contour of the wake.

A robust filtering procedure is implemented at this stage of the data processing to discard erroneous wake tracking resulting from poor spectra quality, poor spatial coverage of the wake, ground or obstacle detection or other unwanted effects. This filtering is based on a plausibility check of the recorded line-of-sight velocities, e.g. wind speeds near or below zero, or very large outliers.

Finally, the line-of-sight velocities are projected on the main flow direction using the

approach described by Machefaux et al. [83]. This method assumes that, for moderate pan, θ_p, and tilt, θ_t, angles of the laser beam, the lateral and vertical wind components are much smaller than the streamwise one and that horizontal homogeneity is fulfilled. This is generally a valid assumption for atmospheric boundary layer flows. However, if the rotor is yawed, the lidar is not aligned with the mean wind direction, and the horizontal homogeneity assumption no longer applies. The mean yaw misalignment is therefore added as a fixed contribution to the pan angle in the projection. A similar correction is necessary to compensate for vertical misalignment between the ground and the zero tilt beam angle, thus:

$$U_{lidar}(t) = U_{los}(t) \cdot \frac{1}{\cos(\theta_p + \theta_{yaw}) \cos(\theta_t + \theta_{tilt})} \tag{5.11}$$

where θ_{yaw} is the yaw angle and θ_{tilt} is the angle between the zero tilt beam angle and the ground. The lidar scanning head was mounted parallel to the ground and therefore $\theta_{tilt} = 0^o$. As the Tellus turbine was not equipped with a yaw sensor, the estimation of the turbine yaw misalignment is based on an empirical model as described in section 5.7.2.

5.7.1.2 Forward scanning lidar blade passage filtering

As the recording of the incoming wind is performed through the Nordtank rotor, frequent signal distortion caused by blade passage occurs. Fig. 5.17a shows the power spectrum of the line-of-sight velocity measured during a 10 minutes time series. Several distinct peaks corresponding to 3P/2, 3P and their higher harmonics are observed. The dominant peak is obtained at a frequency corresponding to 3P/2, meaning that blade detection may not occur at every blade passage as initially anticipated. While this remain under investigation, it is speculated that the continuous change of co- and counter rotating motion of the lidar beam relative to the blades motion may result in situation where blade are not detected by the lidar, specifically in counter rotating situations where the relative velocity of the two motions is very high. For this reason, the recordings of the blade passage are filtered out in the time domain instead.

To do this a simple geometrical model is used as sketched in Fig. 5.17b. This model assumes that the rotational movement of the cylindrical hub extender of diameter $D = 1\ m$ can simplistically be represented as the translation of three cylinder elements passing the laser beam at a constant time interval. The velocity of this translation is easily determined from the constant rotor rotational speed ω and the distance from the rotational axis r as: $V = r\omega$. The distance of the lidar horizontal axis to the rotor rotational axis and the distance from the laser output to the cylinder surface have been estimated from the photographies of the experimental setup to be $r = 1.5$ m and $s = 0.5$ m, respectively.

In Fig. 5.18, the line-of-sight velocities are plotted against the phase angle ϕ of the conical lidar in both linear and polar representation, indicating that the vertical position of the beam pointing upwards is obtained at a beam phase of 0°. From [97] and [11], the expression of the line-of-sight velocity from a spinner mounted wind lidar in the frame of reference aligned with the wind turbine's axis of rotation, neglecting yaw and tilt, is given as:

$$U_{LOS} = u_x \cos\theta_c + u_y \sin\theta_c \sin\phi + u_z \sin\theta_c \cos\phi \tag{5.12}$$

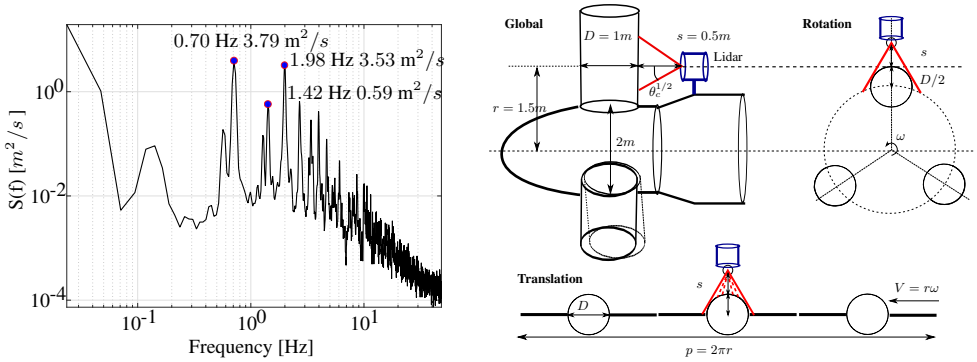

(a) Power spectrum of the raw line-of-sight velocity for a 10 min dataset.

(b) Sketch of the blade detection geometrical model

Figure 5.17: (a) Power spectrum of the raw line-of-sight velocity signal for a time series corresponding to a focus distance of 91 m. The peak with the largest energy content at a frequency of 0.69 Hz corresponds to the 3P/2 frequency. Several higher harmonics are observed. (b) Sketch of the geometrical model for blade detection. The red dashed lines indicates different angles at which the laser hit the moving blade.

where (u_x,u_y,u_z) are the wind components of the instantaneous wind vector, assuming the mean wind to be aligned along the x-axis, θ_c is the lidar off axis deflection angle and equal to 30.4°. Following the assumptions of the simplistic geometrical model, the streamwise and vertical component of the blade motion are assumed to be zero, thus Eq. 5.12 gives:

$$U_{blade} = |r\omega \sin\theta_c \sin\phi| \tag{5.13}$$

This function is show in red in Fig. 5.18a. As a result, all line-of-sight velocities satisfying this equation are discarded.

5.7.1.3 Velocity estimation of the merged wake lidar

The line-of-sight velocities are estimated from the collected Doppler spectra using a median frequency estimator approach, as described in [10]. In this approach, the frequency of the Doppler shift is found by determining and removing the cumulative backscatter signal of the instantaneous spectra and then calculating the median of the obtained distribution. This method is particularly robust when Doppler spectra display two closely spaced peaks, or when the spectral width is large and asymmetric. This is often the case for nacelle based wake measurements, as the turbulence is typically 2 to 3 times higher than for the undisturbed flow, which in turn substantially increase the width of the Doppler spectral peak.

Before applying the median frequency approach, the background noise of the spectra is first eliminated by subtracting the mean noise from the raw signal. This increases the reliability of the median frequency estimator, as only the main Doppler shift peak is left

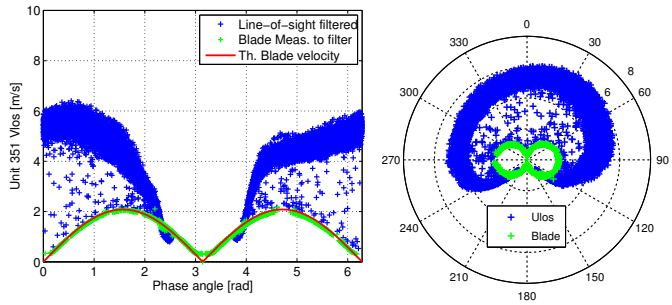

(a) Line-of-sight function of phase angle

(b) Polar plot representation

Figure 5.18: (a) Line-of-sight velocity distribution for a 10 min time series with a scanning range of 91 m as function of the lidar phase angle. The blade detection function is shown in red. A small tolerance is applied to the filter. (b) Corresponding polar plot. The green points are measurements of the blade passage, whereas the blue points are valid line of sight velocities.

in the spectra, and all the other frequencies are zero. An additional filtering is applied to the low frequency part of the spectra, where residual peaks are often present due to ground detection. This can also be seen in the lower part of Fig. 5.16b.

After having determined the line-of-sight velocity the unsteady wake flow field is extracted following the same short term averaging procedure as described in section 5.7.1.1.

5.7.2 Quantification of rotor yaw misalignments

A preliminary inspection of the mean wake profile, as based on a large number of time series, indicated that the reference wake was always displaced to the left in the scanning domain. As this occured systematically, it was conjectured that this was either the consequence of a lidar mounting misalignment (i.e. a constant offset angle between the lidar zero pan angle and the normal direction to the rotor), or a systematic yaw misalignment of the turbine.

In order to investigate this, the wake skew angle χ, defined in Fig. 5.19a, was extracted from the reference lidar measurements. Fig. 5.19b shows the 10 minute averaged χ angle measured at a focus length of $2D_T$ and $3D_T$, respectively, for 330 non continuous datasets obtained throughout the campaign. The mean and standard deviation of the 10-minute χ time series is fairly invariant to focus distance and is 9.3° and 2°, respectively. The most plausible cause for such large skew angles is a systematic turbine yaw misalignment, as the typical mounting precision of the lidar system is in the order of 2°. This assumption was further reinforced by a post campaign inspection of the Tellus and Nordtank rotors for easterly and westerly winds. A clear non parallel behavior was observed between the two rotors well above the wind veer magnitude. It is further speculated that this large yaw misalignment may be caused by the miscalibration of the wind vane connected to the

turbine controller, which in turn assign the rotor azimuthal position. Based on the above condiderations and the fact that no specific information about the lidar mounting error is available, we assume that the mounting errors of all three lidars is zero.

To overcome the lack of an absolute rotor yaw position sensor on the Tellus turbine, the

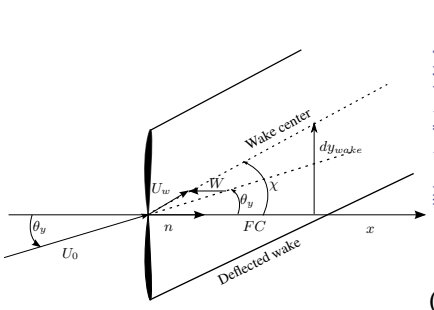

(a) Sketch of a skewed wake.

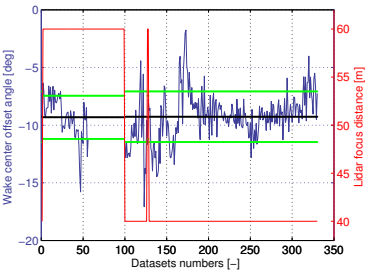

(b) Mean wake skew angle function of FC

Figure 5.19: (a) Sketch of the Tellus rotor in a pronounced yaw. The angle of the deflected wake χ is larger than the inflow yaw angle. The measured lateral wake center displacement dy_{wake} at a given focus distance FC is indicated, together with the normal to the rotor plane n, the mean free stream velocity U_0 and the induced velocity in the wake W. (b) Investigation of the mean skew angle evolution throughout the campaign, performed on 330 10 minutes datasets. The mean skew angle (black curve) appears constant and equal to $-9.26°$ and $-9.31°$ for focus distances of 2D and 3D respectively (green curves). The standard deviation (green lines) of the skew angle also remains constant with respect to the focus distance (red curve) and approximately equal to $2°$.

yaw misalignment is directly estimated from the measured wake skew angle and the thrust coefficient of the rotor using the following result from a theoretical vortex cylinder model [22, 31] combined with investigations by Micallef et al.[90].

$$\chi_{(N,T)} = (0.3C_T + 1)\theta_{y(N,T)} \tag{5.14}$$

where subscripts N and T denote the Nordtank and Tellus turbine. For simplicity, the wake skew angle is assumed constant during the investigated 10-minute periods, and the wake expansion is neglected. The thrust coefficient, C_T, in Eq. 5.14 is computed using a BEM model with 3D tabulated airfoil data of the LM 9.5 m blade.

The validity of the present wake skew angle model in Eq. 5.14 is assessed by applying it to lidar measurements in the wake of the Nordtank turbine and then compare its prediction with the yaw misalignment measured by subtracting the mean rotor yaw position from the mean inflow direction. The dataset used for the validation is the one shown in Fig. 5.16b where a clear wake displacement is observed. The mean wake skewness angle χ_n in Fig. 5.16b is measured to be $\chi_n = -8.46°$, which using Eq. 5.14 gives a yaw angle of $\theta_{yN} = -7.0°$, whereas the directly measured yaw misalignment is $\theta_{yN} = -7.25°$. This

good agreement is repeatedly observed on consecutive datasets, thus validating the present model approach, and at the same time giving sanity of the Nordtank yaw sensor.

5.7.3 Resolving the wake in the meandering frame of reference

In the present study, the wake is resolved in both the nacelle frame of reference (or fixed frame or reference, *FFoR*, assuming no yawing activity in the observation period) and in the meandering frame of reference (*MFoR*). The *MFoR* of the wake follows the center of the wake as it is transported downstream [71]. In order to determine the *MFoR*, a bivariate 2D Gaussian function is fitted to each of the quasi-instantaneous wake slices as described by [152]. However, the quality of the fit depends on how well the quasi-instantaneous wake is resolved by the lidar. In practice it was found that more than one lidar sweep was sometimes necessary to achieve a robust fit especially for the reference lidar after the tilting mechanism failure occurred. However, increasing the number of lidar sweeps used for reconstructing the quasi-instantaneous wake results in an increasingly diffused wake due to large scale wake meandering. The optimal number of sweeps used for the reconstruction is the one where the Gaussian fit yields the most distinct wake, i.e. the deepest and narrowest quasi-instantaneous wake deficit. This is one of the theoretical consequences results from the Dynamic Wake Meandering (DWM) framework [71].
Fig. 5.20a shows the mean normalized maximum velocity deficit in the *MFoR* as a function of the averaging time used for reconstructing the individual wake slices. Additionally, the wake width metric, obtained from the σ_y quantity of the bivariate 2D Gaussian function part of the wake center tracking algorithm, is shown in Fig. 5.20b. The shown curves are based on two 10 minute datasets at similar ambient conditions, and all results are normalized with respect to the value when using only one lidar sweep.
Note that the scatter of the mean profiles in the *MFoR* typically increases when increasing the number of sweeps used for reconstructing each wake slice, because the number of wake slice samples within the 10 minute dataset is then reduced.
From Figs. 5.20a and 5.20b it appears that a scan averaging time of $T = 2\ s$ (1 sweep) best characterize the quasi-instantaneous wake profile of the Nordtank turbine, whereas the corresponding optimal averaging times for the Tellus wake lidar during the design and faulty mode is $T = 12\ s$ (2 sweeps) and $T = 24\ s$ (4 sweeps), respectively.

The identified averaging periods defines the best possible time increments between each wake slice in this experiment. However, in order to facilitate cross-correlation studies between the two type of lidars the temporal resolution of the reference lidar tracking analysis was increased to 2 s. This is achieved by decomposing the 10 min lidar time series into sets of overlapping records defined by a time increment of 2 s and a time span equal to the identified optimal averaging period. The unsteady wake in both the FFoR and the MFoR is then determined for each of these overlapping segments of data.

As argued by Larsen et al. [71], the idealized cut-off frequency, where the split between the large (responsible of meandering) and the small (diffusive) turbulence scales, may be defined as $fc = U/2D_w$, where D_w denotes the instantaneous wake deficit diameter, and U is the mean hub height wind speed.

A relevant validation of the present *MFoR* characterization is to perform a spectral analysis of the meandering paths (i.e. wake center) and observe whether the high energy content

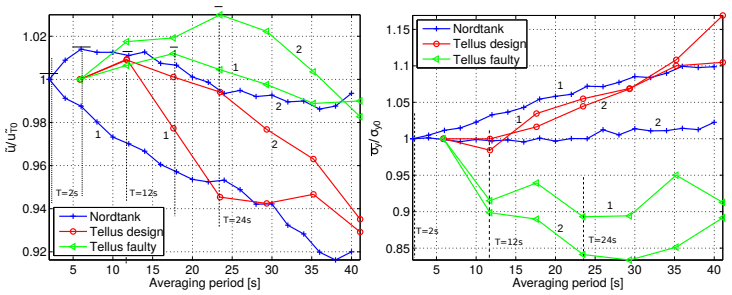

(a) Maximum wake deficit **(b)** Wake width

Figure 5.20: Investigation of the maximum wake deficit (a) and the corresponding wake width (b) as function of the lidar averaging period for both the *reference wake* and *merged wake* lidars. The averaging period giving the deepest and narrowest wake profile is shown in black vertical dashes. Each configuration has two curves corresponding to the two tested time series, labeled 1 and 2.

of the spectra is observed at frequencies lower than f_c. This analysis is conducted on the same datasets as used for Fig. 5.20.

Results of the spectral analysis is shown in Fig. 5.21. It is seen in Fig. 5.21 that the conjectured cut-off frequency associated with the spectra of the Nordtank wake meandering paths (blue curve) delimits well the high and the low energy regimes of the meandering power spectrum. This is not seen in the spectra of the Tellus meandering paths, as the energy has decreased of a factor of 100 when reaching the conjectured cut-off frequency. This is because the reference lidar measurements of the wake effectively have been filtered using a moving window of $T = 12$ s and $T = 24$ s, respectively. This corresponds to effective Nyquist frequencies of approximately 0.04 Hz and 0.02 Hz respectively, which are both larger than the conjectured cut-off frequency for the Tellus turbine. This is however the best possible approach given the technical limitations of the present experiment.

5.7.4 Merged wake test case definition

In this section, a merged wake test case is selected from the campaign using a specific set of criteria. The turbine positions and yaw orientation with respect to the incoming wind are determined using the techniques introduced in the previous section. The relative lateral displacement of the two rotors is determined through a spatial correlation study making use of both the forward scanning and the reference (ZephIR) wake lidar.

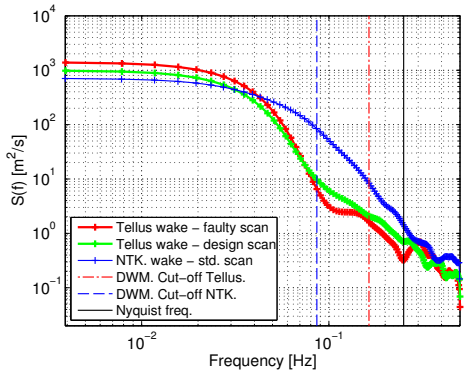

Figure 5.21: Power spectrum of the lateral wake center position. The scan period T is chosen based on the results shown in Fig. 5.20 for the faulty and the design scanning mode of the Tellus wake lidar. The smooth spectra are obtained from windowing of the raw signal. Each time series is divided into 12 equal size consecutive windows, and the presented spectra is the average of the resulting 12 individual spectra. Both the Nyquist frequency and the theoretical DWM cut-off frequency are shown.

5.7.4.1 Selection criteria

During the recording phase of the campaign, more than 28 days of valid measurements were collected where both wake lidar were operating simultaneously. A simple tool is developed to extract possible candidates for a merging wake analysis. The main selection criteria are based on the operational condition of the instrumented downwind Nordtank turbine, and the ambient conditions at the recorded mast.

Firstly, the mean inflow direction measured at the met. mast by the sonic at 34.5 m a.g.l. (above ground level) should be contained between $\pm 15°$ of the theoretical turbine alignment of 197°. Furthermore, the measured rotational speed of the generator should not drop below 1495 RPM, ensuring that no generator decoupling occurs within the 10 minutes period, i.e. the turbine is in full operation. Additionally, a visual inspection of the presence of a reference wake from the Tellus turbine is required to ensure that the non instrumented Tellus rotor is in operation. Finally, at least 90% of the total amount of velocities recorded by the lidars should remain available after filtering. Lower availability are often due to heavy rain or snow conditions, or when the laser is frequently pointed towards a moving obstacle. Applying the preceding set of criteria, approximately 2 hours of merged wake recordings from southerly winds are obtained.

The use of two turbines of different size introduce asymmetries in the test. The reference wake, typically half the size of the Nordtank rotor, causes a situation of partial wake inflow and induced yawing due to a strong azimuthal asymmetry of the incoming flow field downstream to the wind turbine. Therefore, the Nordtank rotor is most of the time operating in yaw when it is in the wake of the Tellus turbine. Furthermore, it was previously observed that the Tellus constantly operates in yaw throughout the campaign, therefore increasing the asymmetry and complexity of the overall test.

Another source of uncertainty originates from the two rotor alignments with the incoming wind. The selection of a dataset associated with a mean wind direction close to 197° (i.e. the theoretical alignment) and based on the sonic recordings at 34.5 m may not guarantee a perfect alignment of the two turbines due to wind directional uncertainties. However, a correlation analysis, based on the use of the forward conical lidar and the reference wake lidar, can as mentioned improve considerably the estimation of the relative lateral turbine displacement δ_l, as discussed subsequently.

A dataset with a mean inflow direction of 191° is selected from the database following the previous acceptance criteria. The mean wind speed measured at 34.5 m a.g.l. is 7.1 m/s, and the streamwise turbulence level of the incoming wind is 14.5%. The atmospheric stability, determined from the Obukhov length at 16.5 m a.g.l., is near neutral, slightly on the stable side. A sketch of this merged wake situation seen from above with all relevant parameters is illustrated in Fig. 5.22. The yaw of the Nordtank, θ_{yN}, and the Tellus, θ_{yT}, determined from the wake skew angle model, are equal to 6° and −10°, respectively. In the same figure, the coordinate systems specific to each lidar is indicated. The idealized deflected wake boundaries and wake centre are drawn, together with the scanning regime of all 3 lidars.

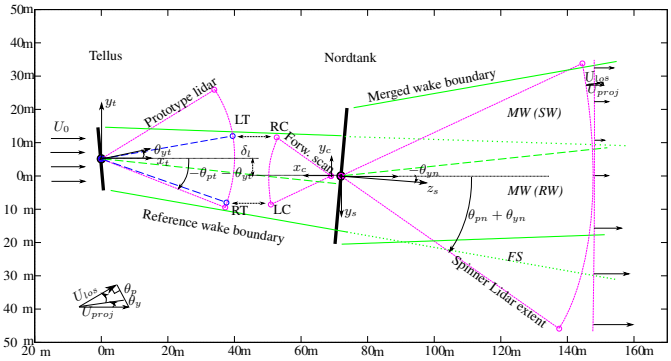

Figure 5.22: Sketch of the selected merged wake event seen from above. The Tellus turbine is yawed positively ($\theta_{yT} = 6°$), whereas the Nordtank rotor is yawed negatively ($\theta_{yN} = -10°$) due to the imposed partial wake situation. The deflected wake boundaries are shown in green, whereas the lidar scanning boundaries are indicated in pink. The coordinate system associated with each lidar is also indicated. Further, the projection from line-of-sight to streamwise component is sketched. DW refers to as double wake, SW refers to single wake, RW denotes reference (or inflow); FS denotes free stream.

5.7.4.2 Estimation of the rotors lateral spacing

The lateral rotor spacing (δ_l as sketched in Fig. 5.22) is another quantity that needs to be determined from the experiment. A rough estimate of δ_l can be found by applying simple trigonometry on the velocity triangle composed by the mean wind direction from the sonic anemometer at hub height and the perfect turbine alignment angle. This estimation may,

however, be biased by strong wind veer across the different turbine hub heights.

A more robust approach is based on a spatial correlation analysis making use of both the Tellus wake lidar and the Nordtank forward scanning lidar. This approach is illustrated in Fig. 5.23a, where the location of the lidars overlapping/redundant measurement points seen from upstream are shown. This overlapping area is constituted by two arcs resulting from the conical forward scanning. A so-called overlapping grid, with a cell width equal to 1 m and a cell height of 0.5 m, is defined around the two arcs.

The cell averaged stream wise velocity is compared between both lidar recordings for each pair of overlapping grid cells (from the left and right arc), at different heights h conditioned on the lateral displacement δ_x. The objective is to minimize the velocity difference metric, denoted $P_n(\delta_x)$, which is defined by:

$$P_n = \sum_{i=1}^{N} [|U_{l,RW}(i) - U_{l,FW}(i)| + |U_{r,RW}(i) - U_{r,FW}(i)|] \tag{5.15}$$

where the subscript l and r denote left and right arc respectively, RW and FW refer to "reference wake" and "forward wake", and i is a counter corresponding to measuring heights between h_0 and H (i.e. the lower and upper vertical position of the overlapping grid).

Minimizing the metric P_n gives the best possible estimate of the rotor lateral displacement, thus $\delta_l = min(P_n)$. For the previously selected dataset, it is found as $\delta_l = 6.5$ m.

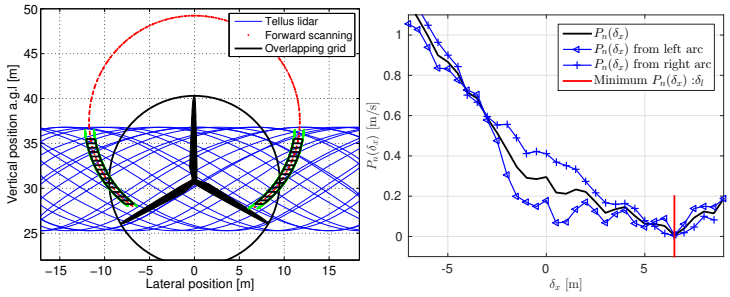

(a) Overlapping scanning area (upstream)

(b) Lateral displacement investigation

Figure 5.23: (a) Upstream view of the overlapping scanning area from the conical forward scanning lidar and the cross sectional reference wake lidar. Only the lower part of the conical scanning lidar overlaps the reference wake lidar scanning due to the hub height difference between the Tellus and the Nordtank turbine. $P_n(\delta_x)$ as function of the lateral displacement of the reference measured profile.

5.8 Numerical simulations

In this section, the numerical simulations used for comparing with the measurements are described.

5.8.1 Numerical methods

The simulations were conducted using the incompressible Navier-Stokes solver EllipSys3D [92, 93, 135] and combines Large Eddy Simulations (LES) of the flow field with actuator disc modelling of the rotors. The atmospheric turbulence is modelled using the method presented by Troldborg et al. [151], where pre-generated turbulence is inserted in a cross-section upstream of the rotors. The used actuator disc model is based on the actuator shape model [116] combined with a blade element approach, where the aerodynamic loading is determined from the local flow conditions at the disc and 3D corrected aerofoil data as described by Réthoré et al. [119]. The LES model uses a sub grid scale model developed by Ta Phuoc [141], and the used solver parameters are identical to previous work [81, 83, 150].

5.8.2 Computational meshes

The simulations are carried out in a regular Cartesian mesh of dimensions ($L_x = 20D_N$, $L_y = 14D_N$, $L_z = 14D_N$) where x, y and z denotes the streamwise, lateral and vertical coordinates, respectively, and D_N denotes the Nordtank turbine rotor diameter. The grid layout and the boundary conditions are in accordance with previous studies [150, 83]. The boundary conditions are as follows: Dirichlet conditions at the inlet and upper boundary ($x = 0$ and $z = 14D_N$), Neumann conditions at the outlet ($x = 20D_N$), symmetry condition at the bottom ($z = 0$) and cyclic boundary conditions on the sides ($y = 0$ and $y = 14D_N$).

In the region around and downstream of the rotors the grid spacing is equivalent to $dx = D_N/60$ in the lateral and vertical direction and $dz = D_N/39$ in the stream-wise direction. The cells are stretched away from the wake region towards the domain boundaries, resulting in a total number of cells of 19.9 millions inside the domain.
Each actuator disc is represented with a separate 2D polar grid with 94 radial and 180 angular elements.

5.8.3 Inflow boundary conditions

The mean inflow used in the simulations was specified to follow a logarithmic profile:

$$U = \frac{u_*}{\kappa} \ln(z/z_0) \tag{5.16}$$

where the roughness length z_0 is determined from the turbulence intensity TI_u measured by the sonic at 16.5 a.g.l. assuming the following empirical expression [102]:

$$TI_u \approx \frac{1}{\ln(z/z_0)} \tag{5.17}$$

The friction velocity u_* is subsequently determined through a least square fit of Eq. 5.16 to the mean velocity profile measured by the cup and sonic anemometers as well as the wake lidars. Note that the shear profile measured by the lidars was obtained by averaging measurements in vertical bands of 3 m in order to reduce scatter. Fig. 5.24a compares the fitted mean velocity profile used for the simulations with the measured profiles and shows that the agreement is good.
The turbulence used in the simulations was generated using the Mann turbulence generator [88], which is based on a model of the spectral tensor. In the present work, the parameters describing the spectral tensor were determined by fitting it to the measured spectral characteristics obtained at the site during the campaign. Fig. 5.24b compares the measured and fitted spectra. Generally, the agreement is good, but there are some differences, which are mainly due to the assumption of neutral stratification in the Mann algorithm. Since the turbulence generated with the Mann generator is not in balance with the flow in which it is inserted, it will be distorted by the Navier-Stokes solver and to compensate for this it is therefore amplified before inserted at the turbulence plane.

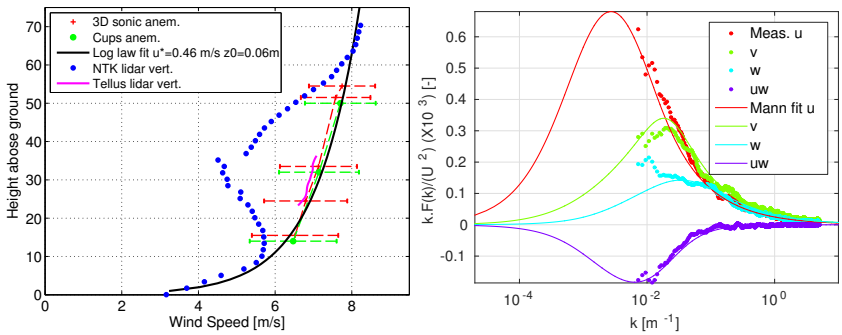

(a) Inflow logarithmic profile. **(b)** Mann model fit to meas. spectra.

Figure 5.24: (a) Logarithmic inflow profile determination using an empirical roughness length and a best fit with the measured sheared profile by the lidars, the cup and the sonic anemometers. (b) Average $u-$, $v-$ and $w-$ spectral components, and the uw co spectrum at 34.5 m a.g.l. extracted from the 3D sonic anemometer during the 10 min selected merged wake case. Full lines are the corresponding Mann model fits. The three obtained model parameters are $\alpha\epsilon^{2/3} = 0.0077m^{4/3}s^{-2}$, $\Gamma = 4.47$ and $L = 61.74m$.

5.9 Results

The present full-scale experimental approach and its subsequent analysis is mutually validated with the EllipSys3D flow solver using the previously described computational set-up. The organized flow structure of the wake, characterized by its deficit and turbulence characteristics is firstly investigated. Finally, the simulated power production and thrust force are compared to the available turbine measurements.

5.9.1 Normalized wake velocity and added streamwise wake turbulence

In Fig. 5.25, the measured normalized wake velocity deficit, defined as the 10 min average wake velocity divided by the mean free stream velocity at hub height U_0, is compared to results from the CFD computations. The comparison is conducted for both the horizontal wake profile at hub height and the vertical profile along the rotor center position.

This analysis is performed for both the *MFoR* and the *FFoR*. Error bars, corresponding to $\pm 1\sigma$ (σ is the standard deviation of the velocity) are added to the measured profile in the *FFoR*. A good agreement is observed for both the reference and the merged wake profiles in Fig. 5.25a and in Fig. 5.25d, respectively. As expected, the wake resolved in the *MFoR* displays a narrower and deeper deficit than the wake deficit resolved in the *FFoR*. Furthermore, the horizontal profiles displays an asymmetric trend due to the simulated yaw misalignment.

Discrepancies in the vertical profile (Fig. 5.25b and in Fig. 5.25e) of the merged wake are observed near the ground. They are a consequence of the no slip wall modeling in the simulations as opposed to the rough wall in the full-scale measurements. As a consequence, speed up effects are seen in down stream cross sections outside the wake affected regime. This does not influence the quality of prediction in the wake region. The inflow mean wind speed profile for the CFD computations is shown in Fig. 5.24(a), where the mean wind speed comes close to zero near the ground. The so-called *wake turbulence factor*, defined as the ratio between the streamwise turbulence intensity in the wake divided by the mean inflow turbulence intensity, is presently investigated. The streamwise turbulence $\tilde{TI}_u$ is defined as $\sqrt{\overline{u'^2}}/U_0$ where u' represents the fluctuating wake velocity. To facilitate the comparison with the lidar measurements, the fluctuating wake velocities from the simulation are extracted at the same frequency as the one the scanning lidars perform, which reduces the variance of the simulated turbulence but improve the consistency of the comparison. In this approach, the lidar measurements are not corrected for volume averaging effects. Results of the comparison is shown in Fig. 5.25c and in Fig. 5.25f for the *FFoR*. It is seen that the *wake turbulence factor* is in good agreement with both the magnitude and the width of the *merged wake* in the limited lidar-resolved region, but slightly less convincing for the *reference wake*, where the CFD predicts lower turbulence factors.

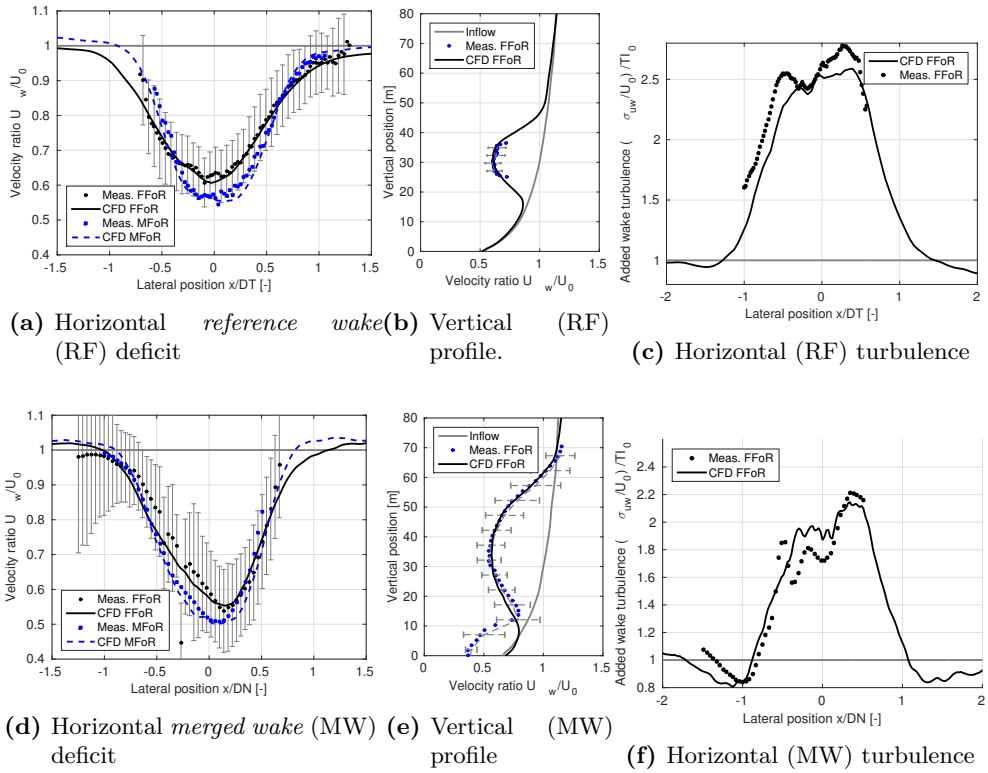

(a) Horizontal *reference wake* (RF) deficit

(b) Vertical (RF) profile.

(c) Horizontal (RF) turbulence

(d) Horizontal *merged wake* (MW) deficit

(e) Vertical (MW) profile

(f) Horizontal (MW) turbulence

Figure 5.25: Comparison between lidar measured and simulated wake profiles for the selected merged wake case in both the *MFoR* (blue dots and lines) and the *FFoR* (black dots and lines). Profiles are extracted at 2 D_T and 2 D_N, from the upstream Tellus turbine and the downstream Nordtank turbine, respectively. Error bars representing the uncertainty on the mean value $\pm 1\sigma/\sqrt{n}$ are indicated in gray for the *FFoR* measured profile. The inflow profiles in (b) and (e) refer to the downstream wind profile outside the wake regime.

5.9.2 Mean power and thrust

The simulated 10 min average mechanical power produced as well as the thrust force are compared to the measurements from the instrumented Nordtank turbine. The electrical power was measured at the generator, whereas the thrust force is derived from the tower bottom strain gauges measurement. According to the technical report of the Nordtank turbine [106], the typical loss from mechanical to electrical power is in the order of 7%. A similar loss is assumed for the Tellus turbine. Results are summarized in Table 5.4.

It is seen from Table 5.4 that the power production of the upstream Tellus turbine agrees well with both power and thrust derived from turbine specifications. For the downwind turbine, the CFD predictions are slightly overestimated in the order of 5 to 10 %. This discrepancies may be explained by uncertainties on the actual rotor yaw misalignment or the amplitude of the wake meandering of the upstream wake. The combined effect of yawed rotor and wake shadowing reduce the power produced of the Nordtank by 40% as compared to free stream velocity based power curve predictions at standard conditions.

Table 5.4: Comparison between simulated and measured power production and thrust force. All quantities are 10 min averages. The last column shows the design value extracted from the measured turbines power curve and thrust curve at standard condition. A BEM generated thrust curve is used for the Tellus turbine, due to the lack of turbine instrumentation.

	Simulated	Measured	Design
Nordtank Elec. power [kW]	86.0 kW	81.8 kW	137.2 kW
Thrust [kN]	28.9 kN	25.4 kN	31.9kN
Tellus Elec. power [kW]	26.2 kW	-	24.7 kW
Thrust [kN]	5.9 kN	-	6.8 kN

5.9.3 Wake accumulation in the double wake experiment

The present CFD model showed accurate prediction of the merged wake profile associated with the correct turbine loading and power production for the selected full-scale measurement time series. Thus, the model can be used to investigate the performance of state-of-the-art wake superposition models. This is done by decomposing the previous merged wake profile into 2 simulated single wake contributions: 1) the single wake (8D downstream) of the Tellus turbine; and 2) the stronger single wake (2D downstream) of the Nordtank turbine. Both contributions are extracted at the same downstream location as the measured merged wake profile, and simulations were performed under the same inflow and yawing conditions as the selected time series.

Four engineering wake superposition models are tested presently: 1) linear summation of deficits (*linear*); 2) Root-Sum-Square operator on the deficits (*RSS*); 3) the strongest (or maximum) wake deficit at a given downstream position which defines the accumulated wake (*maximum*), in [74]; and finally 4) the average results of method #1 and #2 (*ARL*). A complete overview of the wake flow model, typically associated with these accumulation models, is available in [115].

Results of benchmarking is shown in Fig. 5.26a. It is seen in Fig. 5.26a that the best

agreement between the simulated merged wake profile and the accumulated wake is using the *ARL* method. The linear summation of wake overestimates the deficit in the order of 15% at the wake center, whereas the use of the maximum (strongest) wake slightly underestimate the merged wake centerline deficit with about 8%. The good performance of the *ARL* method has been previously observed in the study in [43], where the Horns Rev wind farm wake loss estimated from SCADA data agrees well with the modeled wind farm wake loss obtained by combining the Ainslie eddy-viscosity wake model with the *ARL* overlapping wakes model. In the next section, a generic investigation of single wake summation techniques is performed for several turbine spacing, turbulence intensity and mean wind speed.

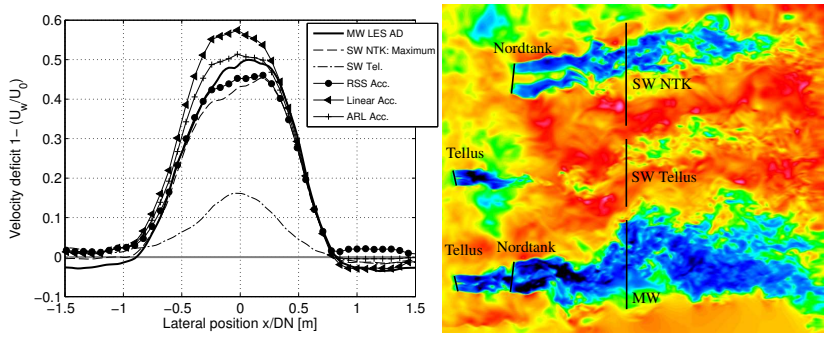

(a) Accumulation investigation **(b)** EllipSys3D LES computations

Figure 5.26: Benchmarking of four wake accumulation model. (b) Snapshot of the streamwise velocity component from the EllipSys 3D LES computation seen from above. Approximate location of the extraction plane and the rotors are shown in black lines. The contour plot was obtained from a slice at the Tellus hub height. The mean wind speed at the Nordtank hub height is 7.1 m/s.

5.10 Summary

In the present study, full-scale lidar based measurements of overlapping wakes generated by two aligned stall regulated turbines have been collected. A thorough analysis and interpretation of the wake measurements using, among other techniques, a cross correlation based analysis of the redundant reference wake measurements combined with an empirical determination of the mean turbine yaw angle, was performed to overcome the uncertainties of the respective turbine yawing and the relative lateral displacement.

An excellent agreement was found between measurements and simulation for both the *reference* and the *merged* wake deficit / streamwise turbulence for a selected time series with the inflow direction aligned with both turbines. The simulated power production and

thrust force agreed also well with the SCADA measurements of the downwind turbine.

Future improvements will be made in the CFD simulation to include a more realistic dynamic yawing of the turbine based on a generic controller implemented in the aeroelastic code HAWC2 [143] coupled to the CFD code.

This will allow a detailed parametric CFD study emphasizing the influence of turbine lateral and longitudinal spacing, free stream turbulence intensity and other relevant parameters on the wake overlapping mechanism.

Finally, the present investigation will be supplemented by analysis of additional single and double wake datasets recorded at a higher scanning speed. The main objectives of the combined study will be: 1) to characterize wake turbulence from lidar spectrum width; 2) to study the impact of wake interaction on the meandering dynamics; and 3) to extend the formulation of the Dynamic Wake Meandering model to multiple wakes on a rational basis.

5.11 Post publication comments

The change of rotor modeling technique from Actuator Line to Actuator Disc was motivated by the gain in computational speed and the strong similarity in wake mean velocity and turbulence profile, as discussed in the work by Troldborg et al. in [148]. An analysis depicted in Appendix A.2 shows the difference in the single and merged wake velocity and turbulence profile for downstream distances ranging from 1D to 5 diameter downstream. This analysis was conducted on a Nordtank turbine using LES under neutral atmosphere at a mean wind speed of 7.5 m/s. The inflow turbulence was identical for the two simulations. In this comparison, the gain of computational time was in the order of 5.

Several TB of data were collected from all three lidars as part of the campaign. A post processing software was developed using a user interface present in Appendix A.1, facilitating the investigation of unsteady wake measurements.

Chapter 6

Modeling of wake superposition

6.1 Parametric Large Eddy Simulation study

6.1.1 Introduction

This chapter presents the initial results of an ongoing (and therefore unpublished) research aiming at a generic study of merging wakes. This analysis therefore complets the present Ph.D. thesis with an analysis of mutual interaction of the organized wind farm flow structures, i.e. the wake deficits studied extensively experimentally and numerically in the 4 previous chapters. The present chapter specifically deals with the evaluation of 3 different engineering wake superposition approaches against detailed CFD simulations, which covers different turbine interspacing, different ambient turbulence intensities and different number of interacting wakes.

As part of the double wake experiment described in Section 5.6, a validation of the Large Eddy Simulation - Actuator Disc approach was performed with 10 minutes lidar measurements of an overlapped wake flow field generated by two turbines in yaw at the DTU Wind Energy test site. Additionally, a preliminary assessment of the performance of commonly used wake summation techniques revealed that averaging quadratic and linear summation of single wake deficit can predict with a fair degree of accuracy the merged wake deficit for a selected datasets associated to a mean wind speed of 7.1 m/s.

This numerical approach is now reused as part of a parametric CFD study aiming at studying the behavior of interacting wakes in a more generic way, i.e. under different turbulence conditions, wind speeds (varying C_T) and turbine spacings. This analysis is conducted on a set up where two Nordtank turbines are used, to relate more closely to conventional wind farms as opposed to the previous Tellus / Nordtank tandem. As the rotational speed is kept constant throughout the parametric study, a wide range of tip

speed ratio and wake flow regimes are covered.

As part of the analysis, two turbine spacings are tested: a 'small' spacing of 4 rotor diameters, corresponding to a rather severe wake condition similar to the Middelgrunden wind farm outside Copenhagen harbor; and a 'larger' 7 diameters spacing often used for offshore wind farm layouts. The two simulated ambient turbulence intensities correspond to typical offshore and onshore values of respectively 6% and 12%. Four mean wind speeds are chosen covering different turbine loadings and thus various wake flow regimes.

The inflow wind profile is assumed neutral and modeled using a logarithmic law, where the roughness is equal to 0.5 and 5 cm, for the low and high turbulence case, respectively. The friction velocity is adjusted to satisfy the prescribed hub height wind speed for all cases. Additionally, single wake simulations under the same atmospheric and inflow conditions as the double wake cases are also performed. This determines the undisturbed wake generated from the most upstream turbine referred to as $T1$ and further used as the wake generated by the downstream turbine $T2$ as part of a first wake summation analysis described subsequently. A test case matrix summarizing the study is shown in Tab 6.1.

Table 6.1: LES parametric study. Test cases matrix. The turbulence intensity corresponds to the free stream turbulence intensity I_{ref}, as resolved by the CFD computations.

	5 m/s		**8 m/s**		**11 m/s**		**15 m/s**	
4D spacing	6.3%	12.2%	6.3%	11.9%	6.3%	11.9%	6.4%	12.1%
7D spacing	6.3%	12.2%	6.3%	11.9%	6.3%	11.9%	6.4%	12.1%
Single wake $T1$	6.3%	12.2%	6.3%	11.9%	6.3%	11.9%	6.4%	12.1%

6.1.2 Numerical set up

6.1.2.1 Computational set up

As part of this parametric study, a similar set up as used in Section 5.8 is adopted. In order to study the double wake profile at several downstream location, the computational grid is extended to $L_z = 24D_N$ in the stream-wise direction, and present a cross sectional dimension of $L_x = 14D_N$ and $L_y = 14D_N$, where D_N is the diameter of the Nordtank turbine equal to 41 m. In the region around and downstream of the rotors, the grid spacing is equivalent to $dz = D_N/60$ in the lateral and vertical direction and $dz = D_N/62$ in the stream-wise direction. The domain has a total of approximately 39.81 millions cells, and its layout is similar to the one depicted in Fig. 6.1a. Boundary conditions are identical to the one applied in Section 5.8. Each actuator disc is represented with a separate 2D polar grid with 94 radial and 180 angular elements. Axial and tangential loads on the disc are extracted at 5 Hz and stored for a future analysis in the study of the time variant rotor flapwise and edgewise loading under half and full wake situations.

6.1.2.2 Extraction of simulation results

The velocity field is extracted along several cross sections in the wake flow field ranging from 1 to 15 rotor diameters from the upstream turbine $T1$ in the configuration where two turbines are inserted in the domain. Each cross section is made of 164 by 80 points in the lateral and vertical directions, respectively. The dimensions of the cross sectional plane are 164 by 80 meters, giving a resolution of 1 m. The solution is extracted every 0.2 s of simulation time, giving a sampling frequency of 5Hz. Additionally, the solution is extracted along an horizontal plane at hub height covering the entire wake region with a resolution of 1 m. Fig. 6.1a shows the coarse representation of the computational domain seen from the top, and the location of extraction planes.

The total computational resources used for simulating all 24 cases listed in Table 6.1 for 10 minutes unsteady simulations was approximately 200000 processor hours, and the total amount of raw binary data extracted is in order of 150GB. Each simulation makes use of 360 processors.

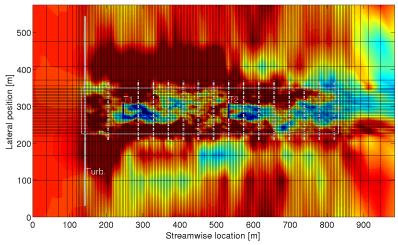

(a) Computational domain seen from the top. Horizontal cross section at hub height.

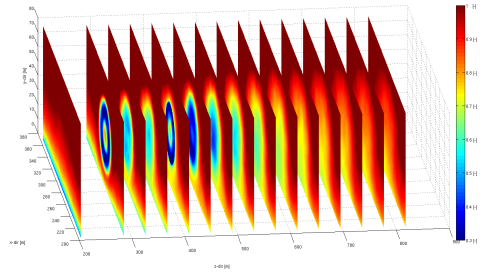

(b) Side view of the cross sections of the wake extracted.

Figure 6.1: (a) Coarse representation of the computational domain seen from the top. The dark colors correspond to the wake of turbine $T1$ and $T2$ separated from 7 rotor diameters. Dash lines are wake cross sections extracted at 5Hz. The white rectangle is a longitudinal extraction plane at hub height also extracted at 5Hz. (b) Side view of the cross sectional contours of the mean wake deficit for a turbine spacing of 4D. The first plane is located 1 diameter upstream of $T1$ and shows the logarithmic inflow profile.

6.2 First modeling approach of wake accumulation

6.2.1 Linear and quadratic superposition

The present section aims at evaluating the performance of the two commonly used approaches to model the merged wake deficit at hub height. Firstly, the linear superposition of wake deficits consisting of a simple summation of the upstream single wake deficits as applied in e.g. Fuga [100]. The normalized wake velocity deficit is presently defined as:

$$\Delta u = 1 - \frac{u_w}{U_0} \tag{6.1}$$

where u_w is the velocity in the wake, and U_0 is the mean free stream velocity. The linear summation of n upstream velocity deficit contributions is then expressed as:

$$\Delta u_{n+1} = \sum_{j=1}^{n} (\Delta u_j) \tag{6.2}$$

The quadratic superposition, as applied in the widely used PARK program [55], is obtained as the square root of the sums of the upstream single wakes contribution. Thus, the quadratic summation of n upstream velocity deficit contributions reads:

$$\Delta u_{n+1} = \sqrt{\sum_{j=1}^{n} (\Delta u_j)^2} \tag{6.3}$$

As a first modeling approach, we consider that the wake deficit profile generated by the second turbine $T2$ at a given downstream position from $T2$ is similar to the one generated by the upstream turbine $T1$ at the same downstream position from $T1$. This presents the advantage of reducing drastically the amount of computations required to perform a wake summation analysis as the single wake computations of the upstream turbine $T1$ can be used to estimate both single wake contributions from turbine $T1$ and $T2$ with only one simulation. However, this is a rather crude assumption as the real inflow conditions of the second turbine is associated to a reduced mean wind speed due to the upstream wake and an increase in turbulence intensity, which, under specific inflow conditions, can generate a quite different wake deficit.

The performance of the linear and quadratic summation is presently assessed on all double wake situations described by the test matrix in Table 6.1. This benchmark serves as basis for the development of a new superposition model. The observations are conducted initially at downstream positions from the second turbine corresponding to the two turbine spacings. Thus, the following set of observation aims at investigating the performance of these two summation techniques to determine the inflow profile of a fictitious 'third' downstream turbines in a uniformly spaced row of turbines. The subsequent set of wake deficits at hub height are shown in both the fixed and the meandering frame of reference of the wake. Due to the large amount of figures, they are shown in a separate Appendix A.4.

6.2.2 Preliminary assessment

From the results presented in Appendices A.5, A.6, A.7 and A.8, one can observe a strong correlation between the performance of each of the summation technique and the simulated mean wind speed.

At low wind speeds and regardless of spacing and turbulence intensity (sub figures (b) in Appendices. A.5, A.6, A.7 and A.8), the quadratic summation seems to accurately determine the merged wake deficit in the fixed frame of reference.

At high mean wind speed (sub figures (k) in Appendix A.5, A.6, A.7 and A.8), the merged wake deficit is fairly well captured by a linear summation of the single wake contributions.

For intermediate wind speeds (sub figures (e) and (h) in Appendix A.5, A.6, A.7 and A.8) both summation techniques appear to poorly represent the double wake deficit. Specifically, the quadratic summation underestimates the deficit, whereas the linear summation overestimates it. Thus, averaging the results of both techniques may enhance the agreement, as observed in Section 5.9.3.

When considering the meandering frame of reference, the quadratic wake summation seems to perform fairly well for all cases regardless of ambient conditions and turbine configuration.

6.2.3 Extension to multiple downstream locations

The previous observations were conducted at a fixed downstream location in the merged wake regime equivalent to the two turbines interspacing. The present section aims at confronting the previous trend to all available downstream distances in the merged wake, i.e. covering the near and the far 'merged wake' regions. Due to limitation of the fixed computational domain length, the analysis is limited to 7 diameters downstream of $T2$ for the large turbine spacing case and to 10 diameters downstream of $T2$ for the low spacing case.

In Fig. 6.2, the maximum wake deficit, in the FFoR, predicted by the two summation rules and the simulated one are plotted against the downstream distance (in rotor diameters) from the downstream turbine. As seen in Fig. 6.2, the difference between the two predicted curves are fairly constant as function of downstream distance.

Additionally, and as previously observed in Section 6.2.1, the merged wake deficit in the meandering frame of reference seems to be well captured by a quadratic summation of the two single wake deficits for all downstream locations presently investigated.

This indicates that the previous set of observations can be generalized to all downstream locations exceeding two rotor diameters. In the vicinity of the turbine, i.e. in the near merged wake region of less than two diameters from the rotor, the present analysis appears biased by the pronounced double bell shape profile displayed by the merged wake deficit. In this region, comparing maximum deficits is therefore not relevant and the wake center deficit may be subsequently used instead.

On Fig. 6.2p, the maximum deficit exceeds substantially the one predicted by the linear summation. An analysis of the mean wake velocity contour at hub height indicates that

the maximum wake deficit of the two single wakes is only in the order of 5% of the free stream velocity at the downstream location corresponding to the turbine spacing. This shows that the linear summation of single wake contribution leads to an underestimation of the merged wake profile for a high wind speed case associated to highly turbulent inflow. In this situation, the upstream wake appears almost fully recovered when the flow reaches the downwind turbine.

FFoR

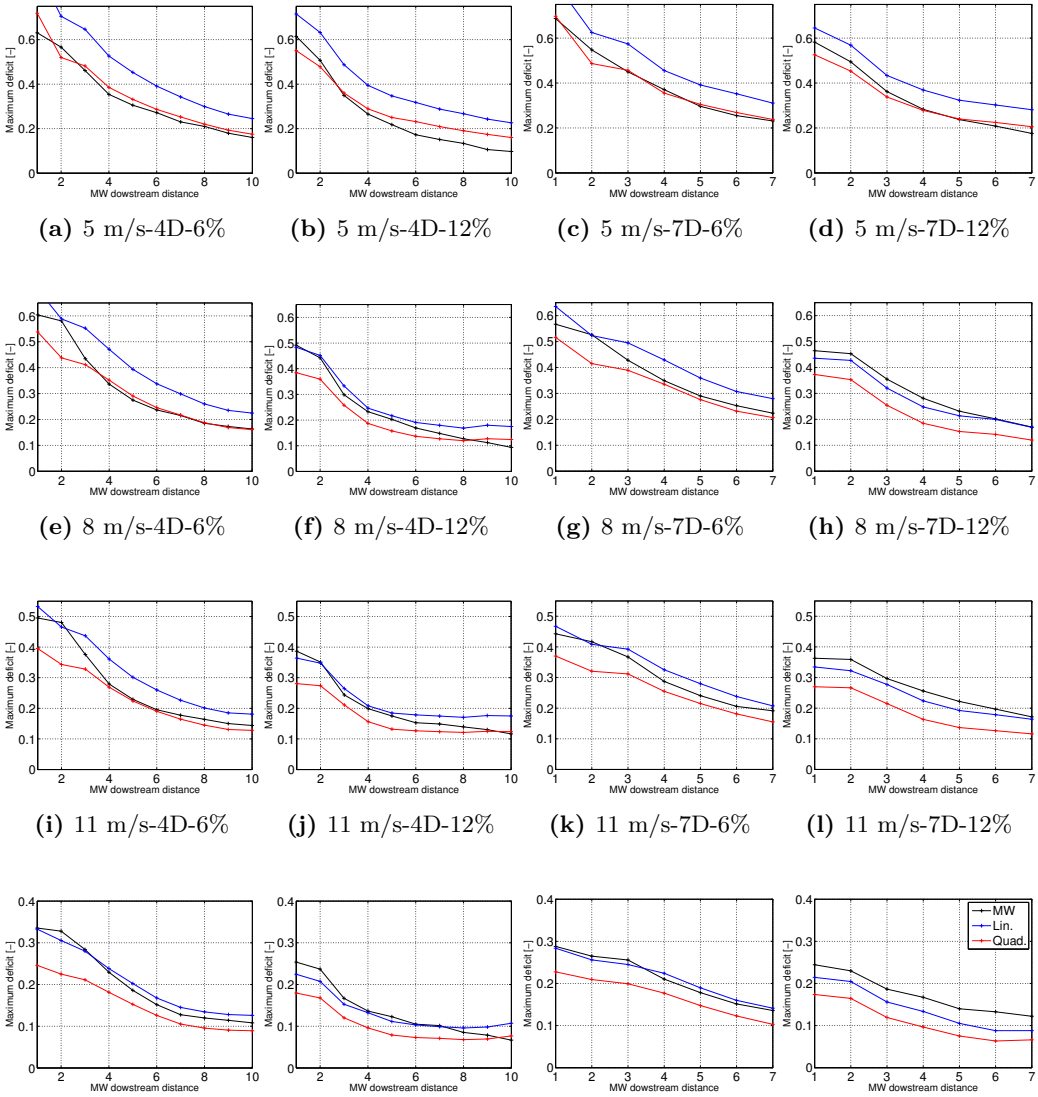

(a) 5 m/s-4D-6% **(b)** 5 m/s-4D-12% **(c)** 5 m/s-7D-6% **(d)** 5 m/s-7D-12%

(e) 8 m/s-4D-6% **(f)** 8 m/s-4D-12% **(g)** 8 m/s-7D-6% **(h)** 8 m/s-7D-12%

(i) 11 m/s-4D-6% **(j)** 11 m/s-4D-12% **(k)** 11 m/s-7D-6% **(l)** 11 m/s-7D-12%

(m) 15 m/s-4D-6% **(n)** 15 m/s-4D-12% **(o)** 15 m/s-7D-6% **(p)** 15 m/s-7D-12%

Figure 6.2: Maximum deficit in the merged wake as function of downstream distance from $T2$ and in the FFoR. For the low spacing cases, the analysis is conducted at locations up to 10 diameters downstream, as opposed to only 7D for the large spacing cases.

MFoR

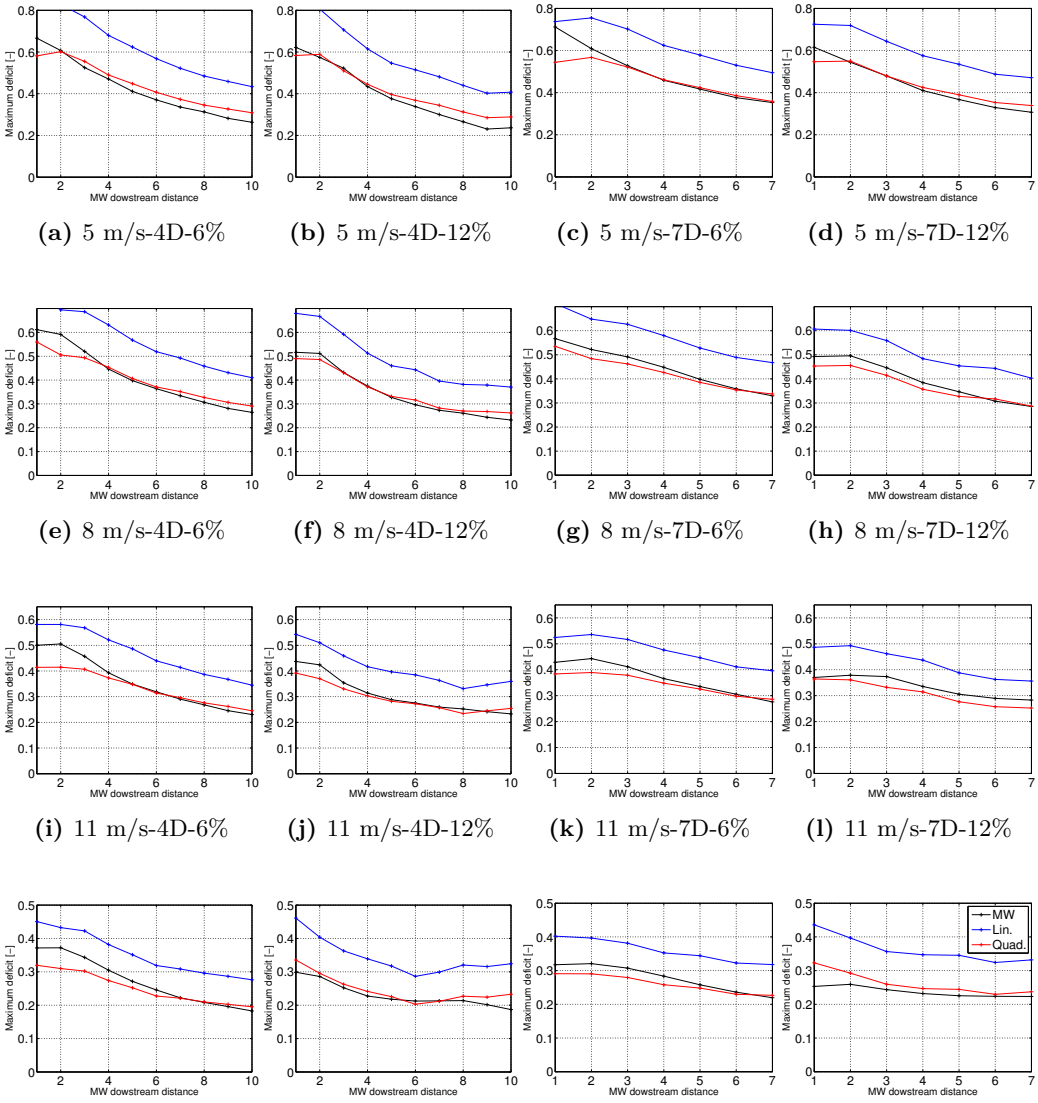

(a) 5 m/s-4D-6% **(b)** 5 m/s-4D-12% **(c)** 5 m/s-7D-6% **(d)** 5 m/s-7D-12%

(e) 8 m/s-4D-6% **(f)** 8 m/s-4D-12% **(g)** 8 m/s-7D-6% **(h)** 8 m/s-7D-12%

(i) 11 m/s-4D-6% **(j)** 11 m/s-4D-12% **(k)** 11 m/s-7D-6% **(l)** 11 m/s-7D-12%

(m) 15 m/s-4D-6% **(n)** 15 m/s-4D-12% **(o)** 15 m/s-7D-6% **(p)** 15 m/s-7D-12%

Figure 6.3: Maximum deficit in the merged wake as function of downstream distance from $T2$ and in the MFoR. For the low spacing cases, the analysis is conducted at location up to 10 diameters downstream, as opposed to only 7D for the large spacing cases.

6.2.4 Definition of wake superposition regimes

6.2.4.1 Basic assumptions

In this first modeling approach, it was observed that the way wakes accumulate is strongly dependent on the wind speed and more specifically on the thrust force acting on the turbine. Low wind speed associated with a high thrust coefficient generates very pronounced wake deficits. Their resulting overlapped wake appears well captured by a quadratic summation in both FFoR and MFoR. Oppositely, at high mean wind speed, the turbine is more 'transparent' to the flow and linear summation of the very attenuated single wakes seems to be more representative of the merged wake deficit. At moderate wind speed, none of the summation technique is able to capture the merged wake deficit. The quadratic summation underestimates the deficit whereas the linear summation overestimates it. Based on this result, and as observed in the analysis in Section 5.9.3, it is assumed that averaging the results of both techniques lead to the most accurate prediction of the overlapped wake deficit.

6.2.4.2 Wake superposition regimes

The present section aims at condensing all the observations from Section 6.2.1 in a generic way in order to quantify the performance of each of the summation techniques as function of the rotor thrust coefficients, and subsequently to formulate a simple empirical approach for predicting the double wake deficit profile. A first approach is to consider the deviation in maximum wake deficit between the various methods.

For this analysis the metric F is introduced. It is defined as the absolute difference in maximum hub height wake deficit (or wake depth) between the profile obtained from each of the summation techniques and the simulated merged wake deficit. This metric is obtained as the average of all available downstream cross sections ranging from 1 to k diameters downstream, in order to account for the various merged wake flow regime. The F metric is expressed as:

$$
\begin{aligned}
F_{lin} &= \frac{1}{k}\sum_{j=1}^{k} \left| \left(max(\Delta u_{T1T2_{|k_1(j)}}) - max(\Delta u_{T2_{|k_2(j)}} + \Delta u_{T1_{|k_1(j)}}) \right) \right| \\
F_{quad} &= \frac{1}{k}\sum_{j=1}^{k} \left| \left(max(\Delta u_{T1T2_{|k_1(j)}}) - max(\sqrt{\Delta u^2_{T2_{|k_2(j)}} + \Delta u^2_{T1_{|k_1(j)}}}) \right) \right|
\end{aligned}
\tag{6.4}
$$

where $k_1(j) = j \cdot D$ is the number of rotor diameters from the upstream turbine $T1$, $k_2(j) = k_1(j) - S$, where S is the turbine spacing in rotor diameters, Δu_{T1T2} is the deficit generated by the two upstream turbines $T1$ and $T2$, Δu_{Ti} is the single wake deficit generated by the turbine Ti, with $i = 1, 2$. From the previously introduced first modeling assumption, the following relation holds:

$$
\Delta u_{T2_{|k_1(j)-S}} = \Delta u_{T1_{|k_1(j)}} \tag{6.5}
$$

Fig. 6.4 illustrates the downstream location where wake deficits are extracted for $j = 6$.

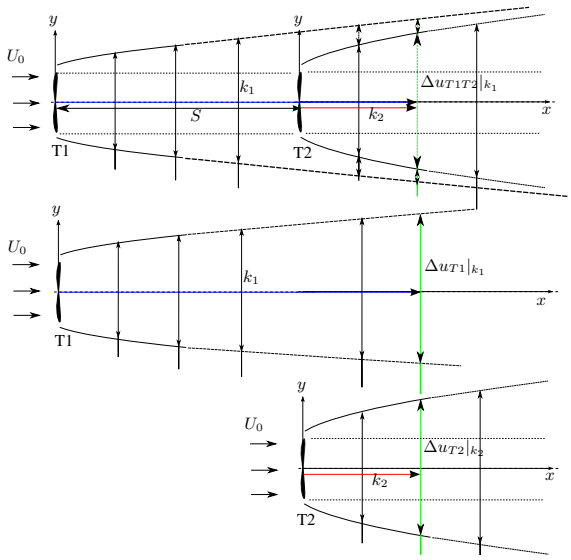

Figure 6.4: Sketch of the wake summation analysis. The merged wake deficit (upper figure) is decomposed into two single wake contributions (middle and lower figures), representing the wake of T1 at 6D downstream and the wake of T2 at 2D downstream, respectively, and under the same inflow neutral logarithmic inflow characterized by a mean wind speed U_0 at hub height.

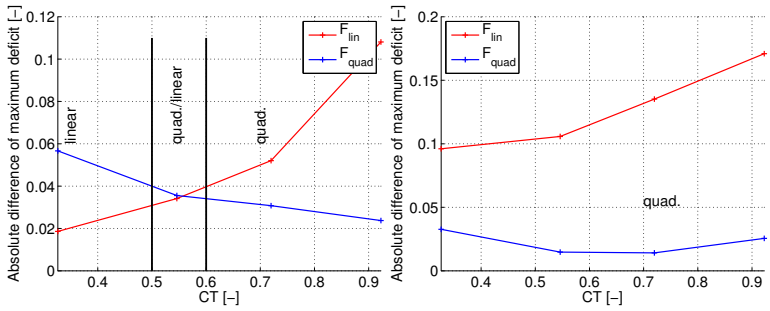

(a) FFoR **(b)** MFoR

Figure 6.5: Value of the metric F for the first modeling approach as function of C_T in the FFoR (a), and the MFoR (b).

Results of the F metric computations are shown in Fig. 6.5. It is seen in Fig. 6.5a, that the three conjectured thrust-dependent summation regimes from the observations Fig. A.5, Fig. A.6, Fig. A.7 and Fig. A.8 can be more accurately specified. The chosen delimitation

of the three regions is the following: the low thrust coefficient region ($C_T < 0.5$) where linear summation is applied; the intermediate region for C_T ranging from 0.5 to 0.6 where the so-called 'ARL' summation formulated in Section 5.9.3 is valid and finally; the high C_T region where quadratic summations provide the best agreement with the simulated deficit.

In Fig. 6.5b, the obtained F metric is the lowest when applying a quadratic wake summation throughout the entire tested C_T range.

6.2.4.3 Relation to the turbine C_T curve

The distribution of the power produced and thrust forces among the 16 test cases listed in Tab. 6.1 is depicted in Fig. 6.6, together with the C_P and C_T curves.

The thrust and power curves were obtained from SCADA measurements collected on the Nordtank turbine for several years. Additionally, a BEM computation using the same tabulated airfoil data as the one used in the CFD Actuator Disk model is used to validate the measured power and thrust curves.

As seen in Fig. 6.6b, the power production of the upstream $T1$ turbine is quasi invariant to each of the 4 tested wind speeds whereas the downstream turbine $T2$ experience a wide range of power production. The most severe power drop is, as expected, observed for the low turbine spacing associated with the lowest turbulence case as shown for the simulation at mean wind speed 11 m/s. In Fig. 6.6c, the thrust coefficient is shown with the three conjectured wake summation regimes. The transition region from quadratic to linear summation region corresponds to the regime just after the maximum CP of the turbine is reached, as shown in Fig. 6.6d. It is further observed in Fig. 6.6c that the magnitude of the thrust coefficient is distributed among the 3 observed regimes, so that the quadratic summation contribution may be proportional to C_T whereas the linear summation contribution appears proportional to $(K - C_T)$ where K is a constant to be adjusted empirically.

6.2.5 Model formulation

6.2.5.1 General formulation

The defined wake aggregation regimes and basic model assumption are formulated into a simple engineering model. In this model, and as conjectured in Section 6.2.1, the double wake deficit at hub height is assumed to be defined by a weighted average of quadratic and linear summation of hub height single wake deficits, where the weighting coefficients is related to the mean thrust coefficient of the two wake generating turbines. The double wake deficit at hub height and in the FFoR generated by the wake interaction of turbine $T1$ and $T2$, denoted Δu_{T1T2} is presently formulated as:

$$\Delta u_{T1T2}|_{k_1} = CT_{T1T2} \cdot \left(\sqrt{(\Delta u_{T1}|_{k_1})^2 + (\Delta u_{T2}|_{k_2})^2} \right) + (K - CT_{T1T2}) \cdot (\Delta u_{T1}|_{k_1} + \Delta u_{T2}|_{k_2}) \tag{6.6}$$

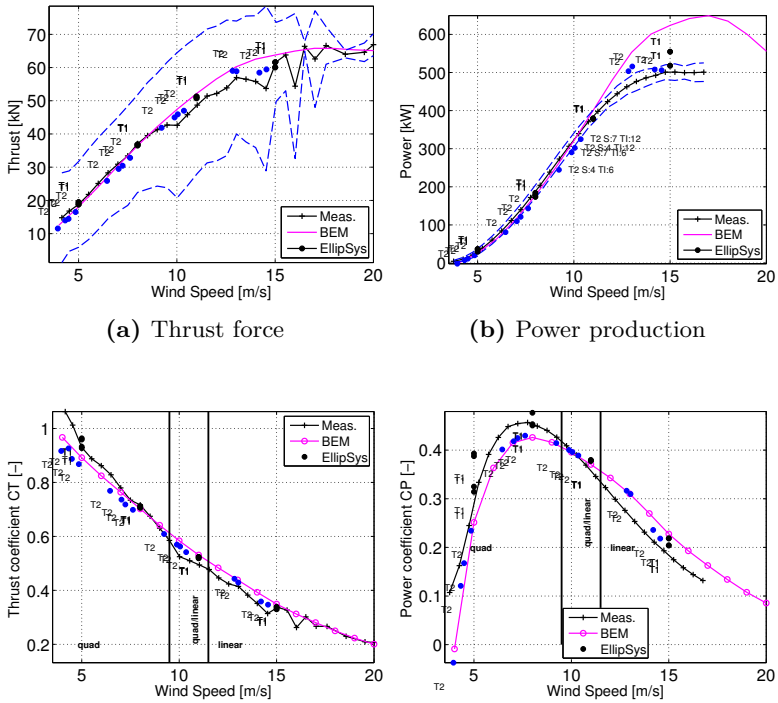

(a) Thrust force **(b)** Power production

(c) C_T curve **(d)** C_P curve

Figure 6.6: Repartition of computed thrust, power, thrust coefficient and power coefficient for all test cases in Tab. 6.1. Black dots represents the power produced by the upstream turbine ($T1$), quasi-invariant to the turbine spacing and turbulence intensity. Blue dots show the production and thrust loading of the downstream turbine ($T2$), affected by the test conditions. The 3 regions preliminary defined are depicted in (c) and (d).

where $k_2 = k_1 - S$, S is the turbine spacing, CT_{T1T2} is the mean of the two turbines thrust coefficient, K is an empirical constant to be determined subsequently, $\Delta u_{T1}|_{k_1}$ is the single wake deficit of $T1$ at a distance k_1, $\Delta u_{T2}|_{k_2}$ is the single wake deficit of $T2$ at a distance k_2.

Based on the previous observations, the corresponding first model formulation in the MFoR is:

$$\Delta\tilde{u}_{T1T2}|_{k_1} = \sqrt{(\Delta\tilde{u}_{T1}|_{k_1})^2 + (\Delta\tilde{u}_{T2}|_{k_2})^2} \tag{6.7}$$

where $\Delta\tilde{u}$ denotes the deficit in the MFoR.

6.2.5.2 Empirical constant calibration

As seen in Fig. 6.6c, and formulated in Eq. 6.6, the C_T coefficient distribution is assumed to be a weighting factor of the quadratic and linear wake summation. The K value is, as a first guess, assumed to be equal to 1. A sensitivity analysis is performed to determine which K value leads to the smallest deviation in maximum deficit between the simulated merged wake profile and the one obtained from the present modeling approach. Results of this sensitivity analysis are shown in Fig. 6.7. It is seen that an adjustment of the K value is necessary to reach the minimum deviation for all tested thrust coefficients.

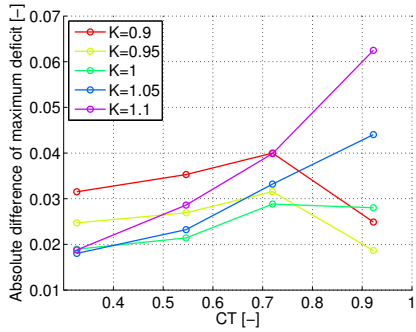

Figure 6.7: Sensitivity analysis for varying K value in the first modeling approach in Eq. 6.6. The minimum deviation is reached for a K value of 0.95 for $0.75 < C_T < 1$, $K = 1$ for $0.45 < C_T < 0.75$ and $K = 1.05$ for $C_T < 0.45$.

6.2.5.3 Model performance assessment

The performance of the present double wake model is tested for several cases, in both the fixed and the meandering frame of reference, at a fixed downstream distance equal to the turbine spacing. Results are shown in Fig. 6.8. The overall agreement seen in Fig. 6.8 is fair, as the model predicts with a good degree of accuracy the maximum deficit. When considering the merged wake expansion, the present summation approach appears to underestimate the wake width with the same magnitude in both FFoR and MFoR.

When analyzing the case with the highest spacing, mean wind speed and turbulence intensity, a poor agreement is observed as shown in Fig. 6.9. In this case, the summation of the two single wake contributions is highly unreliable due to the very low magnitude of deficit caused by the high level of turbulence and wake recovery. The simulated double wake deficit is larger than the one obtained from summation. Increasing the K value to 1.35 enhances the maximum deficit agreement although the wake expansion is not well captured. Similarly, a large underestimation of the wake expansion in the meandering frame of reference in observed in Fig. 6.9b.

The observed discrepancies in mean wake expansion are a consequence of the crude assumption that the single wake contribution of turbine $T2$ is identical to the upstream turbine $T1$ at a given similar downstream distance. In fact, in all simulated cases, the downwind turbine $T2$ experiences a reduced mean speed and thus a higher C_T which, in turn, enhances the downwind wake expansion. This increased downwind expansion will contribute to reduce the observed discrepancies.

6.3 Second modeling approach of wake accumulation

6.3.1 Downwind turbine wake

In order to overcome the uncertainties on the mean wake expansion, the wake generated by the downstream turbine $T2$ is simulated at different inflow conditions than in the first modeling approach where the logarithmic incoming wind of $T1$ was used as depicted in Fig. 6.4.

The new inflow profile presents the same wind shear and turbulence intensity as used for the single wake calculations of $T1$, however, associated to a reduced mean wind speed caused by the upstream wake. This reduced mean wind speed is determined from the mean power produced by turbine $T2$ and the standard turbine power curve depicted in Fig. 6.6b, when the turbine operates in the wake of turbine $T1$. This approach present the advantage of using a more realistic downstream single wake, typically associated to a larger wake expansion, which is expected to reduce the previously observed expansion discrepancies. However, this analysis requires 16 new unsteady LES computations of the wake flow field of $T2$ under the inflow conditions listed in Table 6.2. Because of computational time constraints, the length of the domain has been reduced to $L_z = 17D$, and the single wake cross sections are extracted from 1 to 8D downstream of turbine $T2$.

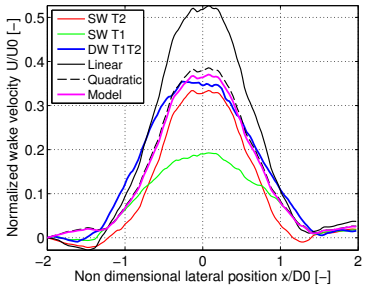

(a) FFoR 5 m/s, spacing 4D, 6%

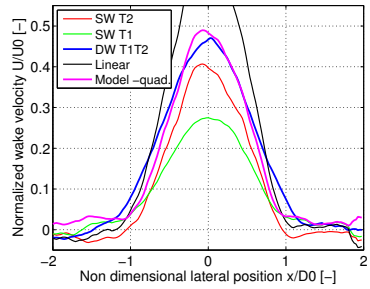

(b) MFoR 5 m/s, spacing 4D, 6%

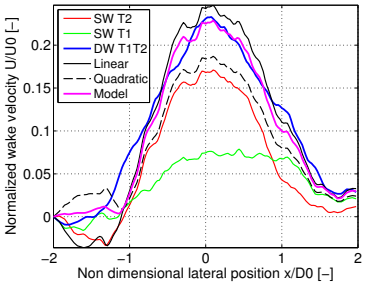

(c) FFoR 8 m/s, spacing 4D, 12%

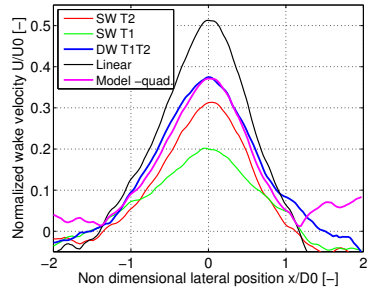

(d) MFoR 8 m/s, spacing 4D, 12%

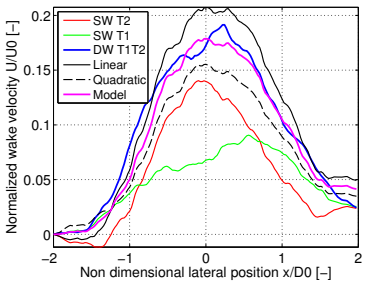

(e) FFoR 11 m/s, spacing 7D, 6%

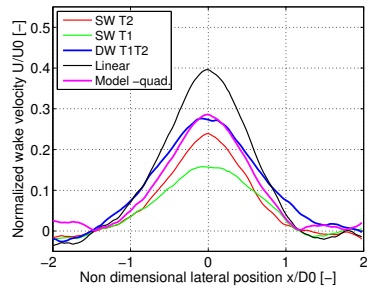

(f) MFoR 11 m/s, spacing 7D, 6%

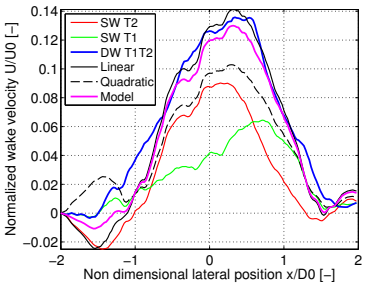

(g) FFoR 15 m/s, spacing 7D, 6%

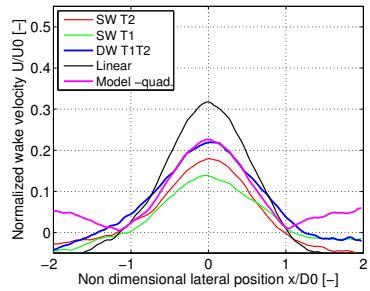

(h) MFoR 15 m/s, spacing 7D, 6%

Figure 6.8: Validation of double wake deficit model for 4 test cases of various spacing

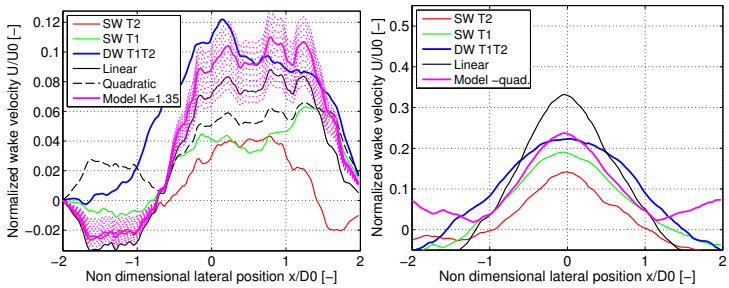

(a) FFoR 15 m/s, spacing 7D, 12%

(b) MFoR 15 m/s, spacing 7D, 12%

Figure 6.9: Investigation of model accuracy for the highest spacing, turbulence intensity and wind speed. A poor agreement is observed in the model under standard empirical K value where the double wake deficit is underestimated. Increasing the K value for 1.35 improves the prediction.

Table 6.2: Large Eddy Simulation of the wake generated by turbine $T2$ at a reduced mean wind speed caused by the upstream wake of $T1$. The turbulence intensity corresponds to the total free stream turbulence intensity I_{ref} for all three velocity components and is assumed to be identical to the free stream turbulence intensity.

	U_0 **T1 5 m/s**		U_0 **T1 8 m/s**		U_0 **T1 11 m/s**		U_0 **T1 15 m/s**	
I_{ref}	6.3%	12.2%	6.3%	11.9%	6.3%	11.9%	6.4%	12.1%
SW $T2$**, 4D**	3.95 m/s	4.5 m/s	6.45 m/s	7.24 m/s	9.22 m/s	10.05 m/s	12.84 m/s	14.02 m/s
SW $T2$**, 7D**	4.32 m/s	4.85 m/s	7.04 m/s	7.62 m/s	9.88 m/s	10.36 m/s	13.04 m/s	14.19 m/s

6.3.2 Model assessment

6.3.2.1 Maximum deficit investigation

In this section, a similar assessment as proposed in Section 6.2.3 is repeated but based on the new approach making use of a more realistic downwind single wake contribution. In Fig. 6.2 and Fig. 6.3, the maximum merged wake deficit as function of downstream distance as simulated by the LES, and predicted by the linear and quadratic superposition are shown.

FFoR

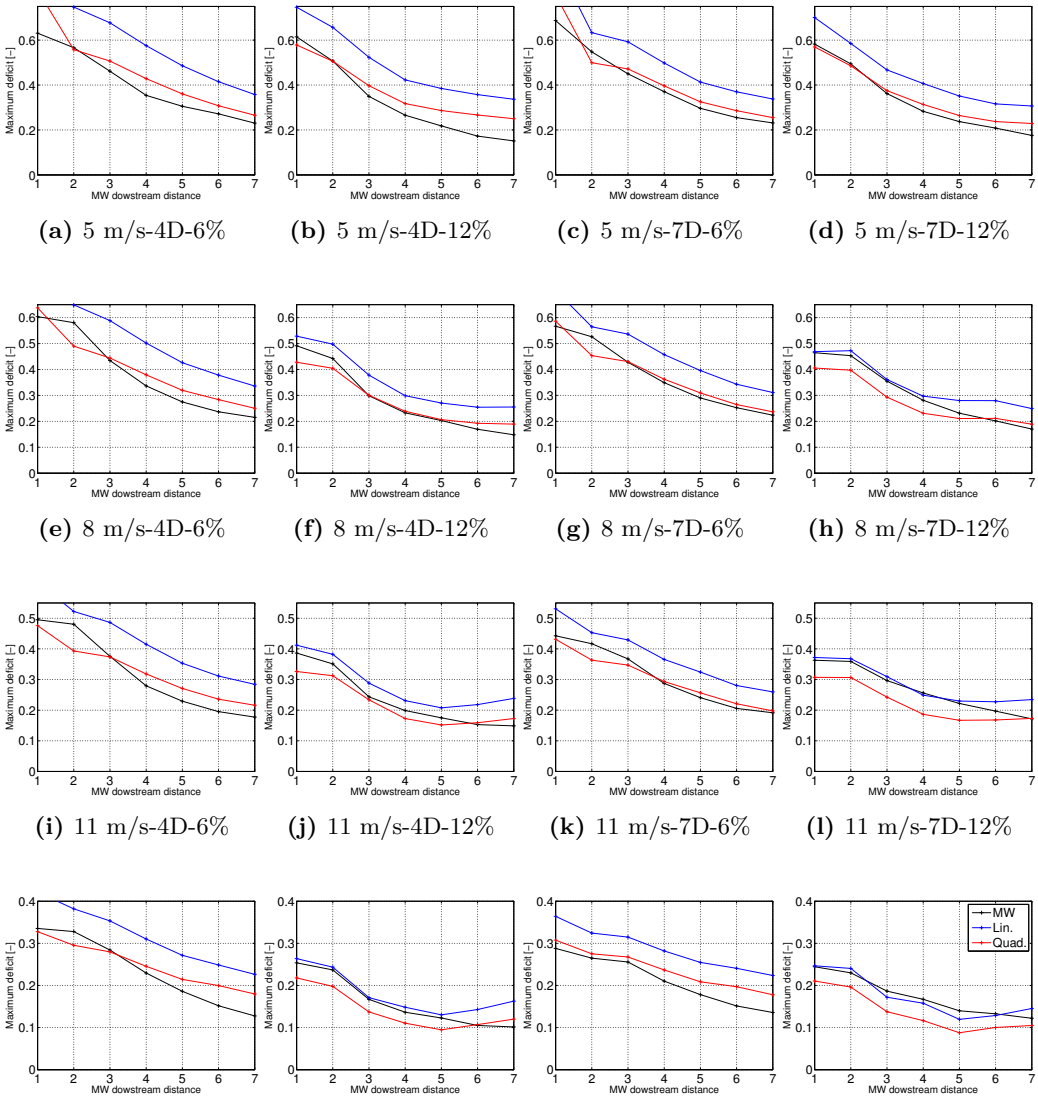

(a) 5 m/s-4D-6% **(b)** 5 m/s-4D-12% **(c)** 5 m/s-7D-6% **(d)** 5 m/s-7D-12%

(e) 8 m/s-4D-6% **(f)** 8 m/s-4D-12% **(g)** 8 m/s-7D-6% **(h)** 8 m/s-7D-12%

(i) 11 m/s-4D-6% **(j)** 11 m/s-4D-12% **(k)** 11 m/s-7D-6% **(l)** 11 m/s-7D-12%

(m) 15 m/s-4D-6% **(n)** 15 m/s-4D-12% **(o)** 15 m/s-7D-6% **(p)** 15 m/s-7D-12%

Figure 6.10: Maximum deficit in the merged wake as function of downstream distance from $T2$ and in the FFoR. For the both turbine spacing, the analysis is conducted at locations up to 7 diameters downstream.

It is seen in Fig. 6.10 and Fig. 6.11 that the conclusions taken from the preliminary assessment of the first modeling approach may differ with the present observations. When considering the FFoR in Fig. 6.10, the maximum merged wake deficit seems to be smaller

than the one predicted from quadratic superposition for situations with high thrust coefficients (Fig. 6.10a, 6.10b) and very close to the curve representing the prediction from quadratic summation for almost all simulated wake conditions. Remarkably, it is only seen in Fig. 6.10p, 6.10p that the linear superposition is valid. This indicates that the previous model calibration constant K which describes the weighting average coefficients should be re-calibrated to fit this new set of observations, as the quadratic summation becomes more important accross the tested C_T range.

MFoR

When considering the meandering frame of reference, the assumption that the quadratic superposition is valid for all conditions does not longer hold. For small velocity deficit, typically obtained at 15 m/s (Fig. 6.11m, 6.11n, 6.11o and 6.11p), the magnitude of maximum deficit is approximately 20% smaller than the one predicted by the quadratic summation rule. This indicates that a similar weighted average formulation than the FFoR is required for the second modeling approach.

6.3.3 Wake summation regimes

The F metric in Eq. 6.4 is recalculated for the second model, in order to quantify the impact of this approach on the previous set of observations. Results are shown in Fig. 6.12. It is seen in Fig. 6.12 that a similar trend as for the first modeling approach is observed, however, associated with a shift in the C_T values where the regions are located. This is explained by a deeper wake deficit generated by $T2$ with the use of the reduced inflow wind speed. This, in turn, causes the quadratic summation region to extend to C_T values ranging from 0.4 to 1. The region where linear summation is the most accurate is not simulated presently, but instead is represented by linear extrapolation of the metric F in the low C_T region as seen in Fig. 6.12 . Similarly to the first model, the quadratic summation is several order of magnitude more accurate for the prediction of the maximum deficit in the MFoR. However, this procedure does not longer shows acceptable performance at low C_T where the absolute difference increases rapidly. Therefore, a new formulation of the wake superposition in the MFoR (Eq. 6.7) is required.

6.3.4 Model formulation

6.3.4.1 General formulation

Based on the observations conducted in Fig. 6.11 and 6.12, a new formulation of the MFoR wake superposition is proposed, following the same methodology as for the FFoR, i.e.:

$$\Delta\tilde{u}_{T1T2}|_{k_1} = CT_{T1T2}\cdot\left(\sqrt{(\Delta u_{T1}|_{k_1})^2 + (\Delta u_{T2}|_{k_2})^2}\right) + (K_m - CT_{T1T2})\cdot(\Delta u_{T1}|_{k_1} + \Delta u_{T2}|_{k_2}) \tag{6.8}$$

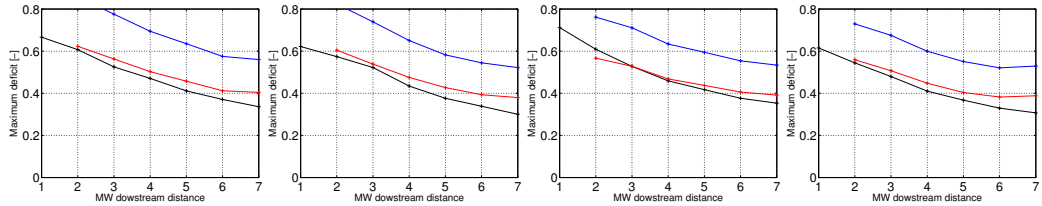

(a) 5 m/s-4D-6% **(b)** 5 m/s-4D-12% **(c)** 5 m/s-7D-6% **(d)** 5 m/s-7D-12%

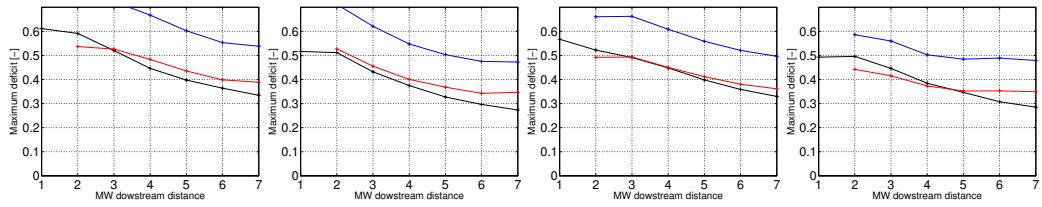

(e) 8 m/s-4D-6% **(f)** 8 m/s-4D-12% **(g)** 8 m/s-7D-6% **(h)** 8 m/s-7D-12%

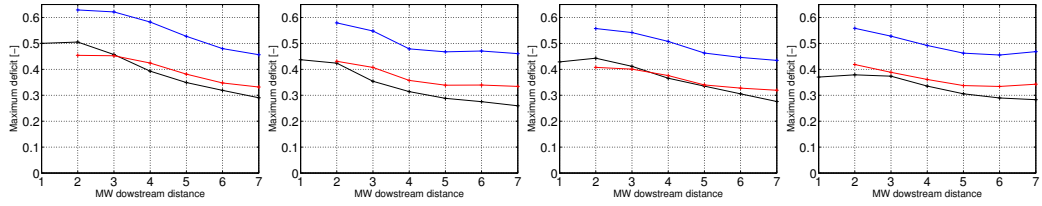

(i) 11 m/s-4D-6% **(j)** 11 m/s-4D-12% **(k)** 11 m/s-7D-6% **(l)** 11 m/s-7D-12%

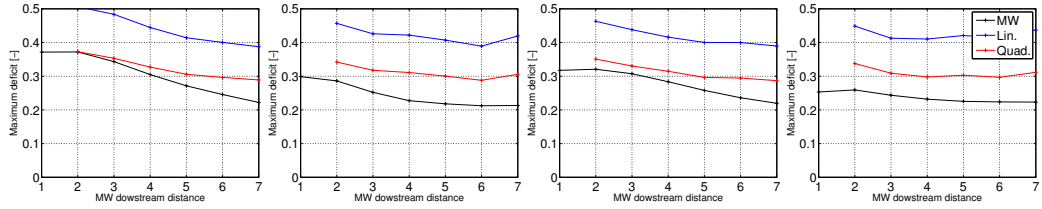

(m) 15 m/s-4D-6% **(n)** 15 m/s-4D-12% **(o)** 15 m/s-7D-6% **(p)** 15 m/s-7D-12%

Figure 6.11: Maximum deficit in the merged wake as function of downstream distance from $T2$ and in the MFoR. For the both turbine spacings, the analysis is conducted at locations up to 7 diameters downstream.

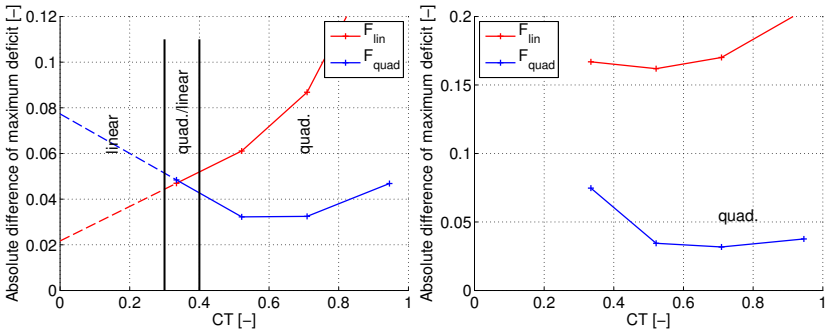

(a) FFoR **(b)** MFoR

Figure 6.12: Value of the metric F for the second modeling approach as function of C_T in the FFoR (a), and the MFoR (b).

where, in the second modeling approach:

$$\Delta u_{T2_{|k_1(j)-S}} \neq \Delta u_{T1_{|k_1(j)}} \tag{6.9}$$

The model formulation for the FFoR is, in this second modeling approach, identical to Eq. 6.6, however, requiring a re-calibration of the constant K to take into account the shit in wake aggregation regimes across the C_T range as observed in Fig. 6.12.

6.3.4.2 Model constant recalibration

The constant K is re-calibrated, similarly to the analysis in Section 6.2.5.2. As seen in Fig. 6.13a, the K value leading to the least deviation is equal to 0.9. Oppositely to the first model analysis depicted in Fig. 6.7, this value seems to be universal for the entire C_T range encountered in the parametric analysis.

As seen in Fig. 6.13b, the calibration of the constant K_m is slightly more challenging as the optimal value varies strongly from 0.75 to 0.95 along the tested C_T range. However, a linear relation relating K_m and C_T can be determined as depicted in Fig. 6.13c.

6.3.5 Model performance

The performance of the newly calibrated second modeling approach is tested against 4 wake overlapping cases of various configurations, similarly to the benchmark proposed in Section 6.2.5.3. The predictions from the first model, the linear and quadratic superposition and the single wake deficit from $T1$ and $T2$, respectively, are depicted in Fig. 6.14. As previously speculated, it is seen that this new approach captures with a higher degree of accuracy the mean merged wake expansion. Specifically, the agreement in the MFoR is very good for both deficit and expansion for the presented configurations involving

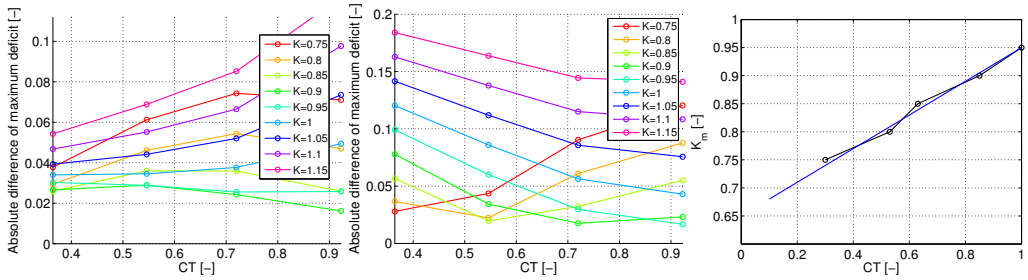

(a) FFoR **(b)** MFoR **(c)** $K_m = f(C_T)$

Figure 6.13: (a) Re calibration of the second model constant K from Eq. 6.6, for the FFoR. The minimum deviation is reached for a K value of 0.9 for all the observed C_T range. (b) Determination of the corresponding model constant K_m, for the MFoR. (c) Linear relationship determination between K_m and C_T: $K_m = 0.3C_T + 0.65$.

various spacings, wind speeds and turbulence intensities. In the FFoR, the model still underestimates the mean wake expansion but less than the first modeling approach.

The cases in Fig. 6.15a depicting the scenario with the highest mean wind speed, turbine spacing and turbulence intensity exhibits a poor agreement as was previously observed with the first modeling approach in Fig. 6.9.

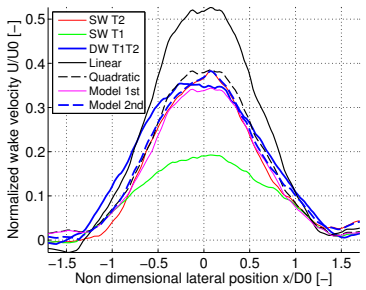

(a) FFoR 5 m/s, spacing 4D, 6%

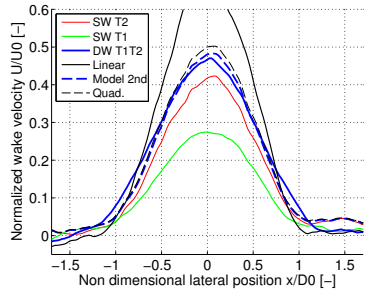

(b) MFoR 5 m/s, spacing 4D, 6%

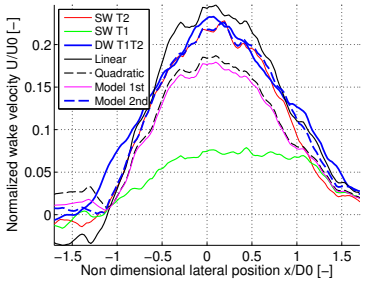

(c) FFoR 8 m/s, spacing 4D, 12%

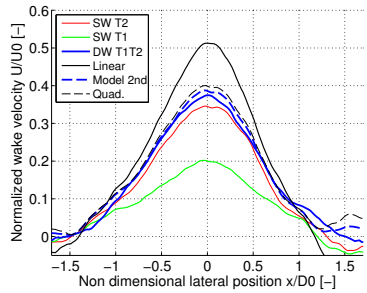

(d) MFoR 8 m/s, spacing 4D, 12%

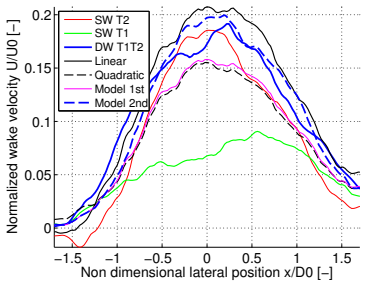

(e) FFoR 11 m/s, spacing 7D, 6%

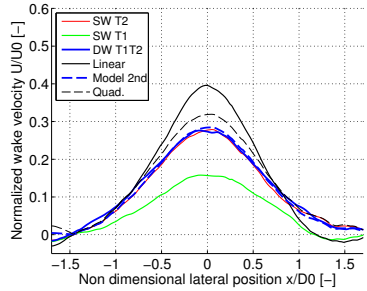

(f) MFoR 11 m/s, spacing 7D, 6%

Figure 6.14: Validation of double wake deficit model for 3 test cases of various spacing, mean wind speed and turbulence intensity.

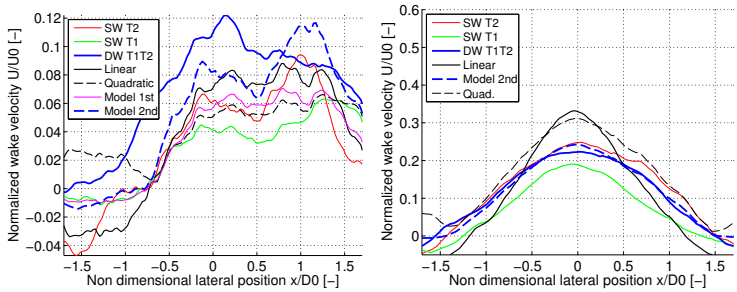

(a) FFoR 15 m/s, spacing 7D, 12%

(b) MFoR 15 m/s, spacing 7D, 12%

Figure 6.15: Validation of double wake deficit model for 3 test cases of various spacing, mean wind speed and turbulence intensity.

6.4 Multiple wake overlapping

6.4.1 Introduction

The two formulated models have proven robust to predict the maximum double wake deficit at hub height for several cases within the limits of ambient flow conditions and turbine spacing of the present parametric study. Additionally, the prediction of the mean merged wake expansion was found good in the MFoR and acceptable in the FFoR when using the second modeling approach. This level of agreement in merged wake expansion was not achieved when using the first model.

This section aims at investigating the performance of the two models for set up involving multiple wakes. Specifically, the present investigations focus on triple wakes and quadruple wakes, i.e. the overlapped wake generated from 3 and 4 closely spaced turbines. The latter configuration is illustrated in Fig. 6.16.

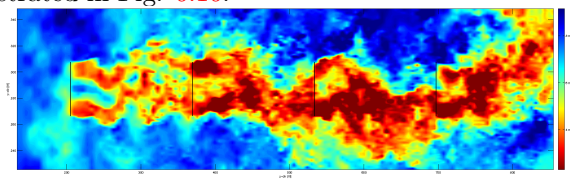

Figure 6.16: Instantaneous streamwise velocity in the wake flow field generated by 4 closely spaced Nordtank rotors at 8 m/s mean wind speed and a turbulence intensity of 12%. Large scale wake structures responsible of the sideways displacement of the superposed wake are clearly visible after the third rotor.

6.4.2 First modeling approach with multiple wakes

In this investigation, two configurations of merged wake deficit are investigated: triple wake (upper Fig. 6.17a) and quadruple wake (upper Fig. 6.17b). In analogy with Fig. 6.4, the 2 configurations seen in Fig. 6.17 are extracted at location shown by the blue line, whereas the single wake contributions are extracted at the dash blue lines on the single wake contour plot.

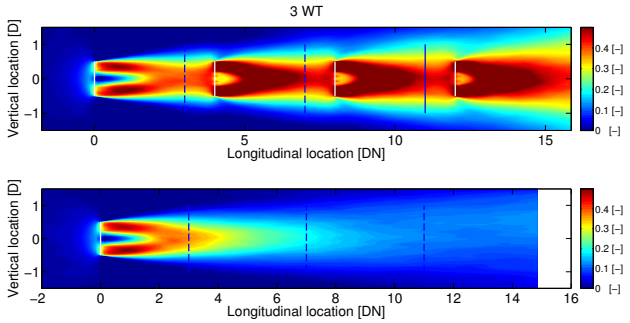

(a) 3 turbines and 3D downstream

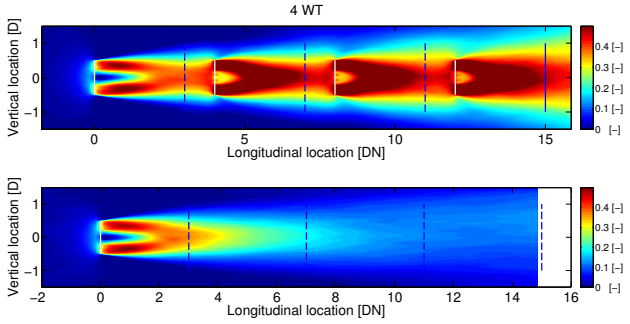

(b) 4 turbines and 2D downstream

Figure 6.17: Average wake deficit and location of extraction plane in both the multiple wake flow field (upper) and single wake flow field (lower) for the 2 tested configurations. The horizontal single wake velocity contour is not complete but cross sectional planes are available up to 14D downstream. White vertical lines represent the rotors. The dash blue lines are single wake extraction locations whereas the full blue line is the merged wake extraction location.

Results of the multiple wake analysis is shown in Fig. 6.18. As observed previously, the wake expansion is underestimated in the triple wake cases. When further increasing the number of turbines, the agreement with the modeled wake expansion becomes worse while

remaining fair for the maximum wake deficit.

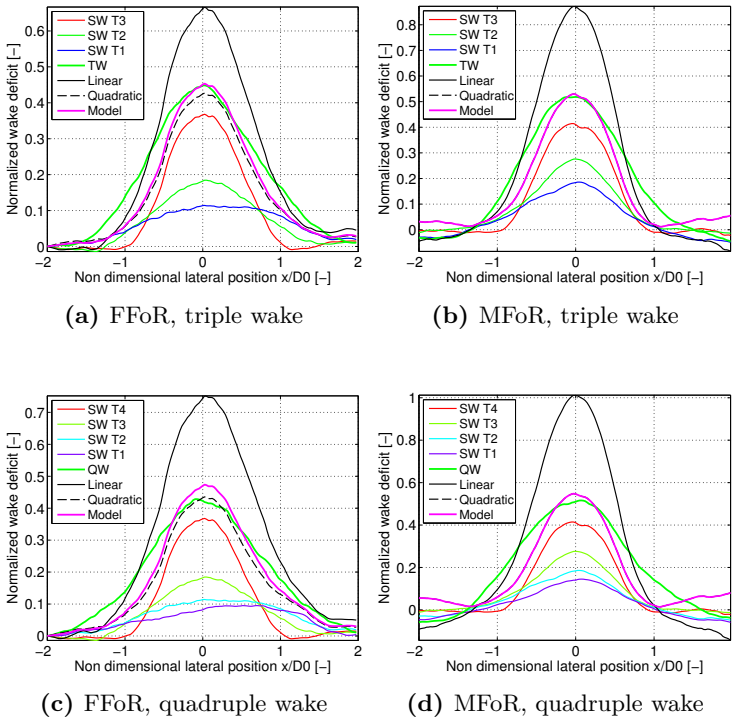

(a) FFoR, triple wake **(b)** MFoR, triple wake

(c) FFoR, quadruple wake **(d)** MFoR, quadruple wake

Figure 6.18: Investigation of the performance of the merged wake deficit model for multiple wake configuration. (a), (c) and (e): FFoR; (b), (d) and (f): MFoR

This indicates that the first model still performs fairly well for predicting the maximum wake deficits of the merged wake in configuration involving multiple turbines, but lack of accuracy in the prediction of the wake expansion.

6.4.3 Engineering wake expansion correction

The need for studying the wake expansion of each individual single wake contributions and the combined multiple wake expansion is motivated by the following:

- the wake expansion discrepancies between the model and the simulated profile increases with increasing number of turbines.
- the maximum wake deficit is well captured by the model in both FFoR and MFoR regardless of the number of turbines.

- the shear layer interaction of all four single wakes depicted in Fig. 6.18c seems to enhance deficit at the edge of the accumulated wake. This effect is underestimated by the present model and may be the source of expansion discrepancies.
- The lateral wake meandering magnitude at any given downstream position may be used to determined the wake expansion as following the modeling approach of Section 3.4.4. This in turn may be used as an engineering-based correction factor for the modeled deficit.

6.4.3.1 Multiple wake meandering

The lateral meandering of the multiple wake depicted in Fig. 6.19a is investigated. As seen in Fig. 6.19c, 6.19d, 6.19e and 6.19f the overall meandering magnitude increases with respect to the downstream distance, following the conjecture of the DWM model for single wakes. However, a decrease in meandering at cross sections 4D, 5D, 8D, 9D, 12D, 13D corresponding to each of the rotor position and 1D downstream of them, respectively, is observed. This indicates that at a location where wake overlapping occurs, the nearest and most dominant wake governs the meandering dynamics and that a sharp decrease in wake expansion is observed. This effect can be observed in Fig. 6.19a. It is also seen that the time lag between the correlated meandering paths gradually increases with respect to the downstream distance, so that the accumulated wake advection velocity gradually decreases. As part of a future analysis, the validation of the empirical advection velocity model of Section 3.3.2 will be performed for multiple wakes.

6.4.3.2 Multiple wake expansion

The model formulated in Eq. 3.25, which relates the wake expansion generated from the lateral wake meandering combined with an initial wake expansion obtained from momentum theory, is presently reused. In Fig. 6.20, the single wake expansion coefficient is plotted together with the wake expansion along the row of 4 turbines as function of downstream distance from $T1$. It is seen in Fig. 6.20 that the along-row wake expansion does not grow monotonically, as opposed to the single wake growth. The expansion gradient is higher after each rotor as the mean wind speed decreases along the turbine row which is associated with an increased C_T.

As seen on Fig. 6.18, the simulated deficit displays a larger expansion that the modeled one. It appears that, in multiple wake configuration, the single wake expansion displayed by the most upstream turbine influences the wake width of the multiple wake more drastically than predicted by the model. Two corrections are considered at this stage: 1) a different wake summation strategy outside the wake core corresponding to the portion of the wake outside the 1 diameter width, which can be motivated by the fact that the axial force distribution along a blade is not uniform or 2), an artificial expansion correction which essentially act as a scaling of the lateral position.

In the latter, the scaling would be determined as the ratio between expansion coefficient from the single wake expansion shown in Fig. 6.20 and the one from the along-row wake

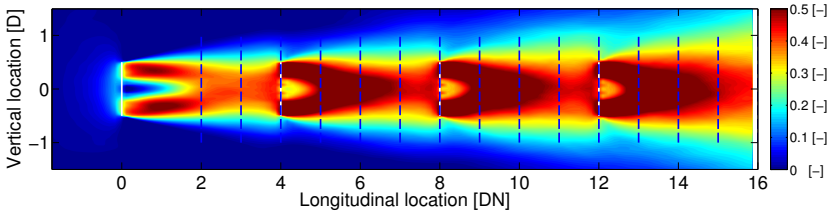

(a) Cross sections for meandering analysis

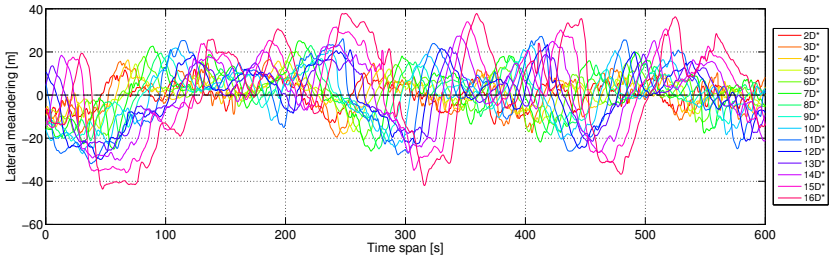

(b) Lateral meandering paths for 10 minute time series.

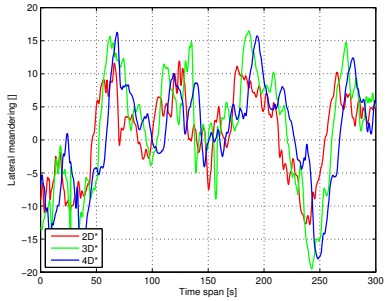

(c) Paths of single wake, 5 min

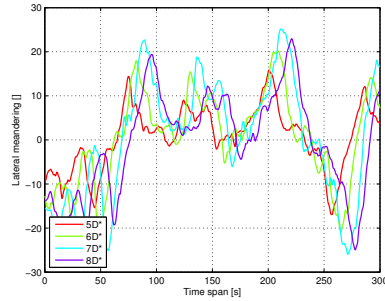

(d) Paths of double wake, 5 min

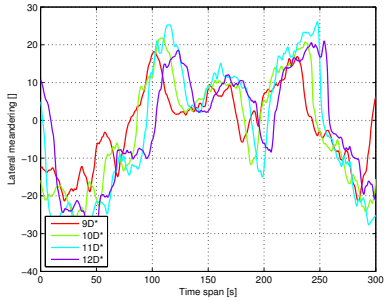

(e) Paths of triple wake, 5 min

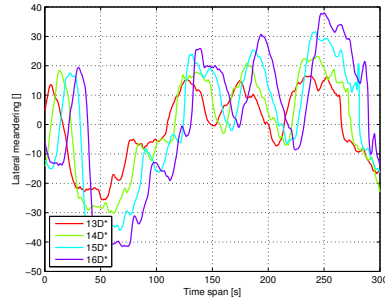

(f) Paths of quadruple wake, 5 min

Figure 6.19: Multiple wake meandering investigation.

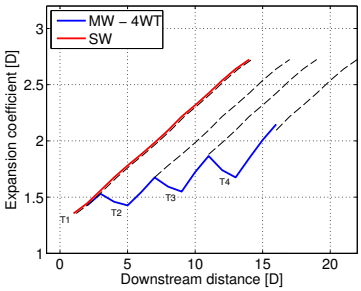

(a) Expansion coefficient

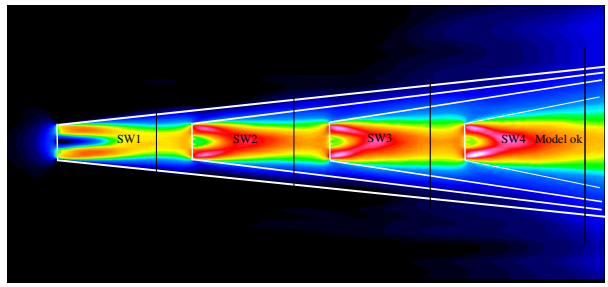

(b) Multiple wake expansion

Figure 6.20: (a) Expansion coefficient for the single wake of $T1$ and the multiple wake as depicted in (b) as function of the downstream distance from $T1$.

expansion, at a given downstream position. Therefore this scaling would increase with increasing number of turbine, as the difference between expansion magnitude becomes larger as we move downstream the row of turbine.

The lateral scaling is then defined as:

$$s(k) = \frac{\tilde{E_{T1k}}}{\tilde{E_{MWk}}} \tag{6.10}$$

where k is the downstream distance in rotor diameters, $\tilde{E_{T1}}$ is the wake expansion coefficient of turbine 1 only, $\tilde{E_{MW}}$ is the multiple wake turbine expansion involving all 4 turbines. The corresponding $s(k)$ values are 1.11, 1,29 and 1.31 for the double, triple and quadruple wake, where $k = 8, 12, 15$ rotor diameters, respectively.

6.4.3.3 Application of engineering expansion correction

The previous wake stretching $s(k)$ coefficients is applied to the uncorrected model results shown in Fig. 6.18. Results are shown in Fig. 6.21. The present calibration expansion seems to enhance substantially the agreement between modeled and simulated deficit after 2, 3, and 4 turbines respectively. However, this lateral stretching is purely engineering-based and therefore is not justified in any physical respect. Furthermore, such artificial expansion correction alter significantly the momentum related to the turbine thrusts. Thus, this analysis should only be regarded as an investigation of the contribution of the most upstream generated wake to the total expansion of 4 overlapped wakes.

6.4.4 Second modeling approach with multiple wakes

The performance of the second model is tested on the configuration involving 3 turbines. Due to the lack of downstream cross section above 8 diameters downstream for $T2$, it was

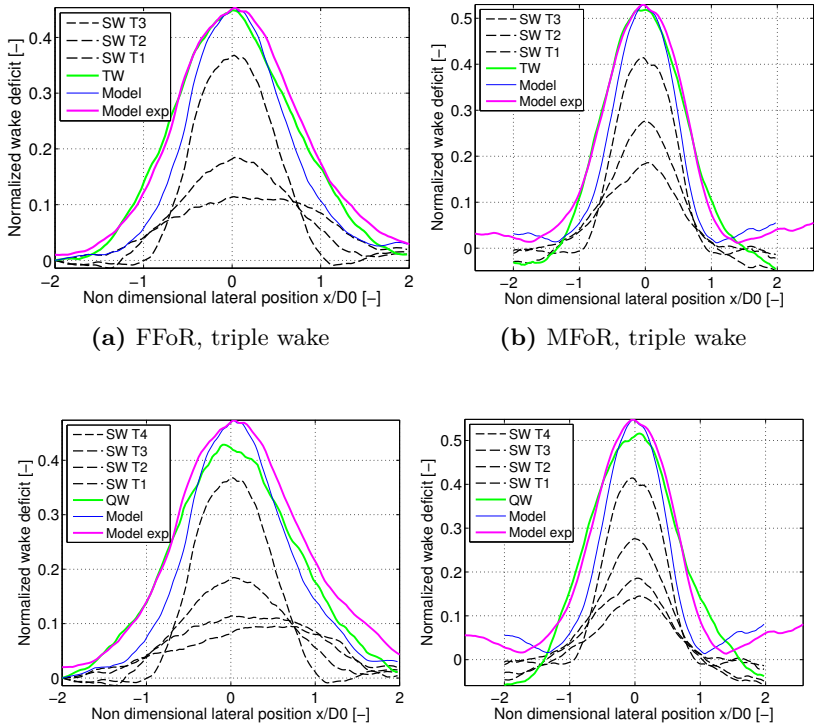

(a) FFoR, triple wake

(b) MFoR, triple wake

(c) FFoR, quadruple wake

(d) MFoR, quadruple wake

Figure 6.21: Investigation of the performance of the expansion correction of the merged wake deficit model for multiple wake configuration. (a), (c) and (e): FFoR; (b), (d) and (f): MFoR.

not possible to perform the analysis for the quadruple wake configurations generated by the 4 upstream turbines.

As seen in Fig. 6.22, the performance of the second modeling approach in triple wake configuration is fair when considering the FFoR and good for the MFoR. Both maximum deficit and wake width are captured with a good level of accuracy.

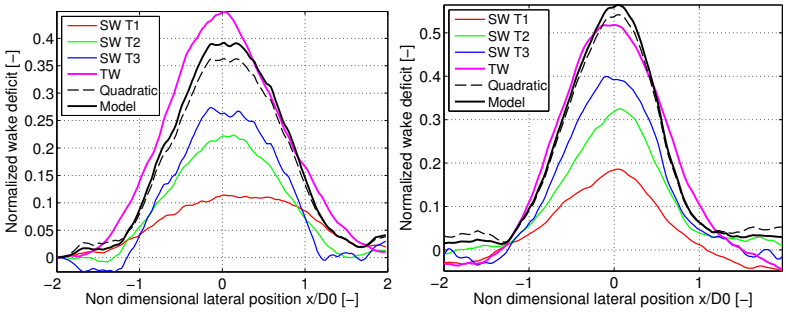

(a) FFoR **(b)** MFoR

Figure 6.22: Comparison of the wake deficit generated by 3 turbines in a row predicted by the second modeling approach with the simulated profile by EllipSys3D.

6.5 Summary

In this chapter, 2 overlapping wind turbine wakes have been studied numerically based on a parametric LES AD study involving 10 minutes unsteady simulations under 4 various mean wind speeds, 2 turbine spacing and 2 turbulence intensities. The performance of two commonly found single wake summation techniques has been assessed using a test matrix covering all kinds of wake flow regime.

As part of a first order approach, the single wake generated by the downstream turbine was assumed similar to the one generated by the upstream turbine, which implies that both inflow conditions of both turbines are identical. This analysis revealed that the performance of each of the summation techniques in the fixed frame of reference is highly dependent on the wind turbine thrust loading. High thrust coefficients obtained at low wind speed generates situations where very pronounced wake deficits should be added quadratically to obtain a fair representation of the double wake deficit profile after the downstream turbine. Single wake generated from wind turbine at low thrust coefficients (high mean wind speeds) should be added linearly to represent with a fair degree of accuracy the double wake deficit. At an intermediate regime, corresponding to thrust coefficients of the order of 0.5, both contribution from quadratic and linear summation should be averaged to properly capture the double wake deficit. In the meandering frame of reference of the wake, the quadratic summation shows a good performance for all tested situations.

An engineering model, based on a weighted average of the linear wake superposition and the square root of sums of squares wake superposition, was developed where the weighting factor is linked to the turbine thrust coefficient. The performance of this model was tested on configurations involving 2, 3 and 4 overlapping wakes, respectively. The prediction accuracy of this new model was found to be fair for predicting the maximum wake deficit in the merged wake flow field, however, associated to a rather large underestimation of the wake expansion.

Furthermore, a second modeling approach aiming at improving the superposed wake expansion was proposed. In this approach, a more realistic inflow conditions, making use of a reduced wind speed generated by the wake of the upstream turbine, was adopted to simulate the double wake flow field. A comparison of model predictions and simulations on 2 and 3 superposed wakes revealed that the model is able to capture with a good level of accuracy both the merged wake maximum deficit and the wake expansion for the present set up involving two stall regulated turbines. A future investigation is required to assess the performance of the model using modern pitch regulated turbines. Specifically, a verification of the present model assumption as well as its calibration is required to further evaluate the model accuracy.

Chapter 7

Conclusion

7.1 Summary of the research

In the present thesis, wind turbine single and multiple wakes have been studied experimentally and numerically. The experimental work comprised a detailed characterization of the wake flow field based on several continuous wave and pulsed lidar measurement campaigns. As part of the pulsed lidar experimental data analysis, basic assumption of the Dynamic Wake Meandering model were validated by studying the so-called meandering path of the wake during its downstream transportation. Furthermore, empirical relationship of wake advection velocity and mean wake expansion were developed, based on the main assumptions of the validated DWM model, combined with momentum and vortex theory.

High speed continuous wave lidars were used to characterize the mean velocity and turbulence field in the wake of 2 turbines at the Tjæreborg Enge wind farm, and at the DTU Wind Energy Risø campus test site. In the latest experiment, the analysis proved challenging due to the lack of properly calibrated sensor and uncertainties inherent to full-scale measurements.

Additionally, the impact of the atmospheric stability on the wind turbine wake dynamics was studied as part of a IEA - Task 31 'WakeBench' benchmark to assess the performance of an in house CFD code to model wakes in non neutral atmospheric surface layer. As part of the analysis, the impact of atmospheric stability on the large and small scale wake flow characteristics was investigated, as well as the applicability of the DWM with non neutral atmospheric flows.

The various full-scale measurement campaigns were used to validate the in house CFD model EllipSys3D, using LES and AL / AD techniques. This high fidelity model was used as part of a parametric study aiming at studying overlapping wake characteristics

in a generic way, i.e. under various turbine loading, spacing and turbulence intensity. A merged wake modeling attempt was proposed based on a combination of quadratic and linear summation of single wake deficits. The present form of the model proved robust for predicting both the maximum overlapped merged wake deficit and the merged wake mean expansion.

7.2 Future work

7.2.1 Experimental work

As part of the double wake experiment, the WindScanner was set to a very high scanning speed corresponding to 400 measurements per second and 1 second per wake lidar sweep during the last week of the measurement campaign. In this period, several single wake situation were recorded at a very high time and spatial resolution. An analysis focusing on the turbulence characterization of these single wake recordings will be conducted in the future using two approaches.

The first approach is to use the measured line-of-sight velocity at this high scanning rate to study the agreement in the average streamwise Reynolds stress tensor between lidar measurement and CFD simulations. This validation may serve as basis to the study of wake added turbulence in a row of wind turbines.

The second approach is to investigate the possibility of extracting the line-of-sight turbulence properties of the flow directly from the analysis of the raw Doppler spectral width as based on the work by Branlard et al. in [21] and Sathe at al. in [126]. This analysis would give more insight into turbulence mechanism in the merged wake flow field.

Another future experimental research will be based on the newly developed 3D WindScanner lidar, composed by 3 synchronized lidar beam capable of resolving the 3D wind components. In order the reduce the uncertainties due to terrain effect observed at the DTU Wind Energy Risø test site, it is recommended that this new experiment would take place in a uniform flat terrain such as the Høvsøre test site. Such measurement campaign would give more insight into the 3D characteristic of the wake flow field and further validate numerical model. Specifically, measurement of the lateral wind component in the atmosphere is of great interest for the study of wake meandering.

Furthermore, the highly detailed wake measurements recorded by the WindScanner can be used as part of a new wake analysis framework making use of Proper Orthogonal Decomposition (POD) of the wake flow field, similar to the work by Andersen et al. in [9]. In this investigation, the main wake turbulent structures from measurements will be compared to CFD using the POD framework, in both single and double wake situations. This analysis would then serve as basis to the development of lower order engineering model of wind farm flows.

7.2.2 Modeling / numerical work

The newly developed advection, expansion and wake deficit accumulation models will be integrated in various in house engineering tools for power and load prediction (DWM model) as well as wind farm topology optimization (TOPFARM platform). A sanity test will be performed on a similar case as the study by Larsen et al in [74]. The performance of the wake expansion model developed in Section 3.4.4 for non neutral flow condition will be investigated in the near future. It is assumed presently that the various atmospheric stabilities are formulated inside this model through the large scale lateral turbulence $\tilde{\sigma_{v_c}}$ which varies with the atmospheric stratification.

The research presented in Chapter 6 will be further extended to study the turbulence characteristics in the merged wake flow field as function of the ambient turbulence and the turbines generated turbulence. This study will be based on numerical simulation of large wind farm making use of modern pitch regulated turbines. Moreover, a new formulation of this model making use of a radially dependent thrust coefficient may also be tested. In this approach, the deficit summation technique would depend on the radial position along the actuator discs, which could lead to a more universal formulation of wake superposition when turbine are not perfectly aligned with each other, i.e. when half wake situation or sideways wake interaction originating from 2 parallel rows of turbine occur. Additionally, the time series of normal and tangential load extracted for all computations at several radial and azimuthal positions on the actuator disc will be analyzed. Specifically, an analysis where correlation between the relative position of the wake (obtained from the meandering paths), the instantaneous power production and the rotor loading will be investigated.

Furthermore, the present sets of computation will be used as part of a wake overlapping benchmark. In this benchmark, two additional models will be tested. The first one is presently used with the Dynamic Wake Meandering model which assumes that the wake affected downstream flow field is determined by a superposition of the ambient flow field and the *dominating* wake among contributions from all upstream turbines at any spatial position (at any time instant). The second approach is based on newly developed overlapping wake model [69]. This model is based on a successive type of approach which combines wake deficits two-by-two where, in each step, the continuity equation as well as momemtum conservation on a control volume approach is assured.

The newly developed in-house coupled Aeroelastic / CFD framework (HAWC2/EllipSys3D) will be used as part of a detailed investigation of wake induced load in half and full wake situation, thus extending the work of Troldborg et al. in [146]. This analysis will benefit from the generic turbine controller implemented in the Aeroelastic code which allow the turbine to freely respond to the incoming wind as opposed to the present approach at fixed yaw position. Therefore, modern pitch regulated turbine will be used as opposed to the stall regulated turbines used in the present research.

Finally, the present LES ABL modeling approach will be further developed to include a more realistic modeling of the rough wall at the bottom of the domain, as well as extending its application to flow over non uniform terrain.

Appendix A

Appendix

A.1 Post processing GUI of multiple lidar campaign

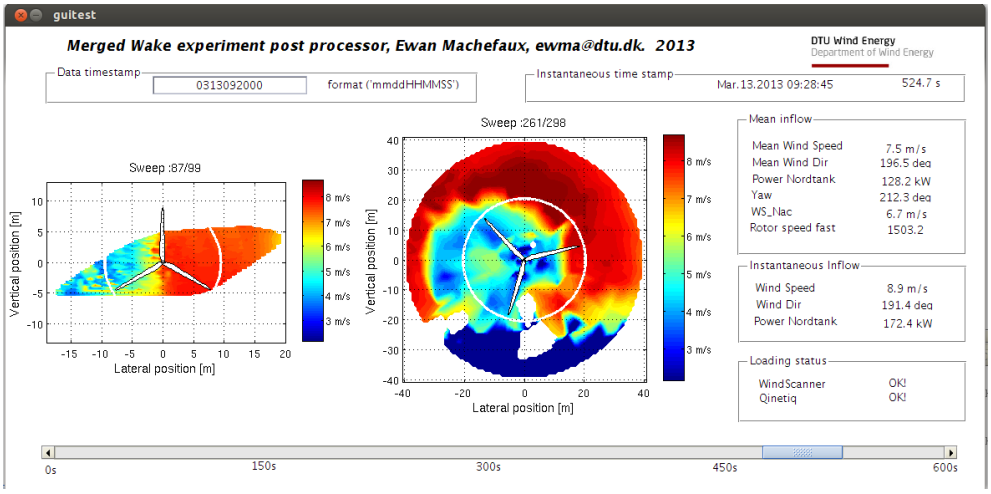

Figure A.1: Screenshot of the post processing program developed as part of the double wake lidar experiment. Investigation of unsteady wake velocity is facilitated by the scrolling bar scanning through the 10 minutes time series.

A.2 EllipSys3D AL and AD comparison

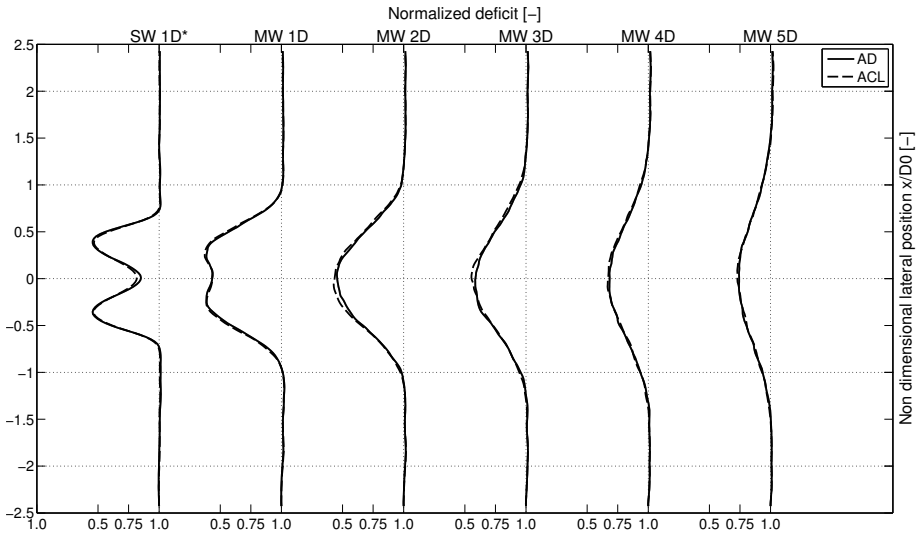

(a) Normalized wake velocity

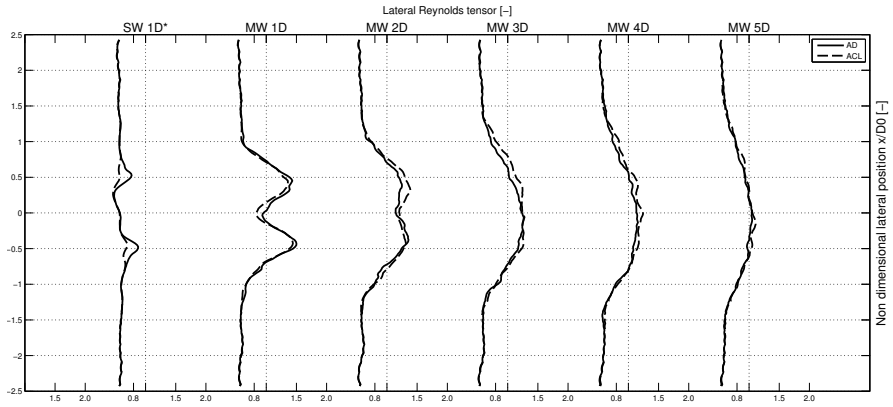

(b) Lateral Reynolds stress

Figure A.2: Double wake analysis using both AD and AL rotor modeling methods. The dash lines showns the AL results and the full line shows the AD results.

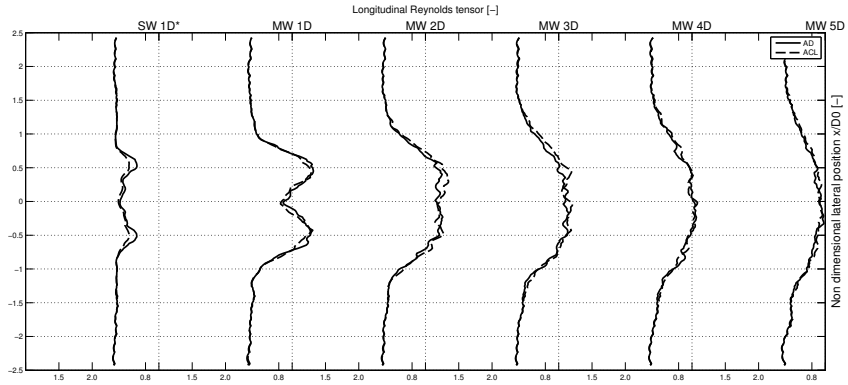

(a) Longi_Reynolds_AD_ACL

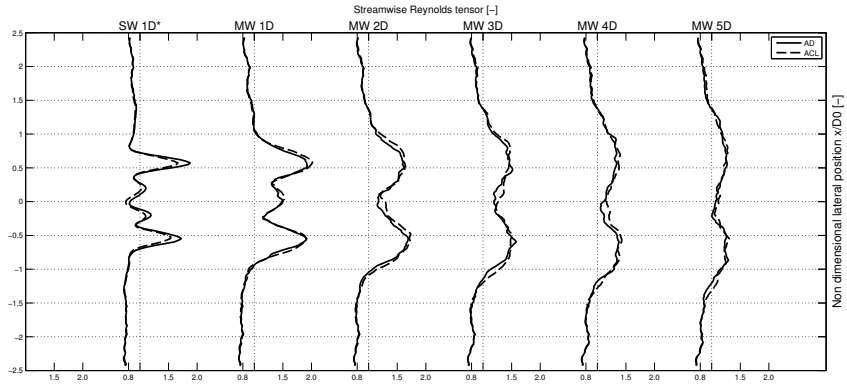

(b) Streamwise Reynolds stress

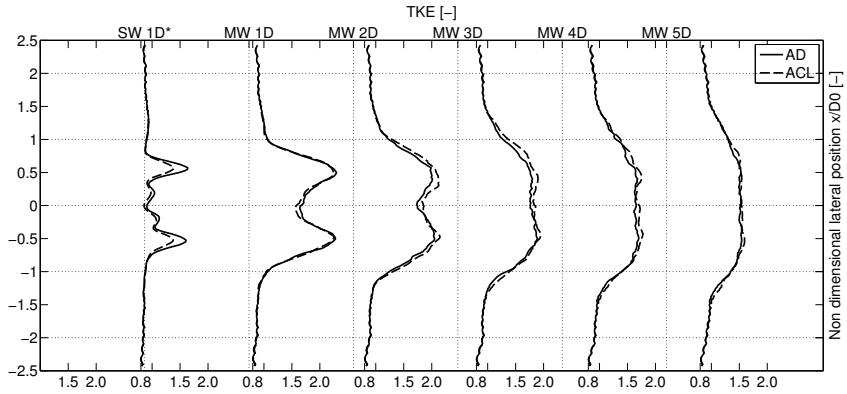

(c) TKE

Figure A.3: Double wake analysis using both AD and AL rotor modeling methods. The dash lines showns the AL results and the full line shows the AD results.

A.3 Wakes in non neutral ABL: validation of 3 neutral test cases

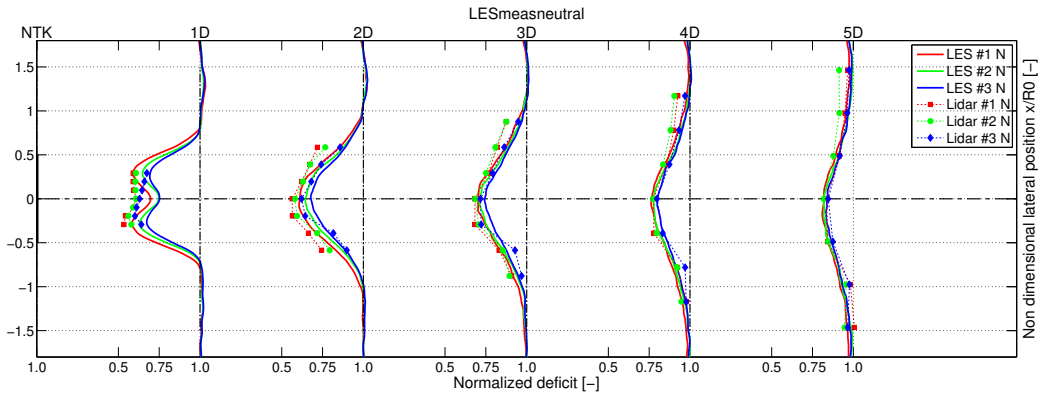

(a) Wake at hub height.

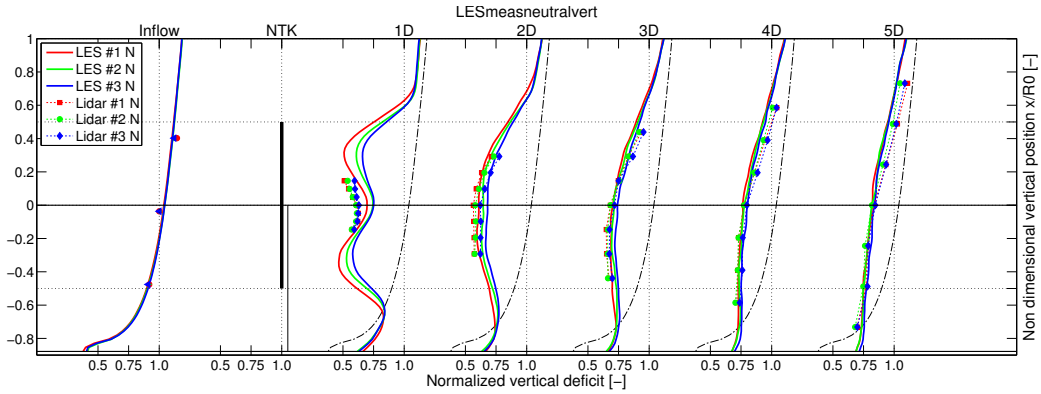

(b) Vertical wake profile.

Figure A.4: Comparison of measured and modeled wake velocity in the near wake of the Nordtank turbine under neutral atmospheric stability conditions for three different wind speeds listed in the table below.(a) represents the wake at hub height and seen from the top. (b) is the corresponding vertical profile along a vertical axis aligned with the turbine tower. Dash lines indicates the mean inflow profile.

Table A.1: Main parameters of the test cases with similar inflow velocities. The values in parentheses correspond to bin mean of all relevant 10 minute wind speed standard deviations and the standard deviation of the bin stability measure, respectively. The shear exponent is obtained from a power law fitting to the inflow measurements at 16.5 m, 34.5 m and 52.5 m altitude.

Test case index	Stability class and bin limits	Obukhov length 16.5m a.g.l. [m]	Inflow velocity at hub height [m/s]	Turbulence intensity at hub height I_{ref} [-]	Turbulent kinetic energy $[m^2/s^2]$	Measured thrust coefficient [-]	Measured Elec. power [kW]	Shear exponent ν [-]	Dataset length [h]
#1 (N)	Neutral $\|(L)\|\geq 500$	1677.7 (362.9)	7.03 (0.89)	0.14	1.42	0.75	125.61	0.19	3.2
#2 (N)	Neutral $\|(L)\|\geq 500$	1326.3 (803.9)	8.92 (1.15)	0.13	1.83	0.66	250.32	0.17	4.7
#3 (N)	Neutral $\|(L)\|\geq 500$	2441.5 (964.0)	9.86 (1.38)	0.14	2.47	0.63	309.88	0.18	5.5

A.4 LES parametric study: merged wake deficits

A.4.1 Observations at 4D spacing and 6% turbulence intensity

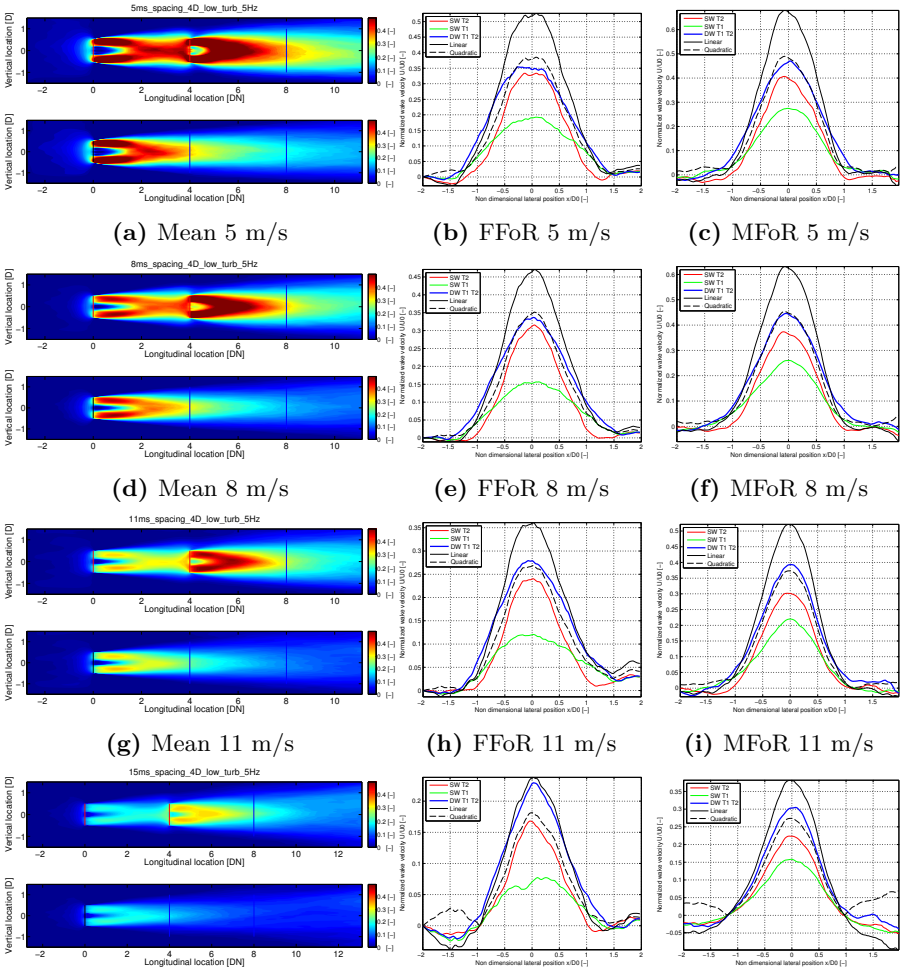

(a) Mean 5 m/s **(b)** FFoR 5 m/s **(c)** MFoR 5 m/s

(d) Mean 8 m/s **(e)** FFoR 8 m/s **(f)** MFoR 8 m/s

(g) Mean 11 m/s **(h)** FFoR 11 m/s **(i)** MFoR 11 m/s

(j) Mean 15 m/s **(k)** FFoR 15 m/s **(l)** MFoR 15 m/s

Figure A.5: Merged wake after two upstream turbines separated by 4 D under low atm. turb. In (a), (d), (g) and (j), the blue line represents the location where wake are extracted and analyzed. In (b), (e), (h) and (k), the single wake contributions are shown in green and red for the most upstream turbine $T1$ and the downstream turbine $T2$, respectively.

A.4.2 Observations at 7D spacing and 6% turbulence intensity

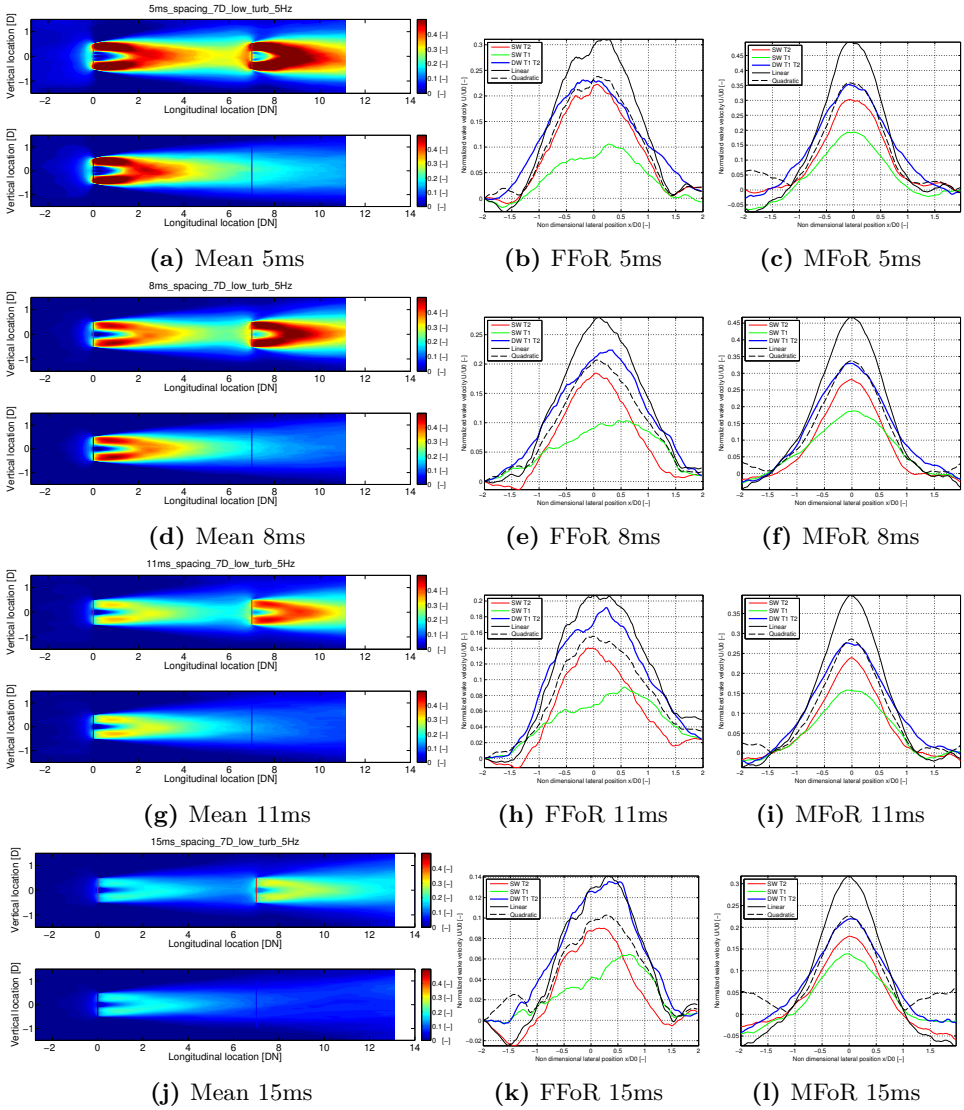

(a) Mean 5ms **(b)** FFoR 5ms **(c)** MFoR 5ms

(d) Mean 8ms **(e)** FFoR 8ms **(f)** MFoR 8ms

(g) Mean 11ms **(h)** FFoR 11ms **(i)** MFoR 11ms

(j) Mean 15ms **(k)** FFoR 15ms **(l)** MFoR 15ms

Figure A.6: Merged wake after two upstream turbines separated by 7 D under low atm. turb. In (a), (d), (g) and (j), the blue line represents the location where wake deficits are extracted and analyzed. In (b), (e), (h) and (k), the single wake contributions are shown in green and red for the most upstream turbine T1 and the downstream turbine $T2$, respectively.

A.4.3 Observations at 4D spacing and 12% turbulence intensity

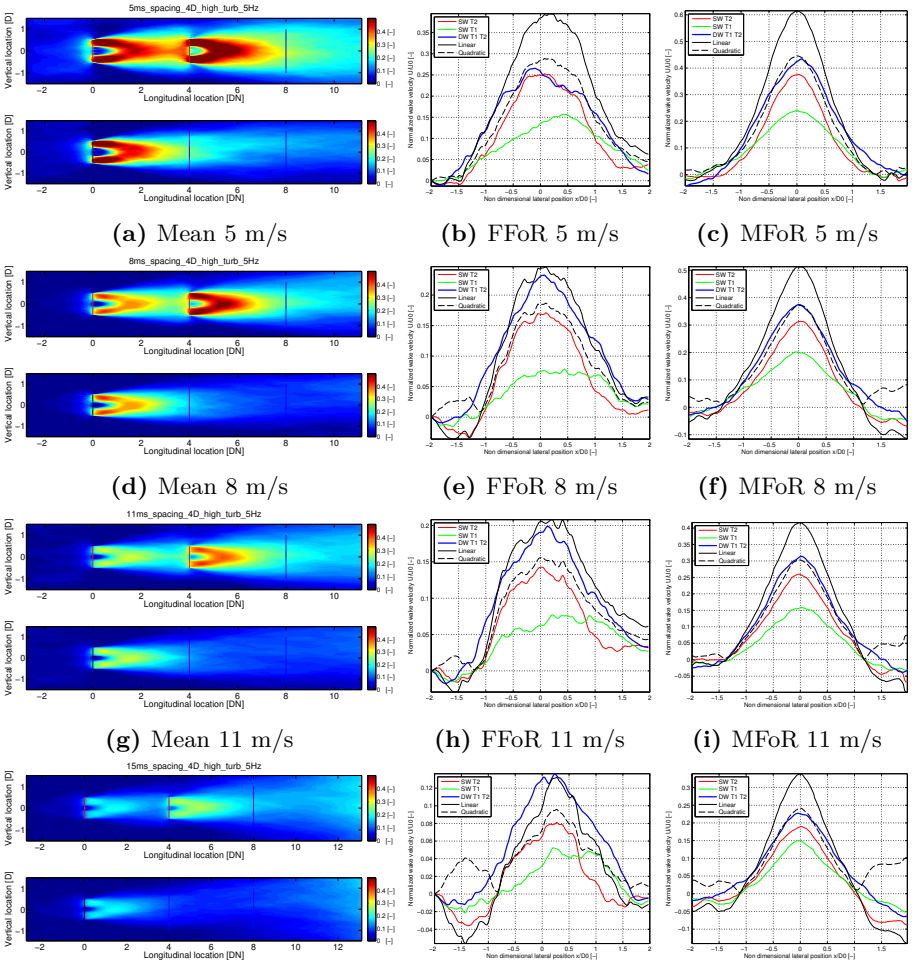

(a) Mean 5 m/s **(b)** FFoR 5 m/s **(c)** MFoR 5 m/s

(d) Mean 8 m/s **(e)** FFoR 8 m/s **(f)** MFoR 8 m/s

(g) Mean 11 m/s **(h)** FFoR 11 m/s **(i)** MFoR 11 m/s

(j) Mean 15 m/s **(k)** FFoR 15 m/s **(l)** MFoR 15 m/s

Figure A.7: Merged wake after two upstream turbines separated by 4 D under high atm. turb. In (a), (d), (g) and (j), the blue line represents the location where wake deficits are extracted and analyzed. In (b), (e), (h) and (k), the single wake contributions are shown in green and red for the most upstream turbine T1 and the downstream turbine $T2$, respectively.

A.4.4 Observations at 7D spacing and 12% turbulence intensity

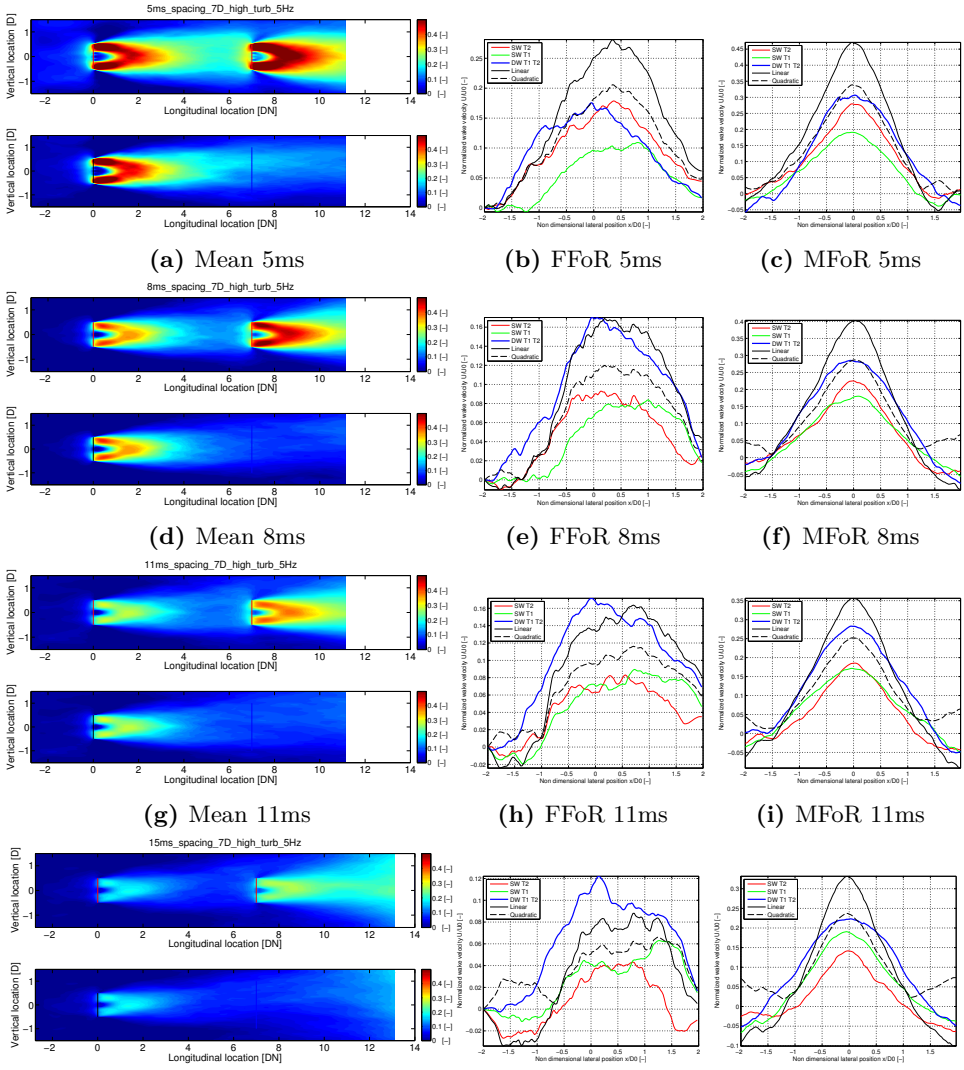

(a) Mean 5ms **(b)** FFoR 5ms **(c)** MFoR 5ms

(d) Mean 8ms **(e)** FFoR 8ms **(f)** MFoR 8ms

(g) Mean 11ms **(h)** FFoR 11ms **(i)** MFoR 11ms

(j) Mean 15ms **(k)** FFoR 15ms **(l)** MFoR 15ms

Figure A.8: Merged wake after two upstream turbines separated by 7 D under high atm. turb. In (a), (d), (g) and (j), the blue line represents the location where wake deficits are extracted and analyzed. In (b), (e), (h) and (k), the single wake contributions are shown in green and red for the most upstream turbine $T1$ and the downstream turbine $T2$, respectively.

Bibliography

[1] World Wind Energy Association. http://www.wwindea.org/home/index.php. Accessed: 2014-09-11.

[2] Mahdi Abkar and Fernando Porté-Agel. Influence of atmospheric stability on wind-turbine wakes: A large-eddy simulation study. *Physics of Fluids*, 27(3):035104, 2015.

[3] Abramovich. *The theory of turbulent jets.*

[4] J.F. Ainslie. Wake modelling and the prediction of turbulence properties. *Proceedings of the 8th British Wind energy Association*, 1986.

[5] J.F. Ainslies. Calculating The Flow Field In The Wake of Wind Turbines. *Journal of Wind Engineering and Industrial Aerodynamics*, 27:213–224, 1988.

[6] Matthew L. Aitken, Robert M. Banta, Yelena L. Pichugina, and Julie K. Lundquist. Quantifying Wind Turbine Wake Characteristics from Scanning Remote Sensor Data. *Journal of Atmospheric and Oceanic Technology*, 31(4):765–787, 2014.

[7] D. G. Akhmetov. *Vortex Rings.* Springer, 2009.

[8] I. Ammara, C. Leclerc, and C. Masson. A Viscous Three-Dimensional Differential/Actuator-Disk Method for the Aerodynamic Analysis of Wind Farms. *Journal of Solar Energy Engineering*, 124(4):345, 2002.

[9] S.J. Andersen, J.N. Sørensen, and R.F. Mikkelsen. Simulation of the inherent turbulence and wake interaction inside an infinitely long row of wind turbines. *Journal of Turbulence*, 14(4):1–24, 2013.

[10] N. Angelou, F. Foroughi Abari, J. Mann, T. Mikkelsen, and M. Sjöholm. *Challenges in noise removal from Doppler spectra acquired by a continuous-wave lidar.* 2012.

[11] N. Angelou, T. Mikkelsen, K.H. Hansen, and M. Sjöholm. *LIDAR Wind Speed Measurements from a Rotating Spinner : "SpinnerEx 2009" Risø-R-Report*, volume 1741. 2010.

[12] C. Bak, J. Johansen, and P.B. Andersen. Three-dimensional corrections of airfoil characteristics based on pressure distributions. *European Wind Energy Conference & Exhibition - Athens, Greece*, 2006.

[13] C. Bak, F. Zahle, R. Bitsche, T. Kim, A. Yde, L. C. Henriksen, M. H. Hansen, J. P. A. A. Blasques, M. Gaunaa, and A. Natarajan. The DTU 10-MW Reference Wind Turbine, 2013. PowerPoint.

[14] R J Barthelmie. Universal benchmarks for wind turbine wake and wind farm models. *Wind Energy*, (April):828655, 2010.

[15] R. J. Barthelmie, K. Hansen, S. T. Frandsen, O. Rathmann, J. G. Schepers, W. Schlez, J. Phillips, K. Rados, A. Zervos, E. S. Politis, and P. K. Chaviaropoulos. Modelling and measuring flow and wind turbine wakes in large wind farms offshore. *Wind Energy*, 12(5):431–444, 2009.

[16] R. J. Barthelmie and L. E. Jensen. Evaluation of wind farm efficiency and wind turbine wakes at the Nysted offshore wind farm. *Wind Energy*, 13(6):573–586, May 2010.

[17] A. Bechmann, J. Mann, J. Johansen, N. N. Sørensen, and J. N. Sørensen. *Large-eddy simulation of atmospheric flow over complex terrain*. PhD thesis, 2007. Risø-PhD-28(EN).

[18] Ferhat Bingöl, Jakob Mann, and Gunner C. Larsen. Light detection and ranging measurements of wake dynamics part i: one-dimensional scanning. *Wind Energy*, 13(1):51–61, 2010.

[19] E. Branlard and M. Gaunaa. Development of new tip-loss corrections based on vortex theory and vortex methods. *The Science of Making Torque from Wind 2012, Oldenburg*, 2012.

[20] E. Branlard, E. Machefaux, M. Gaunaa, H.H Sørensen, and N. Troldborg. Validation of vortex code viscous models using lidar wake measurements and CFD. In *Proceedings of EWEA 2014, Barcelona, Spain*. European Wind Energy Association (EWEA), 2014.

[21] E. Branlard, A. T. Pedersen, J. Mann, N. Angelou, A. Fischer, T. Mikkelsen, M. Harris, C. Slinger, and B. F. Montes. Retrieving wind statistics from average spectrum of continuous-wave lidar. *Atmospheric Measurement Techniques*, 6(7):1673–1683, 2013.

[22] T. Burton, D. Sharpe, N. Jenkins, and E. Bossanyi. *Wind Energy Handbook*. J. Wiley & Sons, 2002.

[23] J.A. Businger. Transfer of momentum and heat in the planetary boundary layer. In *Proceedings of the Symposium on Arctic Heat Budget and Atmospheric Circulation*, pages 305–332, 1966.

[24] M. Calaf, C. Meneveau, and J. Meyers. Large eddy simulation study of fully developed wind-turbine array boundary layers. *Physics of Fluids*, 22(1):015110, 2010.

[25] D.E. Cartwright and M.S. Longuet-Higgins. The statistical distribution of the maxima of a random function. In *Series A 237, pp, Mathematical and Physical Sciences*, pages 212–232. Royal Society of London, 1956.

[26] Leonardo P. Chamorro and Fernando Porté-Agel. Effects of Thermal Stability and Incoming Boundary-Layer Flow Characteristics on Wind-Turbine Wakes: A Wind-Tunnel Study. *Boundary-Layer Meteorology*, 136(3):515–533, June 2010.

[27] Abhijit Chougule. Influence of atmospheric stability on the spatial structure of turbulence Risø-PhD-Report. (May), 2013.

[28] M. J. Churchfield, S. Lee, P. Moriarty, L. A. Martinez, S. Leonardi, G. Vijayakumar, and JG. Brasseur. A Large-Eddy Simulation of Wind-Plant Aerodynamics. *50th AIAA Aerospace, Science Meeting January 2012, Nashville, Tennessee*, 2012.

[29] M.J. Churchfield, S. Lee, J. Michalakes, and P.J. Moriarty. A numerical study of the effects of atmospheric and wake turbulence on wind turbine dynamics. *Journal of Turbulence*, 13:N14, January 2012.

[30] J.W. Cleijne. Results of Sexbierum wind farm; single wake measurements. Technical report, TNO Environmental and Energy Research report, March 1993.

[31] R. P. Coleman, A. M. Feingold, and C.W. Stempin. Evaluation of the induced-velocity field of an idealized helicopter rotor. *NACA ARR No. L5E10*, 1945.

[32] A. Crespo and J. Hernandez. Numerical modelling of wind turbine wakes. In *Scientific proceedings*, pages 166–170. EWEC 1990 Madrid, 1990.

[33] A. Crespo, J. Hernández, and S. Frandsen. Survey of modelling methods for wind turbine wakes and wind farms. *Wind Energy*, 1:1–24, 1999.

[34] Smith D. and Taylore G.J. Further analysis of turbine wake development and interaction data. In *Scientific proceedings*, pages 325–331. 13th BWEA Wind Energy Conf. Swansea, 1991.

[35] Amina El Kasmi and Christian Masson. An extended model for turbulent flow through horizontal-axis wind turbines. *Journal of Wind Engineering and Industrial Aerodynamics*, 96(1):103–122, January 2008.

[36] G. España, S. Aubrun, S. Loyer, and P. Devinant. Wind tunnel study of the wake meandering downstream of a modeled wind turbine as an effect of large scale turbulent eddies. *Submitted for Journal of Wind Engineering and Industrial Aerodynamics*, 2011.

[37] T. M. Fletcher and R. E. Brown. Simulation of wind turbine wake interaction using the vorticity transport model. *Wind Energy*, 2009.

[38] S. Frandsen. On the wind speed reduction in the center of large clusters of wind turbines. 39:251–265, 1992.

[39] S. T. Frandsen. Turbulence and turbulence generated structural loading in wind turbine clusters. Technical report, Risø-R-1188(EN), Risø National Laboratory, Roskilde, Denmark, 2007.

[40] M. Gaumond. Evaluation and Benchmarking of Wind Turbine Wake Models. 2012.

[41] M. Gaumond and P.E. Réthoré. Evaluation of wind direction uncertainty and its impact on wake modelling at the Horns Rev offshore wind farm. *Wind Energy*, 2013.

[42] A. A. Grachev and C. W. Fairall. Dependence of the monin-obukhov stability parameter on the bulk richardson number over the ocean. *American Meteorology Society*, 36:406–414, 1997.

[43] G. Habenicht. Offshore wake modelling. Presentation at Renewable UK Offshore Wind, 2011.

[44] K. S. Hansen, R. Barthelmie, L. E. Jensen, and A. Sommer. The impact of turbulence intensity and atmospheric stability on power deficits due to wind turbine wake at Horns Rev wind farm. *Journal of Wind Energy*, 15:183–196, 2012.

[45] K. S. Hansen, R.J. Barthelmie, L.E. Jensen, and A. Sommer. The impact of turbulence intensity and atmospheric stability on power deficits due to wind turbine wakes at Horns Rev wind farm. *Wind Energy*, 15(1):183–196, 2012.

[46] M.O.L. Hansen. *Aerodynamics of Wind Turbines - Second Edition.* Earthscan, London, Sterling, VA, 2008.

[47] U. Högström, D.N. Asimakopoulos, H. Kambezidis, C.G. Helmis, and A. Smedman. A field study of the wake behind a 2 MW wind turbine. *Atmospheric Environment (1967)*, 22(4):803–820, January 1988.

[48] Giacomo Valerio Iungo and Fernando Porté-Agel. Volumetric Lidar Scanning of Wind Turbine Wakes under Convective and Neutral Atmospheric Stability Regimes. *Journal of Atmospheric and Oceanic Technology*, 31(10):2035–2048, October 2014.

[49] G.V. Iungo, Y. Wu, and F. Porté-Agel. Field Measurements of Wind Turbine Wakes with Lidars. *Journal of Atmospheric and Oceanic Technology*, 30:274–287, 2013.

[50] S. Ivanell. Numerical Computation of Wind Turbine Wakes, PhD Thesis. *Royal Institute of Technology, Stockholm, Gotland University, Sweden*, 2009.

[51] S. Ivanell, R. Mikkelsen, J.N. Sørensen, and D. Henningson. Three dimensional actuator disc modelling of wind farm wake interaction. *interaction*, 1(2):3, 2008.

[52] S. Ivanell, J. N. Sørensen, R. Mikkelsen, and D. Henningson. Numerical analysis of the tip and root vortex position in the wake of a wind turbine. *Journal of Physics: Conference Series*, 75(1):012035, July 2007.

[53] N.S. Jens and Asger Myken. Unsteady actuator disc model for horizontal axis wind turbines. *Science*, 39:139–149, 1992.

[54] N. O. Jensen. A note on wind turbine interaction. Technical report, Risø-M-2411, Risø National Laboratory, Roskilde, Denmark, 1983.

[55] I. Katic, J. Høstrup, and N. O. Jensen. A simple model for cluster efficiency. *In proceedings of the European Wind Energy Association Conference and Exhibition (EWEC), Rome*, pages 407–410, 1986.

[56] R-E. Keck, M. de Maré, M.J. Churchfield, S. Lee, G.C. Larsen, and H. Aagaard Madsen. On atmospheric stability in the dynamic wake meandering model. *Wind Energy*, August 2013.

[57] Mark C. Kelly and Sven-Erik Gryning. Long-term mean wind profiles based on similarity theory. *Boundary-Layer Meteorology*, 136(3):377–390, 2010.

[58] T Koblitz, A Bechmann, A Sogachev, N Sørensen, and P.-E Réthoré. Computational Fluid Dynamics model of stratified atmospheric boundary-layer flow. 2013.

[59] P.M. Laan, van der, N.N. Sørensen, P-E. Réthoré, J. Mann, M. C. Kelly, N. Troldborg, J. G. Schepers, and E. Machefaux. An improved k-ϵ model applied to a wind turbine wake in atmospheric turbulence. *Wind Energy*, 2014.

[60] G. C. Larsen. A simple stationary semi-analytical wake model. *Technical Report Risø-R-1713(EN)*, 2009.

[61] G. C. Larsen, K. S. Hansen, N. Troldborg, J. Mann, K. Enevoldsen, and F. Bingöl. An attempt to characterize the structure of wake turbulence using a combined experimental and numerical approach. *Conference on Turbulence IV, Bertinoro (IT), 19-22 Sep*, 2010.

[62] G. C. Larsen, T. J. Larsen, J. Mann, A. Pena, K. S. Hansen, and H. Aa. Madsen. The dependence of wake losses on atmospheric stability characteristics. Risø National Laboratory for Sustainable Energy, Technical University of Denmark. *EUROMECH Colloquium 508 on Wind Turbine Wakes*, pages 35–37, 2009.

[63] G C Larsen, E Machefaux, and A Chougule. Wake meandering under non-neutral atmospheric stability conditions - theory and facts. *Journal of Physics: Conference Series*, 625(1):012036, 2015.

[64] G. C. Larsen, H. Aa. Madsen, T. J. Larsen, P.-E. Réthoré, and Peter Fuglsang. TOPFARM - A platform for wind farm topology optimization. *Book of Abstracts / Editor: Ivanell S. - Wake conference, Visvy, Sweden*, pages 40–42, 2011.

[65] G. C. Larsen, H.Aa. Madsen, and N. S. Sørensen. Mean Wake Deficit in the Near Field. In *Scientific proceedings*. EWEC 2003 Madrid, 2003.

[66] G. C. Larsen, J. Mann, K. S. Hansen, K. Enevoldsen, and F. Bingöl. Full-scale measurements of wind turbine wake turbulence. Proceedings of Torque 2010. The Science of Making Torque From Wind Energy. *Heraklion, Greece*, pages 391–405, 2010.

[67] G.C. Larsen. *A simple wake calculation procedure*. Risø-M-2760, 1988.

[68] G.C. Larsen. Wind fields in wakes. *1996 European Wind Energy Association*, 1996.

[69] G.C. Larsen. From solitary wakes to wind farm wind fields a simple engineering approach. Risø-R-1727(EN). Technical report, DTU Wind Energy, Roskilde, Denmark„ 2009.

[70] G.C. Larsen, T.J. Larsen, H. Aagaard Madsen, J. Mann, Alfredo P.D., R.J. Barthelmie, and L. Jensen. *The dependence of wake losses on atmospheric stability characteristics*, pages 35–37. Universidad Politecnica de Madrid, 2009.

[71] Gunner C. Larsen, Helge Aa. Madsen, Kenneth Thomsen, and Torben J. Larsen. Wake meandering: a pragmatic approach. *Wind Energy*, 11(4):377–395, 2008.

[72] T. J. Larsen, H. Aa. Madsen, G. C. Larsen, and K. S. Hansen. Validation of the Dynamic Wake Meander Model for Loads and Power Production in the Egmond aan Zee Wind Farm. *Submitted to Wind energy, 2012*.

[73] T.J. Larsen, G.C. Larsen, H. Aagaard Madsen, and K.S. Hansen. Wind farm production estimates. In *Proceedings of EWEA 2012 - European Wind Energy Conference & Exhibition*. European Wind Energy Association (EWEA), 2012.

[74] T.J. Larsen, H.Aa. Madsen, G.C. Larsen, and K.S. Hansen. Validation of the dynamic wake meander model for loads and power production in the egmond aan zee wind farm. *Wind Energy*, 16(4):605–624, 2013.

[75] S. Lee, M. Churchfield, P. Moriarty, J. Jonkman, and J. Michalakes. Atmospheric and Wake Turbulence Impacts on Wind Turbine Fatigue Loadings. *50th AIAA Aerospace, Science Meeting January 2012, Nashville, Tennessee*, 2012.

[76] J. Lemming, P.E. Morthorst, and N-E. Clausen. *Contribution to the Chapter on Wind Power Energy Technology Perspectives 2008*, volume 1674. 2008.

[77] P. Lindelöw-Marsden. Upwind D1. Uncertainties in wind assessment with LIDAR. *Risø-R-1681 (EN), Risø National Laboratory, Roskilde, Denmark*, 2009.

[78] P.B.S. Lissaman. Energy effectiveness of arbitrary arrays of wind turbines. *Journal of Energy*, 3(6):323–328, 1979.

[79] H. Lu and F. Porté-Agel. Large-eddy simulation of a very large wind farm in a stable atmospheric boundary layer. *Physics of Fluids*, 23(6):065101, June 2011.

[80] J.K. Lundquist, E.S. Takle, M. Boquet, B. Kosovi, E. Michael, D. Rajewski, R. Doorenbos, S. Irvin, M.L. Aitken, P. T Quelet, J. Rana, C. Martin, and B. Vanderwende. Lidar observations of interacting wind turbine wakes in an onshore wind farm.

[81] E Machefaux, G C Larsen, N Troldborg, M Gaunaa, and A Rettenmeier. Empirical modeling of single-wake advection and expansion using full-scale pulsed lidar-based measurements. *Wind Energy*, 2014.

[82] E. Machefaux, G. C. Larsen, N. Troldborg, and A. Rettenmeier. Single Wake Meandering, Advection and Expansion - an analysis using an adapted Pulse Lidar and CFD LES-ACL simulations. In *Scientific proceedings*, pages 50–55. EWEC 2013 Vienna, 2013.

[83] E. Machefaux, N. Troldborg, G. C. Larsen, J. Mann, and H. Aa. Madsen. Experimental and Numerical Analysis of Wake to Wake Interaction in Wind Farms. In *Scientific proceedings*, pages 100–104. EWEC 2012 Copenhagen, 2012.

[84] H. Aa. Madsen, G. C. Larsen, T. J. Larsen, N. Troldborg, and Mikkelsen R. Calibration and Validation of the Dynamic Wake Meandering Model for Implementation in an Aeroelastic Code. *Journal of Solar Energy Engineering*, 2010.

[85] Helge Aagard Madsen and Søren Markkilde Petersen. Wind Turbine Test - tellus T-1995, 95kw. Technical report, Risø National Laboratory. DK-4000 Roskilde, Denmark, 1990.

[86] J. Mann. The spatial structure of neutral atmospheric surface-layer turbulence. *Journal of Fluid Mechanics*, 273:p141–168, 1994.

[87] J. Mann. The spatial structure of neutral atmospheric surface-layer turbulence. *Journal of fluid mechanics*, pages 273, 141–168, 1994.

[88] J. Mann. Wind field simulation. *Science*, 13(4):269–282, 1998.

[89] J. Mann, S. Ott, B.H. Jørgensen, and P. Frank. WAsP Engineering 2000. *Engineering*, 1356(August), 2002.

[90] D Micallef. Mexico Data Analysis Stage V - Investigation of the Limitations of Inverse Free Wake Vortex Codes on the Basis of the MEXICO Experiment. Technical report, TU-DELFT, University of Malta.

[91] J.A. Michelsen. Basis3D - a platform for development of multiblock PDE solvers. Technical report AFM 92-05, Technical University of Denmark, Lyngby, 1992.

[92] J.A. Michelsen. Basis 3D - a Platform for Development of multiblock PDE Solvers. Dept. of Fluid mechanics, DTU. *AFM 92-05*, 1994.

[93] J.A. Michelsen. *Block Structured Multigrid Solution of 2D and 3D elliptic PDE's.* AFM 94-05 - Department of Fluid Mechanics, Technical University of Denmark, 1994.

[94] R. Mikkelsen. *Actuator Disc Methods Applied to Wind Turbines.* 2003.

[95] R. Mikkelsen, J. N. Sørensen, and Troldborg N. Prescribed Wind Shear Modelling Combined with the Actuator Line Technique. *EWEC Milan 2007*, 2007.

[96] R. Mikkelsen, J.N. Sørensen, S. Øye, and N. Troldborg. Analysis of Power Enhancement for a Row of Wind Turbines Using the Actuator Line Technique. *Journal of Physics: Conference Series*, 75:012044, July 2007.

[97] T. Mikkelsen and K.H. Hansen. Lidar wind speed measurements from a rotating spinner. *2010 European Wind Energy Conference*, 2010.

[98] A.S. Monin and A. M. Obukhov. Basic laws of turbulent mixing in the atmospher near the ground. pages 151:163–187, 1954.

[99] N.G. Nygaard. Wakes in very large wind farms and the effect of neighbouring wind farms. *Journal of Physics: Conference Series*, 524(1):012162, June 2014.

[100] S. Ott, J. Berg, and M. Nielsen. Linearized CFD models for wakes. *Risø-R-1772(EN). Risø National Laboratory, Roskilde, Denmark.*

[101] J.P. Pandolfo. Wind and Temperature Profiles for Constant-flux Boundary Layers in Lapse Conditions with a Variable Eddy Conductivity to Eddy Viscosity Ratio. *Journal of the Atmospheric Sciences*, 23(5):495–502, September 1966.

[102] H. A. Panofsky and J. A. Dutton. *Atmospheric Turbulence*. Wiley-interscience, 1984.

[103] A. Peña, S-E. Gryning, and J. Mann. On the length-scale of the wind profile. *Quarterly Journal of the Royal Meteorological Society*, 136(653):2119–2131, October 2010.

[104] A. Peña, C.B. Hasager, and J. Lange. *Remote Sensing for Wind Energy DTU Wind Energy E-Report*, volume 0029. 2013.

[105] Alfredo Peña and Ole Rathmann. Atmospheric stability-dependent infinite wind-farm models and the wake-decay coefficient. *Wind Energy*, pages n/a–n/a, 2013.

[106] S.M. Petersen. Konceptundersøgelse Nordtank NTK Måling af effektkurve. *Risø-I-799(DA)*, 1994.

[107] J.L. Phillips, S.D. Cox, A.R. Henderson, and J.P. Gill. Wake effects within and between large wind projects : The challenge of scale , density and neighbours - onshore and offshore. 44(April):1–10, 2010.

[108] S.B. Pope. *Turbulent flows*. Cambridge University Press, 2000.

[109] L. Prandtl. Über die ausgebildete turbulenz,. *Zeitschrift für Angewandte Mathematik und Mechanik*, 5:136–139, 1925. (in German).

[110] K.G. Rados, J.M. Prospathopoulos, N.Ch. Stefanatos, E.S. Politis, and A. Zervos. CFD Modeling Issues of Wind Turbine Wakes Under Stable Atmospheric Conditions. In *EWEC*, 2009.

[111] O. Rathmann, R. Barthelmie, and S. Frandsen. Turbine Wake Model for Wind Resource Software. In *Scientific proceedings*. EWEC 2006 Athens, 2006.

[112] O. Rathmann, S. Frandsen, and M. Nielsen. Wake decay for the infinite wind turbine array. pages 1–16.

[113] P-E. Réthoré. Thrust and wake of a wind turbine : Relationship and measurements. (September), 2006.

[114] P. E. Réthoré. *Wind Turbine Wake in Atmospheric Turbulence Risø-PhD-Report*, volume 53. 2009.

[115] P. E. Réthoré, K. S. Hansen, R. J. Barthelmie, S. C. Pryor, G. Sieros, J. Prospathopoulos, J. M. L. M. Palma, V. C. Gomes, G. Schepers, P. Stuart, T. Young, J. S. Rodrigo, G. C. Larsen, T. J. Larsen, S. Ott, O. Rathmann, A. Peña, M. Gaumond, and C. B. Hasager. Benchmark of wind farm scale wake models in the EERA - DTOC project. *ICOWES 2013 Proceedings*, pages 38–51, 2013.

[116] P.-E. Réthoré and N.N. Sørensen. A discrete force allocation algorithm for modelling wind turbines in computational fluid dynamics. *Wind Energy*, 15(7):915–926, 2012.

[117] P-E. Réthoré, N.N. Sørensen, and A. Bechmann. Modelling issues with wind turbine wake and atmospheric turbulence. *TORQUE Conference proceedings. URL: http://windenergyresearch. org*, 2010.

[118] P-E. Réthoré, N. Troldborg, F. Zahle, and N. N. Sørensen. Comparison of the near wake of different kinds of wind turbine CFD models, 2011.

[119] Pierre-Elouan Réthoré, Paul van der Laan, Niels Troldborg, Frederik Zahle, and Niels N. Sørensen. Verification and validation of an actuator disc model. *Wind Energy*, 17(6):919–937, 2014.

[120] A. Rettenmeier, O. Bischoff, M. Hofsäß, D. Schlipf, and J. J. Trujillo. Wind Field Analysis Using A Nacelle-Based Lidar System. In *Scientific proceedings*. EWEC 2010 Warsaw, 2010.

[121] A. Rettenmeier, O. Bischoff, D. Schlipf, J. Anger, M. Hofsäß, P.W. Cheng, R. Wagner, M. Courtney, and J. Mann. Turbulence and wind speed investigations using a nacelle-based lidar scanner and a met mast. *Presentation Proceedings of EWEA 2012 conference, Copenhagen*, 2012.

[122] Javier Sanz Rodrigo. Generation of validation datasets from complex terrain wind resource assessment campaigns. *IEA Task 31 "WAKEBENCH", 2nd Annual Meeting, Stuttgart 15 November 2013*, 2013.

[123] B. Sanderse. Aerodynamics of wind turbine wakes Literature review.

[124] B. Sanderse. Review of computational fluid dynamics for wind turbine wake aerodynamics. (February):799–819, 2011.

[125] J. Sanz Rodrigo, F. Borbón Guillén, P. Gómez Arranz, M.S. Courtney, R. Wagner, and E. Dupont. Multi-site testing and evaluation of remote sensing instruments for wind energy applications. *Renewable Energy*, 53:200–210, May 2013.

[126] A. Sathe, S-E. Gryning, and A. Pena. Comparison of the atmospheric stability and wind profiles at two wind farm sites over a long marine fetch in the north sea. *Wind Energy*, 14:767–780, 2011.

[127] A. Sathe, J. Mann, T. Barlas, W.A.A.M. Bierbooms, and G.J.W. van Bussel. Influence of atmospheric stability on wind turbine loads. *Wind Energy*, 16(7):1013–1032, October 2013.

[128] J.G. Schepers. Analysis of 4.5 years of EWTW wake measurements. Technical report, ECN, 2009.

[129] D. Schlipf. Analysis of the SWE-scanner on the Risø Nordtank. Technical report, Stuttgart Wind Energy (SWE), 2011.

[130] M. Sjöholm, A. T. Pedersen, N. Angelou, F. Foroughi Abari, T. Mikkelsen, M. Harris, C. Slinger, and S. Kapp. Full two-dimensional rotor plane inflow measurements by a spinner-integrated wind lidar. EWEA 2013, Vienna, 2013.

[131] J. Smagorinsky. General Circulation Experiments With The Primitive Equations. *Monthly Weather Review*, 91(3):99–164, March 1963.

[132] I. N. Smalikho, V. A. Banakh, Y. L. Pichugina, W. A. Brewer, R. M. Banta, J. K. Lundquist, and N. D. Kelley. Lidar Investigation of Atmosphere Effect on a Wind Turbine Wake. *Journal of Atmospheric and Oceanic Technology*, 30(11):2554–2570, November 2013.

[133] D.A. Smith, M. Harris, A.S. Coffey, T. Mikkelsen, H.E. Jørgensen, J. Mann, and R. Danielian. Wind lidar evaluation at the Danish wind test site in Høvsøre. *Wind Energy 9*, pages p87–97, 2006.

[134] J. N. Sørensen and W. Z. Shen. Numerical modeling of Wind Turbine Wakes, Fluids Engineering. *Wind energy*, 124(2):393–399, 2002.

[135] N. N. Sørensen. *General Purpose Flow Solver Applied to Flow over Hills.* PhD thesis, Risø National Laboratory., 1995.

[136] N.N. Sørensen, J.A. Michelsen, and S. Schreck. Navier-stokes predictions of the nrel phase vi rotor in the nasa ames 80 ft by 120 ft wind tunnel. *Wind Energy*, 5:151–169, 2002.

[137] R. Stoll and F. Porté-Agel. Large-Eddy Simulation of the Stable Atmospheric Boundary Layer using Dynamic Models with Different Averaging Schemes. *Boundary-Layer Meteorology*, 126(1):1–28, July 2007.

[138] R. C. Storey, S. E. Norris, K. A. Stol, and J. E. Cater. Large Eddy Simulation of Dynamically Controlled Wind Turbines using Actuator Discs. *50th AIAA Aerospace, Science Meeting January 2012, Nashville, Tennessee*, 2012.

[139] R.B. Stull. *Introduction to boundary layer meteorology.* Springer, 1988.

[140] G. Svensson, A. Holtslag, V. Kumar, T. Mauritsen, G. Steeneveld, W. Angevine, E. Bazile, A. Beljaars, E. de Bruijn, A. Cheng, L. Conangla, J. Cuxart, M. Ek, M. Falk, F. Freedman, H. Kitagawa, V. Larson, A. Lock, J. Mailhot, V. Masson, S. Park, J. Pleim, S. Söderberg, W. Weng, and Zampieri M. Evaluation of the diurnal cycle in the atmospheric boundary layer over land as represented by a variety of single-column models: The second GABLS experiment. *Boundary-Layer Meteorol*, 140(2):177–206, 2011.

[141] L. Ta Phuoc, R. Lardat, M. Coutanceau, and G. Pineau. Recherche et analyse de modèles de turbulence de sous mailles adaptés aux écoulements instationnaires décollés. LIMSI, France. Technical report, LIMSI Report 93074, 2002.

[142] T. Theodorsen. *Theory of propellers.* McGraw-Hill publications in aeronautical science. McGraw-Hill Book Company, New-York, 1948.

[143] A.M. Hansen T.J.Larsen. *HAWC2 - User manual.* DTU-Risø-R-1597, 2007.

[144] N. Troldborg. *Actuator Line Modeling of Wind Turbine Wakes, PhD Thesis.* 2008.

[145] N. Troldborg, M. Gaunaa, and R. Mikkelsen. Actuator disc simulations of influence of wind shear on power production of wind turbines. pages p271–297. Torque 2010, The science of making torque from wind, 2010.

[146] N. Troldborg, G.C. Larsen, and H. Aagaard Madsen. *Numerical Simulations of Wake Interaction between Two Wind Turbines at Various Inflow Conditions*, pages 23–25. Universidad Politecnica de Madrid, 2009.

[147] N. Troldborg, J. N. Sørensen, and R. Mikkelsen. Numerical simulations of Wake Characteristics of a Wind Turbine in Uniform Flow. *Wind Energy, 13, doi:10.1002/we.3452009*, pages 86–99, 2009.

[148] N. Troldborg, F. Zahle, P-E. Réthoré, and N.N. Sørensen. Comparison of the wake of different types of wind turbine CFD models. *American Institute of Aeronautics and Astronautics. Meeting Papers on Disc*, 4:3407–3417, 2012.

[149] N. Troldborg, F. Zahle, P-E. Réthoré, and N.N. Sørensen. Comparison of wind turbine wake properties in non-sheared inflow predicted by different computational fluid dynamics rotor models. *Wind Energy*, pages n/a–n/a, 2014.

[150] Niels Troldborg, Gunner C. Larsen, Helge A. Madsen, Kurt S. Hansen, Jens N. Sørensen, and Robert Mikkelsen. Numerical simulations of wake interaction between two wind turbines at various inflow conditions. *Wind Energy*, 14(7):859–876, 2011.

[151] Niels Troldborg, Jens N. Sørensen, Robert Mikkelsen, and Niels N. SÃÿrensen. A simple atmospheric boundary layer model applied to large eddy simulations of wind turbine wakes. *Wind Energy*, 17(4):657–669, 2014.

[152] Juan-JosÃľ Trujillo, Ferhat BingÃűl, Gunner C. Larsen, Jakob Mann, and Martin KÃijhn. Light detection and ranging measurements of wake dynamics. part ii: two-dimensional scanning. *Wind Energy*, 14(1):61–75, 2011.

[153] L.J. Vermeer, J. N. Sørensen, and A. Crespo. Wind turbine wake aerodynamics. *Progress in Aerospace Sciences*, (39):467–510, 2003.

[154] C.L. Vincent, P. Pinson, and G. Giebel. Wind fluctuations over the north sea. *International Journal of Climatology*, 31(11):1584–1595, 2011.

[155] Rados K.G. Voutsinas S.G. and Zervos A. The effect of the non-uniformity of the wind velocity field in the optimal design of wind parks. In *Scientific proceedings*, pages 181–185. EWEC 1990 Madrid, 1990.

[156] Rados K.G. Voutsinas S.G. and Zervos A. Wake effects in wind parks. a new modelling approach. In *Scientific proceedings*, pages 444–447. EWEC 1993 Travemunde, 1993.

[157] R. Wagner and M. Courtney. *Multi-MW wind turbine power curve measurements using remote sensing instruments - the first Høvsøre campaign Risø-R-Report*, volume 1679. 2009.

[158] S. Wharton, J.K. Lundquist, and N. Marjanovic. Synergistic Effects of Turbine Wakes and Atmospheric Stability on Power Production at an Onshore Wind Farm. Technical report, Lawrence Livermore National Laboratory (LLNL), Livermore, CA (United States), January 2012.

[159] D.C. Wilcox. *Turbulence Modeling for CFD*, volume 2nd Edn. DCW Industries, 2002.

[160] J.C. Wyngaard. *Turbulence in the atmosphere.*

[161] F. Zahle and N. N. Sørensen. Rotor Aerodynamics in Shear Flow. *Proceedings of the 2008 EWEC Conference, Bruxelles*, 2008.

[162] F. Zahle and N.N. Sørensen. On the influence of far-wake resolution on wind turbine flow simulations. *Journal of Physics - Conference Series 75*, 2007.

[163] F. Zahle and N.N. Sørensen. Characterization of the unsteady flow in the nacelle region of a modern wind turbine. *Wind Energy*, 14(2):271–283, 2011.